Digital, statistical and wavelet study of turbulence flow structure in laboratory plunging water waves

by

Raphael Mukaro

A thesis submitted in complete fulfillment of the requirements for the degree of

Doctor of Philosophy (PhD) in Physics

School of Chemistry and Physics
College of Agriculture, Engineering and Science
University of KwaZulu-Natal
Westville Campus
DURBAN

17 January 2014

Dedicated to my wife, daughters (Abigail and Tawananyasha) and sons (Francis and Innocent - aka 'Mr. Outdoor')

This work is also dedicated to the memory of my beloved father, Innocent Mukaro (Senior), who did not live to see this day. That his memory remain with us for ever, like the ever present waves of the ocean.

I hereby declare that the work contained herein represents my own original and unaided work except where specific acknowledgements are made by name or in the form of a reference. This dissertation has not been submitted to any other university for degree purposes.

Digital, statistical and wavelet study of turbulence flow structure in laboratory plunging water waves

Student Number : 209539663

Author email : *mukaror@ukzn.ac.za*

Abstract

This dissertation presents an experimental investigation set out to study the evolution of turbulence in laboratory generated breaking water waves. The waves propagate and break as plunging waves on a 1:20 sloping beach. The aim of the study was to investigate the spatial and temporal evolution of the velocity field and subsequent turbulence structures induced by these plunging waves as they propagate along the flume. Experimental parameters measured included free surface elevations, wave height, mean water levels, wave phase velocity and synoptic measurements of fluid velocities for five accretive runs in the surf zone. Experimental data were analyzed using digital, statistical as well as wavelet approaches, in order to derive other turbulence quantities associated with the flow.

The first set of experiments, performed in the vicinity of the break point, involved measuring the external flow characteristics of the breaker. This was done to get prior information about the breaking behaviour of the wave in terms of surface elevation, wave heights and wave velocities. 0.4 Hz monochromatic waves were generated in a glass-walled flume. A set of capacitive wave gauges were calibrated and then employed to record time series measurements of free surface elevations. Mean water levels, wave heights and phase velocities were then determined from the water level time series. Results show that as the wave propagates from deep water towards shallow water, there is an increase in the wave height, reaching a maximum height at the break point, and then decreases sharply thereafter. Cross correlation techniques were then used to determine the phase difference between the wave near the generator and the wave at various points along the flume. The local wave velocity was obtained by taking the phase difference between two points spaced 0.2 m apart. A comparison of the measured wave phase velocity, with linear shallow water and modified linear wave velocity approximations, is made at various points along the flume.

The second set of experiments involved measuring internal flow parameters of the fluid. The experimental setup for this included a progressive scan digital camera (connected to a frame grabber inserted inside a computer) that was used to capture images of the breaking wave. The flow was seeded with neutrally buoyant, white polystyrene beads. The wave cycle was imaged using twenty fields of view or phases and 100 image pairs of the flow captured at each phase. A pair of strobe lights was used to illuminate the flow when capturing a pair of images which are spaced a few milliseconds apart. Thus, image pairs of the particle image field are captured with a set time interval. A video technique called digital correlation image velocimetry (DCIV) was used to analyze the images. With this method, image pairs were cross-correlated to determine particle displacements and thereby the instantaneous particle velocities. 100 instantaneous velocity flow fields spanning the entire water column including the aerated region were obtained at each phase. This enabled the quantification of the temporal and spatial evolution of the various turbulence parameters associated with the flow. Measurements were taken at five stations across the entire surf zone. Two-dimensional velocity flow fields are presented for phases where turbulence was observed to be predominant. The instantaneous velocities measured are up to two times the wave phase speed.

The instantaneous velocity fields were then processed using phase-ensemble averaging to estimate the phase-averaged horizontal and vertical velocity fields and their corresponding fluctuating parts. Mean

flow fields obtained by averaging 100 instantaneous flow fields at each phase, show the evolution of a shear layer between the nearly stagnant underlying fluid and the fast moving crest flow. Evolution of the stream-wise and along-shore profiles of the mean and turbulent quantities such as turbulence intensity, turbulent kinetic energy and vorticity of the flow are also presented. For this breaker, peak phase-ensemble averaged horizontal velocities were observed to be of the order of 250 cm/s while the vertical was about 50 cm/s. Measurements of the forward and reverse mass fluxes indicate a mean relative density for this plunging breaker to be around 0.44.

Further statistical analysis yielded time-averaged mean horizontal and vertical velocities, root-mean-square (r.m.s) fluctuating velocities, turbulent kinetic energy and vorticity. Evolution results of these flow parameters are also presented in the form of contour plots. Vertical and cross-variation of these turbulence characteristics are also presented for each of the chosen wave phases. Results show that most turbulence parameters appear to rise steadily from the trough, then rapidly, reaching peak values just above the still water line. They also show that a relatively large turbulent motion is initially organized in the crest of the breaking wave region. As the wave crest passes, this turbulent structure will then stretch downward to the lower interior region of the water column. Measurements of the time-averaged turbulence intensities and kinetic energy reveal that vertical profiles of these parameters increase from the flume bed up to a normalized elevation, $z/h = 1.0$. Thereafter, these parameters begin to decrease towards the crest. Peak turbulence parameters were observed near the front part of the wave crest with peak values of 0.11 and 0.06 for normalized horizontal and normalized vertical turbulence intensities, respectively. Froude-scaled turbulent kinetic energy was observed to increase almost linearly from the flume bed up to elevation $z/h = 1.0$. Both normalized, time-averaged turbulence intensity components and the Froude-scaled time-averaged turbulent kinetic energy results show nearly exponential decay towards the shore.

Colour contour plots were used to visualize the evolution of vorticity as flow progressed. Instantaneous vorticity fields were observed to be characterized by patches of counter-rotating eddies. These pairs are generated at the free surface and translated as units in the direction of the flow. Eventually these high vorticity patches are observed to diffuse to the bottom of the flume reaching the flume bed after the crest has passed. While the phase speed is of the order of 150 cm/s, vortex structures were estimated to propagate with a speed of about 6 cm/s. Vorticity of the mean flow revealed a large vortex of peak value of around 150 s^{-1} developing around the shear boundary layer. The phenomenon of vortex shedding was observed in the evolution of mean flow vorticity where the tail of the initially strong shear layer vortex disintegrates as flow progresses.

Finally, a continuous, one-dimensional, complex Morlet wavelet transform was applied to synthesized test signals comprising of three sinusoids of different frequencies. This was done to determine the relationship between the wavelet spatial scales and the period of the signal, from which a one-to-one relationship was obtained. The amount of energy available at each scale of the synthetic signals was then obtained and compared against the expected root-mean-square energy. This was done to calibrate the wavelet algorithm before it was used to extract the turbulent energy of the wave available in the velocity fluctuations. The wavelet energy was compared against the statistically calculated turbulent kinetic energy, and showed very good agreement at each phase, and at each elevation. The wavelet scales in the velocity fluctuations were

then subdivided into three bands that are herein referred to as the micro, mid and macro scales. The wavelet energy spectrum of the flow shows that for the early phases of the flow, which correspond to the approach of the crest, up to 80 % of the wave energy is confined in the micro scales. For the remainder of the flow, micro scales contribute almost uniformly, about half of the maximum (40 %) shedding off excess energy which appears in the macro-scales. Mid scales were observed to contain 15 % of the total energy, almost uniformly throughout the wave cycle. Further energy analysis was performed to examine the variation of the total wavelet energy with scale at different phases of the flow. Results indicate that for phases corresponding to the approach of the crest, most of the energy lies in the micro-scales between 5 cm and 15 cm. The average wavelet energy at each phase of the flow was computed over several cycles at each elevation. Results show that for the three elevations considered, the micro-scales contain most of the energy while mid-scales have the least. The available energy of the wave decreases towards the shore.

Acknowledgements

First and foremost I would like to thank my supervisor Dr. K. Govender for successfully advising and supporting this research effort. The completion of this research was a result of his knowledge and expert advice. Not only has he been an enthusiastic and innovative teacher, but also an inspiring and dedicated mentor. From one day to the next, he has supported my ambitious plans and ideas, and had confidence in me when I doubted myself. He has been an active listener who also takes the time to give advice. He has taught me how to think philosophically, to ask meaningful questions, to approach and identify a research problem, and to precisely carry out a research plan to accomplish any goal. I acknowledge the cold winter nights that he would spent with me troubleshooting the experimental setup until things got going. I also acknowledge the immense contribution from my co-supervisor, Dr. H. McCreadie, for the remarkable suggestions and corrections to the work reported here. Without the enthusiasm, guidance, and compassion of my supervisors, I could not have completed this dissertation.

This research would not have been possible without the efforts of the many dedicated professionals from the Center for Scientific and Industrial Research (CSIR) in Stellenbosch for their valuable contribution to the success of the experimental runs. Special mention goes to the following : Dave Phelp, Kishan Tulsi, Johan Kiviet, Padhraic O'Connor and Greg Davis, for assisting us in various ways. They also constructed the beach slope, and trained me on how to run the wave maker.

Financial support from the Research Office of the University of KwaZulu-Natal through a Competitive Research Grant No. RO 022 182 is gratefully acknowledged. Financial support from CSIR is also acknowledged.

Last but not least, a very special thanks to my family for the loneliness they endured when I was doing the experiments. They may not always have understood what I was doing but gave me all the love and support. I would not have been able to complete this work without them. I would like to thank my precious daughter, Tawananyasha Locadia Mukaro, and my son Innocent Sheano Mukaro, for all the smiles they gave me while I was explaining to them the concept of turbulence and wavelet theory. That they may find as much joy in learning as I do.

Raphael Mukaro

Durban, South Africa

17 January 2014

Contents

List of symbols and notation

A	amplitude of the wave
c	wave celerity
d	still water depth
E	energy of the wave
f	frequency
f_x	image magnification factor in the x-direction
f_z	image magnification factor in the z-direction
g	gravitational acceleration
h	local water depth
h_b	water depth at the break point
h_o	mean water depth near wave generator
H	local wave height
H_b	wave height at break point
H_o	deep water wave height
k	wave number
l	length scale
k'	turbulent kinetic energy
L	local wavelength
M_x	mass flux in the x-direction
n_{rc}	normalized cross correlation coefficient
N_s	repeating number of test runs
p	pressure
R_e	Reynolds number
s	wavelet scale factor
s_{ij}	fluctuating strain rate
S_{ij}	mean rate of strain
S_{xx}	radiation stress
t	time
Δt	sampling time
T	wave period
u	instantaneous horizontal velocity component in the direction of wave propagation
$\langle u \rangle$	phase ensemble averaged horizontal velocity component in the direction of wave propagation
$\bar{u}$	time-averaged horizontal velocity component in the direction of wave propagation
u', w'	horizontal and vertical turbulence intensity components
u_{rms}	horizontal turbulence intensity
w	vertical velocity component perpendicular to the direction of wave propagation
$\langle w \rangle$	phase ensemble averaged vertical velocity component, perpendicular to the direction of wave propagation

W_A	wavelet amplitude
W_E	wavelet energy
w_{rms}	vertical turbulence intensity
W_{jk}	wavelet coefficients
x	x - position relative to still water mark on the beach
z	elevation relative to still water line, vertical coordinate

Greek symbols

α	beach slope
β	coefficient of analyzing wavelet
δ	factor for non-linear wave celerity calculation
δx	spatial separation between two points along the flume
ϵ	turbulence dissipation rate
η	displacement of the free surface relative to still water level
$\overline{\eta}$	mean water level
μ	dynamic viscosity of water
ν	kinematic fluid viscosity
ρ	fluid mass density
ρ_r	relative density of the roller
ω	angular wave frequency ($= 2\pi/T$)
ω_y	vorticity in the y-direction
Φ	phase
σ	statistical parameter - standard deviation
σ_{ij}	stress tensor
τ	wavelet translation parameter
θ	phase angle
ε_o	surf similarity parameter

Acronyms

a.c	alternating current
BIV	bubble image velocimetry
B.P	break-point
CCD	charge-coupled device
CFD	computational fluid dynamics
CRO	cathode ray oscilloscope
CSIR	council for scientific and industrial research
CWT	continuous wavelet transform
DCIV	digital image correlation image velocimetry
DAC	data acquisition computer

DIP	dual in-line package
DPIV	digital particle image velocimetry
DWT	discrete wavelet transform
IDL	interactive development language
IFFT	Inverse Fast Fourier Transform
FFT	Fast Fourier Transform
FOV	field of view
LDA	Laser Doppler Anemometry
LDV	Laser Doppler velocimetry
LED	light emitting diode
MWL	mean water level
NSE	Navier-Stokes Equation
NSWE	non-linear shallow water equations
PC	personal computer
PIV	particle image velocimetry
RANS	Reynolds Averaged Navier-Stokes
Re	Reynolds number
r.m.s	root mean square
SNR	signal-to-noise ratio
SWL	still water line
TTL	transistor-transistor logic
WT	wavelet transform

Subscripts, superscripts and overbars

$_i$	instantaneous
$'$	fluctuating component
$*$	complex conjugate
U	upper
L	lower
$\langle\cdot\rangle$	phase ensemble average operation
$\bar{\cdot}$	time average operation

Chapter 1: Introduction and background

"All achievements, all earned riches, have their beginning in an idea."

- Napoleon Hill

1.1 Origin of ocean waves

In a body of water open to the atmosphere, waves are observed that are a manifestation of forces acting on the fluid. These forces are generated by the action of wind. The forces tend to deform the fluid against the action of gravity and surface tension, which together act to maintain a level fluid surface. The wind creates a disturbance in the sea which is restored to its calm equilibrium position by the action of gravity and hence the resulting waves are called wind generated gravity waves. On the Earth's surface water waves are also caused by the rotation of the Earth. Thus it requires a force of some kind, such as would be caused by a falling stone impacting on the water to create waves. As *Dean & Dalrymple* [1] pointed out, once the waves are created, gravitational and surface tension forces are activated that allow the created waves to propagate, in the same manner as tension on a string causes the string to vibrate. The waves propagate towards the coastline where they are eventually dissipated in the form of breaking waves. The breaking process generates turbulence and vorticity which cause mixing of solutes and sediment in the surf zone (*Liiv* [2]). In water bodies exposed to atmospheric forcings, turbulence generated is the dominant mechanism governing the mass, momentum, and energy transfer processes that occur. In the open ocean, turbulence plays an important role in influencing the Earth's weather and climate through air-sea exchanges of heat and gases, sediment transport, and marine aerosol production (*Melville et al.* [3]).

1.2 Wave transformation

The coastal zone is divided into four separate zones, namely, offshore zone, the breaker zone, the surf zone and the swash zone. Figure 1.1 shows the transformation of the wave as it moves from the offshore zone, across the surf zone to the swash zone. Figure 1.2 shows a schematic sketch of the nearshore littoral region which consists of the surf and the swash zones. Positions of the still water line, (SWL) and the mean water level, (MWL) in this nearshore zone are also shown. The surf zone is the coastal region of

the ocean which contains broken waves. The surf zone is divided in two separate areas : the outer and inner regions. The outer surf zone starts at the breaking point. Here the flow is violently perturbed, highly nonstationary and turbulence is spreading in the whole water column, from the free surface to the bottom. The inner surf zone starts when the flow becomes less turbulent and extends towards the shore line. Then, the wave runs up the beach in the swash zone. The swash zone is defined as that part of the beach between the minimum and maximum water levels during wave run-up and run-down, where intense erosion occurs. The swash zone moves as the water levels vary, extending from the backwash to the limit of the run-up or up-rush. The swash generated in this region consists of two phases : run-up (onshore flow) and backwash (offshore flow). Swash processes determine whether sediment is stored on the upper beach or is instead returned to the inner surf zone and potentially transported offshore acting as a sediment conduit between the upper beach and the surf zone (*Puleo et al.* [4]). Depending on beach slope and wave conditions, total run-up is often described by two or three primary components (e.g., *Komar* [5]): (1) set-up of the mean water line due to radiation stresses induced by breaking waves (*Longuet-Higgins & Stewart* [6]); (2) fluctuations about that mean, due to the swash of incident waves producing run-up and run-down (backwash); and (3) oscillations about the mean at infragravity frequencies, such that swash periods are greater than 20 s, beyond the usual range of incident wave periods.

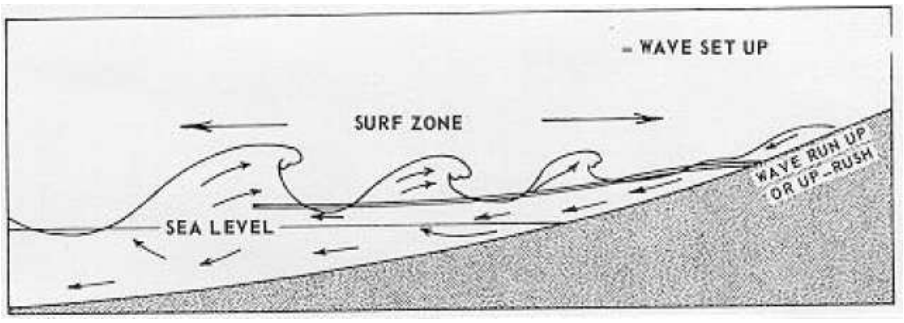

Figure 1.1: Illustration of the effects of breaking waves and wave set-up, superimposed on a storm surge (Bureau of Meteorology, 1978).

For shallow beach frontages, wave set-up can significantly increase the impact of storm tides. For a closed system (where no water leaves the flume), there has to be a return current. In a 2-dimensional wave system, as depicted in Figure 1.1, this return current, called the undertow, occurs below the trough level and flows seawards terminating in the vicinity of the break point. The undertow is generated by the vertical asymmetry (non-uniformity) of the wave radiation stress, which is caused by the wave *roller* (fluid that rides on the front face of the wave). Shear within the roller and between the roller and the fluid below, generates eddies of smaller dimensions, and so on, finally reaching micro-scales where dissipation of the wave energy occurs.

Waves that develop on the open sea propagate towards the shore, undergoing a series of transformations, the description of which presents both theoretical and experimental challenges (*Huntley* [7]). Figure 1.3 shows the wave transformation that summarizes the changes in orbital motion of water particles as the wave moves from deep water to shallow water. The free orbital motion of the water is disrupted, and water particles in orbital motion no longer return to their original position. Beginning offshore where the

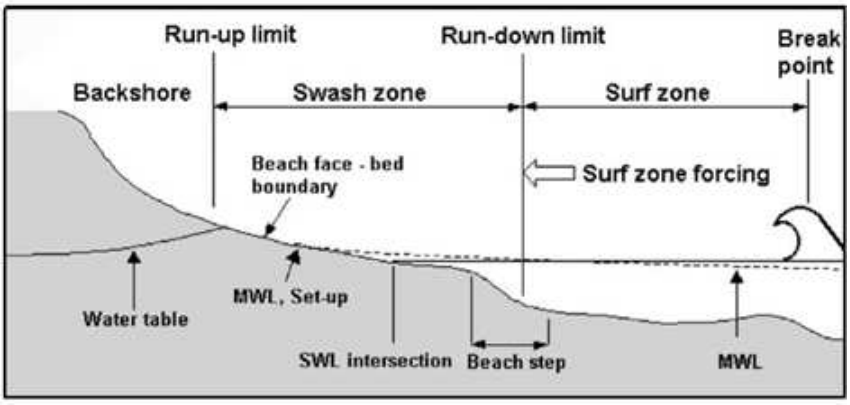

Figure 1.2: Schematic sketch showing characteristic regions of the nearshore littoral zone (*Elfrink & Baldock* [8].

water depth is sufficiently deep and constant, waves are observed to be symmetric with respect to the wave crest (*Hsiao et al.* [9]) before they began to deform due to interactions with the bathymetry. As the waves propagate from deep water to shallow water of the surf zone, they slow down, grow taller and change shape. Since the energy flux is constant, the reduction in speed results in an increase in the wave height, a process known as *shoaling*. Wave shoaling is caused by the fact that the group velocity which is also the wave-energy transport velocity, decrease with the reduction of water depth. The phenomenon of wave shoaling is directly related to bottom slope where on a gentler slope shoaling is greater as compared to a sufficiently steep slope (*Grilli et al.* [10]). At a depth of half its wave length, the rounded waves start to rise and their crests become shorter while their troughs lengthen. How high a wave will rise, depends on its wave length (period) and the beach slope. Although their period (frequency) stays the same, the waves slow down and their overall wave length shortens.

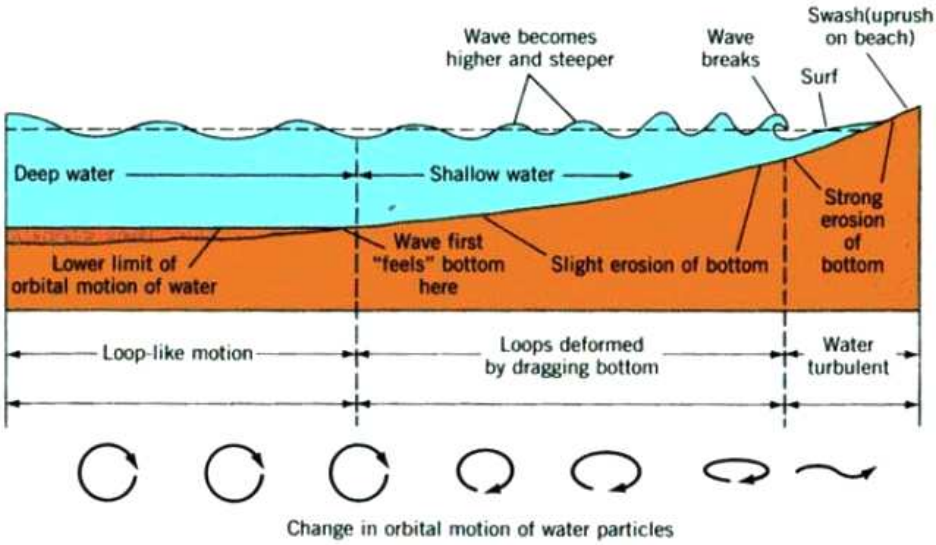

Figure 1.3: Water waves in shallow water [11].

As the waves continue to propagate, the wave heights gradually increase and the waves steepen. Due to shoaling, asymmetry of the wave and the wave height continues to increase until at some critical point where the wave becomes unstable and collapses. During shoaling, there is also a corresponding decrease

in mean water level, known as the *set-down*. This process is called *wave breaking*. This critical point depends on the wave height and the beach slope. The wave breaking process is accompanied by an increase in the mean water level, a process known as *set-up*. Breaking of waves is characterized by top of the crest falling onto the front face of the wave, forming a body of fluid, called the roller, that rides on the wave front. This process entraps considerable amount of air which bursts into small bubbles, and results in energy dissipation and the transfer of momentum to currents. The roller interacts with the fluid below it in a complicated way, exchanging energy and momentum in the process. The roller will eventually dissipate and be completely absorbed by the wave. However if breaking continues to occur, the roller will be sustained for the greater portion of the surf zone. Thus there will be a shoreward mass transport occurring above the trough level. After the wave breaks, it becomes a wave of translation and erosion of the ocean bottom intensifies.

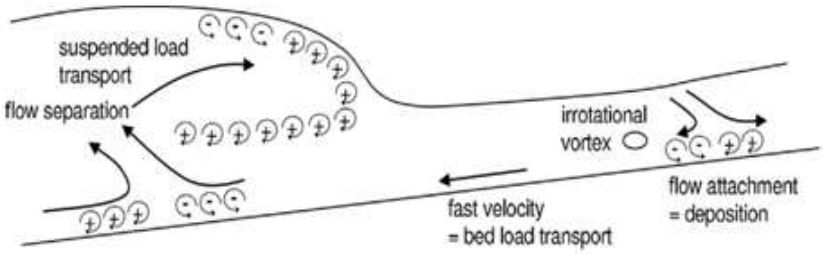

Figure 1.4: Schematic sketch of the flow structure in the surf and swash zones (*Sou & Yeh* [12]).

Figure 1.4 shows a schematic sketch which summarizes the flow structure and flow characteristics in the surf and swash zones. As pointed out by *Sou & Yeh* [12], the primary characteristic of the surf zone that differs from the swash zone is the occurrence of flow separation at the bed when the uprush bore meets with the downwash phase. Flow attachment is observed during the flow reversal.

Measurement or calculation of surf zone wave transformation is crucial for understanding and preventing storm damage, calculating shoreline evolution and cross-shore beach profile change and designing of coastal structures. In addition, a detailed knowledge of the wave breaking process is essential for coastal studies. *De Vries et al.* [13] stated that measurements of water wave characteristics in the surf zone, such as wavelength and wave height is important for monitoring, prediction of erosion, and benchmarking of numerical models. As also pointed out by *Massel* [14], a reliable estimation of the maximum wave height at a particular location is a fundamental requirement in the design of coastal or offshore structures. However, the transient nature of the flow coupled with entrained air bubbles and sediments are some of the factors that increase measurement difficulties encountered in surface elevation measurements in such flows (*Raubenheimer et al.* [15]). Coast and beach protection often involves the erection of offshore breakwaters (*Mory & Hamm* [16]). In order to protect harbours and coastlines engineers often rely on breakwater structures made out of armour units. As pointed out by *Harris* [17], theoretical developments and engineering judgment have proven inadequate for most of the needed designs and laboratory studies of many of the processes involved have been required to provide design guidance. Laboratory wave channels are useful for testing instabilities of revetments, breakwaters, seawalls and reservoirs to wave

action. Hence it is important to understand the dependence of the stability of these structures on various underlying parameters and factors (*Greben et al.* [18]). As pointed out by *Baldock & Swan* [19], the design of coastal structures is to a large extent dependent upon the description of the local wave climate, and in particular calculation of the water surface elevation and the underlying kinematics. *Tsai et al.* [20] pointed out that the prediction of wave shoaling and breaking is essential for the near-shore hydrodynamics as well as for the design of structures.

1.3 Breaker types

There are four basic types of breaking water waves. They are spilling, plunging, collapsing, and surging. When the ocean floor has a gradual slope, the wave will steepen until the crest becomes unstable, resulting in turbulent whitewater spilling down the face of the wave. This continues as the wave approaches the shore, and the wave's energy is slowly dissipated in the whitewater. Because of this, spilling waves break for a longer time than other waves, and create a relatively gentle wave.

A plunging wave occurs when the ocean floor is steep or has sudden depth changes, such as from a reef or sandbar. The crest of the wave becomes much steeper than a spilling wave, becomes vertical, then curls over and drops onto the trough of the wave, releasing most of its energy at once in a relatively violent impact. A plunging wave breaks with more energy than a significantly larger spilling wave. The wave can trap and compress the air under the lip, which creates the "crashing" sound associated with waves. If a plunging wave is not parallel to the beach (or the ocean floor), the section of the wave which reaches shallow water will break first, and the breaking section (or curl) will move laterally across the face of the wave as the wave continues. This is the "tube" that is so highly sought after by surfers. The surfer tries to stay near or under the curling lip, often trying to stay as "deep" in the tube as possible while still being able to shoot forward and exit the tube before it closes. A plunging wave that is parallel to the beach can break along its whole length at once, rendering it unrideable and dangerous.

Figure 1.5 shows an image of a large plunging wave breaking in the open ocean. After the tip of the wave overturns and the jet collapses, it creates a very coherent and defined horizontal vortex. The plunging breakers create secondary eddies down the face of the wave. Small horizontal random eddies that form on the sides of the wave suggest that, perhaps, prior to breaking, the water's velocity is more or less two-dimensional. This becomes three-dimensional upon breaking.

Surging waves originate from long period, low steepness waves and/or steep beach profiles. The outcome is the rapid movement of the base of the wave up the swash slope and the disappearance of the wave crest. The front face and crest of the wave remain relatively smooth with little foam or bubbles, resulting in a very narrow surf zone, or no breaking waves at all. The short, sharp burst of wave energy means that the swash/backwash cycle completes before the arrival of the next wave.

Collapsing waves are a cross between plunging and surging, in which the crest never fully breaks, yet the bottom face of the wave gets steeper and collapses, resulting in foam. On steeper beaches, the energy of

Figure 1.5: Image of a large wave breaking in the ocean [21].

the wave can be reflected by the bottom back into the ocean, causing standing waves (also called surging waves). This can result in a very narrow surf zone, or no breaking waves at all.

The surf similarity parameter, also known as the surf parameter or the *Irribarren number*, is a dimensionless parameter that is used to describe characteristics of ocean wave phenomena. Wave conditions generating a breaking wave are characterized by the surf similarity parameter defined as :

$$\varepsilon_o = \frac{\tan\alpha}{\sqrt{\frac{H_o}{L_o}}} \tag{1.1}$$

where H_o is the deep water wave height and L_o is the deep water wavelength and $\tan\alpha$ is the slope of the beach.

On a uniformly sloping beach, breaker type of the wave is estimated by the following values of the surf similarity parameter :

$$\begin{aligned} \varepsilon_o &< 0.5 \rightarrow Spilling \\ 0.5 < \varepsilon_o &< 3.3 \rightarrow Plunging \\ \varepsilon_o &> 3.3 \rightarrow Surging \end{aligned} \tag{1.2}$$

1.4 Characteristics of turbulent flow

A fluid that moves slowly in layers in a pipe, without mixing among the layers, is referred to as *lamina* flow. This type of flow typically occurs when the velocity is low or the fluid is very viscous. At these low velocities, the fluid tends to flow without lateral mixing and adjacent layers slide past one another

like playing cards. There are no cross currents perpendicular to the direction of flow, nor eddies or swirls of fluids (*Geankoplis* [22]). In laminar flow the motion of the particles of fluid is very orderly with all particles moving in straight lines parallel to the pipe walls. In fluid dynamics, laminar flow is a flow regime characterized by high momentum diffusion and low momentum convection ([23]).

The opposite of laminar, is turbulent flow where considerable mixing occurs and velocities are high. Turbulence is recognized as irregularly fluctuating and unpredictable motion which is composed of a number of small eddies that travel in the current. Turbulent flows consist of two parts, coherent structures and incoherent background flow. Coherent structures in a turbulent flow contain most of the energy of the flow. Usually turbulence consists of many different size eddies superimposed on each other. In turbulent flow, unsteady eddies appear on many scales and interact with each other. Figure 1.6 shows typical turbulence generated from a turbulent jet flow and shows some very distinct characteristics of turbulence. The image shows many eddies, ranging in size from large to small and also shows turbulent fluctuations at various scales. The image clearly shows the inhomogeneities in the turbulent flow, in contrast to a laminar jet [24].

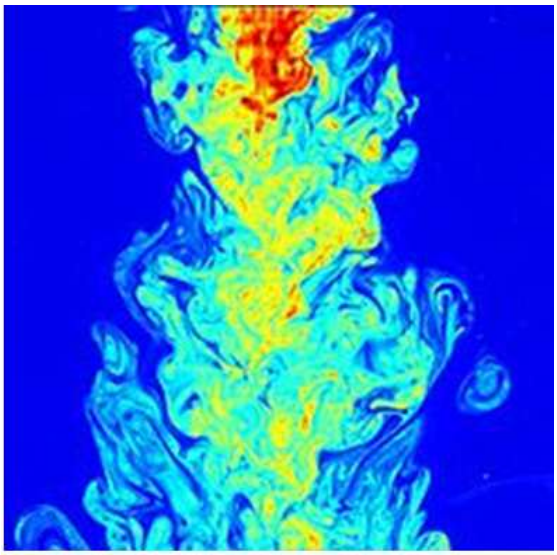

Figure 1.6: Turbulent jet flow showing distinct characteristics of turbulence consisting of many eddies of different sizes [24].

Turbulence consists of a continuous spectrum of scales ranging from the largest to the smallest. *Kolmogorov* [25] developed a theory based on energy spectrum analysis, which describes how energy is transferred from larger to smaller eddies. There is a cascade of energy from the large scales to small scales in a turbulent flow. The role of large eddies is to transfer the kinetic energy to the smaller eddies while the smallest eddies dissipate the energy (*Jalali* [26], *White* [27], *Farge* [28]). The energy "cascades" from these large scale structures to smaller scale structures by an inertial and essentially inviscid mechanism. This process continues creating smaller and smaller structures which produce a hierarchy of eddies. Eventually this process creates structures that are small enough that molecular diffusion becomes important and viscous dissipation of energy finally takes place. The scale at which this happens is the Kolmogorov length scale. In a turbulent flow, most of the kinetic energy is contained in large scale structures.

One of the most basic types of turbulent flows is that which occurs when a fluid passes a boundary, such as air over an airplane wing or the flow of oil within a pipeline. The structure and location of boundary layer separation often changes, sometimes resulting in a reduction of overall drag. The velocity of the flow must match the velocity of the wall at the surface of the boundary. A boundary layer or a turbulent boundary layer is the zone over which the average fluid velocity decreases from freestream value to zero. Drag due to boundary layer skin friction increases. Every flow is characterized by the ratio of inertial forces to viscous forces.

Leonardo Da Vinci was probably the first to distinguish a special state of the fluid motion that is irregular and unpredictable and used the term turbulence. Modern studies of turbulence started with the experiments of Osborne Reynolds in 1883, who analyzed the conditions under which laminar flows of fluids in pipes become turbulent. The study led to a criterion of dynamical stability based on the Reynolds number denoted R_e. Both laminar and turbulent flows can be characterized and quantified using the Reynolds number established by Osborne Reynolds and is given as :

$$R_e = \frac{uL}{\nu} \tag{1.3}$$

where u and L are the characteristic velocity and length scales of the flow, respectively, and ν is the kinematic viscosity of the fluid. The Reynolds number is the ratio of non-linear convective motions responsible for the flow instability, to the dissipative damping, which converts kinetic energy into thermal energy. It may be interpreted as the ratio of inertial to viscous forces present in the fluid, and for an incompressible flow, it is the only control parameter of that system. Turbulence occurs when the inertia term dominates the viscous term. Turbulent motions are variations in fluid properties and velocity due to the decay of large-scale instabilities within the flow. A treatment of turbulence naturally leads to a discussion about statistics of properties of the flow (usually velocity) and their relation to the flow Reynolds number. A critical Reynolds number exists for each geometry, below which laminar boundary layers occur, and transition to turbulent boundary layers occur if a higher Reynolds number is achieved. Often, this transition is desired since an increase in mixing and diffusion is achieved, due to turbulence. While there is no theorem relating Reynolds number to turbulence, flows with high Reynolds numbers usually become turbulent, while those with low Reynolds numbers usually remain laminar.

A turbulent flow is characterized by a hierarchy of scales through which the energy cascade takes place. There is a variation in length and time scales which is a characteristic that is in part responsible for the difficulty encountered in numerical and theoretical analysis of turbulent flows. The largest eddies in the flow account for most of the transport of momentum and energy while the size of the smallest eddies is determined by viscosity. These smallest length scales existing in turbulent flows are those where kinetic energy is dissipated into heat. The energy "cascades" from these large scale structures to smaller scale structures by an inertial and essentially inviscid mechanism. This process continues, creating smaller and smaller structures which produces a hierarchy of eddies. As the eddy size becomes so small, viscous forces become dominant the kinetic energy of the eddies is dissipated. Eventually this process creates structures that are small enough that molecular diffusion becomes important and viscous dissipation of

energy finally takes place.

In order to arrive at an estimate of the scales at which energy is dissipated, a length scale based only on the dissipation rate and viscosity is relevant. Kolmogorov introduced a second hypothesis : for very high Reynolds numbers the statistics of small scales are universally and uniquely determined by the viscosity, ν and the rate of energy dissipation, ε. With only these two parameters, the unique length scale that can be formed by dimensional analysis is the *Kolmogorov length* scale, defined as :

$$\eta = \left(\frac{\nu^3}{\varepsilon}\right)^{1/4} \tag{1.4}$$

where ε is the turbulence dissipation rate. Dissipation of kinetic energy takes place at scales of the order of Kolmogorov length η, while the input of energy into the cascade comes from the decay of the large scales, of order L.

1.5 Significance of turbulence

The turbulence generated during wave breaking is an important process in the ocean. In shallower water, the turbulence generated by depth-limited wave breaking is responsible for sediment suspension and transport through momentum and energy transfer from the waves to the sediments. Further, the breaker turbulence modifies the cross-shore and long-shore currents, which in turn affect the accretional and erosional characteristics of the coastline (*Misra et al.* [29]). The turbulence due to wave breaking is the primary dissipative mechanism causing wave energy decay in the surf zone. Wave breaking is considered to be the most visible process in which waves dissipate energy, with the organized wave energy of rollers being first converted into turbulent kinetic energy, in the form of eddies, and then dissipated into small-scale turbulent motion. The generated turbulence plays a role in the generation of fluid friction losses and fluid induced noise. In the ocean, the turbulence deviations from the mean flow greatly depend on both the deep-water wave conditions and the beach slope (*Ting & Kirby* [30]).

Although turbulence is difficult to understand, it plays a major role in many applications. The characterization of the turbulent oceanic flow and currents has many important implications in environmental studies, such as : dispersion of contaminants, harmful algae blooms or climate change. The analysis of microstructure density profiles, obtained from high-resolution measurements of conductivity-temperature and depth, is a common approach for characterizing environmental turbulent fluid dynamics. At the coast, wave-driven currents caused by wave breaking can result in a movement of sand along the shore, causing erosion or damage to structures during storms. Knowledge of these waves and the forces they generate is essential for the design of coastal projects since they are the major factors that determine the geometry of beaches, the planning and design of marinas, waterways, shore protection measures, hydraulic structures, and other civil and military coastal works. Estimates of wave conditions are needed in almost all coastal engineering studies. *Rapp & Melville* [31] pointed out that current theoretical and numerical treatments of the wave breaking process fail at the point where the surface impacts upon itself,

and models of the later stages of breaking are dependent on experimental measurements for guidance and testing. Field measurements alone cannot fill this need and therefore well-controlled laboratory experiments are necessary to advance our knowledge.

Turbulence also plays an important role in the transport or dispersion phenomena of pollutants and waste water, characterized by an interaction between different phases. The typical case is that of two-phase flows, where a diluted phase is transported within a carrying one (for instance water or air). Turbulent flow structures, entrainment and mixing rate are parameters of great interest among researches. A common civil and environmental application of turbulent diffusion theory is prediction of the mixing of pollutants in rivers and streams.

Due to its practical importance, many scientists have attempted to describe the motion of a turbulent fluid through numerical models. Although the basic equations describing turbulence are well known general principles, their solutions are incredibly complex and require tremendous computing power. These equations of motion have been analyzed in great detail, but statistical studies of the equations lead to a situation with more unknowns than equations. This means that because of "non-deterministic" fluctuations in flow properties, one cannot precisely predict the value of a flow property at a future instant by any known means, since the precise relationship is not known. There are two ways to handle turbulent flows : statistical study of the properties of the fluctuations and semi-empirical modeling of turbulent mean quantities. To reduce the number of degrees of freedom of the system of equations, one can use a turbulence model in which the effects of the discarded modes on the retained modes are modeled (*White* [27]; *Farge* [28]; *Farge* [32]; *White* [33]; *Tennekes* & *Lumley* [34]). Nobel Laureate Richard Feynman described turbulence as "the most important unsolved problem of classical physics", as no solution that unconditionally predicts the motion of a turbulent fluid has yet been found.

Understanding and modeling transport phenomena is of great importance in many application of fluid dynamics, especially in the environment, to enable understanding of the dispersion of solid particulates, and the interaction between turbulence and biological species, etc. The mathematical and physical characterization of these phenomena is the subject of research in many laboratories. Understanding and modeling the physics of turbulent motion is the basis of predicting its effects in these and numerous other examples and controlling it in engineering applications such as the design of air and surface vehicles, efficient engines for propulsion, heat exchangers and heart valves.

Rapp & *Melville* [31] pointed out that modeling breaking in the laboratory allows accurate control over the input wave parameters, and allows use of instrumentation not suited to the field. As the wave is very repeatable, the measurement point can be varied to densely sample the entire turbulent flow field under identical wave conditions. However, the inherent disadvantages of laboratory simulations are reflections due to a finite-length channel and the problem of scaling the results to full scale. An increased knowledge of the structure and evolution of the turbulent field in this regime is essential in order to further understand the role of breaking in airsea interaction and in the formation of the marine boundary layer. However, one of the most challenging aspects in describing and predicting turbulence is that the velocity fluctuates over a large range of coupled spatial and temporal scales (*Ecke* [35]). Since it is not computationally

feasible to numerically simulate a wide range of eddy scales, researchers who are interested in probing these questions must rely on experimental methods to further their understanding.

Researchers in the turbulence community have long been interested in developing a deeper understanding of the key physical mechanisms in turbulent flows. Of particular interest is the question of how eddies contribute to drag, which, if understood, could enable the development of strategies to control eddy generation, scale and organization in order to reduce drag. This would have a major impact on many industries including aerospace, transportation, energy, and chemical processing. For example, reductions in turbulent skin-friction drag over aircraft would result in significant decreases in fuel usage lowering fuel costs, increasing aircraft range, and reducing pollutant and greenhouse gas emissions. Efforts to achieve a fundamental understanding of turbulent flows remain limited mainly because of a lack of understanding of the non-linear interactions that occur between the eddies that make up the motion.

1.6 Review of previous work

In this section a brief overview is given of the scientific motivations from which this work has originated. Laboratory studies have been undertaken to study turbulence structures generated by breaking waves. Much of the work reported in literature deals with spilling waves. Plunging wave studies have mainly been limited to below the trough level of the waves. In addition, many theories and empirical formulae for the calculation of wave shoaling and the prediction of breaking have been proposed in the literature (*Tsai et al.* [20]). For wave height and wave velocity measurements, there has been a number of studies that directly tested theoretical predictions of phase velocity against field data.

Studies of beach profiles and wave breaking turbulence have mostly been conducted in small scale laboratory flumes (e.g., *Melville et al.* [3]; *Stive* [36]; *Nadaoka & Kondoh* [37]; *Ting & Kirby* [30], [38], [39]; *Cox et al.* [40]; *Chang & Liu* [41]; *Govender et al.* [42]; *Kimmoun & Branger* [43]; *Huang et al.* [44]). These studies related to breaking wave phenomena have utilized wave tanks, which are usually characterized as long, narrow channels, with a wave maker of some kind at one end. This was because researchers can utilize well-controlled experimental conditions (e.g., regular waves, a solitary wave, and a planar beach) and state-of-the-art measuring techniques.

1.6.1 Surface profile measurements

In an early investigation, *Suhayda & Petrigrew* [45] used a photographic technique involving calibrated wave poles placed across the breaker zone to measure wave phase speed. The average wave crest speed was approximated by measuring the distance a particular wave crest had moved over the interval of time and then compared to solitary theory. Maximum discrepancies were observed at the breakpoint, where measured speeds were 20 % greater than those predicted by solitary theory, and in the mid surf zone, where measured values were $\sim$ 20 % less than the predicted values. Errors in the calculation were attributed to problems in visually determining the crest of the wave and to the fact that the speed of

the crest does not represent the speed of the wave as a whole. Previous empirical formulae for breaking wave heights have been examined by *Rattanapitikon* & *Shibayama* [46] using 574 cases of published laboratory data, and found that the predictions were unsatisfactory for slopes larger than 1/10. *Stansel* & *MacFarlane* [47] used data from a series of wave gauges 0.1 m apart and fitted the crest position data to a second order polynomial, and differentiating the equation to determine wave velocity.

Yoo et al. [48] measured the celerity of incident waves obtained from oblique video imagery in the near shore. The breaking wave celerity was computed along a cross-shore transect from the wave crest tracks extracted by a Radon transform-based line detection method. The celerity from the nearshore video imagery was observed to be larger than the linear wave celerity computed from the measured water depths over the entire surf zone. Compared to the non-linear shallow water equations (NSWE)-based celerity computed using the measured depths and wave heights, in general, the video-based celerity shows good agreements over the surf zone except the regions across the incipient wave breaking locations. *Lippmann* & *Holman* [49] tested the capability of video data analysis for estimation of phase speed and wave angle of individual breaking waves. Phase speeds and wave angles were calculated using pixel intensity time series collected with a square array. Measured celerities exceeded linear theory by up to 20 %, suggesting some amplitude dispersion.

Tissier et al. [50] performed field measurements and non-linear prediction of wave celerity in the surf zone. Their work is based on an unique dataset inside the surf zone, including data for very shallow water and very strong nonlinearities. They analyzed and quantified the effects of non-linearities and evaluated the predictive ability of several non-linear celerity predictors for high-energy wave conditions. Using cross-correlation techniques, *Tissier et al.* [50] accurately determined the time lag between time series of two waves recorded by two closely spaced wave gauges, to obtain an accurate local velocity prediction. The best theoretical predictor in the form $\delta\sqrt{(gh)}$ was obtained with coefficient $\delta = 1.14$ in their case. The asymptotic behaviour of the different models for high values of the non-linearity parameter were also investigated. Comparison of their measured data and theoretical data showed that the classic bore model was inappropriate for describing wave dynamics when approaching the swash zone.

Holland [51] investigated the validity of the linear dispersion relation, $c = \sqrt{\frac{g}{k}\ \tanh\ (k\ h)}$, for depth inversion. Using field data, he showed that the linear dispersion relation was commonly leading to depth errors of over 50 % inside the surf zone, whereas the average depth estimation error was 3 - 9 % outside the surf zone.

Yoo et al. [52] estimated the celerity of breaking waves in the nearshore using advanced image processing and analysis methods to coastal video imagery. Nearshore bathmetry in and near the wave breaking zone was determined by a non-linear depth inversion algorithm involving three models : a wave breaker model, a wave shoaling model, and a wave dissipation model. The wave breaker model, composed of a modified *Miche* breaker criterion and NSWE-based celerity specification was used to compute the wave height and the water depth at the break point by utilizing video-derived wave properties such as celerity, wave period and wavelength. The wave shoaling model, composed of the Green's law and the NSWE-celerity model, was used to derive the wave height and water depth offshore of the breakpoint. The wave dissipation

model, composed of the Dally wave dissipation formula and the NSWE-based celerity model, was used to compute wave height and water depth inshore of the breakpoint. Good agreement between the predicted and the video-measured wave heights was obtained for depths ranging from 0.1 m to 3 m. Computed beach profiles matched measurements within a biased depth error of 0.06 m, on average, while computed wave heights matched measurements within 0.14 m.

Govender et al. [42] analyzed a video recording of water levels in order to extract time stacks (also referred to as a keogram by *Govender et al.* [53]) of the wave at each position along the flume. A time stack consisted of a single vertical line of pixel intensity values extracted from a sequence of video frames and stacked side by side. The instantaneous water levels were then extracted by tracking the air-water interface using suitable edge detection techniques.

Relevant theory and more discussion on previous work concerning surface profile measurements is provided in sections 2.2.3 and 5.2 of this thesis.

1.6.2 Internal flow measurements

Characterization of the internal flow of the fluid is carried out by means of suitable instrumentation like hot-wire anemometers, laser-Doppler anemometers (LDA) and more recently, with particle-imaging velocimetry (PIV). This characterization is usually done after (or simultaneously with) the water level experiments. There has been a number of experimental measurements published in literature, of turbulence generation particularly in the trough level. The first flow field measurements in the breaking region of these waves was presented by *Lin & Rockwell* ([54], [55]). A review of the available literature shows that knowledge of the flow field evolution in a plunging breaker is limited and not well understood. *Cox & Shin* [56] pointed out that our understanding of the breaking process itself is limited, mainly due to the lack of measurements. Several studies of swash zone hydrodynamics have been performed (e.g. *Cox & Anderson* [57]; *Petti & Longo* [58]; *Archetti & Brocchini* [59]; *Cowen et al.* [60]). Only a few measurements on flow structures in the aerated region of breaking water waves have been reported and among them are the work of *Chang & Liu* [41], *Govender et al.* [42], *Jansen* [61], *Govender et al.* [62], *Ryu et al.* [63] and *Huang et al.* [64]. This is mainly because entrained air bubbles which are ubiquitous in the swash and surf zones make it difficult to measure the velocity flow field in the crest of the wave (*Cox & Shin* [56]). The presence of air bubbles is known to increase attenuation of the incident light under some circumstances making it difficult to extract flow parameters in this region.

Laser Doppler techniques

Longo et al. [65] reviews mainly conceptual models and experimental work, in the field and in the laboratory, to studying turbulence of breaking waves and bores moving in very shallow water and in the swash zone. The phenomena associated with vorticity and turbulence structures measured are summarized, including the measurement techniques and the laboratory generation of breaking waves or of flow fields sharing several characteristics with breaking waves. *Longo* [66] presented measurements and analysis of

fluid velocity in spilling waves. The data were collected using 2-D Laser Doppler velocimetry (LDV) in pre-breaking monochromatic waves generated in a tank. They computed the phase ensemble average vorticity and strain rate at different wavelengths with the analysis of intermittency. The pre-breaking section was selected for convenience with which measurements could be obtained. This as they pointed out is because in the pre-breaking domain, the flow fluid is optically accessible for most of the cycle and the breaker does not entrap air bubbles which often unlock the laser signal.

Shin & Cox [67] obtained laboratory data of free surface elevation and fluid velocities (cross-shore and vertical velocities) using LDV for the case of a periodic wave plunging over an impermeable, steep 1:10 slope with a fixed bottom roughness. Measurements were conducted over 14 cross-shore locations from the outer surf zone to the swash zone with approximately 10 vertical points at each location. The vertical resolution included measurements in the bottom boundary layer and some points above the trough level. To better understand inner surf and swash zone hydrodynamics induced by strongly plunging waves, they estimated various hydrodynamic quantities, including ensemble-averaged turbulent kinetic energy and turbulence intensity. The ratio of time-averaged horizontal turbulence intensity to time-averaged vertical turbulence intensity at an elevation of 1 cm, ranged from 1.30 to 1.69 which is close to prior observations of plane wake turbulence ($u'^2/w'^2 = 1.31$). Near the bottom a large average ratio of 5.9 was obtained. The time-averaged estimate of turbulent kinetic energy was vertically uniform over the inner surf and swash zones.

Ting & Kirby [30], [38] performed LDV turbulence measurements in the surf zone. This was done in order to study the dynamics of surf-zone turbulence caused by spilling and plunging breakers. *Ting & Kirby* [30] used cnoidal waves of period 5.0 s that generated a plunging wave of wave height 12.8 cm in a flume filled with water up to 40 cm. They obtained a breaker depth index of 1.24 at the break point. For internal flow measurements, they could only measure the horizontal and vertical components of velocity independently. Phase-averaged horizontal velocity results were observed to be nearly uniform over the water depth. Normalized peak horizontal velocities $u/\sqrt{(}gh)$ were ~ 0.35 under the crest and -0.10 under the trough. Time-averaged horizontal velocity was about -0.02 at the trough level and the magnitude of the undertow decreased downwards. Turbulence intensity varied greatly over a wave cycle, and was observed to be highest under the wave front decaying rapidly after the wave crest passed. Turbulent energy was observed to decrease downwards indicating that it was dissipated while convecting downward. Transport studies of the turbulent energy also showed that horizontal advection carries turbulent energy shoreward while vertical advection carries the energy up under the wave front. Another important observation was that turbulent kinetic energy was observed to be transported landward under plunging breakers with dissipation within one wave cycle and was transported seaward under spilling breakers with much slower dissipation.

Many other authors used LDV to measure time evolution of velocities under waves propagating in the surf zone (*Cox et al.* [40]; *Petti & Longo* [58]; *De Serio & Mossa* [68]).

Video techniques

More recently, many researchers have applied PIV and its variations to the breaking wave problem. While some were able to make measurements in the entire water column, others focused on the coherent structures below the trough level where the air entrained is lower (e.g *Cox* & *Anderson* [57], *Shin* & *Cox* [67]). *Chang* & *Liu* [69] employed PIV to measure the maximum velocity and associated acceleration and vorticity of the overturning jet of a breaking wave. They were not able to make measurements in the aerated region because of the air bubbles.

Kimmoun & *Branger* [43] used PIV measurements performed in a wave tank under waves propagating and breaking on a 1:15 slope. Waves with a period of 1.275 s were generated and gave a wave height of 11.4 cm in water depth of 70.5 cm. They measured instantaneous velocity field over the entire surf zone by splitting the full field into 14 smaller and overlapping windows of size $37 \times 37\ cm^2$. An instantaneous full velocity field was obtained by combining the 14 instantaneous results. Such a mosaic technique was used by *Melville et al.*, [3] for wave breaking in deep water. Synchronization was done using pre-defined impulse TTL signals. The first TTL pulse started wave gauge data acquisition and the wave maker simultaneously, and the second one, 163.2 s (128 wave periods) later, started the PIV image acquisition. This technique allowed them to obtain a 1 ms precision (electronic precision of the TTL generator) on the synchronization between the different runs. A double charge-coupled device camera with a resolution of 1008×1018 pixels and 256 grey intensity levels was used for capturing the images. Laser pulses were used for synchronizing data acquisition. A total of 45696 image pairs were captured and processed. Phase averaging was performed using 64 instantaneous fields at each phase. Local measurements were synchronized with each other using pulsed TTL triggers and wave gauge data. They were able to measure the complete time-space evolution of the velocity field over the entire surf zone and used contour plots to present their results. Velocities were observed to be positive (shoreward) under the crests, in the entire water column and negative (seaward) below the troughs. Velocity maxima in non-dimensional form were around unity near the tops of the crests at the beginning of the plunging and reached 1.35 just after the splash-up phase. Negative velocities were around -0.4 under the troughs. Fluctuating intensity was observed to be maintained by the moving breaking process and declined after the passage of the bore. The fluctuating intensities have values close to zero under the trough on the back-side of the incipient dominant wave, and around 0.05 under the trough of the wave just behind the propagating bore. Maximum Froude-scaled turbulent kinetic energy was found to be about 0.4, while non-dimensioned phase average vorticity was 3.4. Void fraction was estimated by means of light-intensity image analysis and vertically integrated velocity considerations in the domain. Light scattering theory with the Lambert's law was used to relate void fraction to light intensity. In order to relate void fraction to light intensity, light scattering theory with a Lambert law was used. An exponential decay of void fraction with depth was obtained below the mean sea level, with a good fit to the *Hoque* & *Akoi* [70] semi-theoretical law. Reynolds shear stress and fluctuating shear stress were also determined, and showed that near the bed, Reynolds stress is always positive, except near the splash-up region. This means that transfers very close to the bottom would be directed offshore except during the strong splash-up event. Near the bed, fluctuating stress values were

around -25 cm^2/s^2 which is also agrees with values observed by *Stansby & Feng* [71].

Misra et al. [72] used PIV to understand the detailed dynamics of turbulence generated in a spilling breaker by studying the mean and turbulent flow structure of a weak hydraulic jump. Images were subdivided into finite windows of size 16×16 pixels with 50 % overlap in the horizontal and vertical directions. Velocity measurements were made with a resolution of 0.184 cm for both horizontal and vertical directions. Convergence of turbulent statistics was checked by calculating running averages of the turbulence statistics over the entire ensemble for one measurement point in the crest and another in the trough part of the wave. A conditional averaging technique was used to calculate ensemble-averaged properties of the flow. Vertical profiles of the mean horizontal velocity were presented for two different cross-shore positions. Contour plots were used to present the whole spatial map of the flow field. Mean horizontal velocities were observed to be nearly uniform around mid-depth. Vertical velocity was found to be almost an order of magnitude smaller than the horizontal velocity reaching peak values of 20 cm/s downstream of the toe. A thin region of negative vorticity in the breaker shear layer was also observed. The intermittency factor was derived from turbulent fluctuations of the air-water interface and found to fit theoretical distributions of the turbulent interfaces well. Maximum turbulent kinetic energy was observed at the toe of the breaker. The Reynolds shear stress was found to be negative suggesting that momentum diffuses upward in the shear layer from the flow underneath. Just below the mean surface, the Reynolds stress was observed to be positive indicating a downward flux of momentum from the reverse-flow region into the shear layer. Their results further suggested that breaking is driven by a surface-parallel adverse pressure gradient and a stream-wise flow deceleration at the toe of the breaker.

Huang et al. [64] performed a laboratory study of turbulence and wave energy dissipation of spilling breakers in a surf zone. They measured 2-D instantaneous velocity fields of breaking waves on a 1:20 slope beach. They used seven fields of view to reconstruct a continuous flow field in the entire surf zone. Mean and turbulence quantities were extracted by ensemble averaging of 25 repeated instantaneous measurements at each field of view. The measured velocities were analyzed to yield the distribution and evolution of turbulent kinetic energy, mean flow energy, turbulence dissipation rate and total energy across the surf zone. Their results showed that significant turbulent dissipation occurs initially in the roller region at the frontal wave crest and then spreads to the entire wave crest region after the establishment of a turbulent bore. They associated turbulent dissipation below the trough level with the coherent descending turbulent structures from the crest region. Vertical profiles of the turbulence dissipation rate showed an exponential decay from the crest to the bed. Time averaged turbulence and dissipation rates obtained were normalized and Froude scaled and compared with measurements by *Govender et al.* [73]. The energy distribution and the total energy variation was also investigated. By tracking a particular breaking wave across the surf zone, it was observed that at the incipience of wave breaking, the total energy is mainly composed of 50 % potential energy and 50 % kinetic energy of the mean flow. The energy redistributes and contributes to turbulent fluctuations in the bore region in the form of turbulent kinetic energy as the breaking wave progressed. In the surf zone, it was observed that 70 % of the total energy of the incident energy was dissipated within a horizontal distance of one wavelength.

Roussinova et al. [74] reported on measurements of the instantaneous velocity fields in a smooth open

channel flow. These were analyzed using proper orthogonal decomposition (POD) to expose the vortical structures. These POD results revealed the existence of hairpin vortices of different sizes and energy levels. Most of the large eddies are elongated and inclined toward the boundaries in the streamwise direction.Their results also revealed patterns of strong ejection and sweep events which are common features in wall-bounded flows. They further observed that the distribution of the uniform momentum zones was consistent with the location of the vortices and their induced flow. They also noted that while POD exposed the large- and small-scale structures based on the amount of turbulent kinetic energy, the quadrant analysis performed on the PIV maps showed the spatial distribution of the events related to the momentum transport.

Sou et al. [75] studied the evolution of turbulence structure in the surf and swash zones using PIV Monochromatic waves with a period of 2.0 s were generated in a water depth of 27 cm, giving a plunging breaker with an incident wave height of 2.46 cm. PIV measurements were made at four different cross-shore locations where 6000 images pairs were acquired. Images were processed for instantaneous velocity using a central-difference form of the dynamic sub-window PIV outlined in *Cowen & Monismith* [76]. The images were processed four times using different interrogation window sizes. Phase-averaged mean flow fields showed that a shear layer occurred when the uprush of the bore interacts with the downwash flow. The evolution of turbulent kinetic energy was also presented. Turbulent kinetic energy results indicate that in the outer surf zone,, bed generated turbulence contributes minimally to the total energy during the downwash phases. Using the same PIV technique, *Sou & Yeh* [12] investigated the flow structure of oscillatory broken waves within surf and swash zones of a laboratory flume. They subdivided and imaged the wave cycle into 30 fields of view. In addition to presenting velocity flow field results, they also presented phase dependent vertical profiles of horizontal velocity averaged across the field of view. From the resolved spatial distribution of the velocity fields, they were also able to directly compute phase averaged vorticity of the flow, whose maximum intensity was observed at the shear layer. An important observation from their study was that the internal flow circulation is generated at the flow reversal phase as the flow near the bed responds to the gravitational force earlier than the flow in the upper water column, where the uprush momentum is sustained later in phase. Also the magnitude of the downwash velocity in the swash zone was found to be greater than that of the uprush process.

Ting & Nelson [77] measured the instantaneous turbulent velocity field created by the breaking of spilling regular waves on a plane slope. The measurement plane was located at a height of about 1 mm above the bed. The measurement area encompassed the region where the large eddies generated at incipient wave breaking impinged on the bottom inside the surf zone. A total of 30 trials were conducted under identical experimental conditions. In each trial, six consecutive wave cycles were recorded. The measured velocity fields were separated into a mean flow and a turbulence component by ensemble averaging. The instantaneous turbulent velocity fields were analyzed to determine the occurrence frequency, location, geometry and evolution of the large eddies, and their contributions to instantaneous shear stresses, turbulent kinetic energy and turbulence energy fluxes. The two-phase flow measurements showed that the velocity and displacement of large solid particles on a smooth bed were significantly affected by the magnitude and direction of turbulence velocities. Overall, the study examined the kinematic and dynamic

properties of large eddies impinging on the bed and the interaction of these large-scale turbulent flow structures with the mean flow. The study also highlighted the important role of large eddies in sediment transport.

Govender et al. [42], [73] and [78] performed some work similar to that in the present study. Some of their experiments were performed in the same laboratory as the one used here, but using a hinged wave maker. *Govender et al.* [42] used video images to study surf zone wave and roller structures and flow fields, generated by both spilling and plunging waves breaking on a 1:20 slope. Measurements were performed at three stations. Velocity flow fields were measured using DCIV while water levels and roller geometries were determined through gray scale filtering of the video images. The flow was seeded with neutrally buoyant particles. The fluid was illuminated with strobbed light sheet. A progressive scan charge-coupled device camera that was connected to a computer through a frame grabber, was employed to capture images of aeration and illuminated seed particles. Two video images of the aerated and seeded flow, which were separated in time by a few milliseconds were then captured at 12 wave phases. At each phase 150 image pairs were captured. Cross-correlation techniques were then employed to extract velocity flow fields from the images. A 24×24 pixels interrogation window in one image was cross-correlated with a corresponding subimage in the second image. The position of the correlation peak provided a measure of displacement of the structure in the second subimage relative to that in the first. The velocity at the location of the interrogation window was then obtained by dividing the displacement of the structures in the subimages by the time interval between the images. The interrogation window was then moved vertically and horizontally in steps of 6 pixels and the cross-correlation repeated until velocity fields of the entire images were obtained. Spatial distances in the video images were calibrated using a board onto which grid lines spaced 5 cm apart were marked. The board was placed in the object plane of the camera and some images of the board captured. A conversion factor was then obtained by examining the number of pixels in a specific distance of the calibration image. A sensitivity analysis of the velocity was performed to determine the influence of the ensemble and bin sizes on the convergence of the estimated mean and turbulent velocities. Phase-ensemble averages horizontal and vertical components of velocity and turbulence intensities were then calculated. Time-averaged horizontal velocities, turbulence intensities and turbulent kinetic energy were then determined by averaging across the wave phase. Vertical profiles of these parameters were also presented. Significantly higher velocity and turbulence intensity magnitudes were obtained above the trough levels. In the crest, velocities are $\sim$ 200 m/s and $\sim$ 25 m/s near the trough, for plunging wave at a station located 1.0 m from the break point. For the same station, peak values of turbulence intensity were 180 m/s for the horizontal and 130 cm/s for the vertical. *Govender et al.* [79] reported on the video DCIV measurements of mass and momentum fluxes and kinetic energy in laboratory waves propagating and breaking over a bar. These experiments were conducted in a different facility with a different flume geometry to the one used by *Govender et al.* [42]. The bottom profile of the flume consisted of a 1:20 up slope followed by a 0.1 m flat section forming a crest of the bar and then a 1:10 down sloping section. Waves with a period of 1.5 s and a deep water wave height of 7.4 cm were generated by means of a piston type paddle. The wave began to overturn at the top of the bar, forming a plunging breaker. Waves were video imaged at various positions along the flume. Instantaneous

velocity fields were obtained using DCIV with a 24×24 pixeks interrogation window that was moved in steps of 6 pixels, as described above. The trigger delay was adjusted to capture 150 image pairs of the wave at 12 phases. Two sets of measurements were made, one with the strobe light sheet placed ~ 10 cm from the glass wall. The other set of measurements had the light sheet about 25 cm from the glass wall (at the center of the flume). They observed that turbulence measured at a distance of 10 cm from the wall is not significantly affected by the wall. Undertow measurements at a horizontal distance ~ 0.37 m from the peak of the bar gave peak values of $\overline{u}/\sqrt{gd} \sim 0.08$ and 0.18 for the forward flux. Average relative density estimates obtained ranged between 0.6 and 0.8. *Govender et al.* [78] performed DCIV measurements of the flow fields and turbulence using data reported in *Govender et al.* [79]. Velocities obtained were in the order of 120 cm/s (equal to the wave phase velocity) in the crest, and ~ 10 cm/s in the trough section of the wave. Peak turbulence intensities observed for the crest reached values of ~ 40 cm/s while below the trough levels, they were of the order of 5 cm/s or less. Peak normalized turbulent kinetic energy values of 0.15 were observed at elevations above the still water line.

1.6.3 Application of wavelets to turbulent flow

Wavelets are basis functions which are localized in both space and scale and they can express the frequency category of a signal at a given time or position. Wavelet transform is performed locally on the signal, and the formations and collapses of special structures in a signal can be identified. The time-frequency localization characteristic of wavelet transform enables the detection of the locations of singularities and discontinuities in a signal, which is impossible with ordinary Fourier analysis. Additional interesting applications of wavelets can be found in function approximation, neural network systems, solving partial differential equations and analysis of turbulence in fluid mechanics.

The idea of using the continuous wavelet transform (CWT), to study fluid turbulence was introduced by *Farge* [32], in which some new concepts such as local intermittency, wavelet power spectrum, decomposition energy were introduced with application potentials of the wavelet transforms for turbulence analysis. Several wavelet methods may be used to study turbulence. The time-scale cross section method yields a qualitative picture of turbulence structures occurring at different times and different scales. The wavelet variance method provides a relatively objective estimate of the principal scales, while the wavelet cross correlation helps in identifying motions that are most important in turbulent transport and spatial coherence. The wavelet analysis can also be used to decompose the data for different scales and to detect coherent structure objectively by using the transform coefficient at the principal scale detected by the variance method (*Collineau* & *Brunet* [80]). These methods can help researchers to unfold the data for hidden information that is difficult to obtain from traditional spectral analysis and thus can provide a useful tool for understanding multiscale phenomena in turbulent flows.

Background and some applications of the CWT-based tools such as wavelet coefficient, wavelet spectra for meteorological data and geophysical turbulence were presented by *Kumar* & *Foufoula-Georgiou* [81] and *Torrence* & *Compo* [82]. *Camussi* & *Guj* [83] used orthogonal wavelets and the DWT to identify time information of coherent structures of wind turbulence. *Bienkiewicz* & *Ham* [84]; *Jordan et al.* [85] and

Geurts et al. [86] detected cross correlation between turbulence and induced pressure in the time-frequency plane using the CWT-based wavelet spectral tool. *Kareem & Kijewski* [87] reviewed recent developments and future promise of the time-frequency analysis with emphasis in its applications to correlation detection and system identification, moreover, some higher-order CWT-based tools such as wavelet coherence and wavelet bi-coherence have been also introduced. *Torrence & Compo* [82] investigated time series associated with El Nino/South oscillations phenomena to compare wavelet analysis techniques with results already known.

Wavelet techniques have been applied to observe coherent vortical structures in different turbulent flows (*Huang et al.* [88]; *Schram et al.* [89]; *Camussi & Felice* [90]; *Mallat* [91]). *Longo* [66] used wavelet techniques to analyze velocity signals measured by LDV in the pre-breaking region. In this study, no data is available in the surf zone because LDV is ineffective in the aerated region due to signal drop-out caused by the air bubbles. Vortices were found that have lengths scales ranging from ten times the Kolmogorov microscale to one wavelength.The contribution of different scale vortices was computed and micro-size vorticies and mid-size vorticies were observed to carry most turbulence energy under the wave crest.

Seena & Sung [92] developed a methodology for the selection of wavelet spatial scales to educe dynamic structures in a turbulent cavity flow. The complex Morlet wavelet transform was applied to both the temporal and spatial fields to extract structures from the oscillating shear layer. A one-to-one relationship was obtained between the wavelet spatial scaling and the wavelength. Transformed images of the vorticity, velocity and pressure fluctuations captured the vortical structures at each spatial scale. The contributions of different wavelet scales to the Reynolds stresses was presented. Energy analysis was also performed to examine the contributions of each structure. The energy of only the first four dominant scales were considered. The energy at each scale was then normalized by the maximum total energy. The energy profiles revealed an accumulation of energy in the larger scales for increasing distance from the cavity. The maximum energy gained by the largest structure was 90 % of the total energy prior to impinging on the trailing edge. They also observed that smaller scale features dissipated as the convected downstream due to viscosity effects. The contributions of different wavelet scales to the Reynolds stresses showed that the first two scales of size 0.24 and 0.114 made major contributions to the Reynolds stresses and captured the most energy containing structures of the flow.

An up-to-date review on the application of wavelet techniques in computational fluid dynamics can be found in *Schneider & Vasilyev* [93]. Further review of previous work on the application of wavelet transforms is also given in sections 9.1 and 9.4 of chapter 9.

1.7 Scope of the present work

The scope of this dissertation is to present the concepts and the experimental methods developed to study the evolution of velocity flow fields and turbulence structures in a plunging breaker. This involved the use of well-controlled laboratory experiments. Measurements were performed in the vicinity of the break

point in plunging laboratory waves. Experimental data indicating the nature of the turbulence generated are presented along with the statistics of water surface displacements, wave phase velocities as well as mean water levels in this turbulent flow. Images of the breaking waves were captured by a digital camera. By employing cross-correlation techniques, velocity flow fields were extracted from the images. Statistical and wavelet analysis were further performed on the velocity data to further understand the evolution of the generated turbulence. Results of velocity flow fields, and other turbulence parameters derived there from, are also presented in the form of contour plots. Evolution of the vertical and cross-shore profiles of the parameters as phase progresses are discussed. Our experimental evaluation of the turbulent dynamics of the flow was stimulated by the need for such data in developing turbulence modeling of these flows, as well as to enable detailed comparison with direct numerical simulations.

1.7.1 Objectives

The main objective of this dissertation is to study breaking wave transformation and document detailed statistics of mean and turbulence flow structures associated with waves breaking on a sloping artificial beach. The study was set out to investigate the fundamental characteristics of the turbulent flow structure in the vertical and cross-shore plane as plunging waves evolved from the outer surf zone. As pointed out by *Sou & Yeh* [12], little attention has been focused on the flow structure of a plunging breaker. In attempting to fulfil this objective, a series of experiments have to be performed to examine the sea level rise and variability and to determine the temporal and spatial distribution of the evolution of the turbulence characteristics in the entire water column.

The first part involved measuring the external flow characteristics of regular plunging waves propagating along a 20 m long flume fitted with a 1:20 plane slope. To achieve this, monochromatic waves of a particular frequency have to be generated by a wave maker fitted in a laboratory flume. The waves should break as plunging waves at some point along the sloping beach. A set of parallel-wire capacitive wave gauges have to first be calibrated and then employed to measure statistics of the free surface elevation in the vicinity of the break point, before and after the break point. These measurements are expected to provide an insight into the wave breaking behaviour, in terms of the break point, mean water level, wave height and wave phase speed at various points along the flume. Quantification of these mean macroscopic properties of breaking waves are a necessary prerequisite for more detailed experiments involving internal fluid velocity measurements that constituted the second part of this study.

For these internal fluid flow measurements, DCIV techniques are intended to be employed to capture images of the breaking wave using a digital camera. This would enable the study of phase evolution of velocity flow fields and turbulence dynamics generated in the plunging breaker. The study would involve the investigation of phase averaged kinematics of the breaker obtained from the instantaneous velocity flow fields. Digital signal processing techniques are to be employed to experimentally study the phase evolution and transport of turbulence and coherent structures generated. This involved developing processing algorithms required to correlate the locations of particle clusters within the images so as to estimate the fluid velocity. The temporal and spatial distributions of turbulence characteristics in the

breaking process will then be examined by further analysis of the velocity fields. The analysis is expected to yield other turbulence characteristics such as phase ensemble averaged velocities, velocity fluctuations, turbulence intensity, turbulent kinetic energy and vorticity of the flow and how these characteristics affect the behaviour of the flow.

The key research questions which this thesis aim to address are :

- how the wave height and wave phase velocity of the generated breaking wave vary along the flume.
- how the velocity flow fields evolve spatially and temporally with phase.
- how the velocity flow field components, turbulence and vorticity fields of the flow vary with time.
- how the vertical and horizontal mean and fluctuating velocity profiles vary with phase as flow progresses.
- how turbulence intensity, turbulent kinetic energy and vorticity evolve as flow progresses.
- how the energy contribution by the scale bands varies with phase.
- how much of the wave energy the different wavelet spatial scales contribute to the motion.
- how eddies of different sizes exchange their energy.
- how the energy in the wave varies with elevation.

In attempting to answer the key questions raised above, the following secondary objectives have been identified. More specifically, the research herein has the following detailed objectives :

- Firstly, to identify suitable PIV velocity measurement technique.
- To calibrate an array of wave gauges that will be used to record water level measurements in the flume. These water level measurements are to be performed first as they enable us to get prior knowledge of the breaking behaviour of the wave to be used in the experiment.
- The entire wavelength is too large to fit into one field of view of the camera, so the flow has to be divided into mosaics (or phases), and the measurement system used to measure the spatial and temporal evolution of the velocity field in the turbulent flow at each wave phase.
- To be able to develop digital signal processing algorithms to extract instantaneous velocity flow fields from the captured images, and perform phase ensemble averaging to get the behaviour of the mean flow.
- To further analyze the velocity fields, to extract other turbulence parameters such as turbulence intensity, turbulent kinetic energy and vorticity of the flow.
- To be able to present the phase evolution results and turbulence results in the form of colour contour plots. Such flow visualization techniques are powerful tools with which to experimentally show the phase evolution and transport of turbulence structures. In addition, vertical and cross shore variation of turbulence parameters will also be examined.
- The final objective is to determine how much of the wave energy is contained in the wavelet scales of the velocity fluctuations data. The wavelet transform is the analyzing tool proposed to be used to accomplish this task.

The work in this study follows closely in the footsteps of the above reported previous work by *Govender et al.* [42],[78], [79], [94], in terms of the same DCIV techniques employed. However, the present study provides yet another set of data to validate numerical models. The most notable differences are :

1. *Govender et al.* [42], [73], [94] did not consider wave celerity measurements in all their experimental results, so this is something different from their experiments.
2. *Govender et al.* [42], [94] used a 0.4 Hz and a 11cm deep water wave height whereas in the present experiment a 0.4 Hz, 12 cm wave was used. This resulted in a wave height at break point which is 34% bigger than that obtained by *Govender et al.* [42], [73], [94]. This small increase in wave height at the paddle resulted in a much more dynamic breaking wave, resulting in more turbulence in the flow.
3. Another notable difference is the wavelet analysis of velocity fluctuations which *Govender et al.* [42], [79], [94] did not address at all. This was done to determine how the wave energy is distributed among the various scales of the flow and how this varies as flow progresses and at different elevations.
4. A comparison between the statistically calculated turbulent kinetic energy and the energy obtained from the wavelet coefficients is also work that *Govender et al.* [42], [73], [94] did not consider.

1.7.2 Thesis layout

This dissertation starts by discussing the experimental facility and set up used, the developed instrumentation as well as measurement procedures. Measurement results of the temporal and spatial phase evolution of velocity flow fields and turbulent structures in the surf zone then follow. Results of vorticity of the turbulent flow are also presented. Results of the wavelet analysis of velocity fluctuations are compared against turbulent kinetic energy.

The thesis is organized as shown in Figure 1.7. It consists of ten chapters that have been divided into four main sections, viz, : introduction, methodology, experimental results and conclusions.

Chapter 1 gives a brief overview of the wave transformation and the turbulence generated as a result of breaking. Previous studies of the structure of turbulence generated by breaking water waves are mentioned. Statement of the problem to be solved and objectives of the dissertation are outlined.

Chapter 2 is intended to serve as an overview to the fundamentals of the theoretical concepts used in the study of turbulence. It gives the basic theory of turbulence that will be used throughout this thesis.

The experimental facilities, setup and instrumentation that were employed to perform the current research are presented in **Chapter 3**.

The experimental techniques, procedures and methodology that were employed to study the phase evolution of velocity flow fields and other turbulence parameters are discussed in **Chapter 4**. This chapter explains data reduction techniques on how instantaneous velocity fields are extracted from the corresponding image pairs. Data-analysis algorithms to estimate the instantaneous air-water interface and velocities are developed.

Experimental results are presented and discussed in separate chapters from chapters 5 to 9.

Chapter 5 presents results of water level measurements obtained in order to get prior knowledge of the breaking wave under investigation. Starting from the water level time series, results of mean water levels,

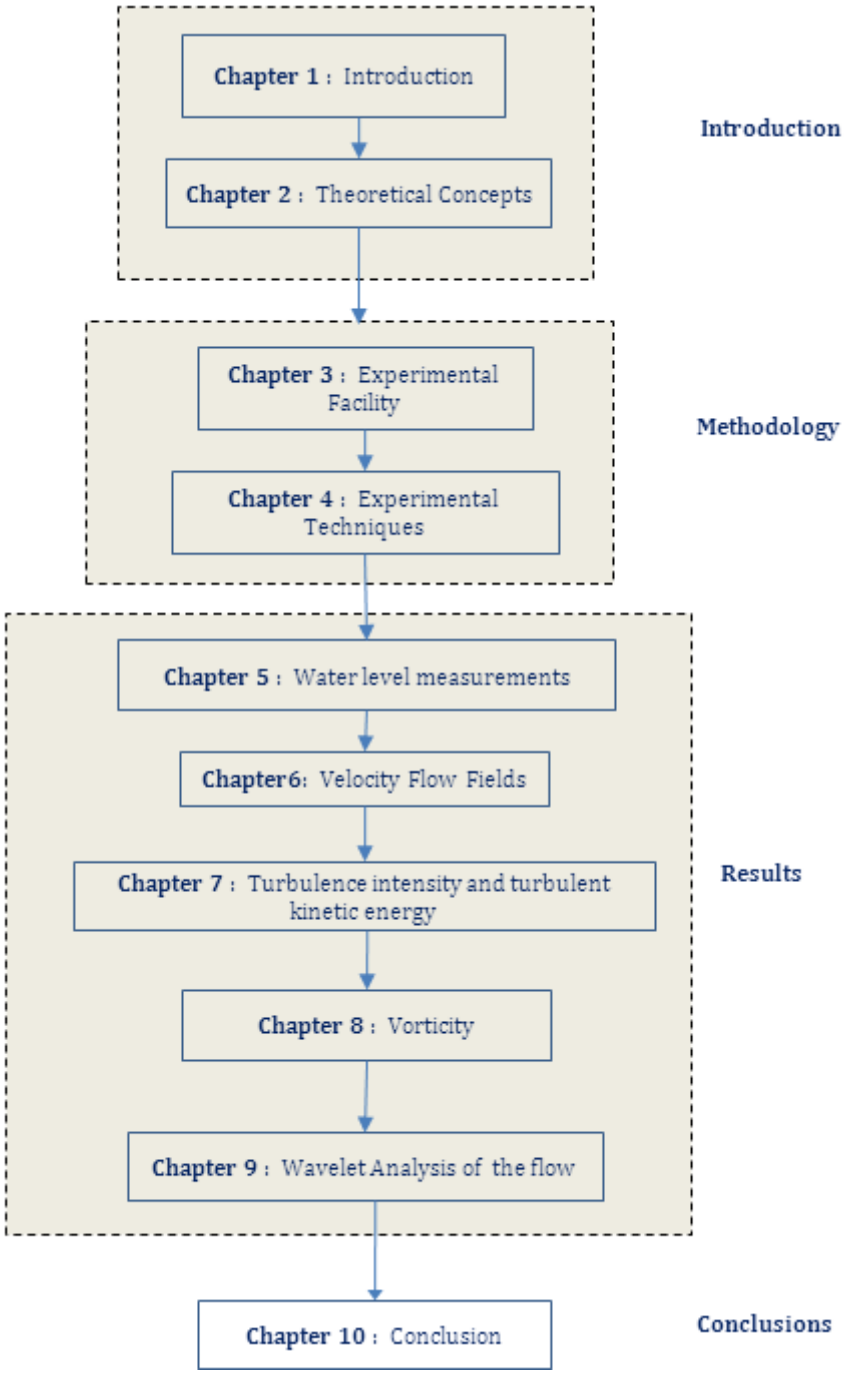

Figure 1.7: Schematic showing organization of this thesis.

wave heights and wave phase velocities obtained at each position along the flume are presented.

Chapter 6 provides detailed results of the evolution of the velocity fields for phases where turbulence was observed to be predominant. Positions of these phases in the wave cycle are discussed. Typical images of the breaking waves at a few selected phases are presented. This is then followed by the instantaneous velocity fields and the phase ensemble averaged fields. Colour contour plots are used to reveal the evolution of these fields. Their vertical and cross-shore variation is also presented. Time-averaged results of the velocity flow fields is also discussed together with the accuracy of the PIV method employed. Fundamental characteristics of the flow structure in the vertical cross-shore plane as plunging

waves evolve from the outer surf zone are presented.

Chapter 7 provides turbulence intensity and turbulent kinetic energy derived from the velocity fields. Their vertical and cross-shore distribution is also examined. The ratio of horizontal to vertical turbulent intensities is also discussed. Time-averaged turbulent kinetic energy results are presented and a comparison is made with other results from literature.

Chapter 8 presents results of the evolution of the vorticity field of the fluid as flow progresses and its vertical variation with depth. Instantaneous and mean flow vorticity components are presented for the same six phases of the flow, where turbulence is predominant.

Chapter 9 : The primary goal of this chapter is to demonstrate effectiveness of the wavelet correlation techniques. The chapter begins by exploring what is known about wavelet transforms and the characteristics of wavelet coefficients. The continuous wavelet transform is applied to the velocity fluctuations data. Firstly the total wavelet energy is calculated from the wavelet coefficients and compared against the turbulent kinetic energy obtained by statistical means. The total wavelet energy is then decomposed into three energy bands and the contribution of each band energy to the total energy is presented. Finally the variation of the wavelet energy with scales is presented and so are the phase variations of the band energies at different elevations.

Chapter 10 summarizes the major findings of this work and also outlines the contributions made by the research work that is reported in this dissertation. The chapter concludes by pointing out future directions and improvements that can be made on this research work.

Chapter 2: Theoretical concepts

" Every formula which expresses a law of nature is a hymn of praise to God. "

-Maria Mitchell (First American professional woman Astronomer, 1818-1889)

2.1 Introduction

This chapter commences by defining wave parameters often used in hydrodynamics and then introduce the simple idea of the ensemble average statistics of the turbulent flow. Water wave equations are given and so is the linear wave solution. The criterion for the wave to break is specified. In later sections of the chapter more statistical concepts are introduced that will enable a discussion of the phase and time-averaged velocity components.

2.2 Hydrodynamic concepts

2.2.1 Definition of wave parameters

A wave that is moving across a surface as a train of crests and troughs is called a progressive wave. Figure 2.1 shows a two-dimensional schematic of a sinusoidal wave propagating in the positive x direction. Significant parameters of this periodic wave are indicated. x, and z axes form a right-handed co-ordinate system with the positive x-axis pointing in the direction of wave propagation. The still water line (SWL) is the level of the water in the absence of waves, corresponding to z=0. The distance between the bed and the SWL, called the still water depth, is represented by d, so that the bed is at $z = -d$. $\eta(x,t)$ represents the displacement of the water surface relative to the SWL.

Three physical parameters uniquely define a wave train and these are the still water depth, d, the wave height, H, and the wavelength, L. For linear waves all other parameters, such as wave induced water velocities and accelerations can be determined theoretically from these three quantities. The wave height is the vertical distance between the crest and the trough, while A is the amplitude of the wave. If the wave of height H is moving in the positive x-direction, then displacement of the water surface relative to the SWL, $\eta(x,t)$, at a distance x at time t is given by :

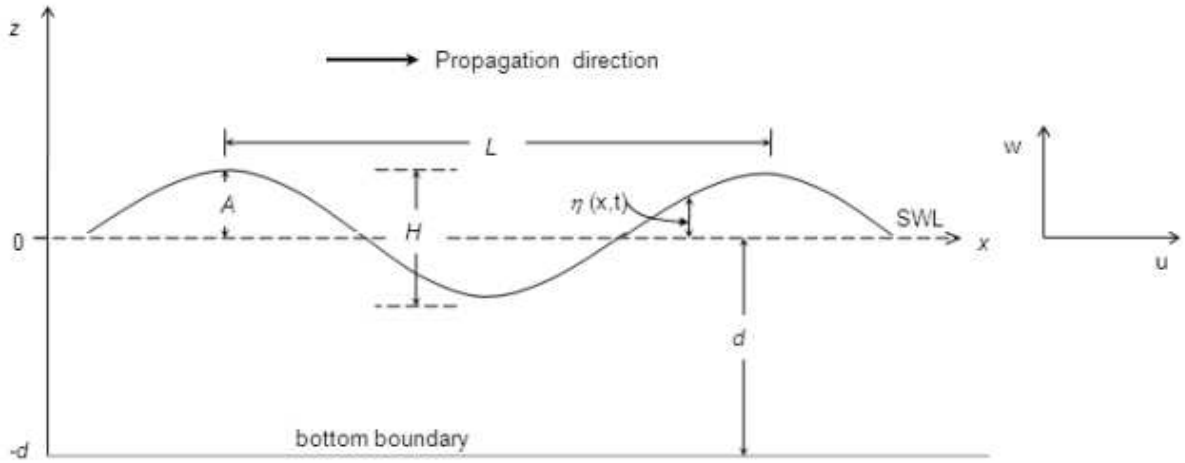

Figure 2.1: Sketch defining the $x-z$ coordinate axes and regular wave parameters. The still water line (SWL) is at z=0. u and w are velocities in the x and z directions, respectively.

$$\eta(x,t) = \frac{H}{2}\cos(kx - \omega t) \tag{2.1}$$

where $\frac{H}{2}$ is the wave amplitude, $\omega = 2\pi f$, where f is the frequency of the wave, and $k = 2\pi/L$ is the wave number. Eqn. (2.1) is the linear wave equation.

At different positions along the flume, the local water depth h, is defined as :

$$h(x) = d(x) + \overline{\eta}(x) \tag{2.2}$$

where $\overline{\eta}$ is the mean water level at a given position as further explained in section 5.2.3.

2.2.2 Water wave equations

The basis of theoretical fluid dynamics rests on the mechanics of an elementary mass of fluid. The equations of water waves are based on the conservation of mass and momentum together with the description of the pressure and the boundary conditions. In this case several assumptions are made and these are :

- that the fluid element is either infinitely small or small enough that all parts of the element can be considered to have the same velocity of translation u and the same density ρ,
- that the fluid is homogeneous, isotropic and continuous in the macroscopic sense and
- that molecular and Brownian motions within the particle are negligible.

Continuity equation

The continuity equation describes the conservation of mass in a closed system. The mass of an isolated system cannot be changed as a result of processes acting inside the system. The differential form of the continuity equation is given by :

$$\frac{\partial \rho}{\partial t} + \nabla \cdot \rho \mathbf{u} = 0 \tag{2.3}$$

where ρ is the density of the fluid and $\mathbf{u}$ is the velocity vector field.

This is the law of conservation of mass in a given space occupied by a fluid, and is known as the continuity principle and the flow field satisfying Eqn. (2.3) is termed a "non-divergent flow". In general, for a three dimensional motion the continuity equation for a fluid whose density ρ is constant in time and space, (i.e. incompressible flow) is given by :

$$\nabla \cdot \mathbf{u} = 0 \tag{2.4}$$

where $\nabla \cdot u$ describes expansion or compression of fluid elements.

Equation (2.4) requires that if there is a change in flow in a particular direction across the volume, there must be a corresponding change in flow in another direction to ensure no fluid accumulation in the volume. It simply implies that there are no sources or sinks of the fluid within the cube.

Conservation of momentum

The law of conservation of linear momentum is a fundamental law of nature, and states that if no external force acts on a closed system of objects, the momentum of the closed system is constant. After applying the continuity equation, Newtons' second law for a flow field can be stated as :

$$\rho \left(\frac{\partial \mathbf{u}}{\partial t} + \mathbf{u} \nabla \cdot \mathbf{u} \right) = -\nabla \left(p + \rho g h \right) + \mu \nabla^2 \mathbf{u} \tag{2.5}$$

where p is the thermodynamic pressure associated with the wave motion, $\rho g h$ is the atmospheric pressure, μ is the dynamic viscosity, ∇ is the gradient operator, t is time, g is acceleration due to gravity, and h is the elevation from the flume bed.

Equation (2.5) is referred to as the Navier-Stokes equations (NSE), which are a set of non-linear partial differential equations that describe the flow of a fluid whose stress depends linearly on velocity gradients and pressures. The NSE ignore the fact that the fluid is made up of discrete molecules. The terms on the left hand side represent the local and convectional acceleration terms. The first term on the right hand side represents the sum of the hydrostatic and dynamic pressure forces, while the second terms represents the viscous force. The NSE are non-linear because of the convective acceleration and the viscosity terms that appear in Eqn. (2.5). In situations where the viscous force is small, the NSE reduces to the Euler equation which is still non-linear due to the convective acceleration term. The ratio of the viscous term to the convective term is used as a measure of the relative strengths of the viscous and convective term. This ratio, estimated using the length scale l, the velocity scale u, of the process, and the kinematic viscosity of the fluid ν, results in the Reynolds number $R_e = \frac{ul}{\nu}$. The Reynolds number is often used to quantify the transition between laminar and turbulent flows.

The shallow water equations are equations of motion that can be used to describe the horizontal structure of an ocean. They describe the evolution of an incompressible fluid in response to gravitational and

rotational accelerations. The solutions of the shallow water equations represent many types of motion, including Rossby waves and inertia-gravity waves. Turbulent flows must instantaneously satisfy conservation of mass and momentum. Thus, in principle, the incompressible continuity and NSE can be solved for the instantaneous turbulent flow field. The difficulty with this approach is that an enormous range of scales must be accounted for in the calculation. To accurately simulate the turbulent field, the calculation must span from the largest geometric scales down to the Kolmogorov length scales. Even with the fastest, largest modern supercomputers, such a calculation can be achieved only for simple geometries at low Reynolds numbers.

Boundary conditions

The turbulent flow field is completely described by conservation equations of *mass*, *momentum* and *energy*, supplemented with appropriate initial and boundary conditions. In the study of waves on a free surface, the following boundary conditions are used (*Fredsoe & Deigaard* [95]):

1. At the bed, the flow velocity perpendicular to the bed is zero, as there is no flow through the bottom. For a plane horizontal bed this gives

$$w = 0 \quad for \quad z = -d \tag{2.6}$$

2. A fluid particle at the free surface must remain at the free surface giving

$$w = \frac{d\eta}{dt} \quad for \quad z = \eta \tag{2.7}$$

3. The pressure at the surface must be equal to atmospheric pressure and can be set to zero.

2.2.3 Linear wave theory

Linear wave theory is the simplest case of wave theory, under the assumption of small wave amplitude and locally horizontal bottom. This theory is referred to as small amplitude wave theory, linear wave theory, sinusoidal wave theory or Airy theory. It was developed by Airy in 1845 gives a reasonable approximation of wave characteristics for a wide range of wave parameters. A more complete theoretical description of waves may be obtained as the sum of many successive approximations, where each additional term in the series is a correction to preceding terms. For some situations, waves are better described by these higher-order theories, which are usually referred to as finite-amplitude wave theories (*Dean & Dalrymple* [1]; *Mei* [96]). Although there are limitations to its applicability, linear theory can still be useful provided the assumptions made in developing this simple theory are not grossly violated.

The assumptions made in developing the linear wave theory are :

- The fluid is homogeneous and incompressible; therefore, the density ρ is a constant.
- Surface tension can be neglected.
- Coriolis effect due to the earth's rotation can be neglected.

- Pressure at the free surface is uniform and constant.
- The fluid is ideal or inviscid (lacks viscosity).
- The particular wave being considered does not interact with any other water motions. The flow is irrotational so that water particles do not rotate (only normal forces are important and shearing forces are negligible).
- The bed is a horizontal, fixed, impermeable boundary, which implies that the vertical velocity at the bed is zero.
- The wave amplitude is small.
- Waves are plane or long-crested (two-dimensional).

The simplest wave theory is obtained by taking the wave height to be much smaller than both the wave length and the water depth. The resulting free surface displacement is expressed by Eqn. (2.1) (*Catalan & Haller* [97]) as :

$$\eta(x,t) = \frac{H}{2}\cos(kx - \omega t).$$

If the fluid flow is irrotational (i.e $\nabla \times \vec{u} = 0$) then the linear solution to the Euler equation can be obtained by using a velocity potential ϕ, such that $\vec{u} = \nabla\phi$, together with the linearized free surface boundary condition. This results in the following expressions for the potential function, particle velocities and dissipation rates (*Le Mehaute* [98]) :

$$\phi = a\frac{\omega}{k}\frac{\cosh\ k(d+z)}{\sinh\ kd}\sin(kx - \omega t) \tag{2.8}$$

where a is the amplitude of the wave ($a = \frac{H}{2}$), d is the local water depth, k is the wave number and ω is the angular frequency.

The velocity components are then obtained using $\vec{u} = \nabla\phi$ to give :

$$u = a\omega\frac{\cosh\ k(d+z)}{\sinh\ kd}\cos(kx - \omega t) \tag{2.9}$$

$$w = a\omega\frac{\sinh\ k(d+z)}{\sinh\ kd}\sin(kx - \omega t) \tag{2.10}$$

It can also be shown that the expression for pressure is given by :

$$p = \rho g a\frac{\cosh\ (kz)}{\cosh\ kd}\cos(kx - \omega t) \tag{2.11}$$

As $\eta = \frac{H}{2}\cos(kx - \omega t)$, Eqn.(2.11) can be written as :

$$p = \rho g\eta\frac{\cosh\ (kz)}{\cosh\ (kd)} \tag{2.12}$$

which at $z = 0$ gives $p = \rho g\eta$.

Wave breaking criterion and wave phase velocity

Wave heights in the near shore regions are often governed by the maximum wave heights that can be sustained in the prevailing water depths (*Nelson* [99]). Two useful dimensionless parameters are wave steepness H/L, and relative depth d/L. The stability of water waves is characterized by the *steepness*. A theoretical maximum value for the steepness was derived by *Miche* [100] and is given by :

$$\frac{H}{L} = \frac{1}{7}\tanh\left(\frac{2\pi d}{L}\right) \tag{2.13}$$

where $2\pi/L$ is the wave number, k.

Approximations to the exact solution of the steepness exist for waves propagating in deep and shallow water. As pointed out by *Stockdon & Holman* [101], in deep water, $2\pi d/L$ is large so $\tanh\left(\frac{2\pi d}{L}\right) \sim 1.0$, so that Eq. (2.13) reduces to :

$$\frac{H}{L} = \frac{1}{7} \tag{2.14}$$

and occurs when the crest angle is 120 ^{o}.

In shallow water $2\pi d/L$ is small so that $\tanh\left(\frac{2\pi d}{L}\right) \sim \frac{2\pi d}{L}$. Thus the maximum wave height that can be generated in the model flume must satisfy the equation:

$$H \leq \frac{2\pi d}{7} = 0.9d \tag{2.15}$$

The speed at which a waveform propagates is termed the phase velocity or wave celerity, c. Since the distance traveled by a wave during one wave period is equal to one wavelength, wave celerity can be related to the wave period and length by :

$$c = \frac{L}{T} \tag{2.16}$$

Inserting $\omega = \frac{2\pi}{T}$ and $k = \frac{2\pi}{L}$ into Eqn. (2.16), wave celerity, c, is related to ω, and k by means of the linear dispersion relation :

$$c = \frac{\omega}{k} \tag{2.17}$$

For linear waves, an expression relating wave celerity to wavelength, in a local water depth h is given by dispersion relation :

$$c = \sqrt{\frac{gL}{2\pi}\tanh\left(\frac{2\pi h}{L}\right)}$$

or

$$c^2 = \frac{\omega^2}{k^2} = \frac{g}{k}\tanh(kh) \tag{2.18}$$

where h is the local water depth, and g is the gravitational acceleration. Equations (2.18) is also termed the dispersion relations since it indicates that waves with different wavelengths in general have different

propagating velocities. For a situation where more than one wave is present, the longer wavelength wave will travel faster.

For waves in the surf zone, and in shallow water ($kh < \pi/10$), Eqn. (2.18) may be simplified to give a linear shallow water expression given by *Tissier et al.* [50], *Stive* [102] and *Dean* [103] as :

$$c = \sqrt{(gh)} \tag{2.19}$$

which shows a direct relationship between the local water depth and wave speed. The wave speed in shallow water is controlled by water depth, that is, there is no dispersion. As pointed out by *Dean* [103], the above equation states that waves of constant period slow down as they enter shallow water and is correct only for very short depths.

Celerity of highly non-linear waves in shallow-water, including the wave breaking zone, can be derived from non-linear wave theories. A recently proposed expression for non-linear shallow water equations (NSWE) based celerity is :

$$c = \delta\sqrt{g\ d} = \delta\sqrt{gx\ \tan\alpha} \tag{2.20}$$

where $\delta = \sqrt{1 + (H/d)}$ and tan α is the beach slope. This is a modified shallow water approximation which shows that phase speed in the surf zone is slightly larger than the linear approximation but still typically proportional to $\sqrt{h}$ (*Svendsen et al.* [104]). This approach has been used in various wave models owing to its simplicity, with a typical value of δ=1.3 (*Schaffer et al.* [105]; *Madsen* [106]). This value is consistent with the surf zone observations of *Stive* [36], which considered regular laboratory waves. *Stansby* & *Feng* [71] presented phase speed data from one laboratory condition (regular wave) and their results showed a monotonic cross-shore variation for the proportionality constant in the range δ=1.06 -1.32. *Thornton and Guza* [107] obtained measurements of phase and celerity spectrum in the surf zone. They compared their results with linear wave theory and showed that waves in the surf zone can show frequency non dispersiveness and amplitude dispersion. They indicated that the phase speed could be related to the speed of propagation of a solitary wave as follows :

$$c = \sqrt{g(h + H)} = \sqrt{gh(1 + H/h)} \tag{2.21}$$

where $H/h = 0.42$ giving δ =1.19. Their results showed agreement with linear theory, accurate to within -10 % to 20 % within the incident band, with some finite amplitude dispersion. *Lippmann* & *Holman* [49] and *Puleo et al.* [108] found good agreement between phase speed estimates using remotely sensed observations and values predicted using Eq. (2.21), the latter using $H/h = 0.5$ or $\delta = 1.225$. A value of δ=1.3 cited by *Schaffer et al.* [105] is also consistent with the solitary wave solution, Eq. (2.21)) using a global value of H/h=0.78.

Mass, momentum and energy fluxes

Instantaneous motions of waves breaking in the surf zone are difficult to understand, so normally it is necessary to investigate average quantities. Some important quantities associated with the flow, such as mass flux, momentum flux, radiation stress and energy flux are defined.

Mass flux in the x-direction is defined as :

$$M = \int_0^z \rho u(z) dz \tag{2.22}$$

and the momentum flux as :

$$F = \int_0^z \rho u^2(z) dz \tag{2.23}$$

where ρ is the density of water, and z is the elevation from the flume bed.

Radiation stress is defined as the excess flow of momentum due to pressure waves (*Longuet-Higgins & Stewart* [109]). When these waves break, the momentum is transferred to the water column, forcing near-shore currents. The principal component of radiation stress in the direction of wave propagation is the difference between the time-averaged total momentum flux in the presence of waves and the mean momentum flux in the absence of waves. For waves propagating in the x-direction, the radiation stress, which is the rate of flow of momentum across the plane perpendicular to the direction of wave propagation, S_{xx}, is given by *Longuet-Higgins & Stewart* [109] as :

$$S_{xx} = \overline{\int_{-d}^{\eta} (p + \rho u^2) dz} - \int_{-d}^{0} p_o dz \tag{2.24}$$

where η is the mean water level, -d is the position of the bed relative to the SWL, p is the hydrostatic pressure and p_o is the atmospheric pressure and the second term is the mean flux in the absence of waves.

The rate of momentum flow across the plane parallel to the direction of wave propagation, S_{zz} and the rate of flow of x- momentum across the plane z, S_{xz} are given respectively as :

$$S_{zz} = \overline{\int_{-d}^{\eta} (p + \rho w^2) dz} - \int_{-d}^{0} p_o dz$$

$$S_{xz} = \overline{\int_{-d}^{\eta} \rho u z dz} \tag{2.25}$$

Using results of the linear wave theory, the radiation stresses in 2-D non-breaking deep water waves are:

$$S_{xx} = E \frac{2kd}{\sinh\ (2kd)} + 0.5$$

$$S_{zz} = E \frac{kd}{\sinh\ (2kd)}$$

$$S_{xz} = 0 \tag{2.26}$$

In different water depths, Eqn. (2.26) simplifies to:

$$S_{xx} = 0.5E \qquad (deep\ water)$$

$$S_{xx} = 1.5E \qquad (shallow\ water)$$

$$S_{zz} = 0.5E \qquad (shallow\ water) \tag{2.27}$$

where E is the energy per unit area of the wave, given by :

$$E = \frac{1}{8}\rho g H^2 \tag{2.28}$$

where H is the wave height.

Mean water level

The equation describing the free surface as a function of time t and horizontal distance x for a simple sinusoidal wave was shown in Eqn. (2.1) to be :

$$\eta = \frac{H(x,t)}{2} \cos\ \theta(x,t)$$

where $\theta(x,t)$ is the local phase of the wave, η is the elevation of the water surface relative to the SWL, and $H/2$ is one-half the wave height which is the wave amplitude. This expression represents a periodic, sinusoidal, progressive wave traveling in the positive x-direction.

Changes in the mean water levels can be described in terms of the radiation stress, S_{xx}. The mean water level is governed by the cross-shore balance of momentum which is given by :

$$\frac{\partial \overline{\eta}}{\partial x} = -\frac{1}{\rho g(d+\overline{\eta})}\frac{\partial S_{xx}}{\partial x} \tag{2.29}$$

where d is the depth below the still water line (SWL) and $\overline{\eta}$ is the mean water level.

Equation (2.29) expresses the balance between the pressure force from the slope of the mean water surface and the gradient of the radiation stress. As the waves move from the open sea towards the shore, they encounter the shoaling area where S_{xx} increases primarily due to the increase of energy which is a consequence of the decrease of the phase speed of the waves as the water becomes shallower. In this shoaling area, the mean water level, $\overline{\eta}$, decreases because $\frac{\partial \overline{\eta}}{\partial x} \propto -\frac{\partial S_{xx}}{\partial x}$. The horizontal particle velocity, however, will increase. This can be shown by taking the shallow water limit of Eqn. (2.9) and noting that the wave amplitude increases in the shoaling region.

Longuet-Higgins & *Stewart* [110] integrated Eqn. (2.29) using conditions imposed by Eqn. (2.27) and the fact that on the seaward side of the break point, the energy flux of the wave is constant. They obtained the following expression for the mean water level :

$$\overline{\eta} = \frac{1}{8}\frac{H^2 k}{\sinh\ (2kh)} \tag{2.30}$$

Beyond the break point, there is a strong energy dissipation and decrease in wave height resulting in a negative gradient in the radiation stress as the waves propagate towards the beach. This negative gradient in the radiation stress results in the increase in mean water level, called setup. The dissipation energy in the surf zone and the associated decrease in wave height towards the shore result in a gradient in the radiation stress. The decrease in radiation stress is balanced by a slope of the mean water surface, the *set-up*. The magnitude of the *set-up* can be determined by the horizontal component of the momentum equation (*Fredsoe & Deigaard* [95]).

The time mean balance equation for horizontal momentum of a vertical column of water extending from the bottom of the surface is given by (*Stive & Wind* [111]) as :

$$\frac{d}{dx}\int_{-d}^{\overline{\eta}} (\overline{p} + \rho\overline{u^2})dz = \overline{p_b}\frac{dd}{dx} - \overline{\tau_b} \tag{2.31}$$

where $\overline{\eta}$ is the mean water level, -d is the position of the bed relative to the SWL, $\overline{p}$ is the mean pressure, $\overline{p_b}$ is the mean bottom pressure and $\overline{\tau_b}$ is the mean shear stress at the bottom.

Defining the mean dynamic pressure on the bottom as the difference between the mean pressure and the mean hydrostatic pressure on the bottom,

$$P_b = \overline{p_b} - \rho g(d + \overline{\eta}) \tag{2.32}$$

Similarly, mean dynamic pressure at a level z within the fluid is given by

$$\overline{P} = \overline{p} - \rho g(z + \overline{\eta}) \tag{2.33}$$

Inserting the definitions of Eqn. (2.32) and (2.33) into Eqns. (2.24) and (2.31), the pressure equation can then be written as :

$$p_b\frac{dd}{dx} - \rho(d + \overline{\eta})\frac{d\overline{\eta}}{dx} - \frac{dS_{xx}}{dx} - \overline{\tau}_b = 0 \tag{2.34}$$

where p_b is the mean dynamic pressure on the bottom surface, τ_b is the mean shear stress at the bottom and the overbar denotes time averaging.

2.3 Statistics of the flow

In Chapter 1 the complexity of turbulent flows and problems encountered in studying it were highlighted. In order to gain physical understanding of turbulent flows, it is convenient to describe the flow in terms of its statistical properties. The study of turbulence normally requires statistics and stochastic processes, simply because the instantaneous motions are too complicated to understand. In this section, some of the

more commonly used single and multi-point statistics used to describe different aspects of the turbulent flow will defined and interpreted.

The phenomenology of turbulence is characterized by simple statistical quantities, such as averages, probability distribution functions, spectra, correlations, etc., which are calculated from velocity flow fields data, experimentally measured or from direct computer simulations. These statistical tools are sufficient to reveal some of the most important universal features of turbulence. Many other quantities important in fluid mechanics, such as vorticity, strain-rate, stresses, dissipation and entropy can be derived from the velocity field, although direct measurements are sometimes possible. From an experimental point of view, it is clear that efforts must be given in developing almost non-intrusive, multi-point systems for the simultaneous measurement of various quantities in the flow field.

The time-averaged mean value of a statistically stationary signal u is defined as :

$$\overline{u(x)} = \lim_{T\to\infty} \frac{1}{T} \int_0^T u(x,t)dt \tag{2.35}$$

Like the true average though, the above expression cannot be evaluated in real laboratory experiments since measurements cannot be made over an infinite time. Instead an estimator for the time average, say u_T, is used, that is defined by averaging the measurements over a sufficiently long period T and is given as :

$$\overline{u_T(x)} = \frac{1}{T} \int_0^T u(x,t)dt \tag{2.36}$$

where T is a time much longer than the longest turbulent fluctuations in the flow. The flow is assumed statistically steady, for otherwise time-averaging will mix together differing statistics from different times and there will be no hope that it will yield ensemble averages corresponding to a specific time (*Mathieu & Scott* [112]). This average only makes sense if the equation is independent of T or for large T (i.e the integral converges). In such a case the flow is called a statistically steady or stationary process. It should be noted that the lower limit of integration is arbitrary and may be shifted as needed. It is clear that the average can no longer be a function of time, and it follows that all time derivatives of $\bar{u}$ are identically zero. Time averaging is, however, inappropriate for unsteady flows. For such cases one must repeatedly carry out the experiment to produce ensemble statistics. If a time average is employed, it includes all stages of the turbulent experiment and neither converges nor yields results which meaningfully describe any given stage. In the case of periodic breaking waves, there are turbulent fluctuations from one cycle to the next. A single realization is therefore not periodic. Statistical properties of the flow, for instance mean velocity, may vary periodically with time. That is the flow statistics vary throughout the cycle, but those at time t are the same as those at time $t + T$, where T is the period of the wave. In that case if the signals exist discretely at N different realizations then the time average velocity can be expressed as :

$$\overline{u} = \frac{1}{N} \sum_{n=0}^{N-1} u(t + nT) \tag{2.37}$$

The first step in analyzing measured turbulent variables is to use Reynolds averaging where the variables are separated into a slowly varying mean part and a rapidly varying turbulent part. Computing ensemble averages results in a set of equations describing the mean and turbulent kinetic energies. When flow is

turbulent, particles exhibit additional transverse motion which enhances the rate of energy and momentum exchange between them thus increasing the heat transfer and the friction coefficient. It is, thus, customary to decompose the instantaneous flow into its mean and fluctuating components. If the instantaneous velocity components in the x and z directions are u and w_i, respectively, then the fluctuations can be expressed as :

$$u' = u_i - \overline{u} \qquad ; \qquad w' = w_i - \overline{w} \tag{2.38}$$

This decomposition technique originally applied to fluid mechanics by Osborne Reynolds in 1895 was thereafter referred to as the *Reynolds decomposition*. From the above definition, the average of the fluctuation is zero, i.e., $\overline{u'} = 0$, while on the other hand, the ensemble average of the square of the fluctuation is not zero.

The velocity field u_i is a function of position and time, and is a random vector field that varies from realization to realization of the flow within the supposed ensemble of different experiments. Its value at any particular position and time $u_i(x,t)$ yields a random vector consisting of three components, which are single random variables. It is apparent that, in principle, a vast amount of statistical information is contained in a turbulent flow, but one is usually concerned with only a few of its simpler statistics of which the mean flow velocity is the perhaps the simplest. As its name implies, the mean velocity field at a given x and t denoted $\langle u_i(x,t)\rangle$ is just the average of $u_i(x,t)$ over the ensemble of flow realizations and is independent of time for a steady flow.

The arithmetic mean value is calculated using :

$$\overline{u} = \frac{1}{N}\sum_{i=1}^{N} u_i \tag{2.39}$$

where N is number of elements in each averaging period.

In a flow configuration where Eqn. (2.35) does not converge, an ensemble average must be used to describe the mean flow behaviour. The ensemble average is defined as :

$$\langle u\rangle = \frac{1}{N}\sum_{i=0}^{N-1} u_i(x,t) \tag{2.40}$$

where the summation is over a number of samples, taken at the same location , x, at the same time, t for N different realizations or experiments. The angled brackets shall be used throughout this thesis to refer to phase-ensemble averaged quantities.

It is often important to know how a random variable is distributed about the mean. In this regard, it is important to examine the statistical properties of the fluctuations about the mean (or simply the fluctuations). This leads to a discussion of the variance and covariance terms describing turbulent fluxes. The variance describes the dispersion of the measurements around a mean value, which also can be expressed as the standard deviation from the mean, defined as the square root of the variance (Eqn. (2.41)) or root mean square (r.m.s). This quantity can therefore be used as a measure of the intensity of

turbulence (*Stull* [113]) :

$$\sigma_x = \sqrt{\overline{u'^2}} = \sqrt{\frac{1}{N}\sum_{i=1}^{N} u_i'^2} \tag{2.41}$$

In fact, the ensemble average of the square of the fluctuation is such an important statistical measure called the variance, and represent it symbolically by $\langle (u')^2 \rangle$. The variance of the turbulence is also a random variable that gives a quantitative measure of how large the variations from the mean can be expected to be. In the terminology of turbulence, researchers often speak of turbulence intensity which is just the root-mean-square of the velocity fluctuations. Turbulence intensity in the x-direction is defined (*Liiv* [2]; *Misra et al.* [72]; *Stull* [113]) as :

$$u'_{r.m.s} = \sqrt{u'^2} = \sqrt{\frac{1}{N}\sum_{i=0}^{N-1} (u_i - \langle u \rangle)^2} \tag{2.42}$$

Similar equations apply for the other components. As its name implies, the value of this term gives a measure of the intensity of the turbulence.

It is sometimes more convenient to deal with values of the cross-variances of two signals, which have been normalized by the appropriate variances. The correlation coefficient is defined as:

$$\rho_{uw} = \frac{\langle u'w' \rangle}{(\langle u'^2 \rangle \langle w'^2 \rangle)^{\frac{1}{2}}} \tag{2.43}$$

The correlation coefficient is bounded by plus or minus one, the former representing perfect correlation and the latter perfect anti-correlation. A positive value of $\langle u'w' \rangle$ indicates that u' and w' tend to vary together. A negative value indicates that when one variable is increasing the other tends to be decreasing. A zero value of $\langle u'w' \rangle$ indicates that there is no correlation between u' and w'. As will be seen below, it does not mean that they are statistically independent. For a random stationary process, the statistics of the process are independent of the origin in time. If the statistics of a process are time independent, then :

$$\langle u(t) \rangle = \langle u(t + nT) \rangle \tag{2.44}$$

where T is some arbitrary translation of the origin in time. The product $\langle u(t)u(t') \rangle$ depends only on the time difference $t' - t$ and not on t (or t') directly. This consequence of stationarity can be extended to any product moment.

One of the most useful statistical moments in the study of stationary random processes (and turbulence, in particular) is the autocorrelation defined as the average of the product of the random variable evaluated at two times, i.e.$\langle u(t)u(t') \rangle$. Since the process is assumed stationary, this product can depend only on the time difference $\tau = t' - t$. Therefore the autocorrelation can be written as:

$$C(\tau) \equiv \langle u(t)u(t + \tau) \rangle \tag{2.45}$$

The importance of the autocorrelation lies in the fact that it indicates the *memory* of the process; that is, the time over which a process is correlated with itself.

Since a random process can never be more than perfectly correlated, it can never achieve a correlation greater than is value at the origin. Thus $C(\tau) \leq C(0)$ An important consequence of stationarity is that the autocorrelation is symmetric in the time difference, $\tau = t' - t$.

It is convenient to define the autocorrelation coefficient as :

$$\rho(\tau) \equiv \frac{C(\tau)}{C(0)} = \frac{\langle u(t)u(t+\tau)\rangle}{\langle u'^2\rangle} \tag{2.46}$$

where $\langle u'^2\rangle = \langle u'(t)u'(t)\rangle = C(0)$

2.4 Theory of turbulence

The turbulent flow field is completely described by the conservation equations of *mass*, *momentum* and *energy*, supplemented with appropriate initial and boundary conditions. In this section we discuss the application of statistical methods to turbulent flow. The Navier-Stokes equation for a fluid, stated in Eqn. (2.5) above, is re-examined in order to further describe the effects of turbulence. The cartesian tensor notation which is used in most treatments of turbulence, will be used in this section. An equation with index i implies that there are three equations corresponding to the three coordinates of the 3-D space, and a repeated index in any term implies the summation over all values of that index.

As seen before, the equations of motion for an incompressible fluid are the momentum and the continuity equations. Using Cartesian coordinates, the momentum equation is given by :

$$\frac{\partial \vec{u_i}}{\partial t} + \vec{u_j}\frac{\partial \vec{u_i}}{\partial x_i} = \frac{1}{\rho}\frac{\partial \sigma_{ij}}{\partial x_j} \tag{2.47}$$

where σ_{ij} is the stress tensor and represents the stresses acting on all sides of a fluid element.

The stress tensor can be expressed in terms of pressure and rate of strain as follows :

$$\sigma_{ij} = -p\delta_{ij} + 2\mu s_{ij} \tag{2.48}$$

where μ is the molecular viscosity and s_{ij} is the rate of strain given by :

$$s_{ij} = \frac{1}{2}\left(\frac{\partial u_i}{\partial x_j} + \frac{\partial u_j}{\partial x_i}\right) \tag{2.49}$$

where the deformation rate tensor, $\frac{\partial u_i}{\partial x_j}$ describes the relative motion of adjacent fluid elements.

It is convenient to split the deformation rate tensor as follows :

$$\frac{\partial u_i}{\partial x_j} = \frac{1}{2}\left(\frac{\partial u_i}{\partial x_j} + \frac{\partial u_j}{\partial x_i}\right) + \frac{1}{2}\left(\frac{\partial u_i}{\partial x_j} - \frac{\partial u_j}{\partial x_i}\right) \tag{2.50}$$

so that

$$s_{ij} = \frac{1}{2}\left(\frac{\partial u_i}{\partial x_j} + \frac{\partial u_j}{\partial x_i}\right) \tag{2.51}$$

represents the pure straining motion (or rate of strain tensor) and

$$R_{ij} = \frac{1}{2}\left(\frac{\partial u_i}{\partial x_j} - \frac{\partial u_j}{\partial x_i}\right) \tag{2.52}$$

describes the rotation of a rigid body.

For incompressible constant density flow, the conservation of mass equation becomes :

$$\frac{\partial \rho}{\partial t} + \frac{\partial \rho u_i}{\partial x_i} = 0$$

or

$$\frac{\partial u_i}{\partial x_i} = 0 \tag{2.53}$$

The momentum equation becomes :

$$\frac{\partial u_j}{\partial t} + \frac{\partial u_i u_j}{\partial x_i} = -\frac{1}{\rho}\frac{\partial p}{\partial x_j} + \nu\frac{\partial^2 u_j}{\partial x_i \partial x_i} \tag{2.54}$$

The Navier-Stokes equation can now be derived from the above equation using the equation of continuity to give :

$$\frac{\partial \vec{u_i}}{\partial t} + \vec{u_j}\frac{\partial \vec{u_i}}{\partial x_j} = -\frac{1}{\rho}\frac{\partial p}{\partial x_i} + \nu\frac{\partial^2 \vec{u_i}}{\partial x_j \partial x_j} \tag{2.55}$$

where $\nu = \frac{\mu}{\rho}$ is the kinematic viscosity of the fluid.

2.4.1 Turbulent transport

This section provides one of the most common approaches by which turbulence is treated and studied from a statistical viewpoint. By decomposing the flow into its mean and fluctuating components as was seen in Eqn. (2.38) and applying the decomposition to transport equations of momentum and kinetic energy, we are able to isolate some of the mechanisms by which the turbulence affects the mean flow.

Effect of turbulence on mean momentum

We have seen that in the case of turbulent flows, it is customary to decompose the instantaneous flow velocity components into its mean and fluctuating components using Reynolds decomposition. The pressure, rate of strain tensor, and stress tensor associated with the turbulent flow can also be decomposed into their respective mean and fluctuating components (*Pope* [114]) as :

$$u_i = \overline{u_i} + u_i' \quad ; \quad p_i = \overline{p_i} + p_i' \quad ; \quad s_{ij} = \overline{s_{ij}} + s_{ij}' \quad ; \quad \sigma_{ij} = \overline{\sigma_{ij}} + \sigma_{ij}' \tag{2.56}$$

where

$$\overline{\sigma_{ij}} = \overline{p}\delta_{ij} + \mu\left(\frac{\partial \overline{u_i}}{\partial x_j} + \frac{\partial \overline{u_j}}{\partial x_i}\right) \tag{2.57}$$

and

$$\sigma_{ij}' = p'\delta_{ij} + \mu\left(\frac{\partial u_i'}{\partial x_j} + \frac{\partial u_j'}{\partial x_i}\right) \tag{2.58}$$

The mean and fluctuating rate of strain tensors are given by :

$$\overline{s_{ij}} = S_{ij} = \frac{1}{2}\left(\frac{\partial \overline{u_i}}{\partial x_j} + \frac{\partial \overline{u_j}}{\partial x_i}\right) \tag{2.59}$$

and

$$s'_{ij} = s_{ij} = \frac{1}{2}\left(\frac{\partial u'_i}{\partial x_j} + \frac{\partial u'_j}{\partial x_i}\right) \tag{2.60}$$

From the definition of the mean values, the mean of the fluctuating parts are zero, i.e :

$$\overline{u'_i} = \overline{p'} = \overline{\sigma'_{ij}} = 0 \tag{2.61}$$

Substituting the above into the NSE Eqn. (2.55) and averaging over the entire equation gives an equation for the *mean* flow :

$$\rho\frac{\partial}{\partial t}\overline{\overline{u_i} + u'_i} + \rho\frac{\partial}{\partial x_j}\overline{\left(\overline{u_i} + u'_j\right)\left(\overline{u_j} + u'_j\right)} = \frac{\partial}{\partial x_j}\overline{\left(\overline{\sigma_{ij}} + \sigma'_{ij}\right)} \tag{2.62}$$

Applying Eqn. (2.61) to Eqn. (2.62) and noting that $\overline{\overline{u_i}} = \overline{u_i}$ yields the final equation for the *mean* momentum transport :

$$\rho\frac{\partial \overline{u_i}}{\partial t} + \rho\frac{\partial}{\partial x_j}(\overline{u_i}\overline{u'_j} + \overline{u'_i u'_j}) = \frac{\partial \overline{\sigma_{ij}}}{\partial x_j} \tag{2.63}$$

Equation (2.63) for the mean momentum resembles the full momentum equation except for the term $\frac{\partial}{\partial x_j}\langle u'_i u'_j\rangle$. If u'_i and u'_j are uncorrelated, this term is zero. However this is not generally the case. Physically, this correlation represents the mean value of the transport of fluctuating momentum by the fluctuating velocity field. So this transport of fluctuating momentum influences the transport of the mean momentum. This term can therefore be interpreted as a mechanism for momentum exchange between the mean flow and the turbulence. In other words, for turbulent flow, the velocity fluctuations produce an additional mean momentum flux that would not appear in laminar flow.

Momentum flux can be associated with a stress field stress in the field. The turbulence momentum exchange mechanism appearing in Eqn. (2.63) is in the form of a divergence of a quantity we can thus associate with stress. Turbulence can therefore be interpreted to produce additional stress in the field. As a result of this behaviour, the correlation $u'_i u'_j$ is called *Reynolds* stress tensor. With this interpretation for the velocity correlation, equation of the mean momentum can be rearranged and written in the form:

$$\rho\frac{\partial \overline{u_i}}{\partial t} + \rho\frac{\partial \overline{u}_i\overline{u}_j}{\partial x_j} = \frac{\partial(\overline{\sigma_{ij}} - \overline{u'_i u'_j})}{\partial x_j} \tag{2.64}$$

The mean stress tensor in the turbulent flow can be expressed as :

$$\overline{\sigma_{ij}} - \overline{u'_i u'_j} = -\overline{p}\delta_{ij} + 2\nu S_{ij} - \overline{u'_i u'_j} \tag{2.65}$$

For constant ρ and μ, the mean momentum equation becomes :

$$\frac{\partial \overline{u_i}}{\partial t} + \frac{\partial \overline{u}_i\overline{u}_j}{\partial x_j} = -\frac{1}{\rho}\frac{\partial \overline{p}\sigma_{ij}}{\partial x_i} + \frac{1}{\rho}\frac{\partial}{\partial x_j}\left(2\nu\overline{S_{ij}} - \overline{u'_i u'_j}\right) \tag{2.66}$$

Equation (2.66) that describes the motion of the *mean* flow cannot be obtained simply by substituting mean quantities into the Navier-Stokes equation, as there is a contribution by turbulence to the mean

flow. Equations describing the mean flow now have additional unknowns in the form of $\overline{u_i' u_j'}$. Thus above decomposition gives more unknowns than the number of equations, resulting in what is known as the *closure* problem. In order to solve these equations, it is therefore necessary to find expressions to model the Reynolds stresses. These expressions are often determined using empirical data, hence the justification for this experimental work. Since the mean values of the fluctuating components are zero, it is difficult to analyze the influence of turbulence to the mean flow. Instead we examine the kinetic energies of the mean and turbulent flows.

2.4.2 Turbulent kinetic energy

During a wave breaking process, the wave energy is converted into two parts : the mean current energy and the turbulent kinetic energy. The turbulent kinetic energy is damped through turbulence viscous dissipation (*Huang et al.* [115]). In this section the effect of turbulence on kinetic energy is discussed as it is useful to understand how the mean flow feeds kinetic energy to the turbulence.

For an incompressible fluid with constant transport coefficients, the transport equation for the kinetic energy is :

$$\frac{\partial}{\partial t}\left(\frac{u_i u_i}{2}\right) + \frac{\partial}{\partial x_j}\left(u_j \frac{u_i u_i}{2}\right) = -\frac{1}{\rho}\frac{\partial u_j p}{\partial x_j} + \frac{\partial u_i 2\nu S_{ij}}{\partial x_j} - 2\nu S_{ij}\frac{\partial u_i}{\partial x_j} \tag{2.67}$$

The terms on the RHS of Eqn. (2.67) represent work done pressure forces, work done by viscous stresses and dissipation, respectively.

The above equation is sometimes written as :

$$\frac{\partial}{\partial t}\left(\frac{u_i u_i}{2}\right) = -\frac{\partial u_j}{\partial x_j}\left(\frac{p}{\rho} + \frac{u_i u_i}{2}\right) + \frac{\partial (u_i 2\nu S_{ij})}{\partial x_j} - 2\nu S_{ij}\frac{\partial u_i}{\partial x_j} \tag{2.68}$$

with the first term on the RHS now representing the work done by the total dynamic pressure.

If we now apply the Reynolds decomposition to Eqn. (2.67), the decomposition of the kinetic energy gives :

$$u_i u_i = \overline{u}_i \overline{u}_i + 2\overline{u}_i u_i' + u_i' u_i' \tag{2.69}$$

Substituting Eqn. (2.69) and Eqn. (2.56)-(2.61) in Eqn. (2.67) and averaging over the entire equation gives :

$$\begin{aligned}\frac{\partial\left(\frac{1}{2}\overline{u}_i\overline{u}_i\right)}{\partial t} + \frac{\partial\left(\frac{1}{2}\overline{u_i' u_i'}\right)}{\partial t} = &-\frac{\partial \overline{u_i}}{\partial x_j}\left(\frac{\overline{p}}{\rho} + \frac{1}{2}\overline{u}_j\overline{u}_j\right) + \nu\frac{\partial \overline{u}_j 2\overline{S}_{ij}}{\partial x_i} - \nu 2\overline{S}_{ij}\frac{\partial \overline{u}_j}{\partial x_i} \\ &-\frac{\partial}{\partial x_i}\overline{u_i'\left(\frac{p'}{\rho} + \frac{1}{2}u_j' u' j\right)} - \frac{\partial \overline{u}_j}{\partial x_i}\left(\overline{u_i' u_j'}\right) \\ &-\frac{1}{2}\frac{\partial \overline{u}_i \overline{u_j' u_j'}}{\partial x_i} + \nu\frac{\partial \overline{u_j' 2 s_{ij}}}{\partial x_i} - \overline{\nu 2 s_{ij}\frac{\partial u_j'}{\partial x_i}}\end{aligned} \tag{2.70}$$

The above equation contains both the mean and the turbulent kinetic energy. To obtain an equation for the mean turbulent kinetic energy alone, we need to multiply Eqn. (2.64) by $\overline{u}_i$. The resulting equation

is :

$$\frac{\partial}{\partial t}\left(\frac{1}{2}\overline{u'}_i\overline{u'}_i\right)+\frac{\partial}{\partial x_i}\overline{u}_i\left(\frac{\overline{p}}{\rho}+\frac{1}{2}\overline{u}_j\overline{u}_j\right)=-\overline{u'_iu'_j}\frac{\partial\overline{u}_i}{\partial x_j}+\frac{\partial}{\partial x_j}\left(-\overline{u'_iu'_j}\overline{u}_i\right)$$
$$+\nu\frac{\partial}{\partial x_i}\overline{u}_j2\overline{S}_{ij}-\nu2\overline{S}_{ij}\frac{\partial\overline{u}_j}{\partial x_j} \tag{2.71}$$

As was the case in the equation for the mean momentum (Eqn. (2.66)), Eqn. (2.71) has additional terms due to turbulence that affect the mean kinetic energy. Because $\overline{u'_iu'_j}$ is normally negative, the action of this term tends to decrease or take away kinetic energy from the mean motion. The first term on the RHS of Eqn. (2.71) represents the deformation work by the turbulent stresses. The second term on the RHS is the work done by the turbulent stresses. Viscosity does not have a significant impact on the mean kinetic energy transport. This shows that the large structures in turbulent flows are relatively independent of viscosity.

More information about turbulence and its interaction with mean flow can be obtained from the transport equation for the turbulent kinetic energy, by subtracting Eqn. (2.71) from Eqn. (2.70) to give :

$$\frac{\partial\left(\frac{1}{2}\overline{u'_iu'_i}\right)}{\partial t}+\overline{u}_j\frac{\partial}{\partial x_j}\left(\frac{1}{2}\overline{u_iu_i}\right)=-\frac{\partial}{\partial x_i}\overline{u'_i\left(\frac{p'}{\rho}+\frac{1}{2}u'_ju'_j\right)}-\overline{u'_iu'_j}\frac{\partial\overline{u}_j}{\partial x_i}$$
$$+\nu\frac{\partial}{\partial x_i}\overline{u'_js_{ij}}-\nu\overline{2s_{ij}\frac{\partial u'_j}{\partial x_i}} \tag{2.72}$$

The mechanisms that affect the turbulent kinetic energy on the RHS of the above equation are the turbulent diffusion of mechanical energy, deformation work on the mean flow by the turbulent stresses, the viscous work by the the turbulent shear stresses, and the viscous dissipation of the turbulent kinetic energy. As opposed to the case of the mean flow turbulent kinetic energy equation, the viscous terms are important to the turbulent kinetic energy balance. The last term in Eqn. (2.72) has a particular significance. It is always positive and therefore indicates a drain of energy. This is the viscous dissipation term.

For a statistically steady flow, the time derivatives in the equations of the mean and turbulent kinetic energy is zero. Also

$$s_{ij}s_{ij}=s_{ij}\frac{\partial u'_j}{\partial x_i}. \tag{2.73}$$

Applying these two conditions, the equation to the *mean kinetic energy* can be written as :

$$\overline{u}_j\frac{\partial}{\partial x_j}\left(\frac{1}{2}\overline{u}_i\overline{u}_i\right)=\frac{\partial}{\partial x_j}\left(-\frac{\overline{p}}{\rho}\overline{u}_j+2\nu\overline{u}_i\overline{S}_{ij}-\overline{u'_iu'_j}\overline{u}_j\right)+2\nu\overline{S}_{ij}\overline{S}_{ij}+\overline{u'_iu'}_j\overline{S}_{ij} \tag{2.74}$$

and that for the *turbulent kinetic energy* can be written as :

$$\overline{u}_j\frac{\partial\left(\frac{1}{2}\overline{u'_iu'_i}\right)}{\partial x_j}=-\frac{\partial}{\partial x_j}\left(\frac{1}{\rho}\overline{u'_jp'}+\frac{1}{2}\overline{u'_iu'_iu'_j}-2\nu\overline{u'_is_{ij}}\right)-\overline{u'_iu'}_j\overline{S}_{ij}-2\nu\overline{s_{ij}s_{ij}} \tag{2.75}$$

These are the same two equations as (3.1.11) and (3.2.1) given by Tennekes and Lumley [34].

Equation (2.75) can be conveniently written as :

$$\frac{\partial k}{\partial t}+\frac{\partial\overline{u}_jk}{\partial x_j}=-\frac{\partial}{\partial x_j}\left(\frac{1}{\rho}\overline{u'_jp'}+\overline{u'_jk'}-2\nu\overline{u'_is'_{ij}}\right)-2\nu\overline{s'}_{ij}\overline{s}_{ij}+\overline{u'_iu'_j\overline{s'}}_{ij} \tag{2.76}$$

where the *ensemble-averaged kinetic energy* is :

$$k = \frac{1}{2}(\overline{u_i' u_i'}) \tag{2.77}$$

and the *instantaneous turbulent kinetic energy* is :

$$k' = \frac{1}{2}(u_i' u_i') \tag{2.78}$$

The first three terms on the right hand side of Eqn. (2.76) are due to the work by the pressure gradient, transport by turbulent velocity fluctuations and transport by viscous stresses, respectively. The last two terms are due to the work associated with deformation. The term $\overline{u_i' u'}_j \overline{S_{ij}}$ is the deformation work term which appears in both equation for the mean and turbulent flows with opposite sign. This term serves to exchange energy between the mean flow and turbulence. The last term is the work due to the deformation by viscous stresses and is always a drain of energy. From the above equations, an estimate of the turbulent energy production, $\wp$ and dissipation, ϵ, rates can be obtained from the following equations:

$$\wp = -\overline{u_i' u'}_j \overline{s_{ij}'} \tag{2.79}$$

$$\epsilon = 2\nu \overline{s_{ij}' s_{ij}'} \tag{2.80}$$

Both $\wp$ and ϵ can be in local equilibrium, however in most cases the energy is produced at one point, transported and dissipated at another point in space or time as described by Eqn. (2.76). It should be noted that the dissipation work term $-\overline{u_i' u_j'} \overline{S}_{ij}$ or equivalently $-\overline{u_i' u_j'} \frac{\partial \overline{u}_j}{\partial x_i}$ appear in both equations for the mean (Eqn. (2.74)) and turbulent kinetic energy (Eqn. (2.75)) but with an opposite sign. We also call this term the production term as the effect of the deformation work is to exchange energy between the mean flow and the turbulence. Usually this term is negative (Reynolds stress is usually negative) so that there is a net flow of kinetic energy from the mean flow to the turbulence. In a purely laminar flow, viscous stresses dissipate the kinetic energy directly into heat. In turbulent flow, however, the deformation work caused by turbulent stresses first converts mean flow kinetic energy into turbulent kinetic energy. It then cascades through the wave number spectrum before it is finally dissipated into heat. The terms in the parentheses on the RHS of the turbulent kinetic energy Eqn. (2.75) are in the form of a divergence of a vector quantity. These are conservative terms that vanish when integrated over an infinite flow field volume. These inertial terms do not create or destroy energy, but simply redistribute the turbulent kinetic energy from place to place in the flow. In a statistically steady homogeneous flow, a further simplification of Eqn. (2.75) can be made. In this case, all spatial gradients of the turbulence transport quantities will be zero. Under these conditions, the only remaining terms give :

$$-\overline{u_i' u_j'} \overline{S}_{ij} = 2\nu \overline{s_{ij} s_{ij}} \tag{2.81}$$

In other words, Eqn. (2.81) implies that the rate of production of turbulent kinetic energy is balanced by the rate of viscous dissipation.

2.4.3 Vorticity dynamics

All turbulent flows exhibit high levels of fluctuating vorticity. Vorticity is considered to be a key ingredient of a turbulent flow and much of the dynamics and structure of turbulent flows can be productively interpreted and analyzed in terms of the vorticity dynamics. Turbulence is rotational and characterized by high fluctuations in vorticity. This vorticity is defined as the curl of the velocity field :

$$\vec{\omega} = \vec{\nabla} \times \vec{u}$$

$$\vec{\omega} = \hat{i}\left(\frac{\partial u_z}{\partial y} - \frac{\partial u_y}{\partial z}\right) + \hat{j}\left(\frac{\partial u_x}{\partial z} - \frac{\partial u_z}{\partial x}\right) + \hat{k}\left(\frac{\partial u_y}{\partial x} - \frac{\partial u_x}{\partial y}\right) \tag{2.82}$$

Fluctuating vorticity is defined as :

$$\omega' = \left(\frac{1}{N}\sum_{i=1}^{N}(\omega_i - \langle\omega\rangle)\right)^{1/2} \tag{2.83}$$

The Navier Stokes equation can be written in the following form :

$$\frac{\partial u_i}{\partial t} + \frac{\partial}{\partial x_i}\left(\frac{1}{2}u_j u_j\right) - \epsilon_{ijk}u_j\left(\epsilon_{klm}\frac{\partial u_m}{\partial x_l}\right) = \frac{\partial \sigma_{ij}}{\partial x_j} \tag{2.84}$$

or in vector notation as :

$$\frac{\partial u_i}{\partial t} + \nabla(\frac{1}{2}\vec{u}.\vec{u}) - \vec{u} \times (\nabla \times \vec{u}) = -\frac{1}{\rho}\nabla p + \frac{1}{\rho}\nabla\tau \tag{2.85}$$

The transport equation for vorticity can be obtained by taking the curl of the momentum equation, so that the vector equation for the vorticity can be written as :

$$\frac{\partial \vec{\omega}}{\partial t} + \nabla \times (\nabla\frac{1}{2}\vec{u}.\vec{u}) + \nabla \times (\vec{u} \times \vec{\omega}) = -\nabla \times (\frac{1}{\rho}\nabla p) + \nu\nabla^2.\vec{\omega} \tag{2.86}$$

Using vector identities it can be shown that the above equation reduces to :

$$\nabla \times (\vec{u} \times \vec{\omega}) = (\vec{u}.\nabla)\vec{\omega} - (\vec{\omega}.\nabla)\vec{u} + \vec{\omega}(\nabla.\vec{u}) - \vec{u}\nabla.\vec{\omega} \tag{2.87}$$

Finally we can write for the vorticity field :

$$\frac{\partial \vec{\omega}}{\partial t} + \vec{u}(\nabla\vec{\omega}) - (\vec{\omega}.\nabla)\vec{u} + \vec{\omega}(\nabla.\vec{u}) = \frac{1}{\rho^2}(\nabla\rho \times \nabla p) + \nu\nabla^2\vec{\omega} \tag{2.88}$$

Terms in Eqn. (2.88) above and their equivalent cartesian forms are given and explained :
1. $(\vec{u}.\nabla)\vec{\omega} = u_j\frac{\partial \omega_i}{\partial x_j}$ is a *convection* term which tells us that the vorticity gets convected (moved around) by the flow field.
2. $(\vec{\omega}.\nabla)\vec{u} = \omega_j\frac{\partial u_i}{\partial x_j}$ is the most important turbulence term which represents enhancement of vorticity by *stretching* and is the mechanism by which turbulent energy is transfered to smaller scales. In 2-D flow, this term is zero. Thus, although 2-D flows can exhibit highly random character, they lack this distributive mechanism and their fluctuations draw their energy directly from the mean motion of the

flow.

3. $\vec{\omega}(\nabla.\vec{u}) = \omega_i \frac{\partial u_i}{\partial x_j}$ describes the effect of *expansion* or *compression* on the vorticity field. In a flow that is expanding, this term is positive, and results in a decrease in the magnitude of vorticity due to the *minus* sign in front of this term. If the fluid is undergoing compression, the magnitude of the vorticity will increase. In incompressible flows, this term will not play a role, but is however a very important mechanism in combustion and non-reacting compressible flows.

4. $\vec{u}(\nabla.\vec{\omega}) = u_i \frac{\partial \omega_i}{\partial x_j}$ is always zero.

5. $-\nabla \times (\frac{1}{\rho}\nabla p)$ which when expanded gives $\frac{1}{\rho^2}(\nabla\rho \times \nabla p)$ is called the *barometric torque* and results in a generation of vorticity from unequal acceleration as a result of non-aligned density and pressure gradients. In a uniform, constant density flow, this term is zero. Suppose the pressure gradient is perpendicular to the density gradient (the case for which barometric torque is largest). The lighter density fluid will be accelerated faster than the high density fluid, resulting in a shear layer, thus generating vorticity.

6. $\nu\nabla^2\omega$ describes the effects of viscous diffusion on the distribution of vorticity. As a result of viscosity, vorticity in the flow tends to diffuse in space. In high Reynolds number turbulent flows, viscous diffusion of vorticity will be dominated by the other mechanisms in the vorticity transport equations. This will be the case unless the length scales of the turbulence are small enough so that contributions of viscosity can be important. The effects of viscocity on the large scale vortex structure in a turbulent flow are generally small.

For constant density, we can write in cartesian form :

$$\frac{\partial \omega_i}{\partial t} + u_j \frac{\partial \omega_i}{\partial x_j} - \omega_j \frac{\partial u_i}{\partial x_j} = \nu \frac{\partial^2 \omega_i}{\partial x_j \partial x_j} \tag{2.89}$$

If we consider 2-D constant density flow, the vorticity equation reduces to :

$$\frac{\partial \omega_i}{\partial t} + u_j \frac{\partial \omega_i}{\partial x_j} = \nu \frac{\partial^2 \omega_i}{\partial x_j \partial x_j} \tag{2.90}$$

Under this restriction, the vorticity simply acts as a passive scalar that follows fluid particle paths so becomes a good indicator of fluid flow patterns. The vorticity vector is therefore confined to a plane perpendicular to the flow, and no enhancement of vorticity of transport to smaller scales by vortex stretching is possible. In this case vorticity just satisfies a standard convection-diffusion equation.

Chapter 3: Experimental facility and setup

"Thought experiment is in any case a necessary precondition for physical experiment. Every experimenter and inventor must have the planned arrangement in his head before translating it into fact".

-Ernst Mach (1838 - 1916)

3.1 Experimental facility

Experiments were performed in a wave tank/flume with a sloping beach at one end. The flume is 20 m long, 0.75 m wide and 0.8 m deep. For visualization purposes, the side walls of the flume are composed of tempered glass. Waves were generated by a servo-controlled piston type wave maker that has a maximum paddle stroke of 0.8 m and is designed for water depths of up to 0.75 m. Complementary documentation on the specifications of the wave maker and wave generation mechanism is available at the *url* indicated by [116]. The flume was also fitted with a cemented beach having a slope of 1:20 (height : length). A 1:20 slope beach was chosen in order to get a long enough surf zone length over which measurements of wave parameters could later be conducted. Choosing a higher slope would result in a very short surf zone, alternatively choosing a smaller slope would result in waves breaking too close to the end of the flume, also resulting in a shorter surf zone. The 1:20 beach slope has also been used as the standard slope by numerous researchers in similar studies (*Sou & Yeh* [12]; *Nadaoka & Kondoh* [37]; *Cowen et al.* [60]; *Lara et al.* [117] ; *Huang et al.* [115]; *Sou et al.* [75]; *Sakai et al.* [118]; *Govender et al.* [73]). *Melville* [119] gives an extensive review of the different breaking wave geometries, wave breaking mechanisms, and evolution of the wave profile for deep water waves.

Figure 3.1 is a picture showing an aerial view of the laboratory flume. The wave maker is located near the bottom left corner. The above facility is located in the Coastal and Hydraulics Engineering Laboratory at the Council for Scientific and Industrial Research (CSIR) in Stellenbosch, South Africa. Figure 3.2 shows the schematic view of the flume illustrating characteristic regions of the flume and giving overall dimensions in addition to showing the sloping bottom and the coordinates system that is used. Coordinate x axis is along the horizontal direction. Coordinate y is perpendicular to the side wall, and z is the vertical coordinate, conventionally established as positive if oriented upward from the still water line. The origin $(x, z) = (0, 0)$ is at the intersection of the beach slope and the still water level. With this convention, it must be noted that horizontal distances measured along the flume relative to the SWL will be negative for position towards the wave maker.

Figure 3.1: Aerial view of the laboratory flume where measurements were performed. Waves generated near the bottom left corner propagate along the flume towards the top right corner.

Figure 3.3 shows measurement stations at which DCIV measurements were made and their location from the SWL mark on the beach. Waves start to overturn and break in window 11a (not shown), so DCIV measurements were made at stations marked 11b to 13b. These stations are about 0.50 m apart. An average water depth of 61.8 cm was maintained in the constant depth section of the flume. Table 3.1 shows the location of the center of each of the five stations relative to the SWL mark and the depth of the flume bed from the still water line. Most of the turbulence results that will be presented were measured at station 12a, whose center was located -2.38 m from the SWL mark on the beach and had a still water depth of d =12.0 cm.

3.2 Instrumentation setup

This facility is used throughout the year for consultancy work. As such, every time the facility was hired to do our experiments, a new beach slope had to be constructed and this usually took 2 to 3 days to allow

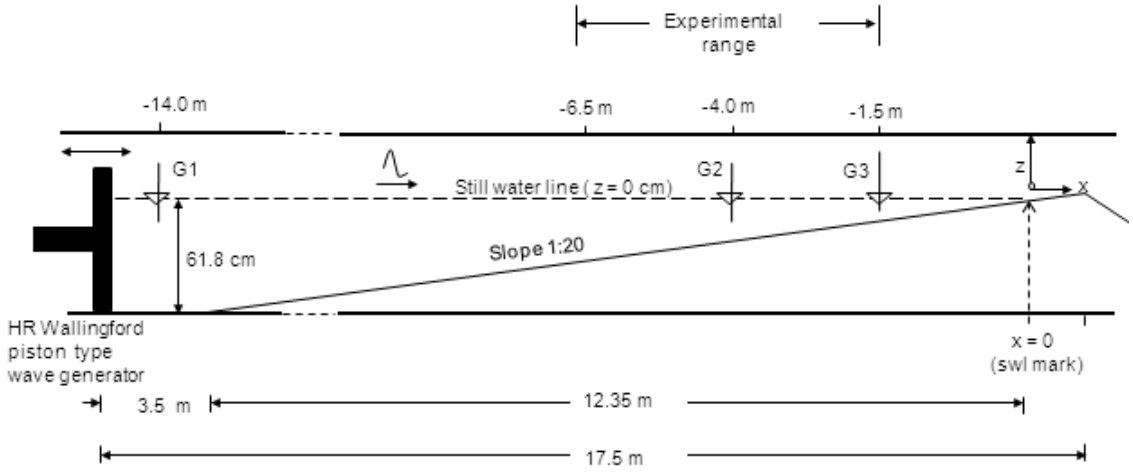

Figure 3.2: Schematic of the flow geometry (not to scale) showing the side-view of the wave flume structure, dimensions and the reference frame used. Initial positions of the wave gauges labelled G1, G2 and G3, are shown. Free surface elevation measurements were made over the experimental range as gauges G2 and G3 were sequentially moved in steps of 10 cm towards the generator. The still water line mark is at $x = 0$, and vertical elevations are measured relative to $z = 0$ which is at the SWL.

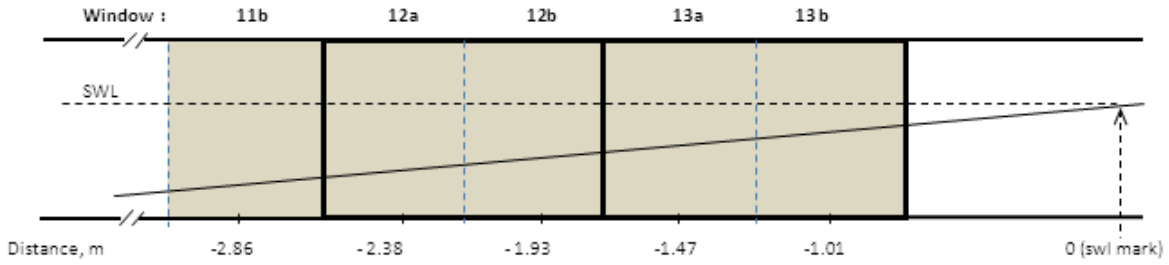

Figure 3.3: Flume windows were PIV measurements were performed and their location relative to the still water line mark. The shaded windows were selected for DCIV measurements reported in this work.

Table 3.1: Distance of center of measurement stations from the still water line mark and the corresponding still water depth at these stations.

Window Number	x (m)	d (cm)
11b	-2.86	14.4
12a	-2.38	12.0
12b	-1.93	9.7
13a	-1.47	7.4
13b	-1.01	5.0

the slope to dry. Once the beach slope had dried, it was thoroughly cleaned to remove excess cement, sand and dirt that may taint the glass wall and give erroneous correlations. When this has been done, the flume was filled with water up to a desired height for DCIV experiments. The flume glass-wall has to be occasionally cleaned during the course of the experiments.

The wave flume is elevated about 2.0 m above the floor. To gain access to the measurement stations, a wooden platform had to be constructed. While the beach slope was drying, setting up continued with

the erection of a wooden platform near the chosen windows onto which the DCIV instrumentation was operated from. Setting up and testing the equipment is usually done during the day. This required covering parts of the flume with black polythene sheets to minimize the amount of light falling into the camera field of view. DCIV experiments were then performed at night with lights switched off. Setting up is a cumbersome procedure that requires a lot of attention and manpower.

3.2.1 Instrumentation for wave generation

Figure 3.4 (a) shows a picture of the control room facilities for wave generation, wave gauge data acquisition and signal conditioning while Figure 3.4(b) shows a schematic of the wave generator control and data acquisition system. The wave generator consists of a servo-driven piston paddle, a servo control unit and a computer for pre-programming of wave heights and frequency. The wave generation control unit is connected to a computer which is simultaneously operated to generate a wave of desired frequency and wave height in the flume. Using the wave generation software running on the computer shown in Figure 3.4 (a), wave properties such as wave-height and frequency were set.

(a)

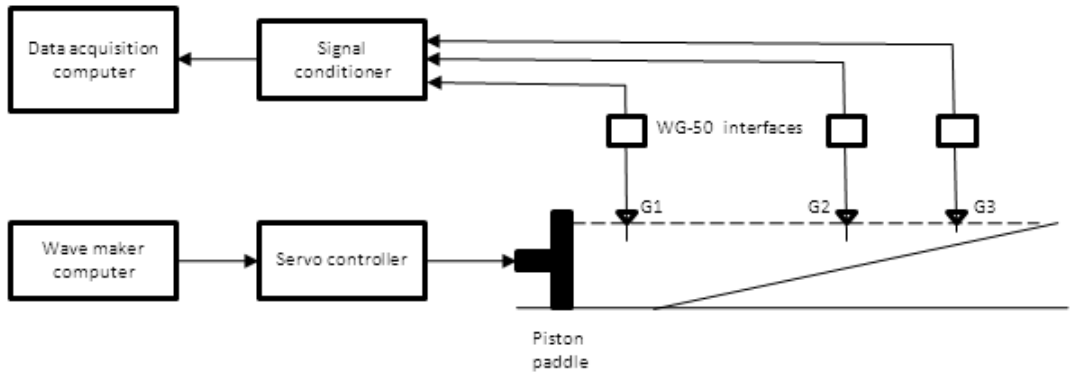

(b)

Figure 3.4: Facilities for wave generation, capacitive wave gauge signal conditioning and data acquisition equipment (a) picture (b) block diagram schematic.

3.2.2 DCIV instrumentation

A typical PIV system is composed of a light source, seed materials, camera, timing controller, and data capturing and evaluating software. Unlike the traditional PIV technique, no laser light sheet was needed to illuminate the flow. Ordinary laboratory strobe lights that produce white light were mounted on the top of the rails of the flume, vertically above the area to be viewed. A charge-coupled device (CCD) camera, connected to a computer equipped with a digital frame grabber was mounted on one side of the flume to image the illuminated field of view. Figure 3.5 shows a picture of the major components used in the image acquisition setup for velocity flow field measurements. These consist of : the camera that is mounted on the side of the flume window, strobe box, onto which four strobe lights are mounted, image acquisition computer with frame grabber, DAC computer for sampling wave gauge measurements, and its BNC wave gauge interface, for conditioning voltage signals from the wave gauges. The strobe light box, strobe electronics box and the image capturing computer are all mounted on a movable trolley placed on top of the flume rails. This was done to make it easier to move the entire setup to the next measurement station.

Figure 3.5: Picture showing major components of the instrumentation. The strobe bank is mounted on top of the flume rails while the camera is mounted on the flume side to image the illuminated field of view.

Figure 3.6 shows the interconnection between the various components of the DCIV measurement system. The setup designed, and developed by *Govender* [94] with minor improvements by the author, was successfully used to obtain the velocity vector fields containing both velocity amplitude and flow direction for the entire visualized flow field.

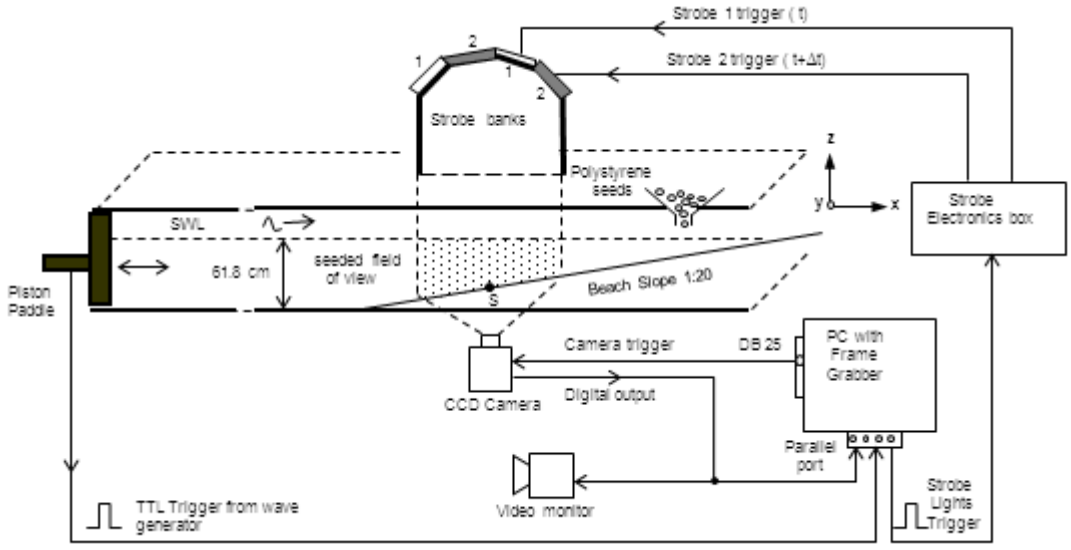

Figure 3.6: Schematic of the interconnection of the experimental setup used for capturing images of the breaking wave.

The following are developments made by the author or differences between the present experiment and that of *Govender* [94]:

1. The piston type wave generator used in this case is different from the double-paddled rectangular board hinged at the bottom that *Govender* [94] used.

2. The setup enabled measurements of wave height and wave phase velocity along the flume in the vicinity of the break point. The setup used by *Govender* [94] is totally different. He obtained time series of the wave surface by measuring the instantaneous water level from a sequence of video images of the wave recorded at various positions along the flume. The images were recorded onto a video tape and analyzed on playback. A keogram was generated from a recording of the wave, from which the time series was extracted by tracking the evolution of air-water interface. The vertical and horizontal distances in the keogram represent height in image coordinates and time increments, respectively. In this dissertation, capacitive wave gauges were calibrated and used to get time series of water levels along the flume. A treatment of the time series led to the calculation phase of wave phase along the flume from which wave phase velocity was determined. *Govender* [94] did not consider wave phase velocity measurements.

3. Another improvement included upgrading the strobe electronics to facilitate easy change of sampling time by means of external toggle switches as opposed to DIP switches which are difficult to change continuously. LEDs were inserted to show in binary, the current sampling time being used.

4. Video capture software was modified to once again facilitate rapid setting up and storing of video files.

The setup consists of an illuminating system consisting of two strobe banks, a video camera, a PC with software to control the entire system. The strobe bank was mounted on top of the flume rails and used to produce a light sheet which is used to illuminate those particles within the focal plane of the camera. Particles in the flow were illuminated by a pair of strobe lights that produce a vertical longitudinal sheet of light at a distance 10 cm parallel to the side wall of the tank, which is far enough to avoid the wall effects. This distance was chosen following the work by *Govender et al.* [79] which showed that undertow

and turbulence measured at distances 10 cm or more, away from the glass wall are not significantly affected by the wall.

The camera provides both analogue and digital outputs via built-in analog-to-digital and digital-to-analog converters. A composite video output signal from the CCD camera was connected to the parallel port of the PC via a frame grabber residing inside the PC. The same signal is also connected to a video monitor which projects the captured image on to the screen, allowing us to check and maintain the required density of seeds in the flow. The video monitor output was projected onto a screen allowing the camera focus to be set to ensure that seeding particles and aeration structures in the image are clearly visible so that good quality images were captured. The DCIV system was triggered and synchronized by a TTL signal derived from the wave generator. This TTL signal was used by the PC as a synchronizing reference to drive the strobe lights while simultaneously driving the camera to capture images at that instant. Upon receiving the trigger pulse from the wave generator, the computer synchronizes the image acquisition process. This enabled the system to capture a pair of images not only at different phases, but more importantly at precisely the same point in the flow, to allow phase ensemble averaging. A pair of images, separated by a few milliseconds, of the beads and aeration due to wave breaking were obtained by strobing the light sheet at the end of one video frame time and again at the beginning of the next. A sequentially increasing delay was implemented in the Microsoft Visual C program running on the computer, driving both the strobes and the camera to enable the system to capture images at different wave phases. Digital images captured were later analyzed using Interactive Data Language (IDL) programs developed for this purpose. Typically each image frame is saved in bit map (*.bmp*) format as a separate file. The files are then read in and converted into binary format for analysis by an IDL program.

Strobe electronics

Flume water was seeded with white, nearly neutrally buoyant spherical polystyrene beads of diameter about 0.5 mm which were used as tracer particles for DCIV measurements. A pair of stroboscopes that produce white light were used to illuminate the plane where the measurements are to be taken. A pair of images was captured within a short period of time but some time is needed to build up energy before the strobes can deliver a new pulse. Therefore, it was necessary to use a pairs of strobe lights for each image. Most of the previous research (e.g. *Sou & Yeh* [12]; *Kimmoun & Branger* [43]; *Huang et al.* [44]; *Ryu et al.* [63]; *Longo* [66]; *Shin & Cox* [67]; *Lennon & Hill* [120]) used lasers for providing the light sheet for PIV measurements and μm diameter particles. Instead ordinary white light and white polystyrene beads of diameter 0.5 mm were employed here. As laser light is coherent, scattering from bubbles and beads cause speckle patterns making it difficult to do cross correlation. In addition, the laser beam usually has an axi-symmetric shape which needs to be shaped with a cylindrical lens in order to form a planar light sheet. In this application the strobe light source was placed on a movable trolley sitting on the flume rails, illuminating a section 10 cm from the glass wall. This was done to avoid wall effects on our DCIV results.

Figure 3.7 shows a strobe box mounted on the flume rails with the strobe lights being connected and

Figure 3.7: Picture showing strobe lights mounted inside the box being connected and tested.

tested. The strobe electronics mainly provide inter-image pair time delay, after which the corresponding strobe light bank is strobed. By adjusting the dual in-line (DIP) switch settings, inter image times ranging from 0.33 ms to 10 ms were obtained. IDL cross correlation algorithms developed to determine velocity fields use a 32×32 pixel interrogation window. The upper limit of 16 pixels, corresponding to about 1.0 cm is the maximum displacement this system can measure. This places a limit of a less than 16 pixels, the maximum displacement this system can measure. Hence small inter image times were used when imaging wave crests as velocities there are large. Larger times were used for imaging troughs were velocities are small, in order to produce measurable displacements. It is feasible using the setup shown to obtain pairs of images that are displaced in time by only a few microseconds, while still working with the standard video format. This is achieved as follows : The video frame rate of the camera is 30 Hz, making a video frame available every 16 ms. The camera shutter is kept open for the entire frame time. The scene to be imaged is illuminated during the time the light sheet is strobed at the end of one frame time and then again at the beginning of the next frame time, as shown in Figure 3.9. Although the CCD face-plate is exposed for the entire frame time, the scene is illuminated during the time that the light sheet is flashed. Thus a pair of images separated by only a few microseconds apart are possible. By strobing the light sheet at the end of one frame time and then again at the beginning of the next frame time, it is possible to obtain images with sampling times ranging from a few microseconds to a few milliseconds while still using the normal frame update time. High sampling rates are desirable especially in the crest of the wave where higher turbulent velocities are present. Synchronization of the camera, stroboscopes and data acquisition of images is under software control. The software for this purpose was written and compiled using Microsoft C for Windows 95 and images were analyzed using software written in IDL.

Imaging equipment

The cross-sectional images of the seeded flow were recorded by a progressive scanning, full-frame, 8-bit CCD camera manufactured by Pulnix (model number TM 9701, Sunnydale, California) with a 752×468 -pixel resolution. The field of view of the camera was 38.6 cm wide and 29.3 cm high at the measurement station whose results are reported in this work. Figure 3.8 shows a picture of the camera mounted on the flume side to image a longitudinally illuminated section of the wave. The camera is attached to a metal support which in turn is attached to the strobe box. It allows the camera to be adjusted up or down. This compact assembly allows for easy sliding of the entire unit to a new measurement station. The camera was positioned at a distance of about 0.5 m from the flume side wall, at the level of the quiescent free surface in the flume, with its axis perpendicular to the length of the flume.

Figure 3.8: Picture showing the Pulnix camera mounted on the flume side to image a longitudinally illuminated section of the flume.

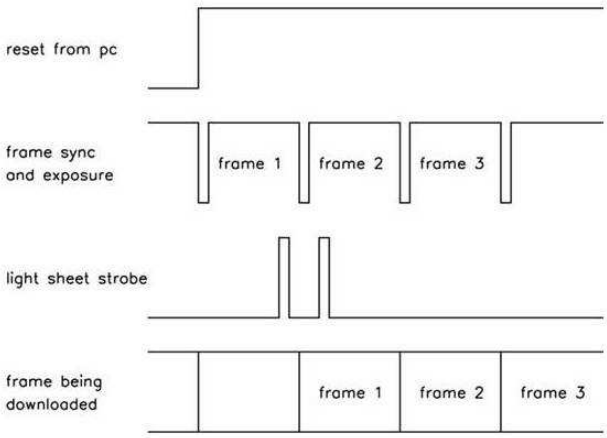

Figure 3.9: Progressive scan video capture timing diagram.

With no waves running, a calibration board, consisting of grid lines was then placed about 10 cm inside the flume, near the plane where our DCIV measurements are to be taken. The camera was then further adjusted to get a clear picture of the markings on the board. A series of images of the immersed calibration board were captured. The board was then removed. Then, with the waves running, the camera was adjusted so that images of the waves that included the beach slope and the crest part of the wave could be obtained. 100 image pairs of the breaking waves were captured at different phases. This procedure produced the best image of bubbles structures and beads in the flow.

During each frame time, the CCD face plate is exposed and at the same time the image from the previous frame time is digitized and made available. The camera is equipped with an internal frame buffer, and it is this buffer that allows the double acquisition as the first image is quickly transferred into the buffer before readout, freeing the CCD for the next image. Upon receiving an external reset signal, the camera immediately discharges the CCD face-plate and begins the exposure of a new frame. This feature is used to capture images of the wave at precise points within the wave period, a feature that is necessary for performing phase ensemble averaging of the velocity flow fields.

PIV puts special demands on the camera that is going to be used, especially if the flow velocity is high, the imaged area is small and if the particles are small. The first two circumstances requires the camera to be able to take two images within a short period of time in order for the same individual particles to appear in both images. Short inter exposure times can be achieved either by having a high speed camera which continuously records images at a rate of several kHz or by using a progressive scan camera.

Figure 3.9 shows the timing diagram for the progressive scan camera, that makes it possible to take a pair of images separated by only a few milliseconds. This is achieved by letting the first pulse come at the end of the exposure of the first image and the second pulse in the beginning of the exposure of the second image. Directly after the first image has been recorded the charge of each pixel is transferred to its designated position in the interline shift register, a new image can now be recorded by the pixels. Video images are captured and downloaded to the frame grabber using standard TV rates of 60 Hz (or 50 Hz). Each video frame is exposed for 16.67 ms. While a particular frame is being acquired or exposed the previous frame is downloaded to the frame grabber.

Wave generator synchronizing trigger pulse

The image acquisition system was triggered to capture an image pair of the flow with a specific temporal delay of $\Delta t = 1.84$ ms, between images. In order to obtain a reliable representation of the wave structure, the measurements were synchronized by a signal that was derived from the wave generator, using an optical switch. This timing and control signal was used by the computer to simultaneously drive the digital camera and acquire an image frame at the same time the strobe lights are triggered to illuminate the camera field of view. Figure 3.10(a) shows a picture of the trigger pulse-generating mechanism mounted near the wave generator. The circuit diagram for trigger generator is shown in Figure 3.10(b). The circuit employs an optical switch that uses a photodiode and a phototransistor, powered by a 9 V battery to generate the trigger pulse. The metal plate on the immediate left of the wooden shaft in Figure 3.10(a) is

attached to the wave generator piston. This ensures that it opens and closes the optical switch, generating the trigger pulse needed to sychronize wave image capturing and strobing of the strobe lights.

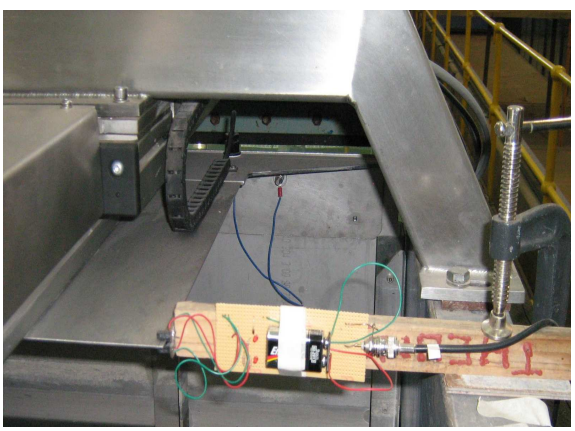

(a)

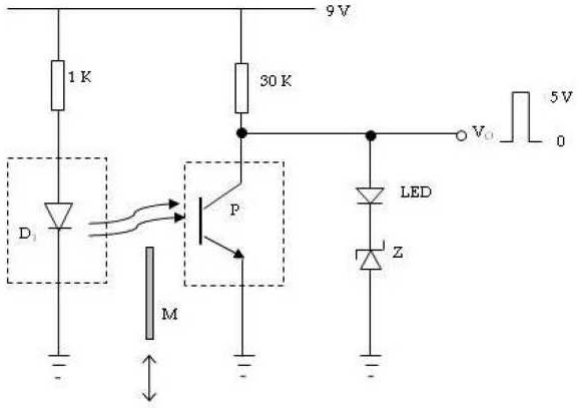

(b)

Figure 3.10: (a)Picture of the trigger pulse generating circuit mounted just behind the wave maker piston. (b) Circuit for generating the TTL synchronizing trigger pulse using an optical switch.

When the metal plate blocks the light falling on the photo-transistor, the photo-transistor is cutoff producing a +5 V at V_o. When the plate retreats, the photo-transistor is driven into saturation generating a 0 V signal. The generated pulse is used by the computer to synchronize image capturing and strobe firing processes. By employing a programmed delay time after the trigger pulse is received, the image capturing computer is able to prolong the delay before capturing wave breaking images at different phases of the flow.

3.3 Summary

The experimental facility and instrumentation setup employed to study breaking wave transformation and turbulent flow hydrodynamics in laboratory water waves has been presented. The flume is fitted with a 1:20 sloping bed. Waves generated by a servo-controlled piston-type paddle propagate, shoal and break on the slope. Details of the flume dimensions and positions of the measurement stations at which internal flow measurements were performed, were given. The coordinate systems used in the measurements has also been presented. Instrumentation for measuring wave height time series consists of a computerized data acquisition system and an array of wave gauges. Instrumentation used for internal flow measurements of the water has also been presented and described in detail.

Chapter 4: Experimental procedures and data reduction techniques

"*Great things are not done by impulse, but by a series of small things brought together.*"

- Vincent van Gogh

4.1 Introduction

It is essential to employ experimental techniques that probe the spatial structure of the turbulent velocity field without interfering with the flow. Experimentally, this is achievable if the velocity fields can be captured simultaneously at different locations in the flow. The prime quantity of interest is the instantaneous velocity flow field from which all other turbulence parameters may be derived. In order to measure the velocity flow fields, a DCIV technique based on the PIV measurement principle was used. Before proceeding with the actual description, it is useful to go over some of the factors that were taken into account prior to establishing the experimental method. A series of comprehensive procedures were carried out in order to successfully measure wave transformation, velocity flow fields and turbulence structures associated with the breaking waves. The following sections examine each experimental procedure in detail.

4.2 Experimental procedures

The wave generator was programmed to generate waves with a wave height of 12 cm and a wave period of 2.5 s, using a still water depth of 61.8 cm, in the flat section of the flume. This resulted in plunging waves which broke approximately 4.0 m from the still water line mark on the beach in a local water depth of approximately 23 cm.

4.2.1 Calibration of water level sensors and water level measurements

The instantaneous water levels were measured using a set of three capacitive wave gauges of the type WG-50 manufactured by RBR Ltd. Each wave gauge consisted of a 1 mm wire pair, which was mounted

rigidly on a stainless steel frame. Each wave gauge was connected to an electronic circuit which consisted of two oscillators - one of fixed frequency and the other made variable by means of the changing capacitance of the probe due to changes in water level. The difference in frequency was transmitted to a frequency-to-voltage converter which provide a d.c voltage linearly proportional to the frequency difference. The wave gauge manufacturer specifies a response time of 2 ms for a step change in water level. This more than satisfies our requirement of using 2.5 s period waves. The gauges were supported as shown in Figure 4.1. Wave gauge G1 was fixed near the generator at $x = -14.0$ m and the other two, above the sloping part of the beach, with G2 initially at $x = -4.0$ m and G3 at $x = -1.5$ m.

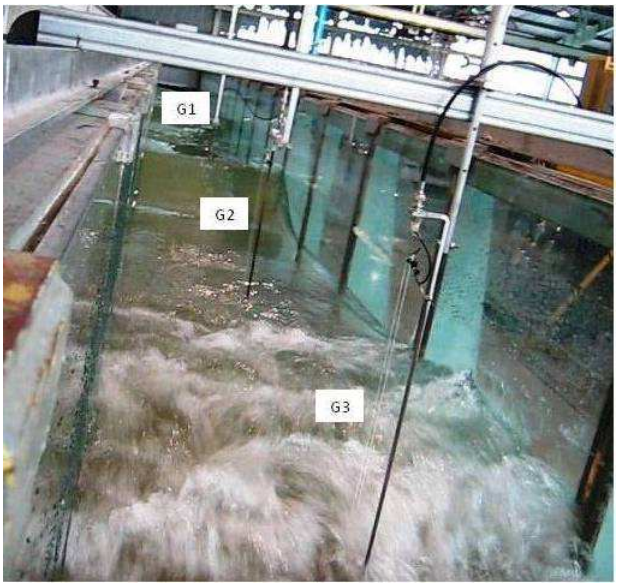

Figure 4.1: Parallel-wire capacitor wave gages used for free surface elevation measurements in the flume, looking towards the wave generator.

In order to obtain the relationship between the water level and the output voltages from the wave gauges, a proper calibration of gauges was performed prior to water level measurements. This was done with still water in the flume. The calibration was accomplished as follows :

1. With no waves running all three guages were sampled and the output voltage was noted. This corresponds to zero displacement of the water level.
2. The gauges were then moved vertically down 5 cm and the output voltage noted. This corresponds to a displacement of the water level by 5 cm upwards.
3. Finally the gauges were moved vertically up 5 cm from the original position in 1 above and the output voltage noted. This corresponds to a displacement of the water level by 5 cm downwards.

Annexed in Appendix A are the calibration results for the three wave gauges showing the least squares linear fit results. A maximum error of about 0.56 % over the range used was determined for wave gauge G1. This translates to an error of approximately 0.12 cm for a maximum displacement of 21 cm of the water level, which is a typical maximum wave height at the breakpoint in the present experiment.

External flow properties of the breaking waves were investigated through time series measurements of the

water level along the flume. The waves were allowed to run for approximately 30 minutes to ensure mean parameters, such as the position of the breakpoint, mean water levels across the flume and currents, had stabilized. Water level measurements were conducted with gauges G1, G2 and G3 initially located at $x = -14$ m, $x = -4.0$ m and $x = -1.5$ m, respectively. With the waves running, the gauges were sampled at 50 Hz over a period of two minutes. Then gauges G2 and G3 were moved 10 cm towards the generator and sampled again. This process was repeated until a total distance of 5 m spanning the breaking and pre-breaking region was covered (see Fig. 3.2 and Fig. 3.4(b)). With a sampling frequency of a reading every 0.02 s (50 Hz), there are 125 samples over a wave period of 2.5 s and a total of 6000 over a test time of 120 s. Thus 6000 samples contained approximately 48 wave cycles. Data sampled from all three gauges at each position were saved in a single text file. Each probe contributed 6000 samples, and the data from three probes resulted in a text file of size 283 kB. After the calibration process the probes were then set to an appropriate level at the starting position along the flume and re-zeroed. When this was done the probes were now ready to measure wave heights along the flume. The measured time series data were analyzed at each flume position to obtain statistics of the free surface elevation, wave height and wave velocity as the wave propagates across the surf zone. Results for water level measurements are presented in the next chapter.

4.2.2 Calibration of board for converting camera pixels to cm

To obtain velocity vectors from the DCIV images one needs the precise magnification factor between the illuminated object plane and the image plane of the camera film. The conventional way of doing this is to place a marked plate with large square grids of known size and spacing in the plane where the flow is to be illuminated. The gridded board was then photographed with no waves running. By measuring the grid size in the images it is possible to then obtain the magnification or calibration factors in the longitudinal and transverse directions (*She et al.* [121]).

In this case a rectangular perspex board was marked with equidistant 5 cm spacings between consecutive vertical and consecutive horizontal lines. The board was placed longitudinally, at a position 10 cm away from the flume glass, vertically below the light sheet, at the same position in the window where the DCIV measurements are intended to be taken. This position was chosen so as to avoid wall effects on our DCIV results. The camera was moved back and forth until the board filled the entire field of view of the camera. The focus was then adjusted to give a clear picture of the board after which it was locked at that position. Calibration of this system was achieved by photographing the perspex board. Figure 4.2 shows one such image of the calibration board used at a measurement station whose center is -238 cm from the SWL mark. In this image the still water level is just above the horizontal line marked 2. The acquired images of the board were later read into a computer program to determine the number of pixels between two chosen points in either direction. The distance between any two points in the x and z directions was then used to convert camera pixel displacements into physical units for the corresponding axis. Calibration results at this station gave calibration factors of $f_x = 19.5$ pixels/cm for the x direction and $f_z = 16.0$ pixels/cm for the z direction.

Figure 4.2: Typical image of a marked *calibration board* used for image rectification, placed at station whose center is -238 cm from the SWL mark. Vertical and horizontal lines are equidistant, with a separation of 5 cm. Calibration results obtained for this position for the x and z directions were 19.5 pixels/cm and 16.0 pixels/cm, respectively.

4.2.3 Flow seeding

After successfully measuring wave heights along the flume, the gauges were then removed from the flume so that the gauges did not interfere with the flow for DCIV measurements that followed. The flume was then seeded with light reflecting particles, polystyrene spherical beads with an average diameter of 0.5 mm, in order to be able to visualize the flow field. DCIV technique was used to extract velocity flow fields from which a planar cut of the velocity field is inferred from images of the distribution of particles in the measurement plane. By correlating these snapshots it is possible to obtain a 2-dimensional projection of the velocity field in the measurement plane. Two critical requirements for accurate DCIV measurements are that the particles are small, with a density close enough to the density of the fluid that it can be assumed that the particle movement is the same as the fluid movement and that the same particles are visible within the measurement space for two closely spaced time intervals.

To meet the first requirement, unexpanded beads were heated in water maintained at 85^{o}C for 60 s, before the experiments. This was done to lower their specific density so that they become neutrally buoyant to be able to follow the flow accurately. It was preferable to have some denser particles which sediment in the bottom of the flume than overheating them which results in a cloud of these bead particles accumulating at the free surface preventing the strobe light from above to illuminate the particles below (She *et al.* [121]). Small mismatches are acceptable, depending on the application and, in practice, really neutrally buoyant particles are rarely available (*Raffel et al.* [122]). The success of the DCIV technique is also based on seeding the flow with particles, so the other precaution observed was that the particle density was made large enough to be able to resolve the smallest scales in the flow. Figure 4.3 is an image showing typical seeding density used for the PIV experiments. The image shows the trough part of the wave. The light sheet thickness and particle density were such that about 12 particles were present

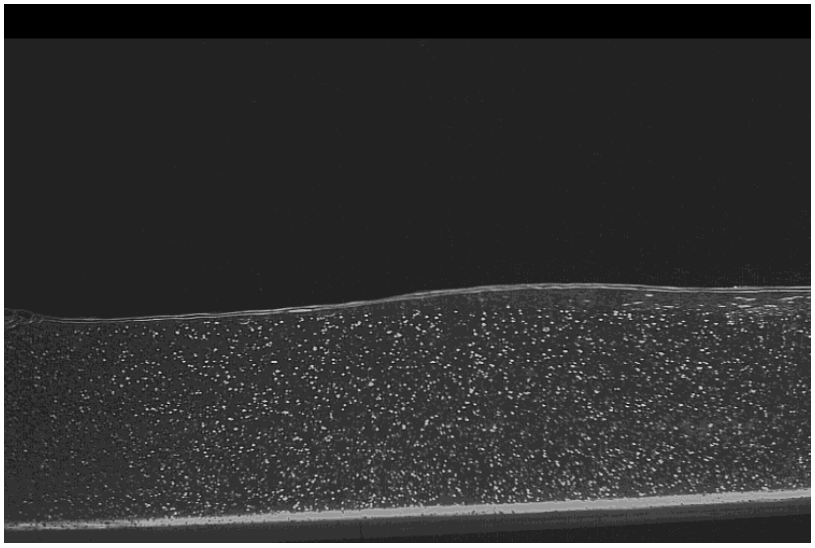

Figure 4.3: Image of the wave trough showing typical seeding density used for DCIV experiments.

per square centimeter of the measurement area. The size of seeding particles used is $\sim$ 0.5 mm. The uncertainties in the measured instantaneous velocities are of the order of $\sim$ 2.0 cm/s.

4.2.4 Wave phase labelling

The wavelength of the generated wave is about 6.0 m yet the camera can only view a 40 cm portion of the wave. In order to image a full cycle of the incident breaking wave, the wave was sub-divided into 20 overlapping phases or fields of view (FOV). A TTL trigger pulse from the wave generator made it possible to capture an image at any one of these phase positions. This enabled the measurement system to capture images of the breaking waves at different phases. The synchronizing pulse also enabled the image acquisition computer to capture images at precisely the same point in the wave cycles so that phase ensemble averaging could be performed. Images from the 20 wave phases are numbered relative to the wave period, T, with $\frac{t}{T}=\frac{0}{20}$ representing the first phase, through to phase $\frac{t}{T}=\frac{19}{20}$ for the twentieth phase as shown in Figure 4.4. These wave phases were conveniently labeled 0.00, 0.05, 0.10, $\cdots$, 0.90 and 0.95. More detail is given in section 6.2 of Chapter 6.

4.2.5 DCIV procedure

Velocity flow fields were measured using the DCIV technique. This is a non-intrusive measurement technique that does not disturb flow field. The principle of this technique is the same as PIV, the only slight difference being that while PIV tracks the motion of particles, DCIV tracks the motion of groups of particles and aerated structures in the flow to determine the velocity flow fields. The DCIV system measures the displacement of a group of particles in a two-dimensional illuminated plane inside the flow. The displacements divided by the time separation between the images, gives the velocity for a small

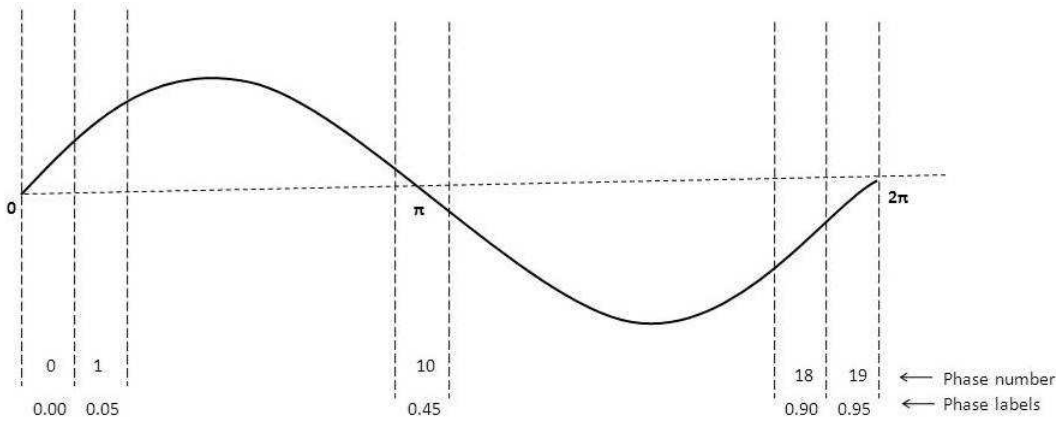

Figure 4.4: Schematic showing how phases are labeled relative to the wave period.

sub-region of the whole imaged area.

The primal use of PIV in the field of water waves is classified in two ways. One is to compare the kinematics of existent analytical or numerical wave theory with the PIV measurements (e.g. *Skyner & Easson* [123]; *Jensen et al.* [124]; *Buick et al.* [125]). The other is to obtain some knowledge about a wave field involving extreme flow conditions (e.g. *She et al.* [121]; *Fritz et al.* [126]) or interactions with structures (e.g. *Chang et al.* [127]; *Jo et al.* [128]) where theoretical approaches are difficult. Figure 4.5 summarizes the procedure for performing DCIV whose working principle is as follows : The flow is seeded with white, neutrally buoyant reflecting particles. A light sheet is periodically strobed, illuminating the particles in the measurement plane and a camera is used to take two exposures of the illuminated plane. Seed particles within a 2-D slice of the flow are imaged producing a sequence of flow images in time. The two exposures should be taken within a short interval, so that the same particles are caught in both exposures. The two exposures can be taken either as a double exposure of one image or as two different images. The double exposure technique is based on an autocorrelation and this results in an directional ambiguity (since it is impossible to tell whether an imaged particle was in the first or second exposure), thus the flow can only be in one direction when this method is used. Hence, the method with two images and cross-correlation is more commonly used and the remaining part of this section will deal with this technique. Pairs of digital images taken are then downloaded onto the image acquisition computer that was fitted with a frame grabber.

These pairs of images are each broken into 32×32 pixels subimages with each pair of these interrogation windows producing a single fluid velocity vector. The displacement is determined by computing the spatial cross-correlation of these two subimages. The peak of the cross-correlation gives a measure of particle displacements between subimages. More detail of the computational procedure is given in the sections following this. The mean displacement and direction of the velocity vector can then be determined from the location of the peaks in the cross-correlation function. The interrogation window was then moved vertically and horizontally in steps of 8 pixels and the above procedure was repeated for each subsection of the image pairs, producing vectors which describe the velocity flow field. The typical field of view is 38.6×29.3 cm^2. This area was digitized at 752×468 pixels^2. The DCIV vector processing cross-

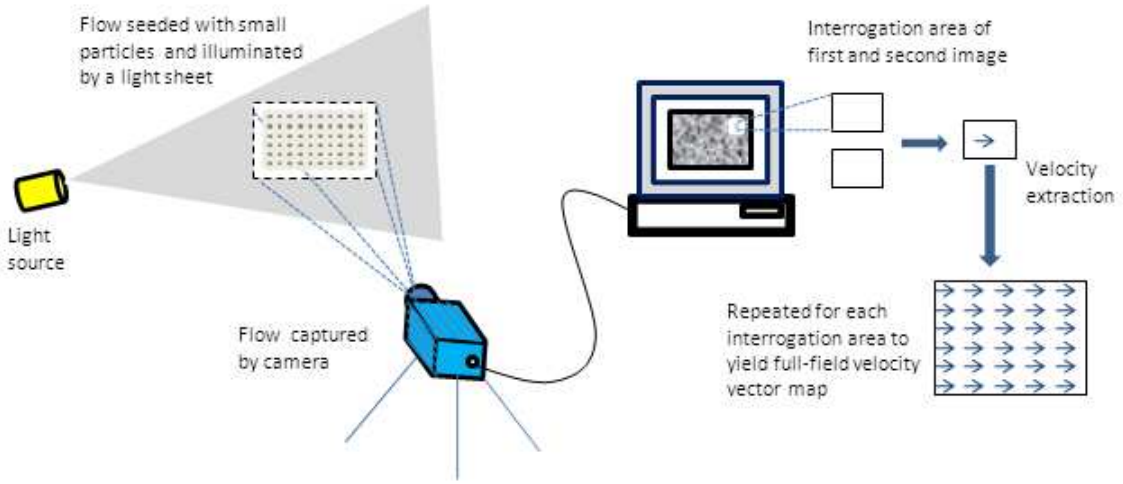

Figure 4.5: PIV process for obtaining velocity vector map.

correlation algorithm developed here used interrogation windows of 32×32 pixels with an overlap step of 8 pixels (75 % overlap) in each direction. The resulting velocity vector fields have a vector arrow density of 1 vector per 8×8 pixels. This produced for each image pair a 91×56 array of velocity vector maps with a resolution of 4.1 $mm \times 5.0$ mm for the horizontal and vertical directions, respectively. A good reference which deals with most of the aspects of PIV and its application to water waves is a book by *Raffel et al.* [122] and an article by *Grue et al.* [129]. *Westerweel* [130] details the measurement principle of digital particle image velocimetry (DPIV) which is described in terms of linear system theory. Limitations of the method arising from consequences of the implementation are also presented.

100 DCIV image pairs were captured each of the 20 phases at one measurement station. This resulted in 100 instantaneous velocity flow fields for each phase. A total of 4000 images were acquired and analyzed giving a total of 2000 velocity fields. Instantaneous velocities were obtained by measuring the combined displacements of polystyrene particles and air bubbles entrained in the flow by the breaking waves. Phase averaging these data sets at different phase angles allows us to estimate both profiles of horizontal and vertical velocities. Ensemble averaging over many runs of the experiment was found to be an appropriate method of determining the mean and turbulent quantities in this non- stationary flow. Experimental results of the structures of distributions and the evolution of velocity flow fields are presented for six phases that include the crest, at which turbulence is predominant. The subsequent vertical and cross-shore distribution of the velocity profiles associated with the mean flow for these phases are also presented.

Image analysis

Almost all algorithms for the estimation of the displacement of a group of tracer particles use cross-correlation techniques. The aim of the cross-correlation is to find the distance that the particle pattern has moved during the inter image time and translate that into a velocity measure. Cross-correlation functions can be calculated in a number of different ways.

For a digital image pair of the same size $m \times n$, the discrete cross-correlation function is defined as:

$$C(m,n) = \sum_{i} \sum_{j} GL_1(i,j) GL_2(i-m, j-n) \tag{4.1}$$

where $i = 0,\ 1,\ 2,\ .\ .\ .\ m-1$; $j = 0,\ 1,\ 2,\ .\ .\ .n-1$; and GL_1 and GL_2 are regions in the first and second images, respectively. The maximum peak location in *C (m, n)* indicates the speckle displacement. Equation (4.1) can be computed either directly in the spatial domain or in the frequency domain via a Fast Fourier Transform (FFT) algorithm (*Abolhassani et al.* [131]; *Huang et al.* [132] and *Willert and Gharib* [133]). The FFT algorithm was implemented as it provides a fast implementation of Eqn. (4.1), especially when the sizes of GL_1 and GL_2 are the same. In the spatial correlation map, different correlation peaks appear which attest to the presence of several matching particles in the window. As statistically the other peaks have small probabilities of having the same location for new double images, the final signal peak increases with the number of the correlated image pairs (*Billy et al.* [134]). In this application, cross-correlation of a group of particles (Eqn. (4.1)) is computed in the Fourier space. This cross-correlation of two functions is equivalent to a complex conjugate multiplication of their Fourier Transforms (*Brigham* [135]; *Bendat* & *Piersol* [136]). This fact is actually exploited to speed up the calculation dramatically as Fast Fourier Transforms can be calculated with a number of operations proportional to $N \log N$, compared to N^2 required by Eqn. (4.1) (*Prieto* [137]).

Velocity extraction using FFT cross correlation

IDL software programmes were developed that compute velocity fields of a captured flow field by estimating particle displacements between two consecutive frames with FFT-based cross-correlation peak search algorithm. The mean d.c intensity level of PIV images was removed prior to the analysis. Figure 4.6 shows a flowchart of the Fourier cross-correlation procedure that was used to extract instantaneous velocity fields from image pairs. A more detailed description of the cross-correlation technique used here can be found in *Willert* & *Gharib* [133] and *Raffel et al.* [122]. A pair of bit map *bmp* images was first read into the IDL program developed to perform 2-D cross correlation in the Fourier domain. Before the cross correlation was performed, the 32×32 pixel subimages were first copied into center of 64×64 pixels to avoid data overrun in the Fourier cross correlation calculation. *Govender et al.* [53] describes in detail how FFT algorithms are used to extract velocity fields from the images using the DCIV procedure.

The grayscale level in a subsection of first image, 1, $f(m,n)$, (taken at time t), and the gray scale level of a corresponding subsection in image 2, $g(m,n)$, (taken at time $t+\Delta t$), both obtained from an interrogation window of 32×32 pixels, centered around point (i,j), were then converted to the frequency space using Fast Fourier Transforms (FFT) as follows :

$$F(u,v) = FFT(f(m,n))$$

$$G(u,v) = FFT(g(m,n)) \tag{4.2}$$

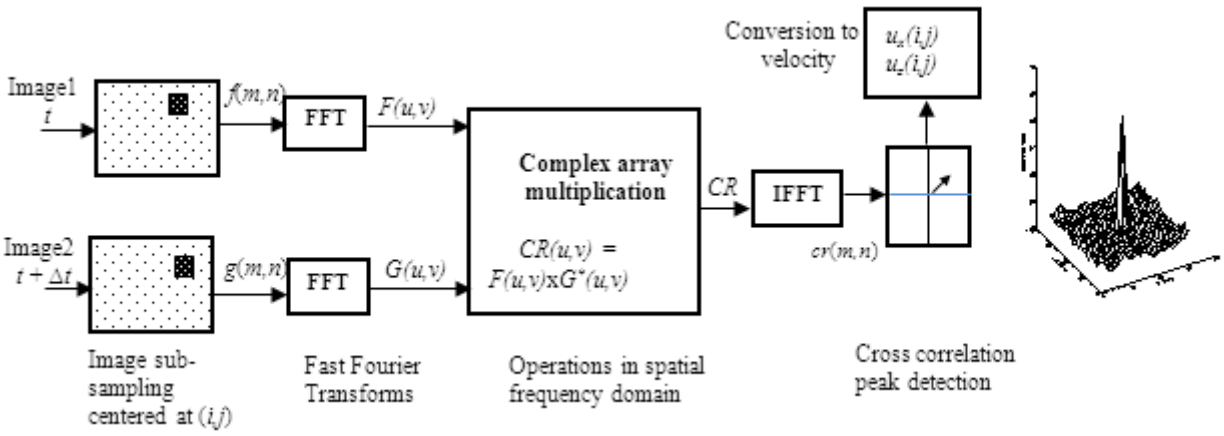

Figure 4.6: Flow chart of DCIV implementation. Cross-correlation estimates are calculated by FFT algorithm to obtain the spatial shift of particles (Adopted from *Willert & Gharib* [133] ; *Weng et al.* [138]; *Ruan* [139]).

where $F(u,v)$ is the Fourier Transform of subimage $f(m,n)$ in the first image and $G(u,v)$ is the Fourier Transform in the corresponding subimage $g(m,n)$ in the second image. The two subimages in the frequency space are multiplied to produce a 2-D Fourier transform of the cross-correlation function of the subimages :

$$CR_{fg}(u,v) = F(u,v) \times G^*(u,v) \tag{4.3}$$

where G^*(u,v) is the complex conjugate of $G(u,v)$, the Fourier Transform corresponding to subimage, $g(m,n)$ in the second frame.

An inverse FFT is then performed on the convolution product to give the cross correlation result given as :

$$cr_{fg}(m,n) = FFT^{-1}(CR_{fg}(u,v)) \tag{4.4}$$

where $cr_{fg}(m,n)$ is the computed 2-D cross correlation function of the two sub-images.

The correlation procedure yields a landscape of peaks for varying displacements. A typical cross-correlation plane is illustrated in Figure 4.7. The single main peak in the figure corresponds to the average correlation of each particle image in the first frame with itself in the second frame. It also contains smaller peaks corresponding to random background noise, which results from correlations with other particles. The displacement of the main peak from the center of the plane corresponds to the average displacement of particles in the images and its height is determined by the number of particle pairs with that displacement. Thus $cr_{fg}(m,n)$ represents the spatial correlation function where the distance of the peak from the center is equivalent to the average fluid displacement in a given time.

Peak detection and sub pixel displacement interpolation

Since velocity vectors are obtained based on pixel resolution, a positional uncertainty of ± 1 pixel can occur (*Hyun et al.* [140]). To enhance the accuracy, a subpixel resolution method was adopted. Sub pixel interpolation refers to the interpolation done on grid points to find the point with maximum cross

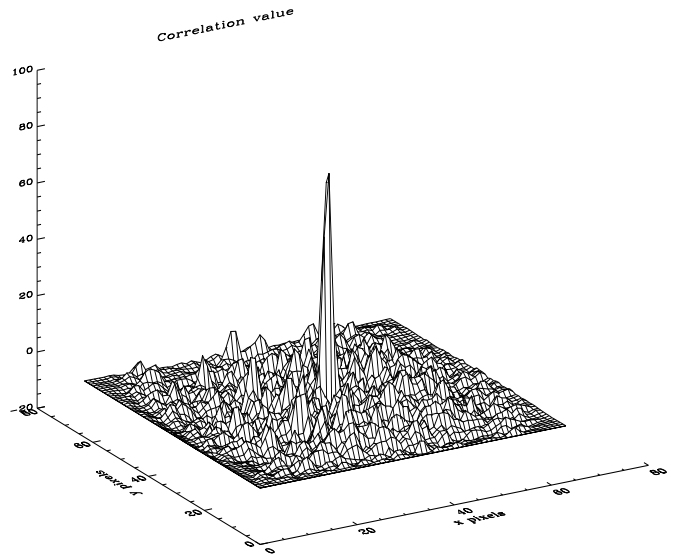

Figure 4.7: Typical unnormalized 2-D spatial cross-correlation function $cr_{fg}(m,n)$ obtained from 32×32 pixel subimages. The cross-correlation map shows a single dominant peak corresponding to the magnitude and direction of particle shifts.

correlation coefficient near the grid points. When the cross-correlation has been performed a measure of the displacement is found by detecting the location of the highest correlation peak. The highest peak for an interrogation area is located at a discrete pixel location, due to the discrete nature of the input signal. This would introduce an error of ± 0.5 pixels in the determined displacement. The accuracy in the peak position can be increased substantially by curve fitting on the dominant displacement peak. In some cases displacement is determined by applying a (multi point) Gaussian peak fit to the correlation peak (*Zeilstra et al.* [141]). In other cases interpolation in the Fourier domain is used to determine the displacement of the image to sub pixel accuracy. These procedures are very helpful for the improvement of DCIV accuracy and are especially effective for the case when average displacement of the particles is small between two images (*Hu et al.* [142]).

In this application, the position of the peak was estimated to within subpixel resolution interpolation in the Fourier domain as follows : A vertical slice passing through the cross correlation peak is extracted and a 64 point, 1-D Fourier transform of this computed. This 1-D spectrum is then zero-padded to a length 2048 and the inverse FFT computed giving a signal which is interpolated by a factor of 32. The z position of the peak is estimated to within subpixel resolution using this interpolated slice through the original cross correlation. A similar procedure is adopted for the horizontal slice passing through the cross correlation peak. The subpixel displacement was divided by the inter image time, Δt to get the velocity.

Normalizing the cross-correlation cr_{fg} using Fourier transforms

The cross-correlation cr_{fg} defined by Eqn. (4.4) is sensitive to intensity changes (*Huang et al.* [132]; *Abolhassani et al.* [131];). To avoid this, the cross-correlation is normalized via the Fourier domain by

using the sub image autocorrelations. These autocorrelations were computed as follows :

$$acf_1(u,v) = F(u,v) \times F^*(u,v)$$

$$acf_2(u,v) = G(u,v) \times G^*(u,v) \tag{4.5}$$

where $F(u,v)$ and $G(u,v)$ are the Fourier transforms of the two subimages as defined in (4.2) and * denotes the complex conjugate of the subimage.

Inverse Fourier Transforms (IFFT) are then computed as follows :

$$ac_1(m,n) = FFT^{-1}(acf_1(u,v))$$

$$ac_2(m,n) = FFT^{-1}(acf_2(u,v)) \tag{4.6}$$

where *ac1* and *ac2* are the autocorrelations of the two subimages.

If the maxima of the autocorrelations are mx_1 and mx_2 respectively, then the variances are defined as :

$$\sigma_1^2 = mx_1$$

$$\sigma_2^2 = mx_2 \tag{4.7}$$

Normalization of cross-correlation is performed by dividing cr_{fg} by the product of the standard deviations of the two subimages as :

$$ncr_{fg} = \frac{cr_{fg}}{\left[\sigma_1^2 \sigma_2^2\right]^{1/2}} \tag{4.8}$$

ncr_{fg} is now normalized and has values lying between 0 and 1.

Spurious vector detection

A major difficulty in DCIV is the occurrence of secondary maxima of the cross correlation, which can spuriously exceed the maximum associated with the local displacement. The raw velocity vector matrix calculated by the software was further subjected to post-processing in which spurious vectors involved were eliminated to obtain a better flow field. Two methods of removing spurious vectors were employed. One method compared the height of the peak in the correlation to the next highest peak. Figure 4.8 shows a pair of typically normalized correlation functions obtained after the pairs of subimages in the crest and trough respectively, were cross correlated to give functions that vary in both peak height and width. Figure 4.8 (a) shows the spatial correlation results from the trough part of the wave, where velocities are low and particles clearly defined, while (b) shows results from the fast moving crest part that contains both seed particles and bubble structures that result in smearing of the correlation result. For Figure 4.8 (a) the normalized height of the main peak is $m_1 = 0.71$ and the secondary peak (noise peak) has a height, $m_2 = 0.08$. Figure 4.8 (b) $m_1 = 0.44$ and $m_2 = 0.13$. The ratios m_1/m_2 are therefore 8.16 and 3.1, respectively. The other method compared each vector to its 8 neighbouring vectors. A vector that differs from its neighbour by a predetermined factor was removed and replaced by the average of

its neighbouring vectors. The larger the difference between the main peak and the largest noise peak, the more accurate the results of the PIV analysis generally are (*Zeilstra et al.* [141]). *Adrian* [143] and *Kimmoun and Branger* [43] used a limit of 1.2 in addition to the average median criterion where the velocity vector should not differ by more than 50 % in modulus and $\pi/6$ in direction from the median value of all the neighbouring vectors. The correlation techniques gave obviously bad results in areas of high intensity. Further discussions on the cross-correlation are done in section 4.3.3 of this chapter.

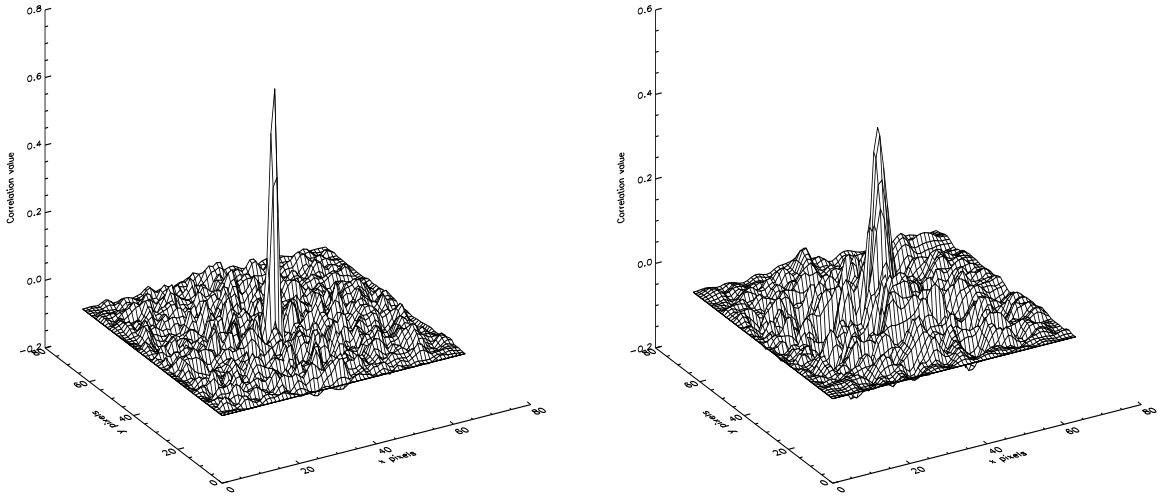

Figure 4.8: Typical *normalized spatial cross-correlation* functions, *cr(m,n)* corresponding to (a) the trough and (b) the crest section of the wave. In (a) $m_1 = 0.71$ and $m_2 = 0.11$ giving $m_1/m_2 = 6.5$. The subpixel interpolated displacements in the x and z directions are obtained from the relative shift of the peak from the center.

Conversion to velocity

After obtaining particle pixel displacements, dx and dz, in the x and z directions, respectively, the displacement results were converted to horizontal velocity, u cm/s and vertical velocity, w cm/s, using relations :

$$u = \frac{dx}{f_x \Delta t} \quad ; \qquad w = \frac{dz}{f_z \Delta t} \tag{4.9}$$

wheref_x and f_z are the *pixel/cm* calibration factors in the x and z - directions, respectively, and $\Delta t =$ 1.842 ms, is the inter-image time. Table 4.1 shows the calibration factors at each of the five measurement stations, in $pixels/cm$. As the water depth decreased towards the shore, the camera position was shifted closer to the flume glass, and therefore larger calibration factors obtained.

4.2.6 Mean and turbulence parameters measured

Figure 4.9 is a schematic showing mean and turbulent parameters that were derived from the measured instantaneous horizontal velocities, u_i. Similarly for the vertical velocity component, w_i. The arrows

Table 4.1: Calibration factors used at the five measurement stations.

Station	f_x (pix/cm)	f_z (pix/cm)
win11b	19.3	15.8
win12a	19.5	16.0
win12b	23.7	19.8
win13a	29.0	23.5
win13b	35.5	29.5

show which quantities were used to calculate each given parameter. Mean parameters were calculated using phase-ensemble averaging and time-averaging techniques.

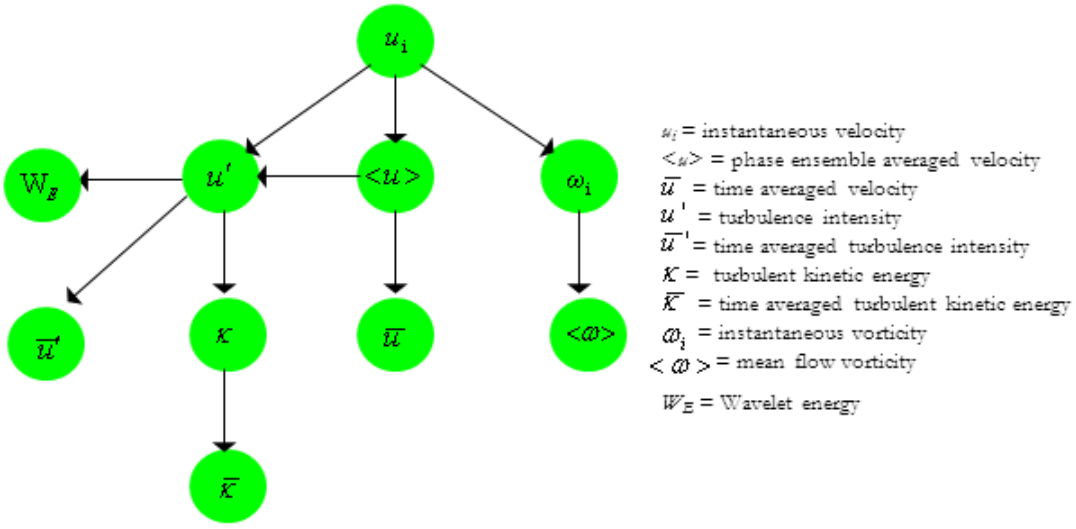

Figure 4.9: Schematic showing mean and turbulent parameters derived from the measured instantaneous velocities.

4.3 Experimental Accuracy

4.3.1 Spatial resolution of velocity measurements

Since the velocity is averaged across the interrogation window, DCIV resolution is an important issue. One of the major difficulties in flow imaging is achieving adequate spatial and temporal resolution. This is particularly the case when flows are turbulent because the resolution requirements are typically very severe if it is desired to resolve the smallest scales at which fluctuations occur. Laminar flows, however, pose substantially less stringent requirements on resolution, compared to turbulent flows. The primary issue when considering the resolution requirements is the gradient of the flow property that is being measured because the gradient determines the amount of averaging that occurs across the resolution volume.

In turbulent flows, the spatial fluctuations in flow properties, such as velocity, range in scale from the largest physical dimension of the flow (e.g., the local width of the boundary layer or jet) to the scale at

which diffusion acts to remove all gradients. The largest scales are often called the macro scales or outer scales, whereas the smallest scales are the micro or inner or dissipation scales because these are the scales at which the energy of fluctuations, whether kinetic or scalar, is dissipated.

The resolution that one can achieve in practice using these image-based techniques depends on a number of factors, including but not limited to camera resolution, lens optical quality, and marker size and quality. In the present study velocity fields were calculated based on the FFT-correlation algorithms. Similar to the work by *Raffel et al.* [122], each pair of images was processed from an interrogation window size of 32× 32 pixels using 75 % overlap. The interrogation window was moved vertically and horizontally in steps of 8 pixels producing vectors which describe the velocity flow field for the entire image. The resulting velocity vector field has a vector arrow density of 1 vector per 8×8 pixels. Using calibration factors of 19.5 and 16.0 pixels/cm obtained for the x and z directions, respectively, this produced for each image pair, a 91×56 array of velocity vector maps with a spatial resolution of 4.1 $mm \times 5.0$ mm for the horizontal and vertical directions, respectively. This spatial resolution does not resolve velocities at the scale of dissipation. However, dissipation can be estimated from the velocity measurements by other means such using the slope of the Fourier spectra in the frequency range above the micro scales (e.g *Govender et al.* [73], *Huang et al.* [115]). The choice of a 32×32 interrogation window was based on our sampling time of 1.84 ms which resulted in maximum particle displacements of 16 pixels. The sensitivity of interrogation window depends on having a significant number of particles within the window averaged over a number of waves. Previous analysis of window size sensitivity has been done by *Govender* [94] and since we are using similar settings, the optimum window size they determined is employed here. Many previous researchers such as *Ting* [77], *Govender et al.* ([42], [73], [79], [78]) and *Huang et al.* [44] have used 32×32 pixel size interrogation windows.

4.3.2 Experimental accuracy

The experimental nature of this DCIV study may affect the results with several error sources. Considering the complexity of quantifying a priori all the error sources, only the most relevant ones will be briefly analyzed. A more detailed analysis can be found in the work of *Silva* [144]. A primary error source is related to inertial effects between the particles displacement and the fluid motion. At sub-micron scales Brownian motion can assume a significant influence in the physical description of the tracer particles motion (*Devasenathipathy et al.* [145]). For the present case, where tracer particles mean diameter is 0.5 mm, and their displacement is computed through an ensemble time-average algorithm, Brownian motion effects have a negligible influence. For a cross-correlation algorithm the in-plane velocity is computed by locating the highest peak in the correlation plane. The uncertainty in locating this correlation peak is closely related to the particles image size, d_e. As demonstrated by *Prasad et al.* [146], as long as d_e is resolved by 3 to 4 pixels, the uncertainty, Δu, in locating the correlation peak and thus the error estimate in computing the in-plane velocity can be estimated as :

$$\Delta u = \frac{d_e}{10M} \tag{4.10}$$

where M is the magnification of the camera lens, which is 19.5 pixels/cm in this case. This gives Δu = 0.2 mm which is about one order of magnitude smaller than the characteristic flow length-scale of 5.0 mm, chosen herein as the distance between adjacent velocity vectors. Thus this uncertainty does not influence significantly the in-plane velocity results. The presence of out-of-plane particles contributing to the in-plane velocity can bias the computation of the latter if the measurement volume is too thick and strong velocity gradients in the out-of plane direction exist simultaneously (*Silva et al.* [147].

4.3.3 Assessment of the DCIV technique

Since its introduction, DPIV has seen a series of improvements in both the experimental and the post-processing stage (*Westerweel et al.* [130]; *Jones* [148]; *Scarano & Riethmuller* [149]), increasing the accuracy and reducing noise in the PIV representation of the actual flow field. Improvements like these are particularly very useful for comparisons of experimental results with theoretical models or Navier-Stokes simulations. Experimental accuracy in DCIV tends to be good, provided that the experimental parameters, such as : seed particle diameter, interrogation window size, etc. are suitably chosen. While no straight-forward formula for predicting accuracy exists, some estimate are available from *Raffel et al.* [122]. Their Monte Carlo simulations suggest that, for a 32×32 interrogation window and particle image diameters of 13 pixels, displacement uncertainty is around 0.02 - 0.04 pixels. For the present experiments, computed mean particle displacements were consistently around 3-4 pixels, indicating that the uncertainty was of the order of a few percent. *Hyun et al.* [150] provide a discussion of the factors that determine the accuracy of PIV data.

In PIV measurements, seed particle size must be small enough to faithfully follow the flow without disrupting the flow field, and producing unnecessarily large images. At the same time, particles must be large enough to be adequately imaged and to dampen the effects of Brownian motion (*Santiago et al.* [151]). Figure 4.10 shows two marked subsections in one of the images chosen to closely examine the DCIV results. Two boxes marked A and B in the image show 32×32 pixel sub-images (not drawn to scale) in the trough region and the crest region, respectively. The crest region consists mainly of bubbles while the trough region consists of beads. The intention is to determine the correlation peaks and the resultant displacement for these two different sections of the wave.

Figure 4.11 shows an expanded view of the subimages from the two positions and the resulting surface and intensity plot of the normalized cross-correlation results. On average there are more than 40 beads in each 32×32 pixel interrogation subimage and each bead in the image occupies about 3-4 pixels. In Figure 4.11(a) it is possible to identify corresponding particles in both subimages labeled by 1 and $1'$; and 2 and $2'$. The displacement of the peak from the center is equivalent to the displacement of beads and bubble structures during a certain time interval. Figure 4.11 was included to show the effects of air bubbles to the overall flow. During a small inter image time of 1.84 ms, the bubbles buoyancy effects are negligible as can be seen from Figure 4.11(b) and so the bubbles are considered to be locked with the flow. *Govender et al.* [42], [73], [79] used similar air bubbles together with seed particles to track the flow patterns and obtained results that compare well with PIV measurements.

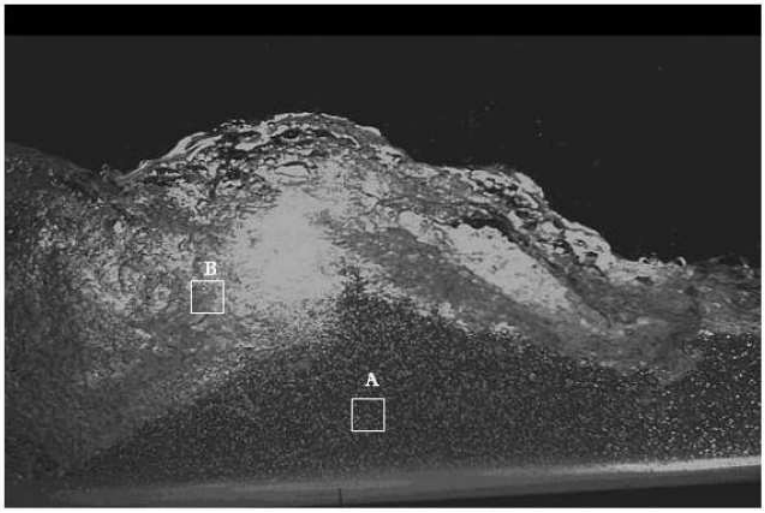

Figure 4.10: Typical images for a 0.4 Hz plunging breaking wave captured by a monochrome digital camera. Zones marked A and B are 32×32 pixel sub images consisting of mainly beads for area A, and bubbles for B.

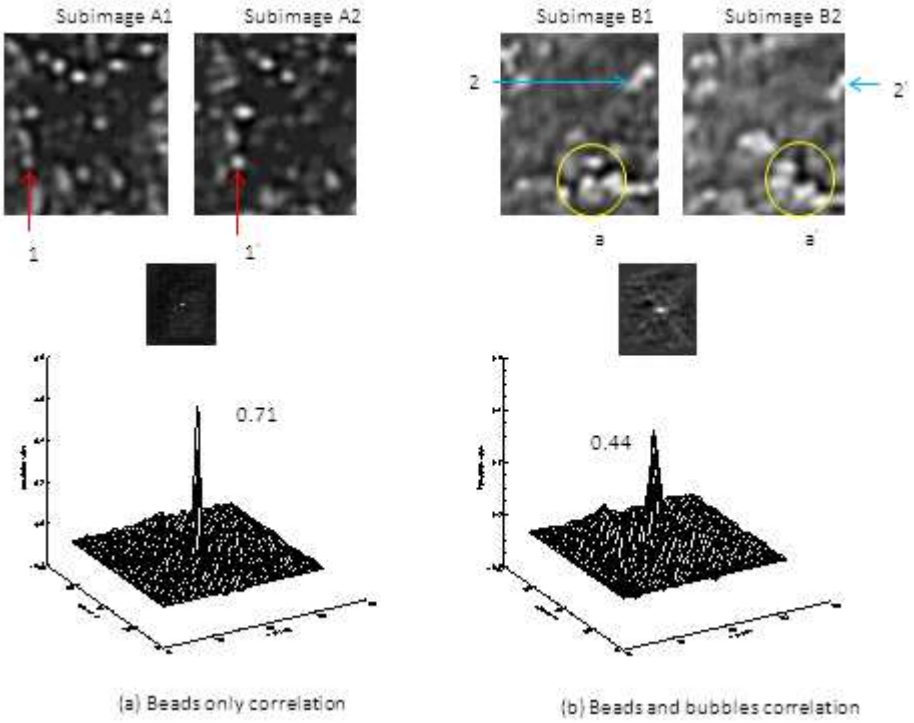

Figure 4.11: Expanded view showing 32×32 pixel subimages shown in Figure 4.10 and surface plots of the resulting cross-correlation functions, $cr_{fg}(m,n)$ and its intensity plot for : (a)-beads only area (b)-bubbles and beads area.

The spatial cross-correlations between the subimages A1 and A2 and between B1 and B2 are shown near the bottom. A perfect match in the two subimages gives rise to a sharp peak in the cross correlation result as seen for Figure 4.11(a). A plot of the intensity profile for subimages A, show a well defined point. The actual subpixel displacements in the x and z direction are 6.03 pixels and 1.16 pixels, respectively. In Figure 4.11(b) a few matching particles such as 2 and $2'$ and bubble structures a and a' are observed. Bubble structures are spread out, that is why the resultant cross correlation is not as peaked as in (a). The resulting plot of intensity profile is thus smeared out. The horizontal displacement is 8.03 pixels while for the vertical it is -1.42 pixels. A "signal-to-noise" ratio, (SNR), defined here

as the ratio of the cross-correlation peak to the second highest (noise) peak was used to detect spurious vectors. In the analysis, velocity vectors with a *SNR* ratio under 1.5 were removed as explained previously.

4.3.4 Error analysis in the velocity measurements

Because PIV is based on the statistical correlation of imaged subregions to determine local flow velocities, it is subject to inherent errors that arise from finite tracer particle numbers, sample volume size, and image resolution. These errors, in extreme cases, are relatively easy to detect as they tend to vary substantially from neighboring vectors in both magnitude and direction. One fundamental source of these errors arises from the implementation of cross correlation. Other major sources of these errors arise from the peak-finding scheme, which locates the correlation peak with a sub-pixel accuracy, and noise within the particle images (*Huang et al.* [132], *Fairweather* & *Hargrave* [152].

There are two major sources of error that may be of concern in our DCIV measurements of fluid velocity in the breaking wave crests. The first is the *r.m.s* error associated with the accuracy of estimation of the location of the displacement correlation peak. The second is downward biasing of the velocity measurement due to gradients in the velocity field. Appropriate references are *Huang et al.* [132], *Westerweel et al.* [130] and *Keane* & *Adrian* [153]. Generally one would not expect the total velocity measurement error to exceed 2% - 3% in well-prepared PIV experiments (*Stansell* [154]). From Figure 1. of *Westerweel et al.* [130] it is possible to estimate the *r.m.s* error. Typical pixel displacements in our PIV images are about 5 pixels. Seeding particle image diameters are about 3-4 pixels. From Figure 1. of *Westerweel et al.* [130] it is observed that the expected value of the *rms* displacement error will be no more than about 0.2 pixels. This gives an upper bound on the *rms* error in the velocity measurements of about 2%. A typical value for the minimum measurement error is 0.05 to 0.1 pixel units for a 32×32 pixel interrogation region. This implies a relative measurement error of about 1% for a displacement that is one quarter of the interrogation window size (8 pixels) (*Westerweel et al.* [130]). When setting up a DCIV measurements, the side length of the interrogation area, d_I, and the image magnification, M are balanced against the size of the flow structures to be resolved. One way of expressing this is to require the velocity gradient to be small within the interrogation area. According to *Keane* & *Adrian* [153] the dimensionless parameter, p_v that represents the performance of DCIV with regard to velocity biasing is given by:

$$p_v = \frac{M|\Delta u|\Delta t}{d_I} \tag{4.11}$$

where M is the magnification factor in units of pix/m, $|\Delta u|$ is the maximum variation of velocity across the interrogation region of size d_I pixels and Δt is the time interval in seconds between light pulses. The condition given by *Keane* & *Adrian* [153] for optimum performance of PIV with regard to velocity biasing is :

$$\frac{M|\Delta u|\Delta t}{d_I} < 0.05 \tag{4.12}$$

The highest measurable velocity is constrained by particles traveling further than the size of the interrogation area within the time, Δt. The result is lost correlation between the two image frames and thus loss of velocity information. The upper bound on $|\Delta u|$ is given by :

$$|\Delta u| < \frac{0.05 d_I}{M \Delta t} \tag{4.13}$$

For the present experiments, d_I =32 pixels, $M = 19.5\ pixels/cm$, and $\Delta t = 0.00184$ s. This sets the upper bound of $|\Delta u| < 0.45$ m/s. The maximum observed $|\Delta u|$ is about 0.25 m/s, which is well within the optimum limit.

The uncertainty in instantaneous velocity measurements, Δu and Δw, estimated from the $r.m.s$ deviation is about 2.0 cm/s. The mean velocities $< u >$ and $< w >$ have an uncertainty : $\Delta u/\sqrt{N} = 0.2$ cm/s, where N is the sampling number used in the ensemble average.

4.4 Summary

This chapter described methods and experimental procedures that were followed in order to meet objectives of the study. Calibration of water level sensors and how the sensors were used to measure water levels in the flume is well explained. The use of a gridded perspex board to convert coordinates of wave images from camera pixels to physical units is described. Since the camera used could not image the entire wavelength, the wave cycle was divided into several phases and how these phases are labeled relative to the wave period is explained. Digital image velocimetry techniques were used to extract velocity flow fields from the wave images. These velocity flow fields were measured by tracking the displacement of neutrally buoyant particles and aeration structures over a known time interval. An error of 2.0 cm/s was estimated for instantaneous velocity measurements. Methods employed to remove spurious velocity vectors from the flow field are also presented.

Chapter 5: Water level measurement results

"A lake is the landscape's most beautiful and expressive feature. It is Earth's eye; looking into which the beholder measures the depth of his own nature".

- Henry David Thoreau

5.1 Introduction

Measurements of wave breaking behaviour in turbulent flows are important in providing prior information required in model experiments involving turbulent flows as well as in computational fluid dynamic models. Such measurements involve water surface elevations, wave phase velocity, wave height and the location of the break point. Measurements of the free surface displacement may also be used to estimate the momentum and energy fluxes due to waves propagating down the channel. However, it is often difficult to obtain such measurements because of the transient nature of the flow coupled by the presence of entrained air bubbles present in the flow (*Raubenheimer et al.* [15]). *De Vries et al.* [13]) stated that measurement of water wave characteristics in the surf zone, such as wavelength and wave height is important for monitoring, prediction of erosion, and benchmarking of numerical models. As also pointed out by *Massel* [14], a reliable estimation of the maximum wave height at a particular location is a fundamental requirement in the design of coastal or offshore structures. Knowledge of the magnitude and behaviour of waves at site is an essential prerequisite for almost all activities in the ocean including planning, design, construction and operation of harbour, offshore and coastal protection structures. The design of coastal structures is to a large extent dependent upon the description of the local wave climate, and in particular calculation of the water surface elevation and the underlying kinematics (*Baldock & Swan* [19]. Calculation of surf zone wave transformation is crucial for understanding and preventing storm damage (flooding and wave damage), determining shoreline evolution and cross-shore beach profile change and designing of coastal structures.

Initial experiments were performed using a 0.7 Hz, spilling wave with a wave height of 15 cm. Water level measurement results from the initial experiment, together with preliminary turbulence information were presented at an international conference (*Mukaro et al.* [155]) and published in *Mukaro et al.* [156]. Water level measurement results for the 0.4 Hz plunging wave reported here were published in *Mukaro & Govender* [157].

The breaking wave used in the study is first characterized. Results in the vicinity of the break point

of mean water levels, wave heights as well as wave phase are then presented. In the open ocean, such information will help to provide a comprehensive and insightful gauge of sea-level rise and variability, which are important aspects of coastal zone management. These well-controlled laboratory experiments are necessary to advance our knowledge of the wave breaking process and are useful for calibrating wave models developed using computational fluid dynamics (*Kimmoun* & *Branger* [43]). This first set of experiments for quantifying the mean macroscopic properties of breaking waves are often a precursor to experiments involving measurement of internal flow parameters of breaking waves. Detailed experimental results involving internal fluid velocity measurements will follow in the next chapters.

5.2 Wave transformation results

For the experiment reported here, the surf similarity parameter, given by Eqn. (1.1) as :

$$\xi = \frac{tan\alpha}{\sqrt{\frac{H_o}{L_o}}}$$

was found to be 0.36, where tan α is the beach slope. This value usually characterizes a spilling breaker, however the breaker appeared to be more of a plunging than a spilling one, and would be classified as a mild plunger. As pointed out by *Lakehal* & *Liovic* [158], the lack of a widely accepted and unique weak plunger definition (*Battjes* [159]) makes the regime delineation using the surf-similarity parameter particularly fuzzy and worth remedying.

The still water depth at the measurement station was $d = 12$ cm and the flow was fully developed at the measurement station with maximum velocity of 250 cm/s. The corresponding Reynolds number, based on the water depth d and peak velocity was calculated from Eqn. (1.3) as :

$$R_d = \frac{U_o d}{\nu} \approx 29,880 \tag{5.1}$$

where ν is the kinematic viscosity.

Measurements of some basic flow properties such as as wavelength, wave height, wave velocity were analyzed to understand the characteristics of this turbulent flow. These are presented in the chapters following.

5.2.1 Water level time series

Table 5.1 shows characteristic parameters relating to free surface water level measurements, wave height and wave velocity calculations. f is the frequency of the wave, f_s is the sampling frequency, t_s is the total sampling time, n_s is the number of samples captured per period of the wave, N_s is the sample size in 120 s and N_f is the number of full waves in the time record.

To characterize the wave field, free surface elevation measurements were made in the vicinity of the break point. Figures Figures 5.1 and 5.2 show time series of the free surface instantaneous displacements $\eta(t)$

Table 5.1: Parameters for free surface elevation measurements and wave height and velocity calculations.

f (Hz)	f_s (Hz)	t_s (s)	n_s	N_s	N_f
0.4	50	120	125	6000	48

for a 0.4 Hz plunging and 0.7 Hz spilling wave, respectively. These were measured at three positions along the flume, corresponding to (a) near the wave generator, (b) just before the break point and (c) after the break point. These signals are sampled at different times and so do not have the same phase. As already mentioned, the wave gauges were sampled for 120 s, but only 20 s of the time series are shown.

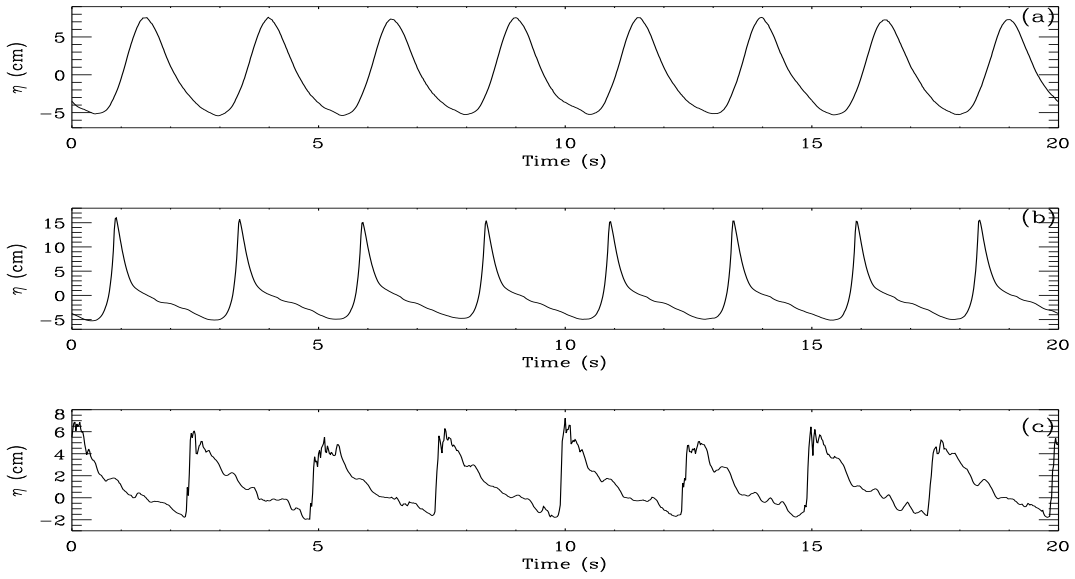

Figure 5.1: Time series showing variability of the wave profiles for a 0.4 Hz plunging wave, over a 20 s record measured by wave gauges at three different positions : (a) Reference gauge, G1-near wave generator at (x= -14.0 m), (b) G2 - before the breaking point at (x= -4.0 m) and (c) G3 - after the break point at (x= -1.5 m). h_o = 62 cm, H_o = 12.0 cm.

In deep water, the waveforms for both plunging (Fig. 5.1(a)) and spilling (Fig. 5.2(a)) cases are close to perfect sinusoids. As the wave shoals, the wave motion is affected by the bottom slope and the wave height increases and wavelength decreases to produce a steeper wave, which departs from a sine wave form towards a trochoidal form (Fig. 5.1(b)). It is evident from the figure that as the waves propagate from deep to shallow water, the wave profile changes from being close to sinusoidal to being more peaked at the crest while the troughs become drawn out. After the break point (Fig. 5.1(c) and Fig. 5.2(c)), measurements have a typical saw-tooth shape, revealing an onshore asymmetry due to the shoaling of the waves (*Rivillas-Ospina et al.* [160]).

Turbulence generated after wave breaking and variations in the free surface elevations are observed from the irregular surface elevations shown in Fig. 5.1(c). Amplitudes of wave crests are much higher than amplitudes of wave troughs during wave breaking, leading to the well-known horizontal crest-to-trough asymmetry (*Kimmoun* & *Branger* [43]). Troughs are observed to reach a level of approximately 5 cm below the SWL. Results also show a deep water wave height of about 12 cm (Fig. 6 (a)), which rises to more than 20 cm just before breaking (Fig. 5.1(b)).

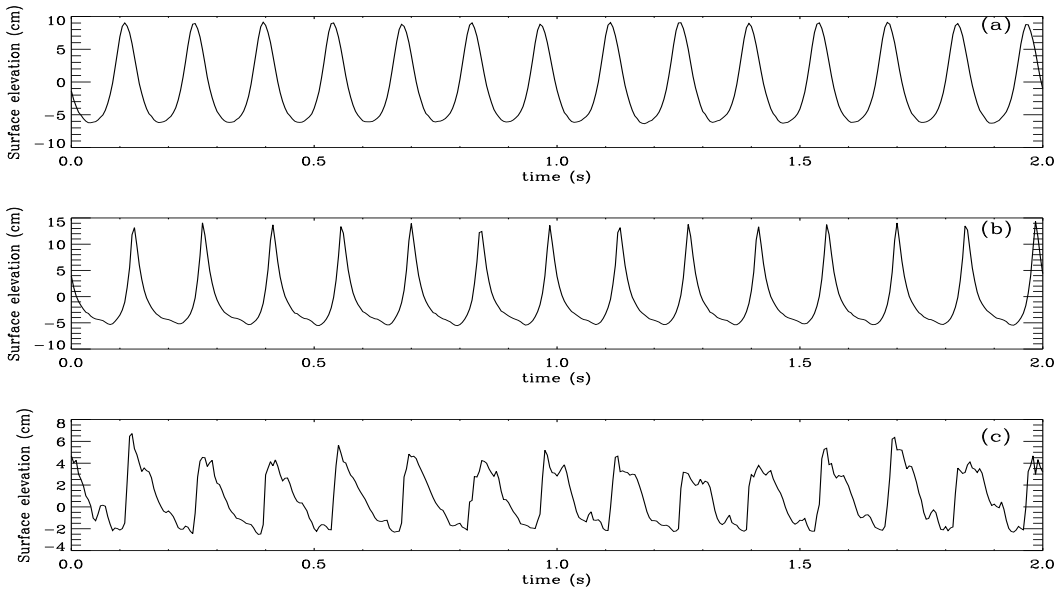

Figure 5.2: Time series showing variability of the wave profiles for a 0.7 Hz spilling wave, over a 20 s record measured by wave gauges at three different positions : (a) Reference gauge, G1-near wave generator at (x= -7.1 m), (b) G2 - before the breaking point at (x= -4.5 m) and (c) G3 - after the break point at (x= -5.5 m) from the still water line mark. h_o = 48 cm, H = 15.0 cm.

5.2.2 Wave height measurements

Wave height profiles are estimated from the in situ wave gauge data series. This section describes in detail how wave height statistics are obtained from the measured free surface elevation time series. Wave height, H, refers to the mean vertical distance from the bottom of the trough to the top of the crest, as already shown in Fig. 2.1. From the time series, the variation of the wave height along the flume was obtained at each position after locating a maximum and a minimum in each of the 48 full waves. To achieve this, the time series was windowed in time with a box-car function $G_s(m)$ which is a square wave derived from the wave gauge time series signal using the following mathematical definition :

$$G_s(m) = \begin{cases} 1 & \text{if } \textit{time series signal} \geq 0, \\ 0 & \textit{otherwise} \end{cases} \tag{5.2}$$

where m represents the time sample number.

This gating function defines a square wave signal (shown in Fig. 5.3(b)) that is used to identify the duration of positive going peaks in the free surface elevation time series. Thus the gating function is used to locate the start and end points of full wave cycles in the time series. This is accomplished by subtracting the previous gating data point from the present, resulting in a sync function, $S(m) = G_s(m) - G_s(m-1)$, shown in Fig. 5.3(c). The sync function was then used to give indices of the start of each wave cycle. For each of the 48 full wave cycles, the 125 samples whose indices lie between two consecutive positive sync peaks (i.e data points in a full wave) are searched for, to get a maximum and a minimum for each wave gauge position. The 48 maxima and 48 minima were then separately averaged out to obtain the mean crests and troughs positions, respectively, together with estimate of the variability measurement

error estimate. Individual wave heights are calculated as the crest-trough vertical distance.

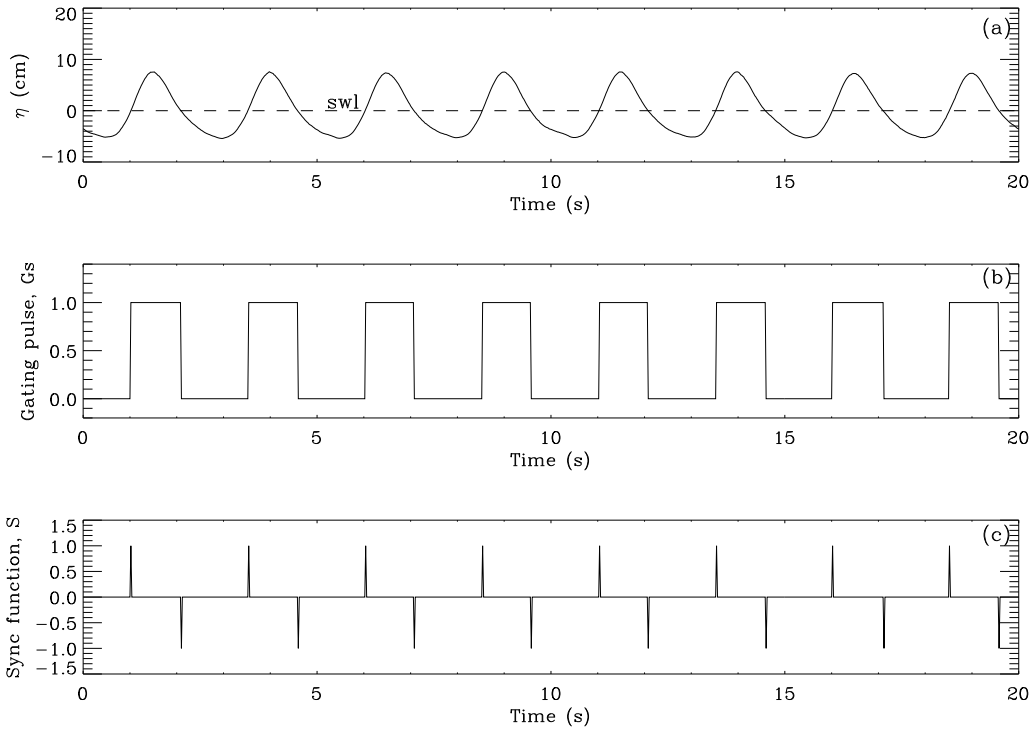

Figure 5.3: Signals used for determining wave height (a) instantaneous free surface elevation time series (b) gating signal and (c) sync function, used for locating a full wave cycle in the sampled data.

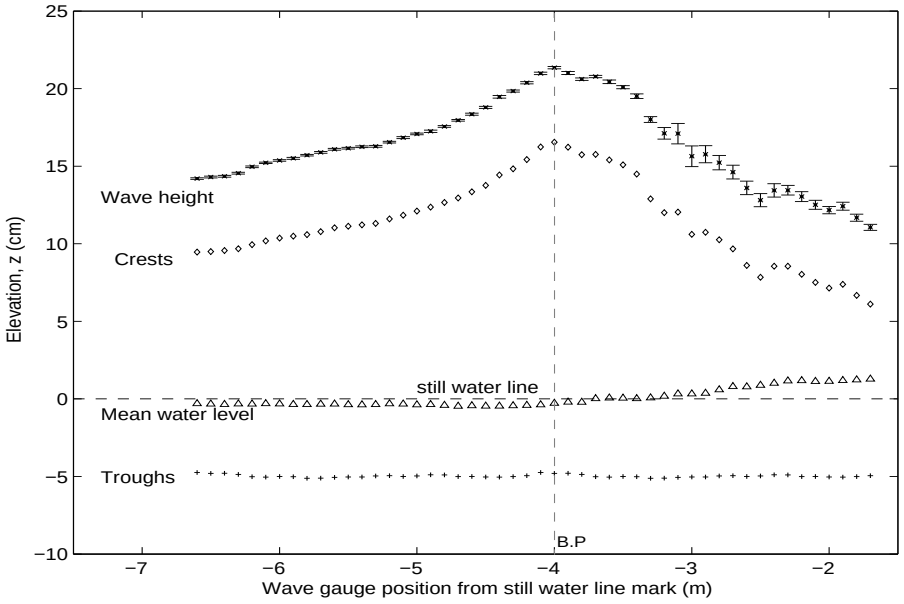

Figure 5.4: Wave height variation along the flume relative to the still water line mark. Breaking occurs at a point x= -4.0 m from the still water line mark and is marked by the inscription B.P. Uncertainty bars were estimated from the standard deviations and show variations in the wave heights at each point.

Figure 5.4 shows measurements of the mean crest and trough positions as a function distance along the flume relative to the still water line mark on the beach. Also shown in the figure are the mean water levels, which will be discussed in the next section. Figure 5.4 also shows the SWL mark and the position of the

break point. From the figure it can be seen that as the wave propagates from deep water towards shallow water (the shore), there is an increase in the wave height, H, reaching a maximum height of about 21.5 cm at the break point, and then decreases sharply thereafter. The increase during pre-breaking is due to the fact that the wave celerity, c, decreases as the waves move up the slope as predicted by Eqn. (**??**). However, since the energy flux, is constant, the wave height has to increase. A wave height peak at the break point is an indication of highly non-linear behaviour. The decrease in wave height after breaking is due to loss of wave energy. The mean wave height calculated at each position has a confidence interval based on the standard deviation of the data around the estimate. Wave height uncertainty estimates were made on the basis of a 95 % confidence interval $\Delta H_{95}(x)$ associated with the mean of the wave height was defined as :

$$\Delta H_{95}(x) = \frac{1.96 s(x)}{\sqrt{N}} \tag{5.3}$$

where $s(x)$ is the standard deviation of the wave heights measured at position x and $N = 48$, is the number of wave height data points. This measure of uncertainty was taken as a useful proxy for wave height error bars *Stockdon & Holman* [101], as shown in Figure 5.4 which show variations in wave heights at each point. The uncertainties are observed to increase from ± 0.06 cm before breaking, to about ± 0.7 cm after the break point, decreasing to about ± 0.2 cm towards the shore. The maximum uncertainty observed in the wave height measurements is about 5 %. The error bars are however, not due to instrumental measurement uncertainty. They are due to variations in the wave heights, from cycle to cycle, as already shown in Figure 5.1(c), which is probably due to the fluctuation and the establishment of near bottom return current. Regular wave breaking in a closed wave tank produce strong positive current near the surface, and a weaker undertow return current near the bottom. There are natural oscillations of this return near bottom current and so it takes some time for this current to be stationary. Slight modifications of the return current will change from time to time the location of the breaking, the phase speed and the wave height at the breaking location.

Table 5.2: Characteristics of the weak plunging breaker under study.

f (Hz)	d_b±0.1 (cm)	h_b±0.1 (cm)	H_b±0.1 (cm)	L_b±30 (cm)	H/d_b ±0.01	H_o±0.1 (cm)	L_o±30 (cm)	c_o±20 (cm/s)
0.4	20.0	19.7	21.5	415	0.61	12.0	610	246

In summary, characteristics of the turbulent flow generated and used in the experiments reported here are listed in Table 5.2. f is the frequency of the wave, h_b is the local water depth at the breaking point (B.P), including the change of water level due to wave set-up, d_b is the still water depth at the breaking point, H_o is the wave height near the wave maker, L_o is the wavelength near the wave maker, H_b is the wave height at the breaking point. In the present experiment the linear wave celerity near the wave maker is about $c = 246$ cm/s. The wave height in deep water was $H_o = 12$ cm. The wavelength in deep water was $L_o = 610$ cm so that the measured ratio $H_o/L_o = 0.0197$. *Ting and Kirby* [38] measured the transformation of regular waves on a 1 : 35 sloped beach. The deep-water wave height was 12.7 cm, and

the wave period was 2.0 s for a spilling breaker. The corresponding value of H_o/L_o obtained was 0.020. The value of our ratio is very close to their observed for almost the same wave height.

Results show a wave height of about 12 cm, rising to 21.5 cm at the breakpoint, which is at x = -4.0 m from the SWL mark. Thus there is a 79 % increase in wave height at the breakpoint. *Stive* [36] conducted water level measurements in waves having a period of 1.79 s and found a 22.75 % increase in wave height at the breakpoint. At the break point, the mean water level, $\overline{\eta}$= -3.0 mm and the local still water depth, d_b= 20.0 cm giving a local water height, h_b= 19.7 cm and a linear wave celerity, c = 139 cm/s. The breaker depth index, H_b/h_b, describes a dimensionless breaker height of the wave just before it breaks and is commonly used to define the wave height at breaking (*Yoo* [52]; *Camenen* [161]). At the break point, H_b/h_b = 1.08. *Camenen & Larson* [161] undertook a study to establish the most reliable breaker depth index formula that will yield satisfactory predictions for a wide range of hydraulic and beach conditions. Their results presented in Figure 5.5 show how the breaker depth index, γ_b, depends on the surf similarity parameter or Irribaren number, ξ_∞ for different wave conditions. In the present study, ξ_∞ = 0.36, and the figure shows that γ_b goes up to 1.2 for a plunging breaker, as shown by the red vertical line. In their work on the dynamics of surf-zone turbulence in a strong plunging breaker, *Ting & Kirby* [30] observed a value of H_b/h_b = 1.24 at the break point.

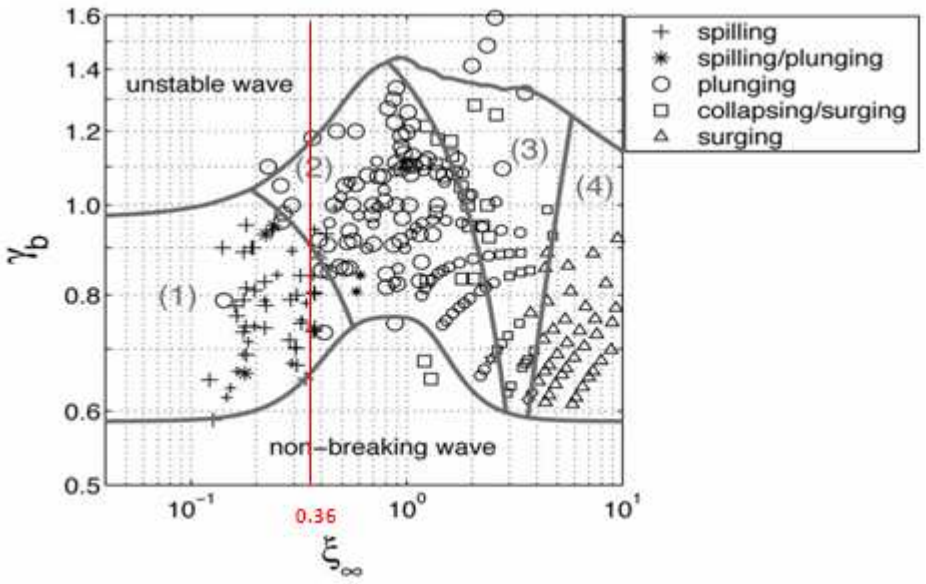

Figure 5.5: Observation of different breaker types with respect to the surf similarity parameter or Irribaren number ξ_∞ and the breaker depth index, γ_b, for different breakers. Adopted from *Camenen & Larson* [161].

The value of still water depth at the break point, d_b can also be evaluated analytically by using a theoretical expression derived from solitary wave theory ([162]; *Lesnik* [163]; *Sakai & Kobayashi* [164]) :

$$d_b = \frac{H_b}{b - \frac{aH_b}{gT^2}} \tag{5.4}$$

where

$$a = 43.75(1 - e^{-19\alpha}) \tag{5.5}$$

and

$$b = \frac{1.56}{(1 + e^{-19.5\alpha})}. \tag{5.6}$$

giving $d_b \approx 23.4$ cm for a bed of slope $\alpha = 0.05$, a theoretical value which compares reasonably well with the measured value of 20.0 cm given in Table 5.2

The maximum wave height that can be sustained for a given water depth is given by (*Miche* [165]) as :

$$H_{max} = 0.142 L_o \tanh\left(\frac{2\pi h}{L_o}\right) \tag{5.7}$$

In deep water, Eqn. (5.7) reduces to a maximum wave steepness $H_{max}/L_o = 1/7 = 0.142$, and in shallow water, it reduces to a maximum height-to-depth ratio $H_{max}/d = 0.88$ (*McKee Smith* [166]). This criterion is powerful because it includes both the impacts of depth and steepness-limited breaking. Our experimental value of H_{max}/d at the break point is 1.08 and is reasonably consistent with the above result for shallow water, and close to the theoretical value of 0.9 predicted by Eqn. 2.15. Standard deviations of the 84 wave height measurements at each position were used to determine the variability of the wave heights. Standard deviations of the order ± 0.2 cm were observed before breaking while after breaking they were of the order 2.0 cm. This amounts to a variability of about 10 % in the wave height.

5.2.3 Mean water level

The mean water level, $\overline{\eta}(x,t)$, was obtained by averaging over the 6000 surface elevation samples at each wave gauge position. The procedure was repeated for all the 50 wave gauge positions. Figure 5.6 shows an expanded graph of the variation of mean water level, $\overline{\eta}$, at the 50 locations along the flume. It shows how the mean water level is related to the wave height measured at each position. The position of the SWL is at mean water level $\eta = 0$ mm, while the break point is marked by the gray vertical line with inscription *B.P* that lies at x= -4.0 m. Results show a maximum depression of the mean water level of about -4 mm before the wave breaks and -2.8 mm at the break point. After the break point, the mean water level rises almost linearly, by about 5 mm per every 1 m exceeding 13 mm towards the shore. Clearly there is a lowering of the mean water level before breaking, called the set-down, and a rising of the mean water level after breaking, called the setup. The gradient in the mean water level, $d\eta/dx$, is proportional to the negative gradient in wave height, $-dH/dx$. Thus prior to breaking dH/dx is positive and this results in a decreasing mean water level (*Le Blond* & *Mysak* [167]. The opposite occurs after breaking. Wave set up indicates the rise in the mean water level due to wave generated onshore transport of water mass. When the waves break in the surf zone, the broken water mass gets piled up against the slope following conversion of kinetic energy to potential energy. As a result the water level for a considerable distance offshore rises. The increase in mean water level after breaking has been observed in other previous experiments (*Cox* [40], *Govender et al.* [42], *Kimmoun* & *Branger* [43], *Petti* [58], *Battjes* [168], and *Mocke et al.* [169]). As the water depth decreases the wave height increases and the mean water level is lowered by the presence of unbroken waves resulting in mean water level below the still water line. After the breakpoint there is a increase in mean water level towards the shore, as the wave height decreases.

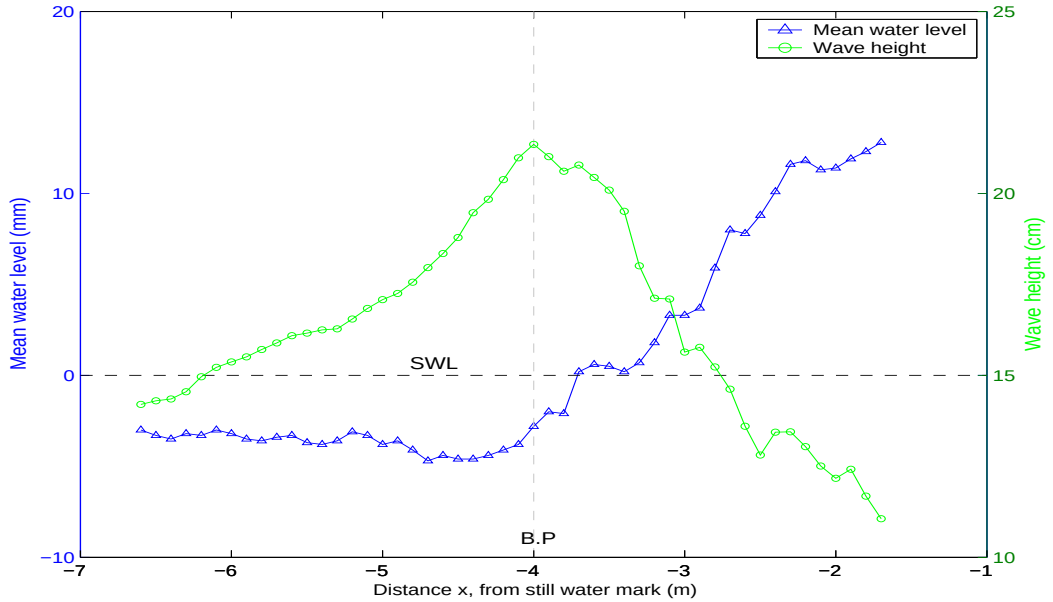

Figure 5.6: Zoomed-in variation of mean water levels (blue) along the flume and how they relate to the wave height (green) at that position. Note that the SWL is at mean water level = 0 mm. The grey vertical line at x = -4.0 m marks the break point.

Calculation of wave set up is necessary to know whether low lying coastal area would be flooded or not in stormy waves. Quantitatively, it is the depression of MWL below the SWL (the water level in absence of any waves) at the point of wave breaking and is denoted by S_b. From this point onwards there is an increase in MWL. The maximum MWL occurs when it touches the beach slope.

The set down at the break point, S_b, can be estimated from :

$$S_b = \frac{H_o^2 T(g)^{\frac{1}{2}}}{64\pi d_b^{1/5}} \tag{5.8}$$

giving a value of 5.0 mm which compares well with the measured value of about 4.0 mm. In the real ocean the setup can translate to a few meters so that the contributions of wave setup under storm conditions can be substantial, adding several meters to the elevated water levels. A higher mean water level in the surf zone coupled with high levels of turbulence and currents will result in greater amount of erosion and sediment transport.

5.2.4 Wave phase celerity

The phase celerity was estimated by first determining the phase relationship of the wave at various positions along the flume relative to that at the position of wave gauge G1. Once the relative phase across the flume is known, the velocity between any two points was determined using the phase difference between these points.

Let $G_1(t)$ and $G_3(t)$ be the free surface elevations measured by the reference wave gauge G1 and wave gauge G3. The cross correlation function between these two signals is given by :

$$R_{g1g3}(\tau) = \int_0^T G_1(t)G_3(t+\tau)dt \tag{5.9}$$

where the time series of G3 is shifted from G1 by τ, and $\tau = 0, 1, 2, \cdots$. The cross correlation procedure was performed in the Fourier domain using FFTs.

The phase at position x for G3, relative to wave gauge G1 is then calculated from,

$$\Phi_{13}(x) = \frac{R_{g1g3}(x)}{0.02} \tag{5.10}$$

where 0.02 is the sampling time. Similar expressions were used to get the phase Φ_{12} using signals from G2 relative to G1.

After getting the relative phase across the flume, the phase difference $\Delta\Phi$, between any two points was the calculated from :

$$\Delta\Phi = \Phi_{x+\Delta x} - \Phi_x \tag{5.11}$$

Figure 5.7 shows the time series of the wave at four positions along the flume together with that measured by gauge G1. The phase relative to gauge G1 is shown in each case. The average phase at a particular position (x) was determined by cross correlating the signal from gauge G1 with the signal from the gauge at position x. From Figure 5.7 it can be seen that the relative phase between the signal from gauge G1 and that from the other gauge increases away from the generator. The original time series at different positions were sampled at 20 ms. These signals were then interpolated by a factor of 4 using a perfect reconstruction filter which uses a *sinc* function interpolation routine. This interpolation can easily be implemented using FFTs, followed by zero padding and inverse FFTs (*Oppenheim & Schafer* [170]). Thus our interpolated signal has a new sampling time of 5 ms and our cross-correlation is accurate to within 5 ms.

Figure 5.8 shows the phase measurement across the flume at positions before and after breaking. At some point, there will be a 2π phase shift between the signals. This has been catered for in Fig. 5.8. As pointed out by *Kimmoun & Branger* [43], the phase shift is due to (i) friction effects on the bottom which slow down velocities near the beach, and (ii) the negative transport near the bottom which acts against the wave. The shear of the current under the crests during the breaking process has been observed by *Govender et al.*. [42]. Average phase measurements are provided every 0.1 m. It may not be so clear from the figure, but there is a non-linear increase in the measured phase, away from the generator, ranging from 3.0 *rads* to 10.8 *rads*.

The local wave celerity at a particular position, x was estimated by computing a central difference using phases at $x\pm$ 0.1 m. This resulted in a local velocity, averaged over a distance of 0.2 m which was calculated from (*Thorton & Guza* [107]) as :

$$c = \frac{2\pi f \delta x}{\Delta\Phi} \tag{5.12}$$

where δx is the separation distance between two phases, $\Delta\Phi$ is the phase difference and f is the fundamental frequency of the wave.

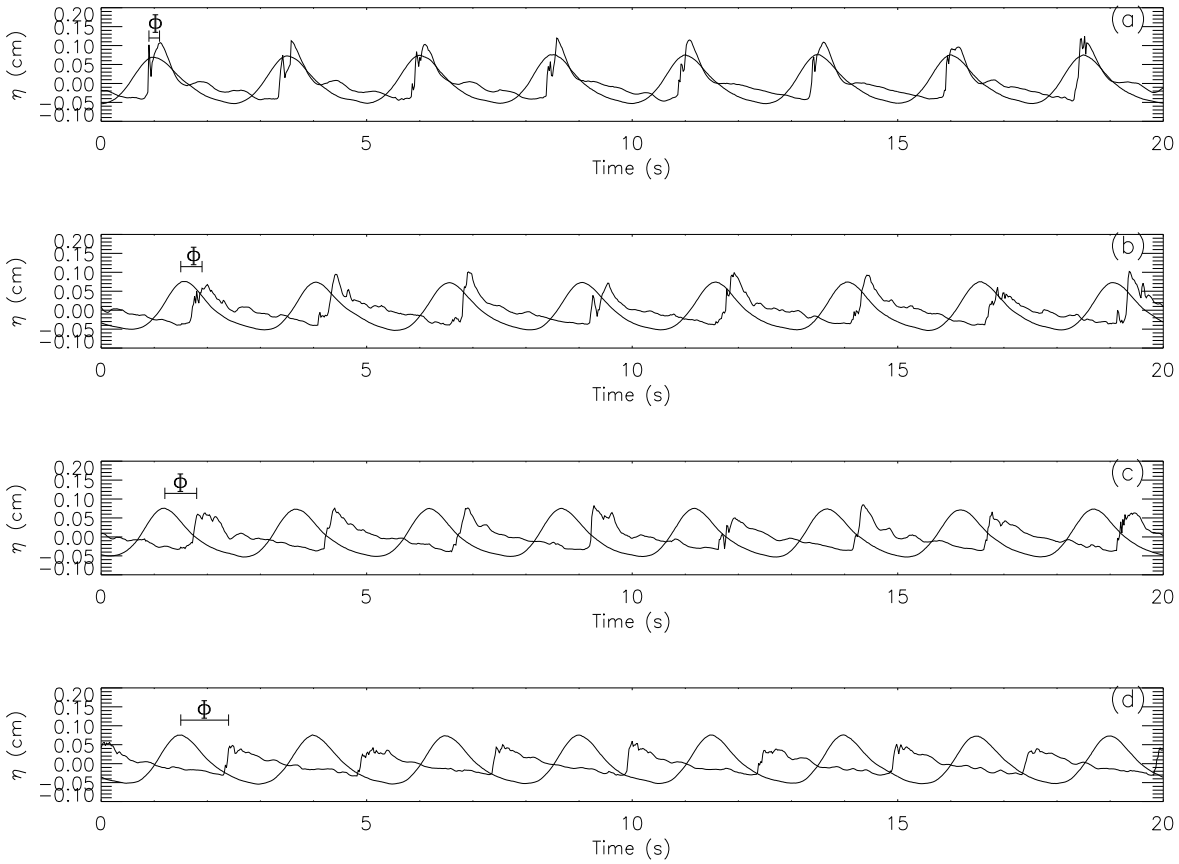

Figure 5.7: Time series showing phase at that point relative to wave gauge G1 for positions (a) -3.1 m (b) -2.7 m (c) -2.3 and (d) -1.7 m from the still water line mark.

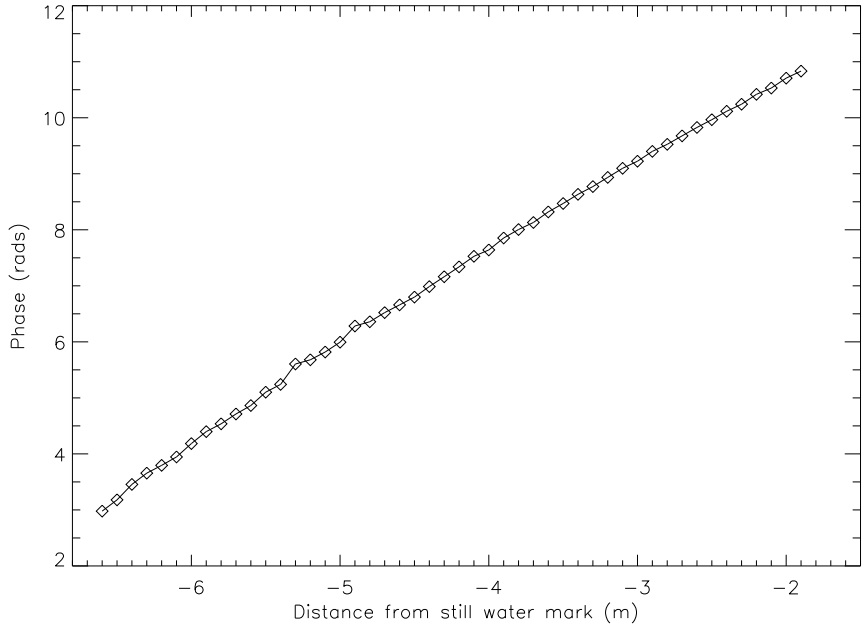

Figure 5.8: Variation of the measured wave phase along the flume for points 0.1 m apart. These were measured relative to the time series of wave gauge G1. Note that the wave propagates from left to right.

As already stated in section 2.2.3, in addition to the shallow water approximation, an empirical alternative arises from observations showing that the phase speed in the surf zone is slightly larger than the linear approximation but still typically proportional to $h^{1/2}$ (*Svendsen et al.* [104]). Thus, a simple approach is to model phase speeds with a modified shallow water approximation,

$$c = \delta\sqrt{gh} \tag{5.13}$$

where δ is the constant to be determined. This approach has been used in various wave models owing to its simplicity, with a typical value of δ=1.3 (*Schaffer et al.* [105]; *Madsen et al.* [106]). This value is consistent with the surf zone observations of *Stive* [36], which considered regular laboratory waves. This value is also consistent with the solitary wave solution Eq. (2.21) using a global value of H/h=0.78. *Stansby* & *Feng* [71] presented phase speed data from one laboratory condition (regular wave) and their results showed a monotonic cross-shore variation for the proportionality constant in the range δ = 1.06 - 1.32.

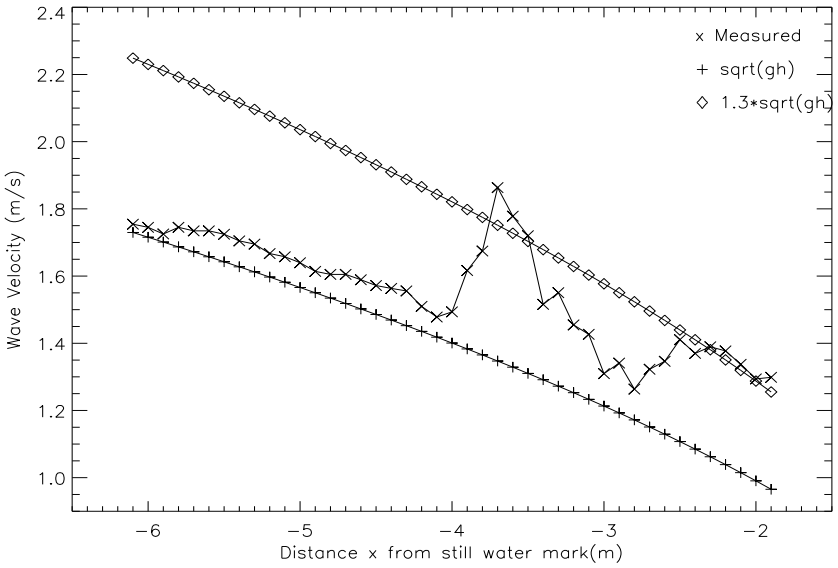

Figure 5.9: Variation of the measured *average wave velocity* along the flume and the theoretical estimates calculated using linear and non-linear wave theories. The average wave velocity was computed from the phase difference of pairs of points 0.2 m apart in Fig. 5.8.

Figure 5.9 shows the measured celerity or velocity, together with that predicted by linear theory $\sqrt{gh}$ and an equation using the roller model concept, $1.3\sqrt{gh}$, developed by *Schaffer et al.* [105]. The average wave velocity was computed by averaging the phases given in Figure 5.8, over a distance of 0.2 m. As can be seen from Fig. 5.9, wave celerity estimates are bounded by the celerity estimates obtained by linear wave theory and non-linear wave theory, but show a some amount of variability after breaking. Before the break point, (-6.0 m $< x <$ -4.0 m), measured celerities are greater than $\sqrt{gh}$ by approximately 6 %. It can also be observed that there is a rapid increase in wave celerity just after breaking reaching a peak value of 1.86 m/s and decreasing thereafter. It should be noted that the measured velocities, especially the jump at the break point, correspond to that of the top of the wave rather than the bulk of the wave.

Using a general expression for a phase celerity local in space and time, *Stansel* & *MacFarlane* [47] obtained a phase speed of 1.67 m/s at the break point. The maximum phase speed in the vicinity of the break point is greater than that predicted by $\sqrt{(gh)}$ by approximately 38 % and it is also greater than that predicted by $\delta\sqrt{gh}$ by approximately 5 % where $\delta = 1.3$. After the break point, there is a decrease in the wave phase speed reaching a minimum at x = -2.8 m. Thereafter the measured phase celerity are in good agreement with roller model results as calculated from $1.3\sqrt{gh}$. As pointed out by *Stive* [102], this indicates that non-linear effects are important, as expected for this region. The possible reason for the observed dip in the wave celerity around x = - 3.2 m may be due to the undertow reaching its maximum value in that region. The depth averaged undertow measured using video techniques was in the order of 0.15 m/s over that region. However this is still under investigation. Results obtained in this study are similar to those measured by *Stive* [102], who conducted experiments on spilling and plunging waves breaking on a 1:40 plane slope beach. He measured wave phase celerity and obtained deviations from the theoretical wave phase velocity by as much as 28% at the break point for a spilling wave and 19 % for a plunging wave, decreasing close to the shore. *Okamoto et al.* [171] conducted similar experiments but for waves breaking over a triangular bar consisting of a 1:20 up slope. Their results for positions prior to breaking and immediately after breaking are similar to that in the present investigation. *Tissier et al.* [50] determined the time lag between two wave height time series recorded by two closely spaced wave gauges, in the field. They used a cross-correlation technique in a study that involved field measurements of wave celerity in the surf zone and obtained an estimate of the local velocity which compares well with $\delta\sqrt{gh}$, where $\delta = 1.14$. Measurement results by *Suhayda* & *Pettigrew* [45] showed that the measured celerity reached 1.2 times the non-linear celerity $\delta\sqrt{gh}$, at the break point.

Errors associated with the phase measurements are due to errors in estimating the position of the peak in the cross correlation. The position of the cross correlation peaks were estimated to within 5 ms, which represent one source of error. Another source of error is associated with the sampling jitter. This is determined by the speed of the computer clock, which is in the order of nanoseconds. Thus the biggest uncertainty in the position of the cross-correlation peak comes from the 5 ms interpolation. Using an average speed of 1.7 m/s in the surf zone, the average time it takes a wave to traverse a distance of 0.2 m is 118 ms. Thus the 5 ms error translates to a velocity uncertainty of $\sqrt{2}$*5 ms/118 ms = 6.0 %. The $\sqrt{2}$ factor is due to there being two sources of error from the two wave gauge positions.

5.3 Summary

Free surface elevation measurements have been presented for a 0.4 Hz wave propagating and breaking on a 1:20 beach slope fitted in an open channel. The measured mean water levels were observed to vary from around -4 mm just before the break point to about 14 mm towards the shore. Wave heights at several positions along the flume were later estimated from the measured surface elevations. The wave height rises from 12 cm near the wave generator to about 21.5 cm at the breakpoint before decreasing sharply to around 10 cm after breaking. This decrease in wave height after breaking is due to loss of energy through currents and turbulence. Local wave phase velocity for points 0.2 m apart was estimated

using cross-correlation techniques and showed that linear shallow water approximation underestimates the phase velocity. In the vicinity of the break point, the measured phase velocity was observed to lie in the range $\sqrt{gh} < c < 1.3\sqrt{gh}$. An important observation from this study is that the wave phase velocity does not depend on depth (linear theory), but increases just after the break point. This is also as a result of the energy released by the breaking process. The minimum estimated uncertainty in the wave velocity was 6 %.

One of the contributions of this research is a consistent data set of wave celerity for positions prior to and after breaking, in addition to wave heights and water level measurements. These measurements also provide prior knowledge about the wave breaking process which is useful for internal flow measurements, the results of which are discussed in the next chapter.

Chapter 6: Velocity flow field results

" *The breaking of a wave cannot explain the whole sea.*"

- Vladimir Nabokov (1899 - 1977)

6.1 Introduction

In this chapter measurement results of internal flow parameters of the plunging wave are reported. The chapter discusses instantaneous, u_i, phase-ensemble averaged $\langle u \rangle$ and time-averaged, $\overline{u}$ velocities. A significant portion of the chapter deals with the determination of average velocity profiles for both the horizontal and vertical directions. The mean flow is the organized wave-induced flow defined as the phase average of the instantaneous velocity, while the turbulence is taken as the deviation from the phase average. Results of the phase evolution of instantaneous and mean velocity vector fields are discussed with the aid of contour plots in addition to their vertical and horizontal profiles. Results presented here provide a general qualitative and quantitative assessment of the flow structures and properties during wave breaking on a beach. Such experimental measurements and analysis generate lots of data and therefore to keep the number of pages reasonable, only selected experimental results from one station, 12a, are presented herein. Results from all five measurement stations are consolidated to show how time-averaged velocity flow fields and other turbulence parameters vary along the flume. The chapter concludes with a statistical analysis to check the convergence of the various parameters on the sample sizes. Most of the results will be presented in a non-dimensional form for easier comparison with previous experiments in literature. For the velocity vector fields and their corresponding contour plots, elevations are presented relative to the still water line (SWL), which is at $z = 0$ cm. For the vertical profiles of turbulence parameters, elevations have been normalized by the local water depth, h, at the measurement station in question. For station 12a whose results are presented here, $h = 12$ cm. Velocities and turbulence intensities were normalized by the linear wave celerity, $c = \sqrt{gh}$ to enable comparisons with available data.

6.2 Breaking wave images at different phases

Before presenting velocity measurements, a sequence of some photographic pictures of breaking waves that were captured and analyzed is presented. These photographs are intended to illustrate the qualitative features of the waves that were analyzed to extract velocity flow fields. The synchronizing pulse

from the wave maker enabled the measurement system to capture images at precisely the same point in the wave cycle so that phase ensemble averaging could be performed. In order to capture these images at different phases, the trigger delay was automatically and sequentially adjusted in software by the image acquisition computer, enabling it to capture images at increasingly delayed times.

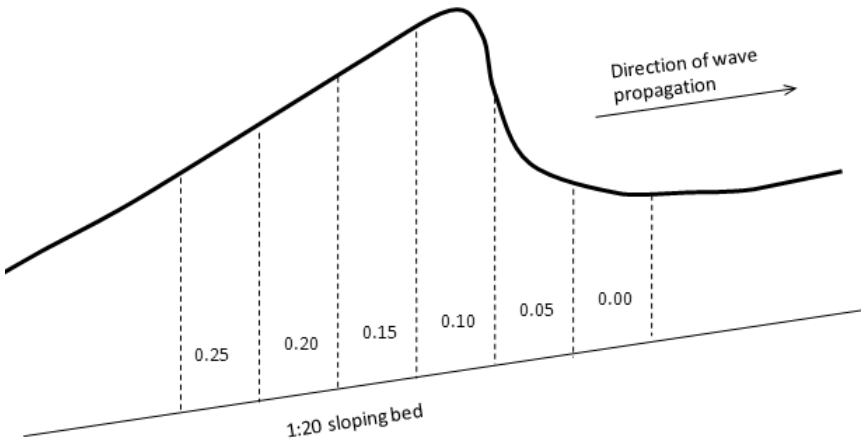

Figure 6.1: Schematic showing the relative positions of the six wave phases of interest in the breaking wave cycle at station 12a.

Figure 6.1 is a schematic showing a cycle of the breaking wave. As previously mentioned in section 4.2.4 the cycle of the incident wave was subdivided into twenty phases and images were captured at each phase. Turbulence was observed to be predominant at six of the twenty phases. The relative positions of these six phases in the breaking wave cycle are marked on Figure 6.1 and these are centered mainly around the crest. At each phase position, several images of the wave approximately 38.6 cm wide were captured by the camera and saved on the computer. These then constituted overlapping images of the breaking wave that were later analyzed using specially developed algorithms. Figure 6.2 shows typical images of the 0.4 Hz plunging wave captured at a measurement station centered around -238 cm from the SWL mark on the beach, for the six phases in question. These waves are, however, from different wave cycles. Each image is one from a pair of images at that phase and show scenes containing bubbles resulting from the wave breaking and white polystyrene seeds used as tracer particles. The images at these phases contain the most dynamic part of the wave so velocity and turbulence results will only be shown for these six phases. Some of the images captured at each of the twenty phases are annexed in Appendix C. Except for the six phases whose results are presented here, most of the images show the trough part of the wave which is not as dynamic and so the images are very similar.

As already mentioned in section 4.2.5 of Chapter 4, images from the 20 wave phases are labeled relative to the wave period with $\frac{t}{T} = 0.00$ representing the first phase through to phase $\frac{t}{T} = 0.95$ for the twentieth phase. The images shown in Figure 6.2 correspond to phases : $\frac{t}{T}$= 0.00, 0.05, 0.10, 0.15, 0.20 and 0.25 respectively, as indicated in the top right corner of each image. These images which evolve in time from left to right show the temporal evolution of the breaking process. The wave image corresponding to $\frac{t}{T}$=0.00 shows an image of the breaking wave at the phase when the crest is just coming into the field of view of the camera. The last image ($\frac{t}{T} = 0.25$) shows the image at a later phase when the crest has just passed. As the wave approaches breaking, its profile becomes asymmetric with a steeper front face. The

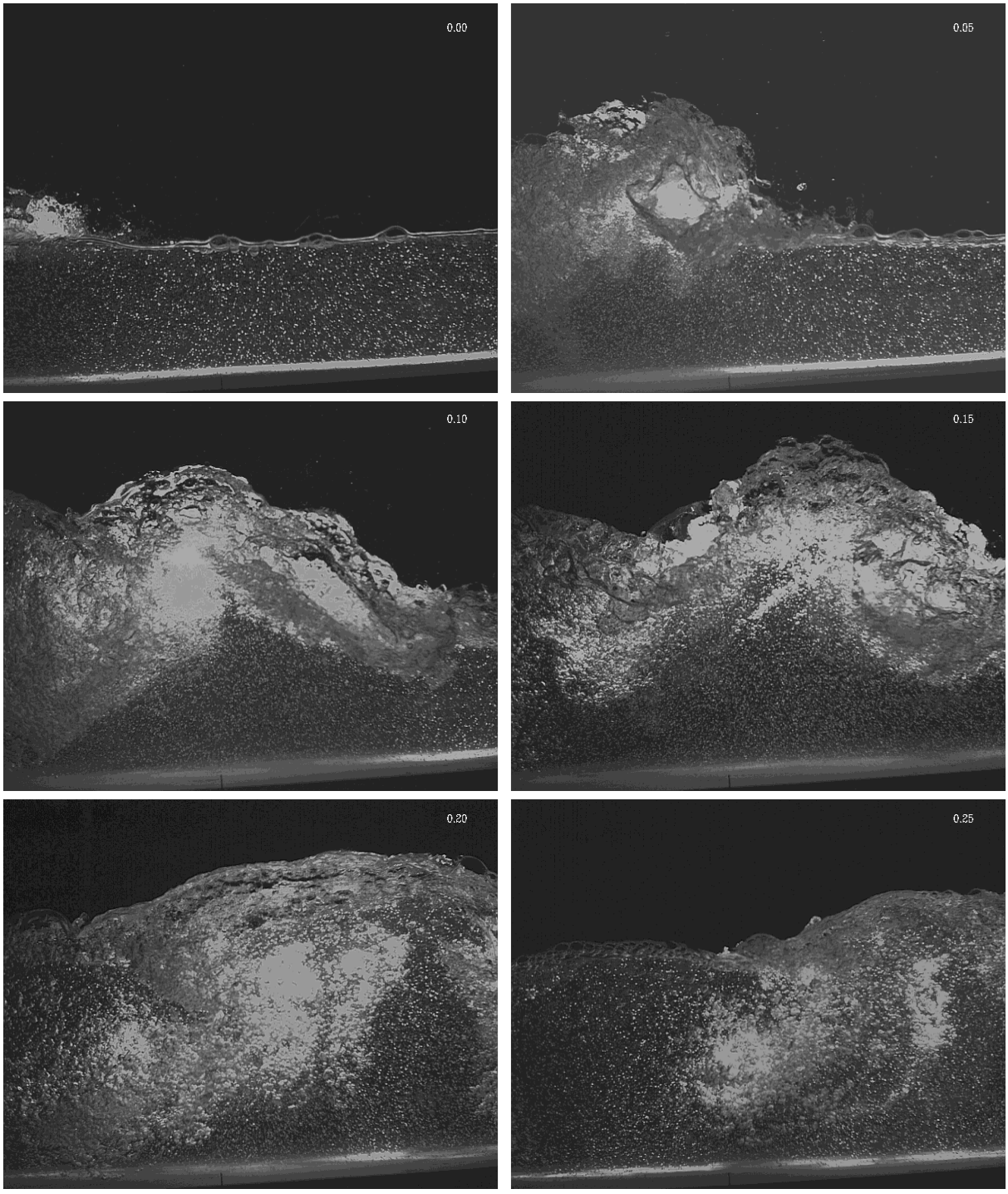

Figure 6.2: Typical grayscale level *images* of the 0.4 Hz breaking wave captured at six different overlapping and consecutive phases, that include the crest. These images are for phases : $\frac{t}{T}$= 0.00, 0.05, 0.10, 0.15, 0.20 and 0.25 as indicated in the top right corner of each image. The wave is propagating from left to right. Note that each image shown here is one from a pair captured at each phase. Each image is 38.6 cm long and 29.3 cm wide. The oblique white line at the bottom of each image shows the beach slope of 1:20.

free surface breaks up as fluid appears to erupt from a point just forward of the crest and air is entrained forming bubbles or whitecap (*Massel* [172]). White polystyrene beads that were used as tracer particles together with air bubbles, to determine the velocity flow fields, are clearly visible in the images. The whitecap in the images show aerated water.

6.3 Velocity flow fields under plunging waves

This section discusses the evolution of the velocity flow fields that were extracted from the captured images. As mentioned previously, instantaneous velocity flow fields were extracted from each pair of images using the DCIV method explained in section 5.3.2. Instantaneous velocity fields are presented first, followed by phase-ensemble average velocities and then time-averaged velocities. Measurements were performed at 5 stations located almost 50 cm apart. For the sake of brevity, only detailed results of the evolution of velocity flow fields, turbulence intensity, turbulent kinetic energy and vorticity, are presented for only one station, 12a. The center for this station is located at x=-238 cm from the SWL mark on the beach and 162 cm from the break point. Only merged results of time-averaged velocity components are presented for the other stations, to get the general trends in their variation along the flume. Other turbulence characteristics of the flow may be derived directly from the velocity fields.

6.3.1 Instantaneous velocity fields

Mean and fluctuating velocity fields as well as some basic turbulence characteristics were extracted from the measured instantaneous velocity fields. Figures 6.3 - 6.4 show the evolution of instantaneous velocity fields at different phases as flow progresses, which correspond to a mosaic of images shown in Figure 6.2. They show velocity vector fields computed from a cross-correlation analysis of a two-frame particle image pair at each phase. Measurements of the velocity vector fields were made over the entire image including the aerated portion, which is not possible using techniques such as LDA. Results show that the instantaneous velocity flow fields are characterized by large velocities in the crest and low velocities in the trough region, which lies below the SWL. The breaking process is observed to create a high speed flow that rides on the front face of the wave. The general flow structure formed by the white cap in the aerated region is discernible in the corresponding instantaneous velocity flow fields.

Velocity vector fields show that highest instantaneous velocities occur in the crest part of the wave with peak instantaneous horizontal velocities exceeding 200 cm/s. The continuous line at the top of each vector field shows the position of the air-water interface or the free surface at that time. The still water line is at elevation $z = 0$ cm. The bottom figure of Figure 6.4 shows a clockwise rotating vortex centered around $(x, z) = (-239, -8)$ cm that is created following the passage of the crest. Such vortices are observed to quickly break up into incoherent, two-dimensional turbulence as flow progresses. Some of the vortices may, however, survive through the entire water column to impinge on the seabed and suspend sediments from the sea bed (*Ruessink* [173]). This may increase the turbulence levels near the trough section of the wave. Such clockwise rotating vortices will trail behind the crest and gradually weaken as flow progresses. Using a mean local water depth of 12 cm corresponding to the middle of the images associated with our measurement station $12a$, a linear wave phase velocity of $c = 110$ cm/s was obtained. The instantaneous velocities in the upper part of the wave are approximately a factor of 2 times greater than the linear phase velocity.

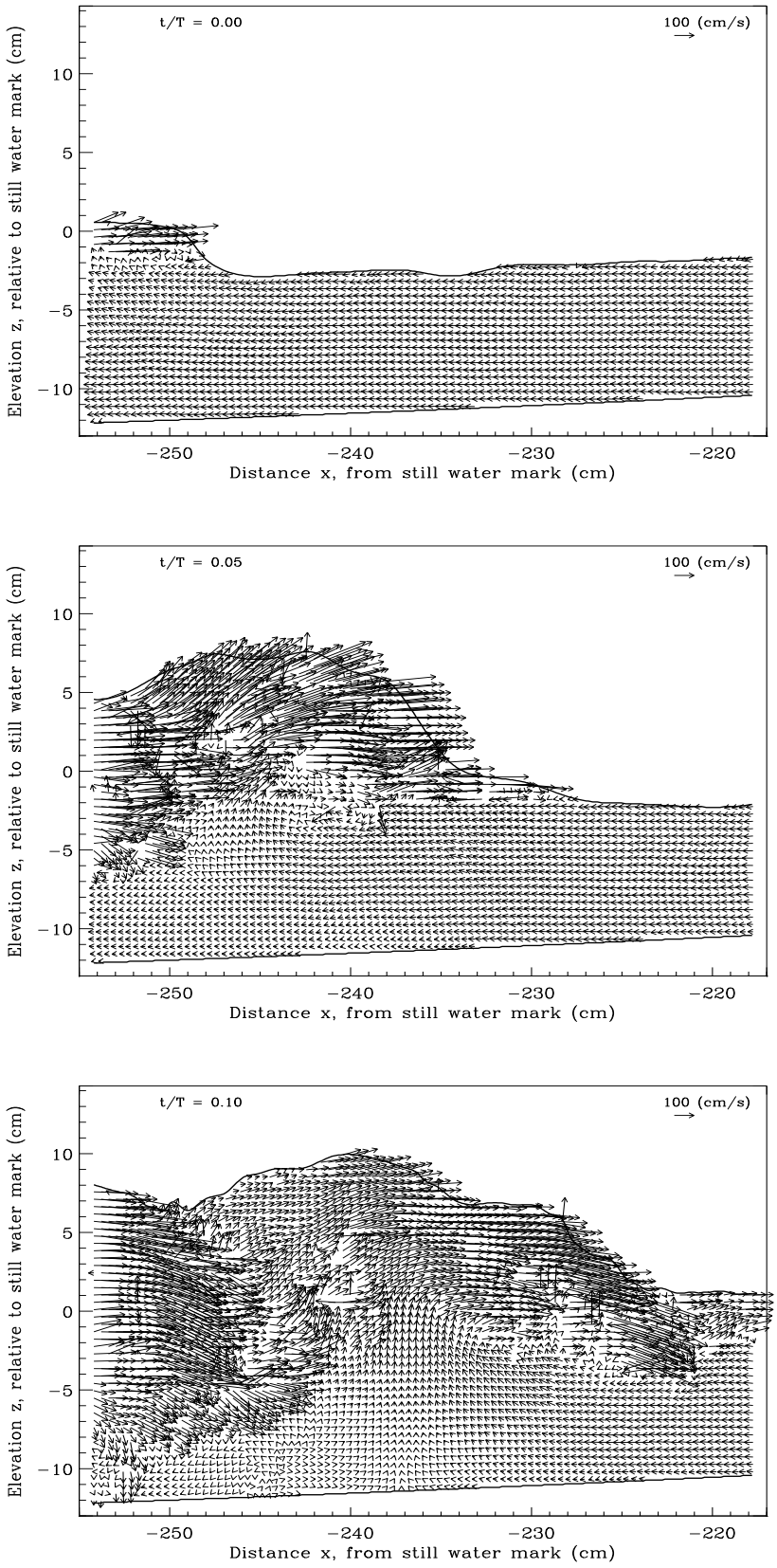

Figure 6.3: Spatial evolution of instantaneous velocity flow fields during the breaking process, for wave phases 0.00, 0.05 and 0.10 shown in Figure 6.2. A scale arrow vector of magnitude 100 cm/s is shown in the upper right corner. The still water line is at z=0 cm.

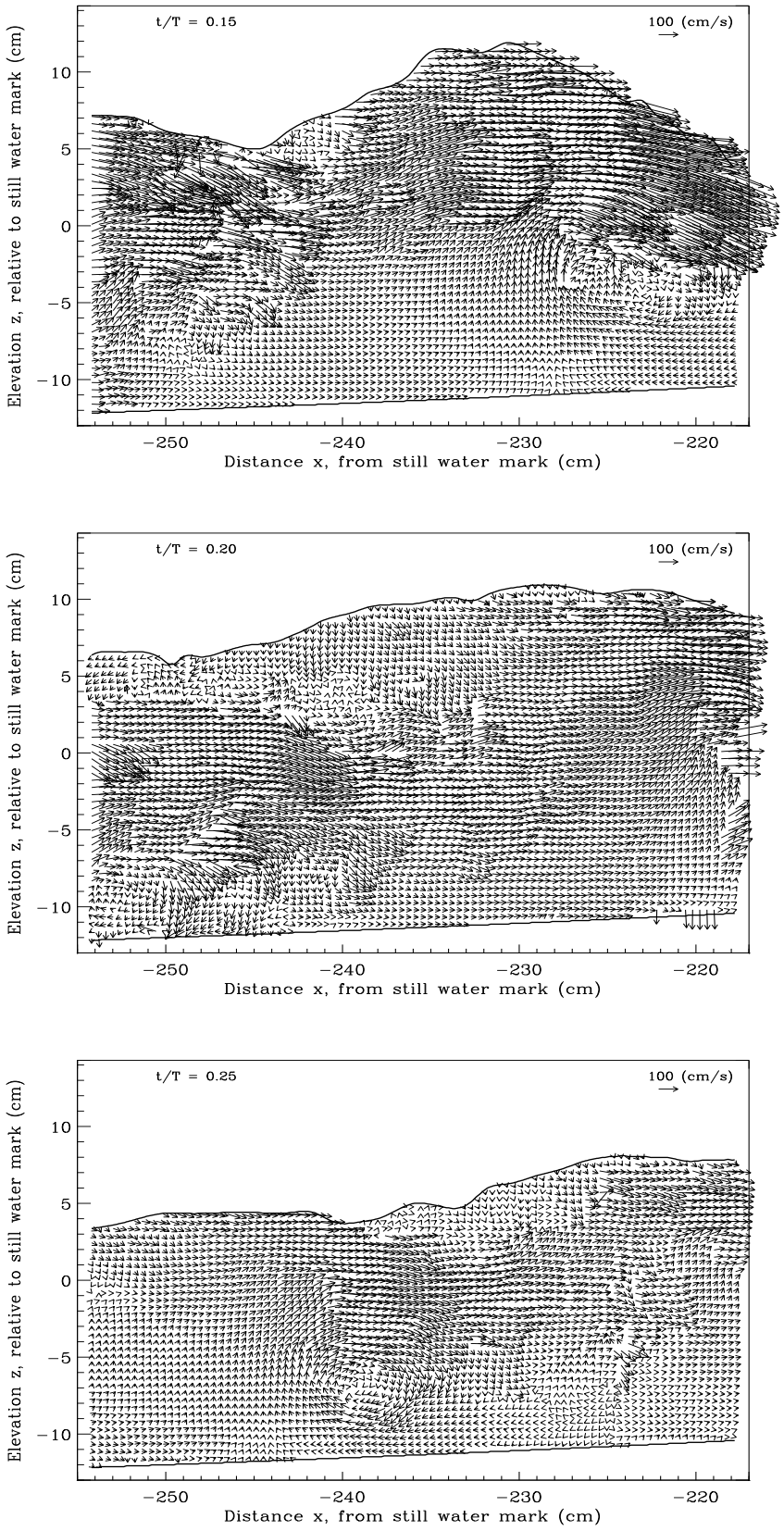

Figure 6.4: Spatial evolution of instantaneous velocity flow fields during the breaking process, for wave phases 0.15, 0.20 and 0.25 shown in Figure 6.2. A scale arrow vector of magnitude 100 cm/s is shown in the upper right corner. The still water line is at z=0 cm.

6.3.2 Mean ensemble-averaged velocity fields

At least 70 different instantaneous velocity fields representing 70 wave cycles at a particular phase were computed. The phase-ensemble average of the velocities and free surface water profiles were obtained by averaging all the instantaneous data that were acquired at the same phase. The mean flow is an important term of comparison with numerical predictions and represents the base flow upon which the motion of organized structures is superimposed (*Ubaldi & Zunino* [174]). The phase averaging method is commonly used to study periodic events and was frequently applied in previous studies on breaking waves over a uniform slope beach (e.g. *Sakakiyama & Liu* [175]). Mean velocity flow fields in the measurement plane are characterized by the mean horizontal and mean vertical velocity components.

The phase-ensemble average of a measured periodic quantity, say, u, with period T, and total temporal length $T^{'} = NT$, is defined (*Sou & Yeh* [12], *Liiv & Lagemaa* [176]) as :

$$\langle u(\tau) \rangle = \frac{1}{N} \sum_{i=1}^{N} u(\tau + iT) \tag{6.1}$$

where τ lies in the interval (0; T), and N is the number of samples used at a particular phase.

Figures 6.5 - 6.6 show the phase-ensemble-averaged velocity fields for the phases represented in Figure 6.2. The results have every alternate row and column of velocity vectors omitted for clarity of the fields. The continuous line at the top of each vector field now show the phase averaged free surface at that phase, which is computed from the average profile of at least 10 wave cycles in the 70 cycles considered for each phase. As previously stated, the still water line is at an elevation of $z = 0$ cm. It is important to note that when phase-ensemble averaging is performed, the wave profile for each cycle differs from the next (i.e no two cycles are exactly the same). Each sample of the phase average may not come exactly from the same phase in the wave relative to a characteristic point (such a zero up-crossing, the toe or the wave crest). As pointed out by *Svendsen* [177], even for waves that are generated monochromatically, the wave period in the surf zone is not exactly the same. This is because irregularities in the propagation speed of the individual breakers caused by nonlinearities tend to accumulate as the waves move shoreward. This inevitably results in smearing at the crests of the phase as seen for phases 0.15 and 0.20.

Figure 6.7 shows the phase ensemble-averaged velocity fields measured at station 12a, as flow progresses. There is a rapid increase in the horizontal component of velocity from the flume bed going up to some elevation, before decreasing towards the free sufrace. Velocities for the trough section are $\sim$ 10 cm/s rising to about 200 cm/s in the crest part of the wave.

Figures 6.8 shows vertical profiles of phase ensemble-averaged velocity fields under the crest phases, measured at different cross-shore positions along the flume at the five stations. The profiles are for chosen wave phases that contain the crest at each station. Bed positions and positions of the SWL are shown in the plots. Reverse flow below elevation z = -2.5 cm reflects the undertow while the flow above is due to the mass flux in the crest of the wave. The undertow decreases significantly towards the shore. Different calibration factors were used to convert camera pixels into distance as already indicated

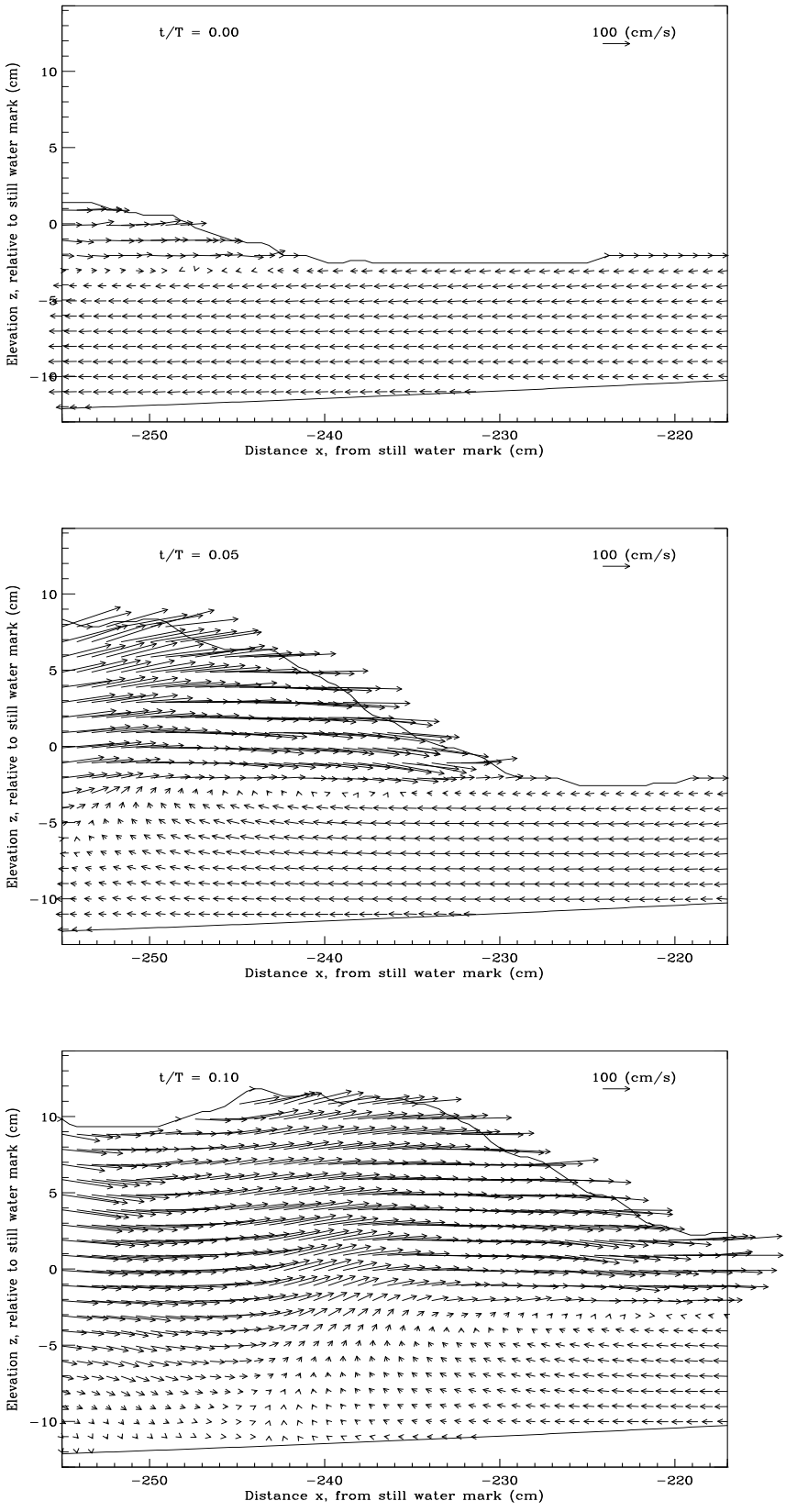

Figure 6.5: Partial phase ensemble average velocity flow fields for phases : $\frac{t}{T}$= 0.00, 0.05 and 0.10. The results have every alternate row and column of vectors omitted for clarity of the velocity fields. Each vector is an average of at least 60 instantaneous vectors.

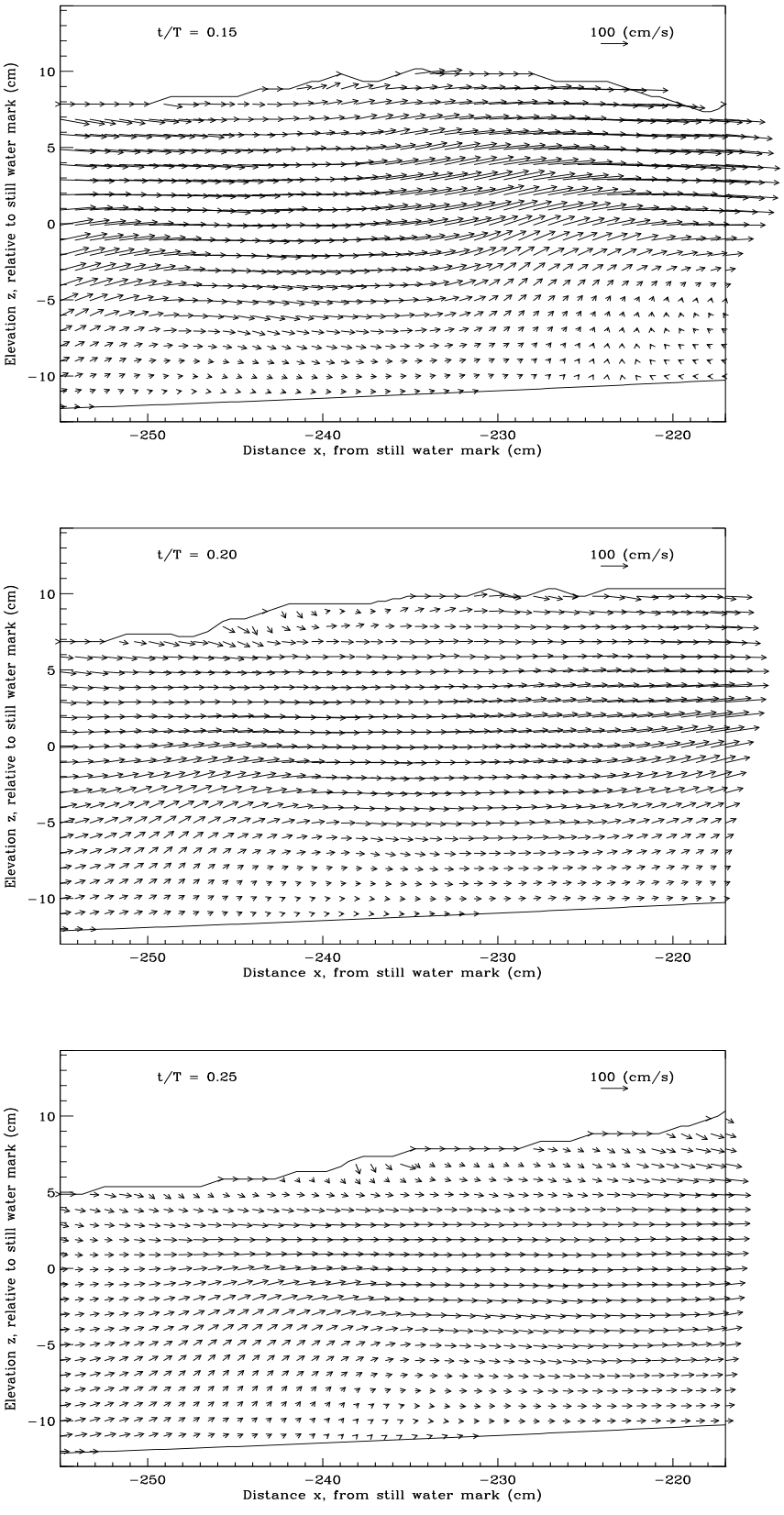

Figure 6.6: Partial phase ensemble average velocity flow fields for phases : $\frac{t}{T}$= 0.15, 0.20 and 0.25. The results have every alternate row and column of vectors omitted for clarity of the velocity fields. Each vector is an average of at least 60 instantaneous vectors.

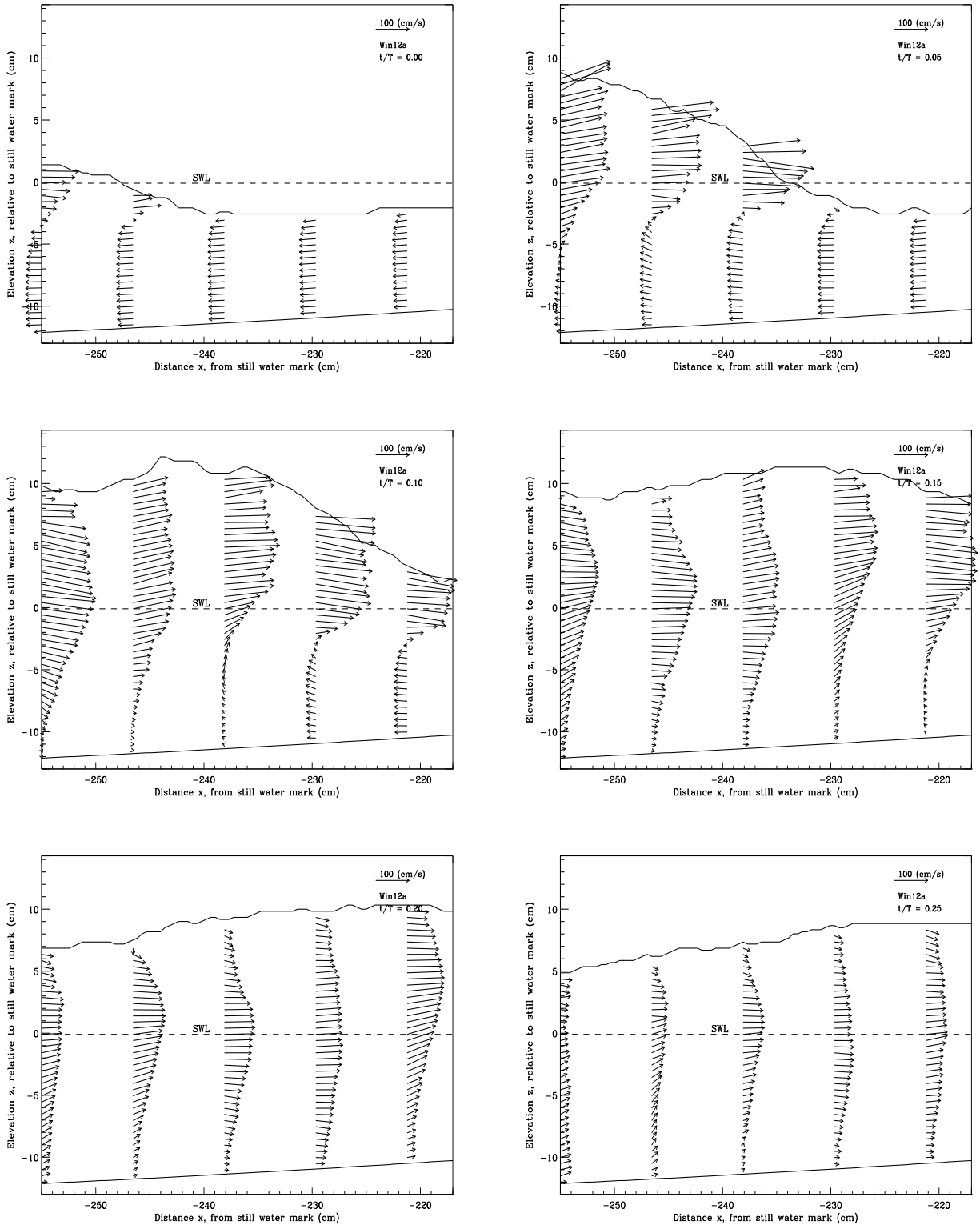

Figure 6.7: Vertical profiles of phase ensemble-averaged velocity flow fields measured at station 12a as flow progressed.

in Table 4.1. This means that the resolution of the measurements are different at each station. This is why the legends showing 100 cm/s arrow vectors in these plots have different lengths. There is a general decrease in the fluid velocity towards the shore.

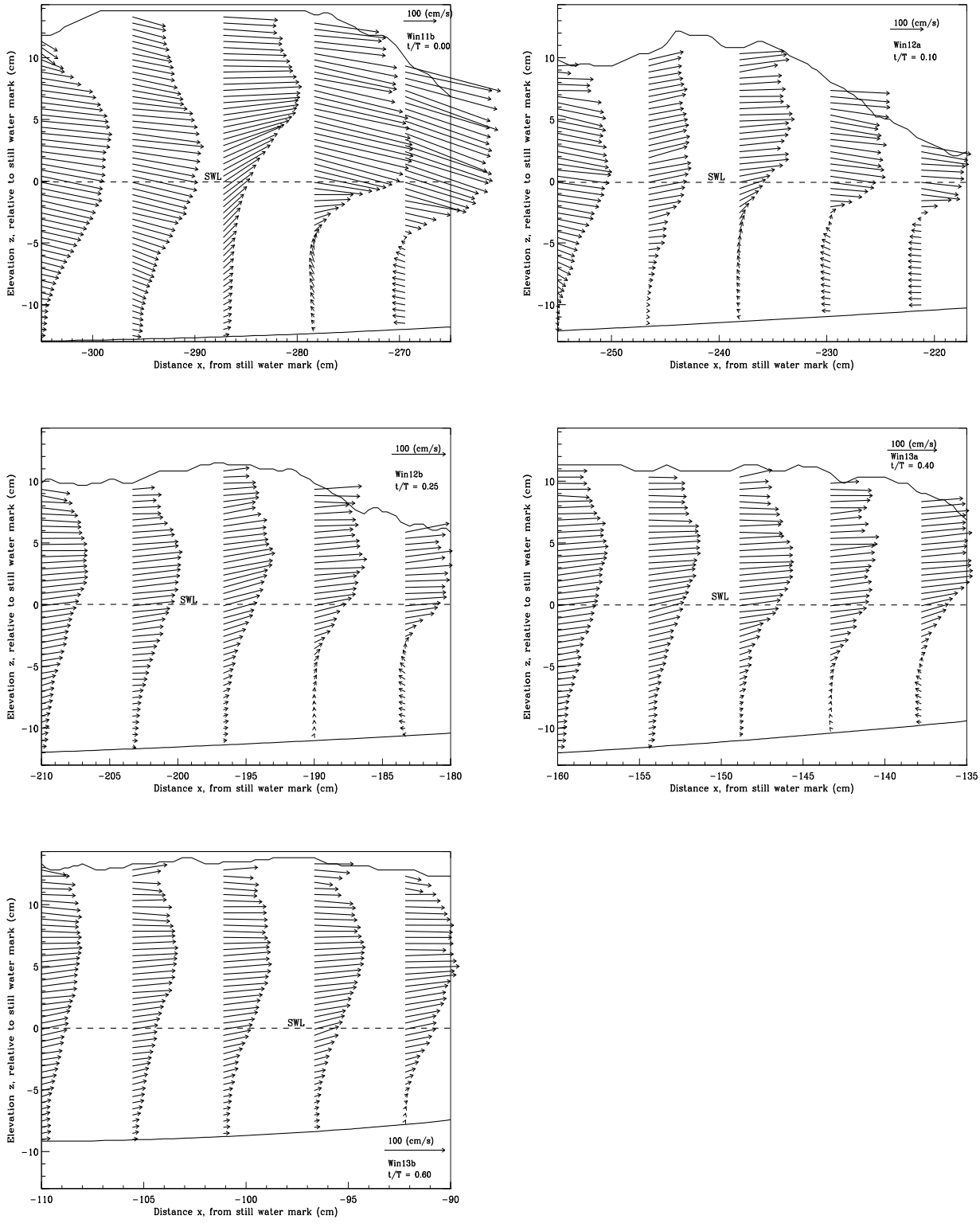

Figure 6.8: Vertical profiles of phase ensemble-averaged velocity fields under the crest phases, at different cross-shore positions along the flume at the five measurement stations. The position of the SWL is shown in each plot.

Although the spatially dense velocity vector field measurements afford a whole map of the flow, it is instructive to look at filled contour plots of mean flow which present the whole spatial map of the flow field. Figure 6.9 shows colour contour plots of the mean horizontal velocity component for the six phases

under consideration. DCIV cross correlation analysis was performed by moving the interrogation window is steps of 8 pixels both vertically and horizontally. Therefore the jags/jumps observed on the average free surface and bed slope of these and all other contours that follow represent jumps of 8 pixels which correspond to $\approx$ 5 mm. As mentioned by *Kimmoun* & *Branger* [43], owing to PIV interrogation window size resolution, it was not possible to measure velocities exactly at wave crest, and edges, but at half interrogation window size i.e. 1.0 cm below the wave crest and1.0 cm away from the edges. The colour bar represents the magnitude and direction of the velocity vector, with red pointing in the positive x-direction and blue in the negative x-direction, respectively. Thus for the horizontal velocity component, negative values represent seaward flow, while positive indicate onshore flow.

The vector and contour plots show some prominent features. The horizontal velocity profiles feature a relatively broader region of shoreward liquid surface current driven by the shoreward wave propagation and breaking, and a narrower seaward undertow region that serves to ensure volume conservation and hence no change in the time-averaged shore position. Before the crest arrives, water in the flume (at phase 0.00) is moving seaward (to the left). When the crest eventually arrives, there is strong mixing that creates a shear boundary layer between the shore bound crest and the bottom sea- bound undertow (phases $0.05 - 0.15$). Eventually there is flow reversal that culminates in the bulk of the flume water moving shore-ward. From phase 0.15 onwards, it is observed that the flow is completely reversed and all water is flowing towards the shore with peak velocities exceeding 200 cm/s, which gradually decreases with increasing phase or passage of the crest. The fluid with fast longitudinal mean velocity moves between elevation z = -5 cm and the free surface (phases $0.05, 0.10$ and 0.15) while the fluid with low velocity is confined to below the elevation z = -5 cm. Peak horizontal velocities are observed to dwell on the front face of the crest and decrease in intensity as the crest passes. Experimental and RANS results of the phase-ensemble averaged results by *Rivillas-Ospina et al.* [160], for plunging waves with $H = 10$ cm and $T = 1.5$ s and breaking on a 1:5 slope, show peak phase-averaged horizontal velocities of over 150 cm/s. Our results are also in good agreement with the results obtained by *Pedrozo-Acuna et al.* [178] for a similar plunging breaker type. When the fast moving crest fluid meets the trough water moving in the opposite direction, it is observed that the bottom surface of the fast moving crest gets deformed because of friction at the shear boundary layer. The development of the shear layer is evident from the regions of high velocity vectors. This shear layer grows in thickness with distance from the leading edge of the breaking region and significant downstream flow appears at the free surface upstream of the wave crest. A similar trend was observed by *Coakley* & *Duncan* [179]. Figure 6.10 shows contour plots of the mean horizontal velocity component at later phases in the flow, that include the trough part of the wave. This shows decreasing peak shoreward horizontal velocity at selected phases later in the flow, which eventually reverses direction as flow progresses.

Figure 6.11 shows colour contour plots of the mean vertical velocity component of the flow for the phases under study. Contrary to fluid with high horizontal velocity residing near the crest, fluid with high vertical velocity is observed under the crest. These plots also reveal that as the crest comes into view, there is a strong upward flow as seen at $\frac{t}{T} = 0.05$. This upward flow is caused by the interaction of two opposing motions - the high velocity, shore bound crest fluid and the sea bound trough fluid. This strong

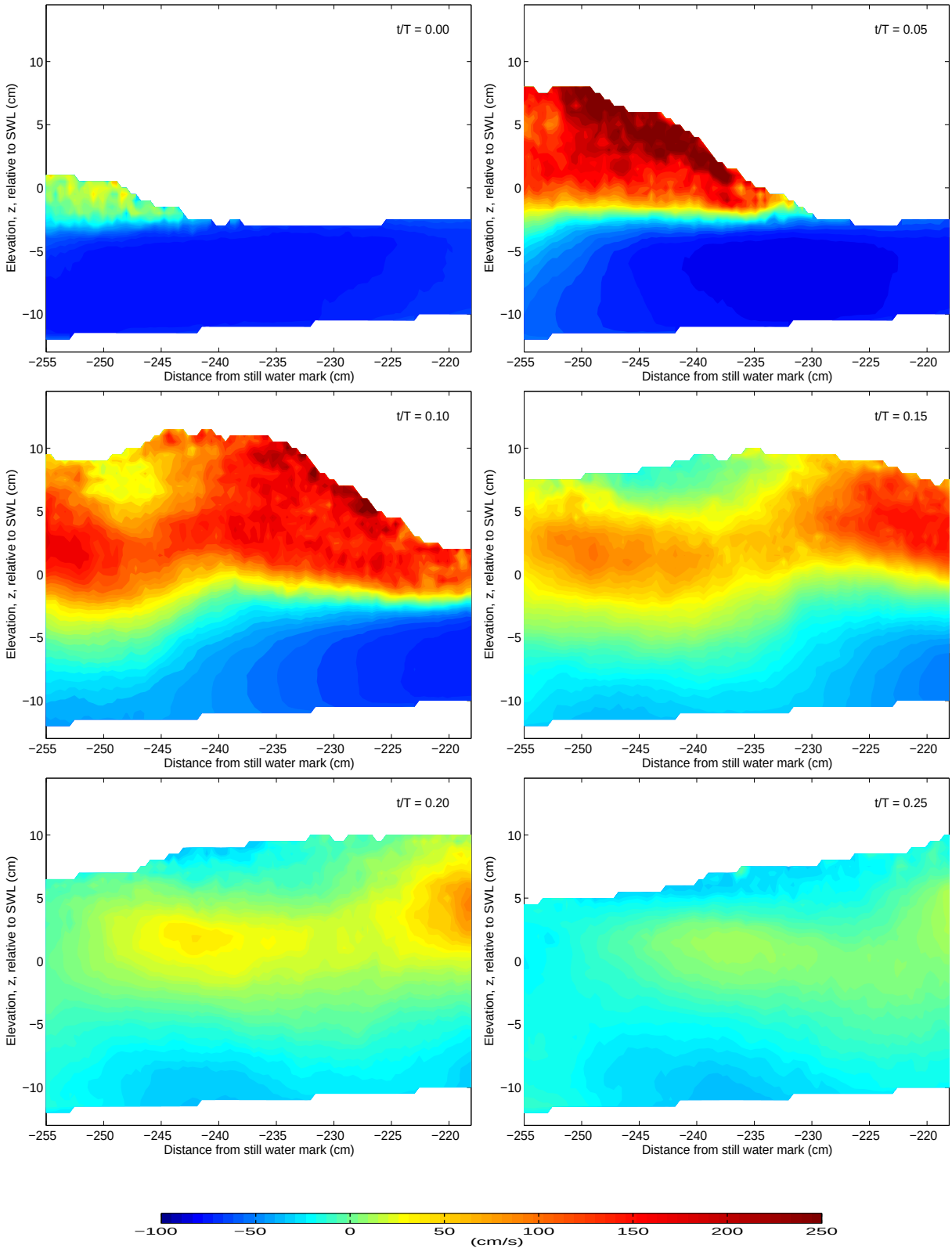

Figure 6.9: Contour plots of the evolution of mean horizontal velocity component, $\langle u \rangle$ with wave phase. The colour bar represents the magnitude and direction of the velocity vector, with red pointing in the positive x-direction, while blue points in the negative x-direction.

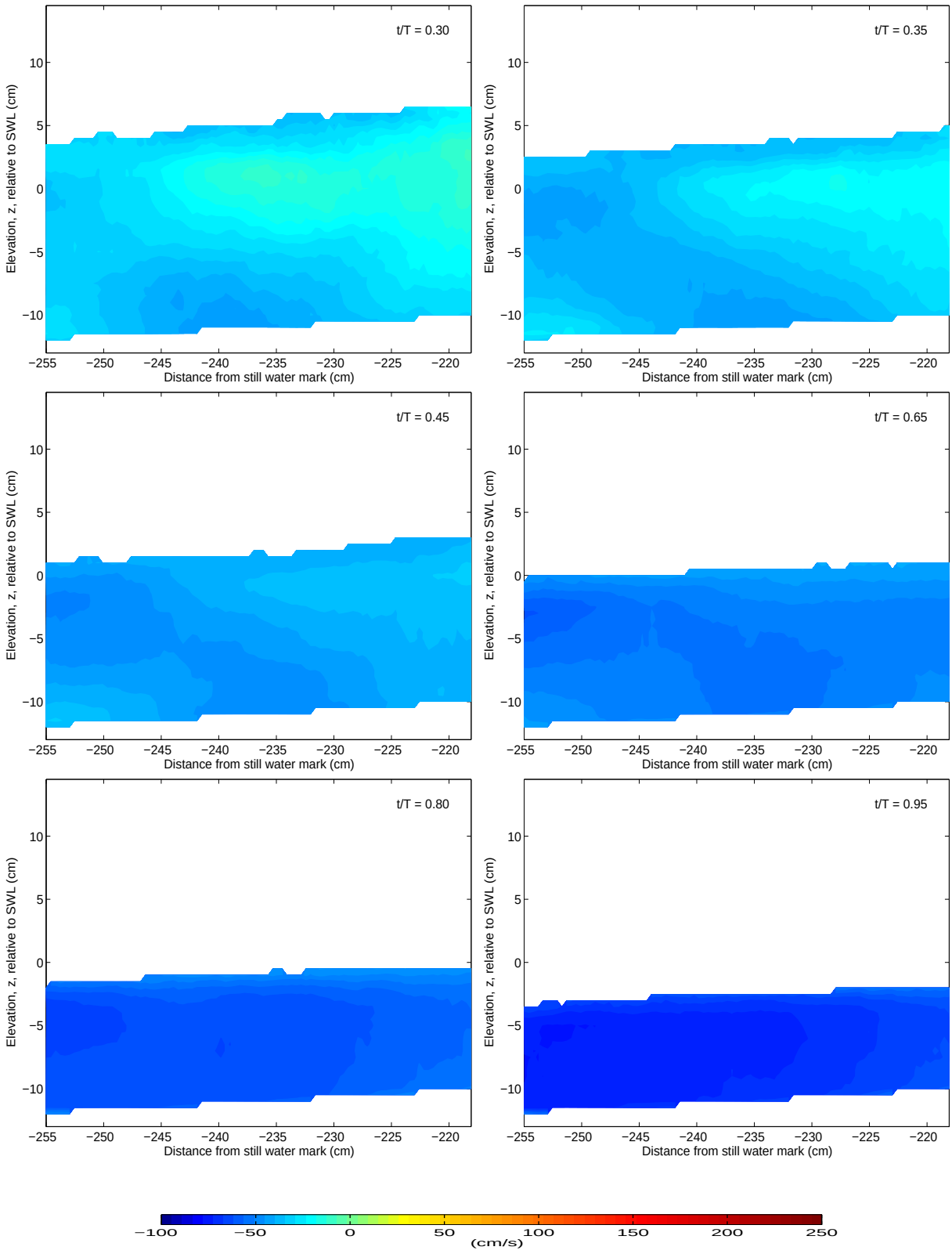

Figure 6.10: Contour plots of the evolution of mean horizontal velocity component, $\langle u \rangle$ at other selected phases later in the flow : $\frac{t}{T} = 0.30$, 0.35, 0.45, 0.65, 0.80 and 0.95.

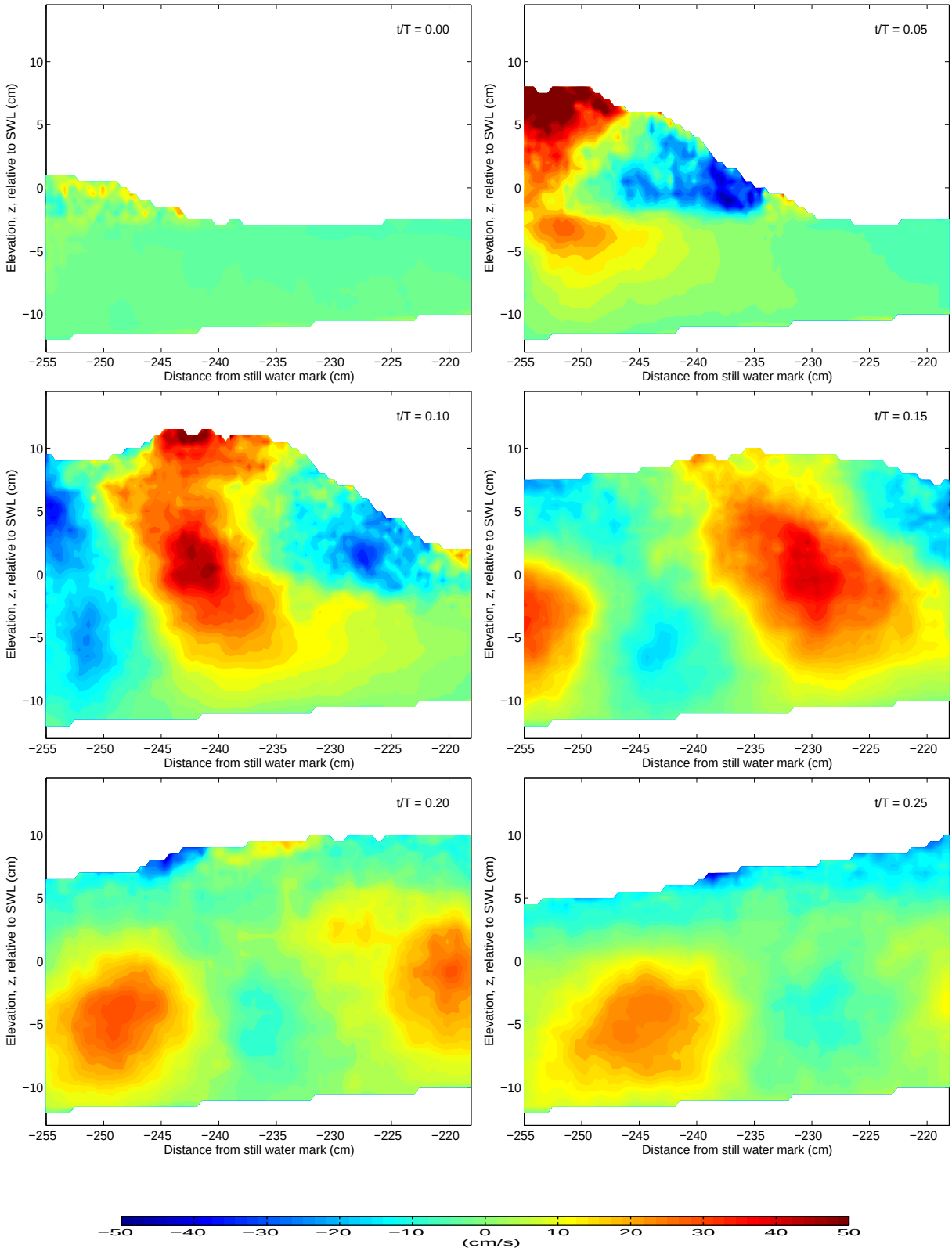

Figure 6.11: Contour plots of the evolution of mean *vertical velocity* component, $\langle w \rangle$ with wave phase. The colour bar represents the magnitude and direction of the velocity vector, with red pointing in the positive z-direction, while blue points in the negative z-direction.

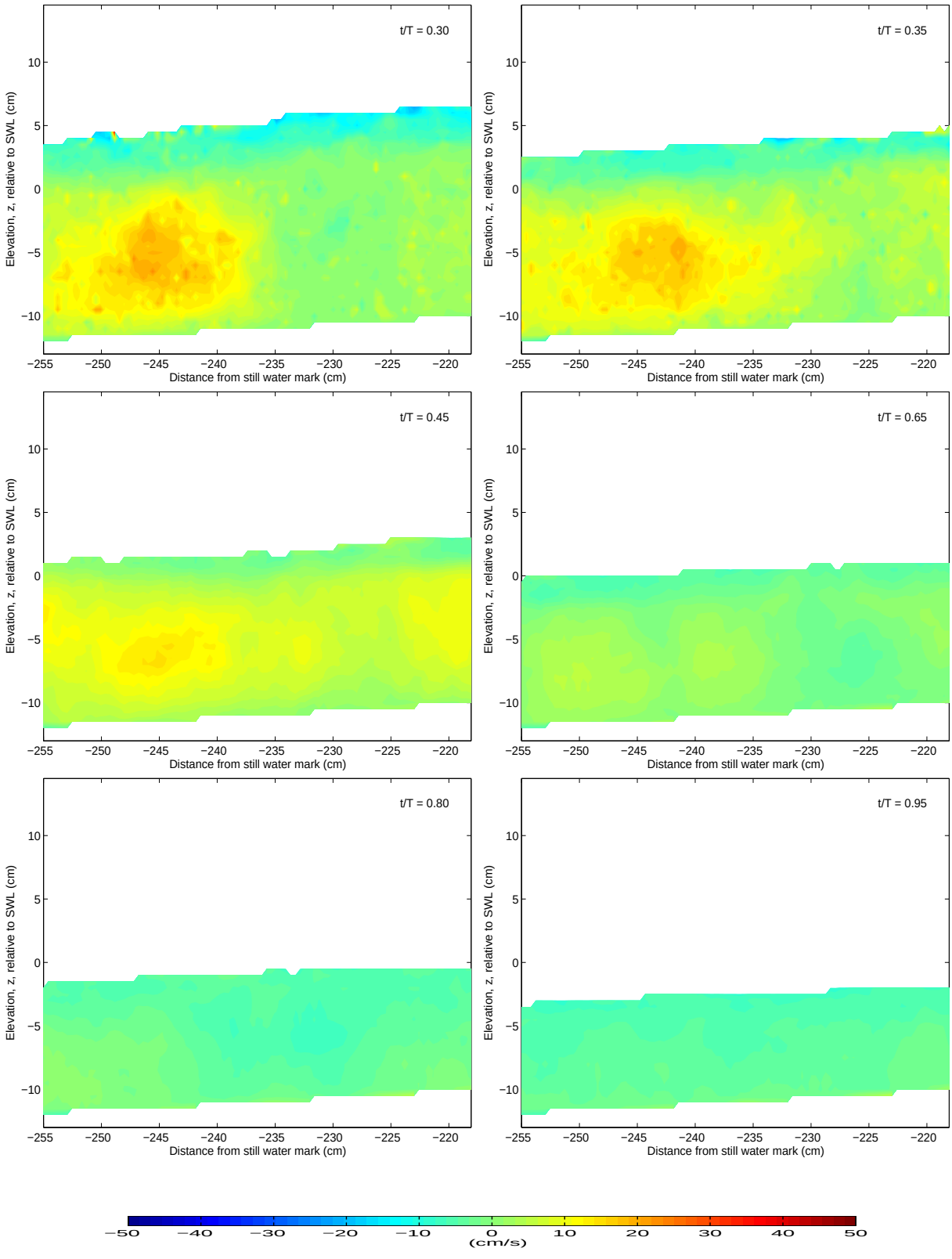

Figure 6.12: Contour plots of the evolution of mean vertical velocity component, $\langle w \rangle$ at other selected phases later in the flow. The phase numbers corresponding to these plots are shown near the top right corner.

upward moving jet causes the wave to rise as the water has nowhere else to go and further break up. This upward moving flow may be responsible for lifting up sediments from the bottom as the crest passes. As flow progress, it is observed another strong vertical flow whose center is located about 30 cm behind the first, emerging at phase $\frac{t}{T} = 0.10$ and moving along the direction of the flow, while at the same time diffusing towards the flume bed. The effect of these two strong vertically upward flows creates a saddle point located between two peaks observed at some phases. The two peak upward velocity centers eventually diffuse below the trough and continue to move downstream and finally disappear from the flow. Patches of blue, representing downward fluid motion observed on either side of the strong upward fluid motions are responsible for mixing. Both horizontal and vertical velocity components of the flow are observed to weaken gradually as flow progresses.

Figure 6.12 shows contour plots of the mean vertical velocity component at other later phases as flow progresses. These show that as the flow progresses, fluid pockets with high vertical velocity are slowed down as they homogeneously mix with the return current moving sea-ward. At depths below the wave trough vertical mean velocity decays to zero near the bottom. Peak phase-ensemble averaged vertical velocities of about 40 cm/s are observed. These results are in good agreement with results by *Rivillas-Ospina et al.* [160] who obtained peak, experimental and RANS phase-ensemble averaged vertical velocities of the order $\sim$ 60 cm/s for waves with $H = 10$ cm and $T = 1.5$ s, breaking on a 1:5 slope.

Mean velocity profiles of both horizontal and vertical velocity components along the vertical direction of the shear are presented in Figure 6.13. These profiles were extracted from the center of each contour plot for each phase. i.e. at x = -238 cm. High horizontal velocities are observed at phases $0.10, 0.15$ and 0.20. Vertical velocities are more or less uniform with minor variation across the depth. Results of the vertical profile of $\langle u \rangle$ are similar to those given by *Cowen et al.* [60] for a plunging wave, although theirs were obtained for a weakly plunging breaker with a water depth of only up to about 6.0 cm.

Figure 6.14 shows the phase evolution of the vertical profile of normalized horizontal velocity, $\langle u \rangle / c$, measured at x = -238 cm for all the six phases. Above z/h = -0.5 cm, the velocity is observed to decrease with increasing phase. Comparing the magnitudes of the maximum velocities between the normalized uprush and normalized downwash shown in Figure 6.14 it is observed that the normalized downwash is 50 and uprush is up to four times greater. *Sou and Yeh* [12] gave a similar phase dependent vertical profile of horizontal velocity averaged across the field of view of the camera, but observed that the magnitude of the uprush and downwash velocities are similar (22 cm/s) in the surf zone. The difference could be due to the fact that *Sou & Yeh* [12] used a water depth of only 4 cm, whereas a water depth of more than 25 cm in the surf zone was used in this study.

Figure 6.15 shows the evolution of vertical profiles of the normalized vertical velocity component, $\langle w \rangle / c$, measured at x=-238 cm as flow progresses. Below an elevation of z/h = -0.5 cm, the magnitude of the peak normalized vertical velocity for most of the phases is about 10 while above this elevation it is around 30 near the crest. Above z/h = -0.5 cm, the velocity is observed to decrease with increasing phase. Figure 6.16 shows a plot of the phase ensemble averaged velocity flow field for the entire wave measured at a fixed point corresponding to middle of each image. This plot was generated by extracting

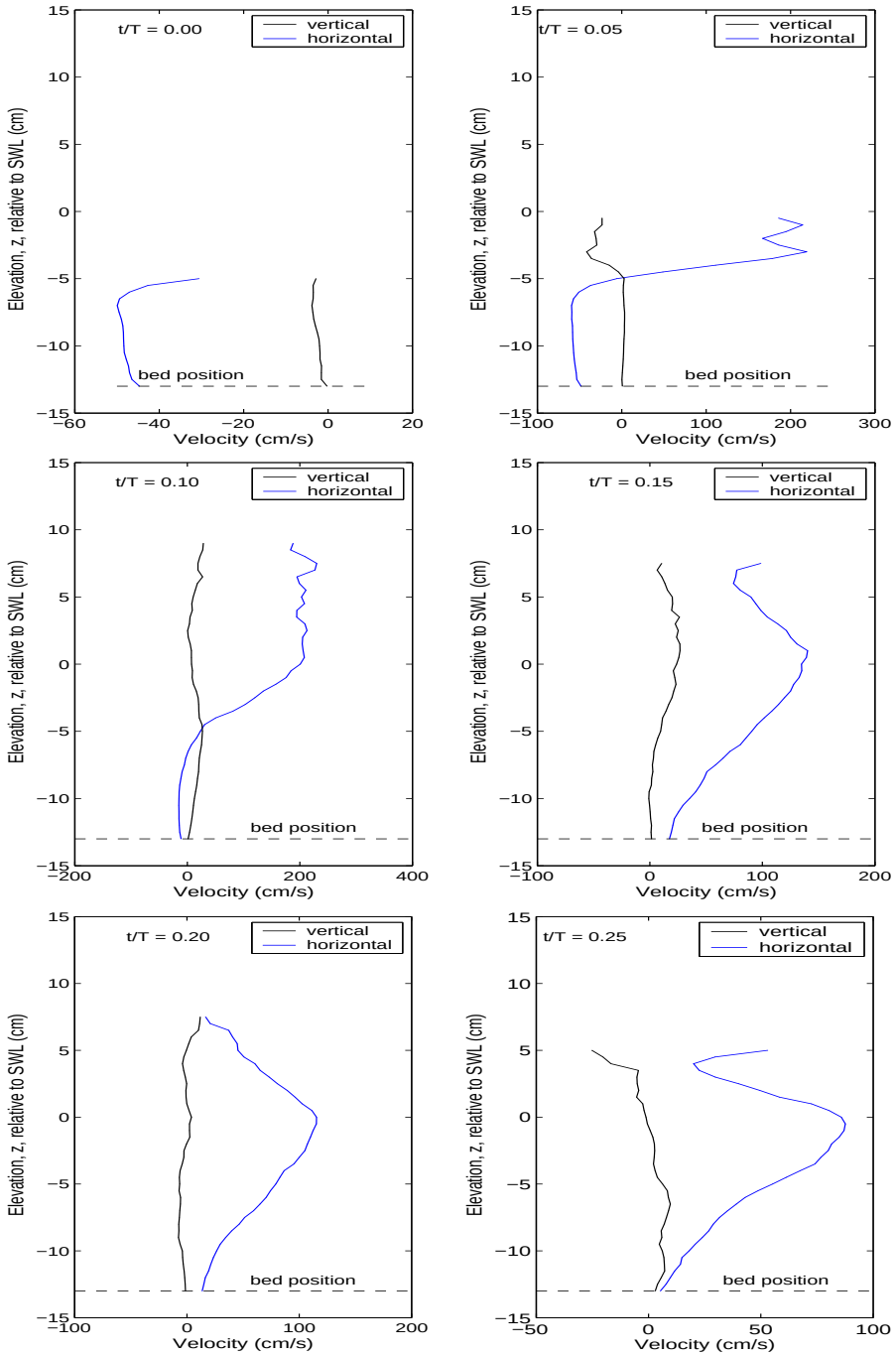

Figure 6.13: Variation of phase-ensemble averaged horizontal velocity as a function of depth, measured at the center of the images (at x= -238 cm) for each phase : horizontal component, $\langle u \rangle$,-(blue) and vertical component, $\langle w \rangle$, -(black).

a vertical column of vectors at x= -238 cm from each phase ensemble velocity flow field and stacking them side by side, and then rearranging the phases so that the crest lies in the middle. Phases of interest $\frac{t}{T}$ = 0.0, 0.05, 0.10, 0.15, 0.20, 0.25 now lie at new phase positions : 0.55, 0.50, 0.45, 0.40, 0.35 and 0.30 respectively. It is only here that new phase labels are used, however, the original phase labels will be used in rest of the discussions coming up in later chapters. A scale vector is provided to give indication of magnitudes of the velocity vectors. The vertical profile of the horizontal velocity can be noted from this figure. The dotted line is an estimated profile for one full wavelength. The front face of the wave is steeper and relatively flat behind the crest. Velocities fields near the bottom decrease due to boundary

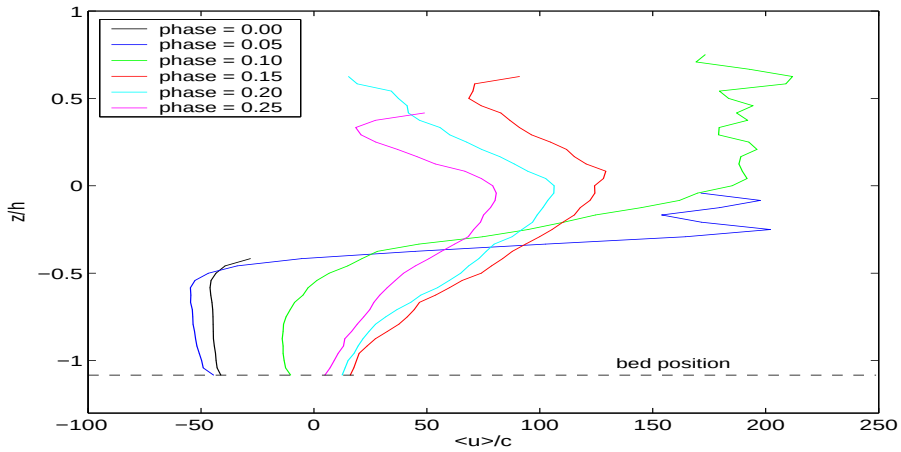

Figure 6.14: Evolution of the profile of normalized horizontal velocity, $\langle u \rangle / c$, as a function of normalized depth z/h, measured at at x=-238 cm as flow progresses. Local water depth, h = 0.12 m and $c = \sqrt{(gh)}$ = 1.08 m/s.

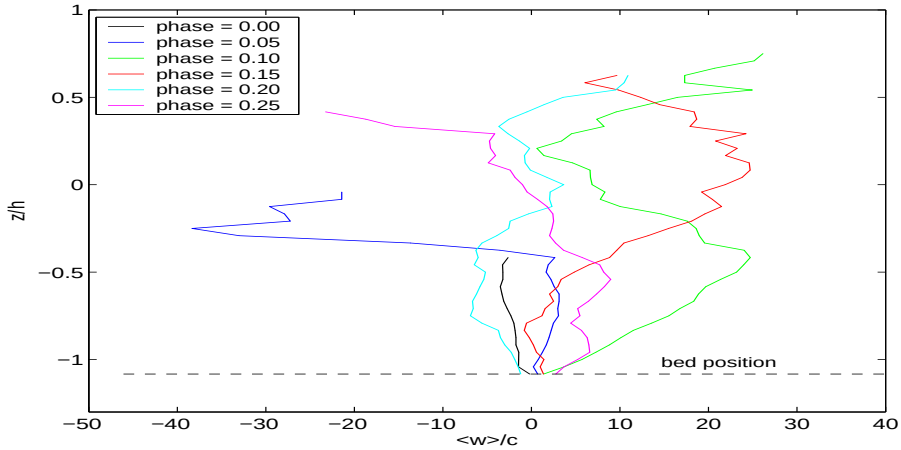

Figure 6.15: Evolution of the profile of normalized vertical velocity, $\langle w \rangle / c$, as a function of normalized depth z/h, measured at x=-238 cm as flow progresses. Local water depth, h = 0.12 m and $c = \sqrt{(gh)}$ = 1.08 m/s.

layer effects. These velocity field results are consistent with the results obtained by *Govender et al.* [42] for plunging waves.

Figure 6.17 shows the phase dependence of phase averaged velocity components with elevation at three elevations z = -8 cm, -3 cm and +2 cm for both horizontal (a) and vertical (b) components. Both graphs show that at an elevation of z=+2 cm (near the crest), there is missing data at some phases for both horizontal and vertical velocity components. This is due to the fact that for these phases the wave profiles lie below the elevation being considered. Horizontal velocity is observed to increase with elevation above the bed for all the phases. For the vertical (Figure 6.17 (b)), the only significant feature occurs when the crest arrives, at which point strong vertical velocity components are observed at phase 0.40. At this phase, water near the bed (black line) is moving in the negative z direction with velocities up to -5 cm/s while at an elevation z = +2 cm (red graph) peak vertical velocities exceed 20 cm/s. Figure 6.18 shows the phase dependence of the ratio of horizontal to vertical velocity components at several elevations in the flow. At elevation z = -3.0 cm, this ratio is around zero for most phases. Large fluctuations are observed for elevations towards the crest, z=+2 cm.

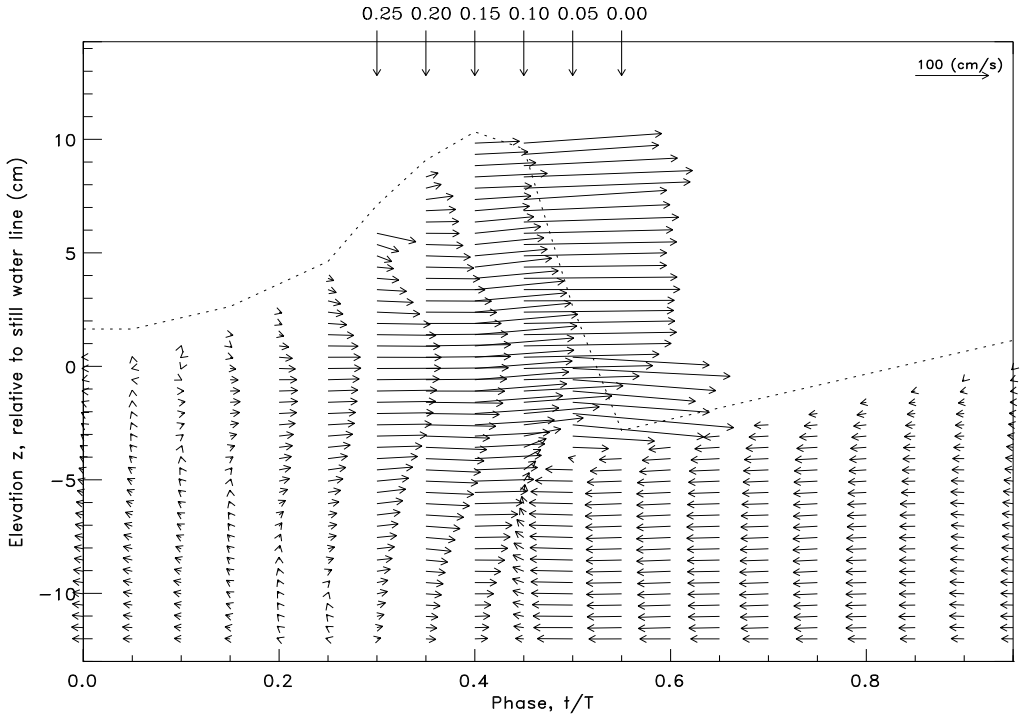

Figure 6.16: Profile of phase-ensemble averaged velocity fields for all 20 phases measured at x = -238 cm as a function of depth. The phases have been shifted so that the wave crest lies in the middle. In this plot, the phases of interest $\frac{t}{T}$ = 0.0, 0.05, 0.10, 0.15, 0.20, 0.25 now lie at 0.55, 0.50, 0.45, 0.40, 0.35 and 0.30 respectively.

6.3.3 Time-averaged velocity

Time-averaged velocity is important in the study of sediment transport within the surf zone (*Govender et al.* [53]. Figure 6.19 shows time-averaged velocity fields, $\overline{\langle u \rangle}$, at several positions within station 12a, that were obtained by averaging across all the wave phases at each vertical position. Positions of the bed and the SWL are marked. The velocity magnitude decays with water depth, as expected. These results are given for positions 4.1 cm apart, and show that the maximum time-averaged velocities below elevation z = -2.5 cm are of the order of -12 cm/s while above the SWL they are $\sim$ 30 cm/s. Similar results of the variation of time-averaged horizontal velocity component with height were observed by *Govender et al.* [42], for a plunging breaker.

Time-averaged velocity at each depth was averaged over the viewing window at station 12a to give a mean time-averaged velocity at the center of the station. These results are presented in Figure 6.20 in non-dimensional form together with results obtained by *Govender et al.* [42] for both spilling and plunging waves. Present results are in good agreement with spilling wave results by *Govender et al.* [42] for elevations below $z/h = 1.0$ (i.e. below the still water line). Huge discrepancies with results from this experiment are observed near the crest for both spilling and plunging cases. For the undertow, *Govender et al.* [42] results for the plunging wave are up to 40 % higher than both the present experiment undertow results and their spilling wave results. The horizontal velocity profiles feature a relatively broader region of shoreward liquid surface current driven by the shoreward wave propagation and breaking, and a

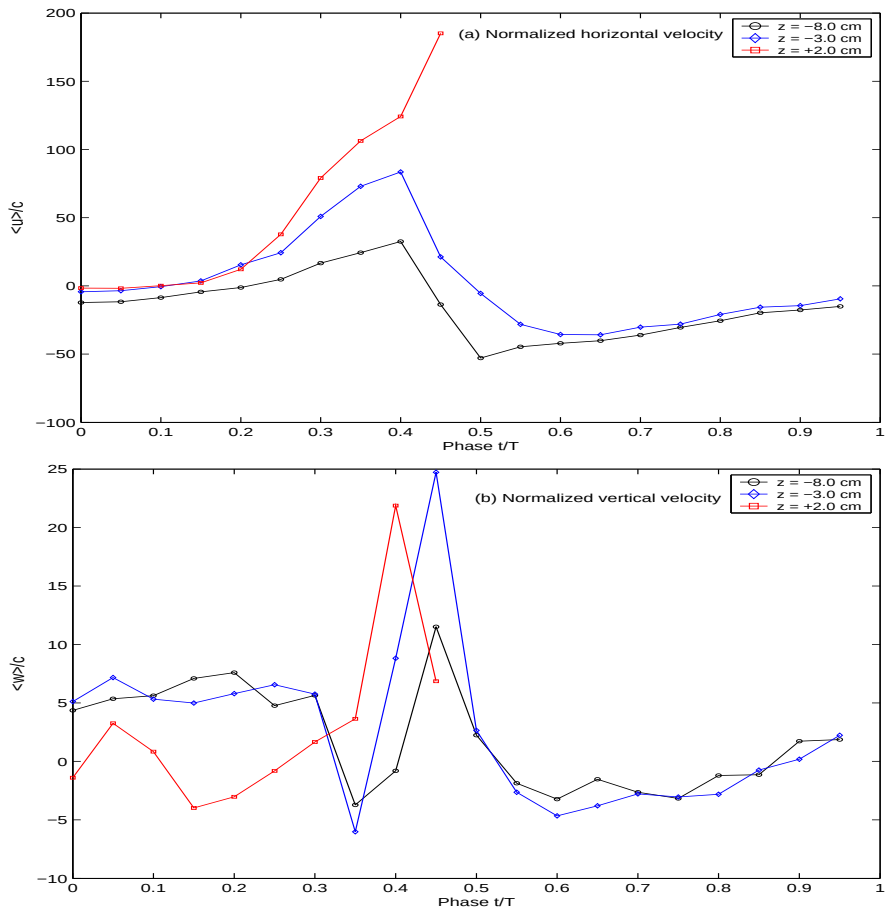

Figure 6.17: Phase dependence of the normalized ensemble averaged velocity components with distance from flume bed, measured at x = -238 cm : (a) horizontal (b) vertical, with - (*black*) : near the bed z = -8 cm, (*blue*) : z = -3 cm and (*red*) : z = +2 cm.

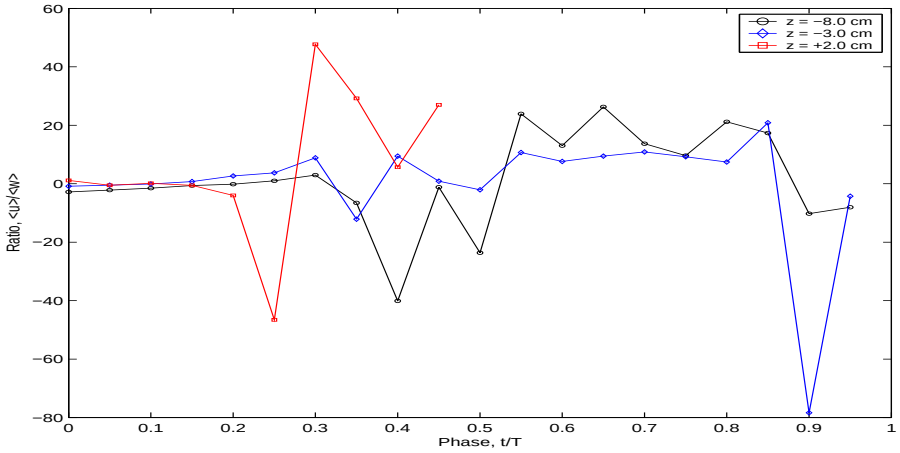

Figure 6.18: Phase dependence of the ratio of phase-ensemble-averaged horizontal to vertical velocity components, $< u > / < w >$, at different elevations from the flume bed , (*black*) : near the bed z = -8 cm, (*blue*) : z = -3 cm and (*red*) : z = +2 cm.

narrower seaward undertow region that serves to ensure volume conservation and hence no change in the time-averaged shore position.

Results from this study show that the normalized mean time-averaged velocity $\overline{u}/\sqrt{(gh)}$, have peak velocity values of up to -0.13 in the undertow and up to 0.30 for the shoreward current, at a station 162 cm from the break point. *Govender et al.* [42] obtained peak normalized horizontal velocities of magnitude

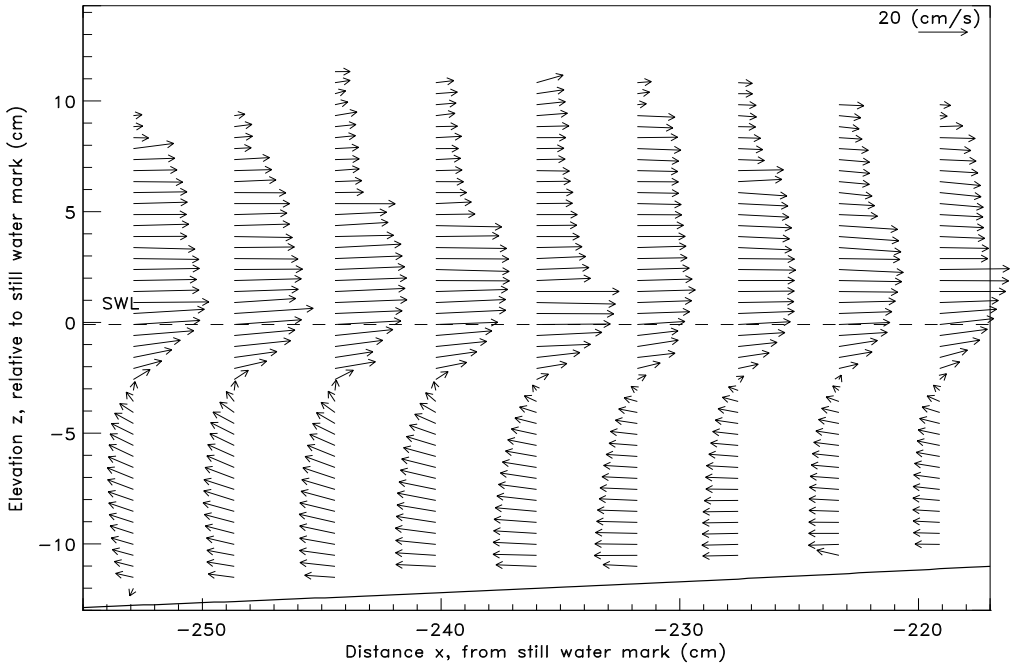

Figure 6.19: Time-averaged velocity fields for selected points 4.1 cm apart at station12a.

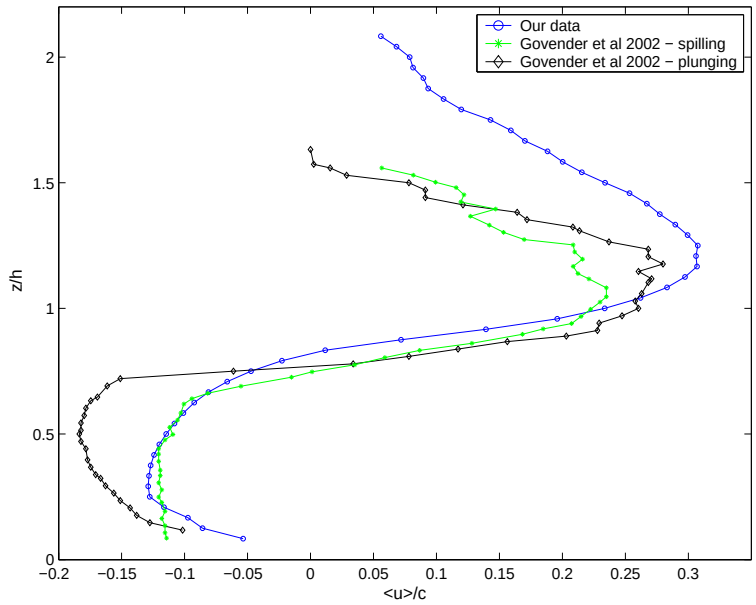

Figure 6.20: Comparison of the vertical profile of non-dimensional time-averaged horizontal velocity component, $\overline{\langle u \rangle}/\sqrt{(gh)}$, as a function of elevation above the bed for : (○) - our data at center of station located x = -238 cm from SWL and 1.62 m from the break point, and *Govender et al.* [42] data obtained for wave characteristics which given in Table 7.1 - (∗) spilling wave (⋄) - plunging wave.

-0.12 and 0.24 for the undertow and shoreward flows, respectively, for a spilling breaker at a station 122 cm from the break point. For a plunging breaker, *Govender et al.* [42] obtained peak normalized horizontal velocities of magnitude -0.18 and 0.28 for the undertow and forward flows, respectively, at a station 101 cm from the break point. *Govender et al.* [78] performed DCIV measurements of flow fields and turbulence in waves breaking over a bar. They obtained peak values of -0.10 for the undertow and 0.23

for the forward flux. Results from the present experiment provide peak normalized horizontal velocities that agree with DCIV results of both spilling and plunging wave by *Govender et al.* [42], and plunging wave by *Govender et al.* [78]. *Govender et al.* [79] obtained peak values of the normalized mean time-averaged velocity $\overline{u}/\sqrt{(gh)}$ for the undertow of about -0.08 and 0.18 for the shoreward current, for waves with period, $T = 1.5$ s, deep water wave height of 7.4 cm at a station with still water depth of 20 cm. Table 6.1 gives peak values of the normalized undertow (column 9) and forward horizontal velocities (column 10) from the present experiment in comparison to data in literature. *Kimmoun & Branger* [43] observed that near the bottom, maximum reverse non-dimensional velocities reach 0.17 while the forward flux gets up to 1.30. The undertow comparable to that obtained here, but the forward flux is an order of magnitude greater. Undertow results from the present experiment and others quoted from literature do not agree with LDV measurements of a plunging breaker by *Ting & Kirby* [30] who obtained peak vaues of -0.02 for the undertow and could not get values in the crest because of the limitation of LDV in bubbly flows. The low value for the undertow obtained by *Ting & Kirby* [30] may suggest signal drop out suffered by LDV when bubbles diffuse below the trough level.

Table 6.1: Peak values of normalized time averaged-horizontal velocities, $\overline{u}/\sqrt{(gh)}$, for the undertow (column 9) and forward current (column 10), and how they compare with results from other experiments.

	slope	T (s)	h_o (cm)	H_o (cm)	d (cm)	H_b (cm)	ξ	$\frac{\overline{u}}{\sqrt{(gh)}}$	$\frac{\overline{u}}{\sqrt{(gh)}}$	type
Present Exp 2	1:20	2.5	62	12.0	12	21.5	0.36	-0.13	0.30	plunging
Govender [42]	1:20	1.1	77	16.0	16.9	22.1	-	-0.12	0.24	spilling
Govender [42]	1:20	2.5	77	11.0	11.9	16.1	-	-0.18	0.28	plunging
Govender [79]	1:20	1.5	-	7.4	0.764	20.0	-	-0.07	0.23	spilling
Govender [78]	1:20	1.5	6.7	7.4	-	-	0.32	-0.10	0.25	plunging
K & B [43]	1:15	1.275	70.5	11.4	-	14.0	0.28	-0.17	1.30	spil-plung
T & K [30]	1:35	5.0	40	12.8	15.6	19.1	0.20	-0.02	-	plunging

[1]

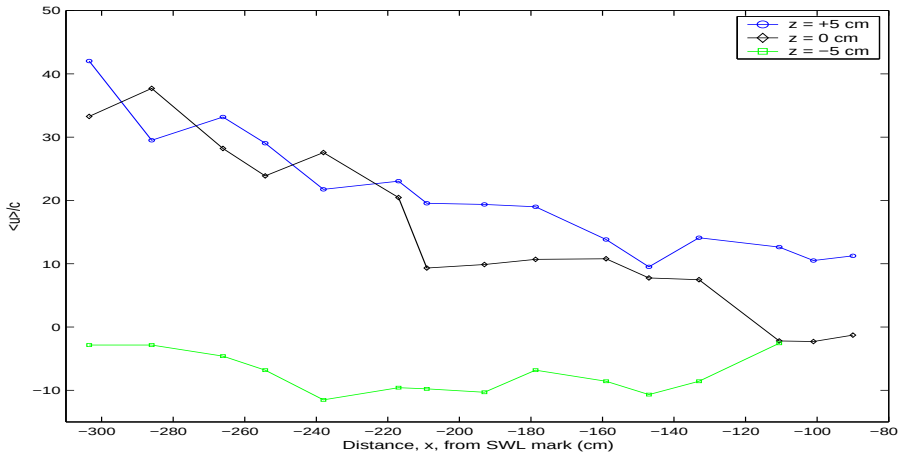

Figure 6.21: Variation of normalized time-averaged horizontal velocity, $\overline{\langle u \rangle}/c$, with position along the flume at three different elevations from the flume bed. $c = \sqrt{(gh)}$

Figures 6.21 and 6.22 show the variation of normalized time-averaged horizontal, $\overline{\langle u \rangle}/c$, and vertical, $\overline{\langle w \rangle}/c$ velocities, respectively, at several elevations from the flume bed. These were measured at different

[1] In Table 6.1, K & B [43] refers to *Kimmoun & Branger* [43] ; T & K [30] refers to *Ting & Kirby* [30]

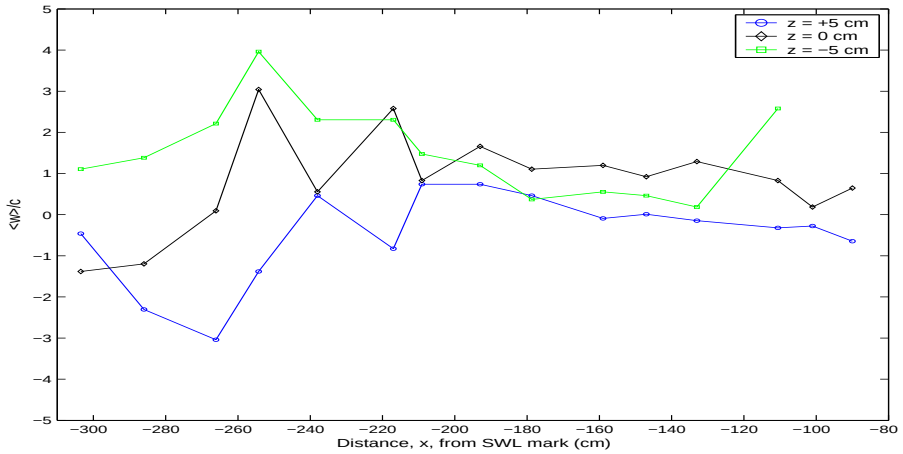

Figure 6.22: Variation of normalized time-averaged vertical velocity, $\overline{\langle w \rangle}/c$ with position along the flume at three different elevations from the flume bed.

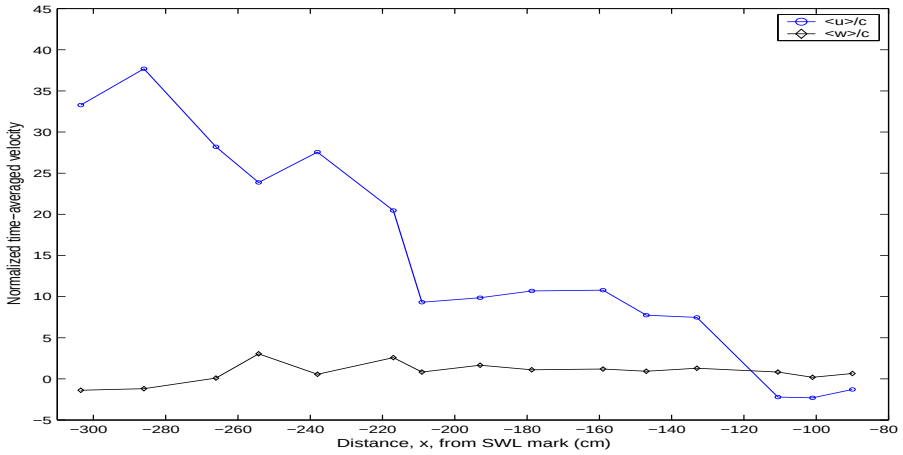

Figure 6.23: Variation of normalized time-averaged velocity components with position along the flume at elevation z = 0 cm.

positions along the flume length. Results show that near the flume bed (z = -5 cm), $\overline{\langle u \rangle}/c$ is negative and more or less constant at all the x-positions. There are no values for both time-averaged horizontal and vertical velocities at elevation z = -5 cm because of the flume bed at this elevation for $x > -110$ cm. For elevations $z = 0$ cm and $z = +5$ cm, an almost linear decrease in the $\overline{\langle u \rangle}/c$ is observed, from around 40 near the break point to a minimum of -2.0 towards the shore. The normalized time-averaged vertical velocity, $\overline{\langle w \rangle}/c$ varies between -3.0 and 4.0 along the flume. For positions close to the break point, there is a strong variation in $\overline{\langle w \rangle}/c$ for $x < -210$ cm, while for $x > -210$ cm, the time-averaged vertical velocity steadily decreases from around 1.0 to 0 towards the shore. The normalized time-averaged vertical velocity at elevation $z = 5$ cm is less than those below this elevation for almost all flume positions. That means time-averaged vertical velocity near the crest is less than that at the shear boundary layer. Figure 6.23 shows a comparison of the variation along the flume of normalized time-averaged horizontal and vertical velocities at elevation $z = 0$ cm, (SWL), as a single plot for easy comparisons. Normalized time-averaged horizontal velocity decreases almost linearly towards the shore, from about 40 at x = -2.90 m down to about -2.0 at $x >$ -110 cm from the SWL mark. Normalized time-averaged vertical velocity is relatively uniform, only fluctuating between +2.0 and -2.0 along the entire flume length considered.

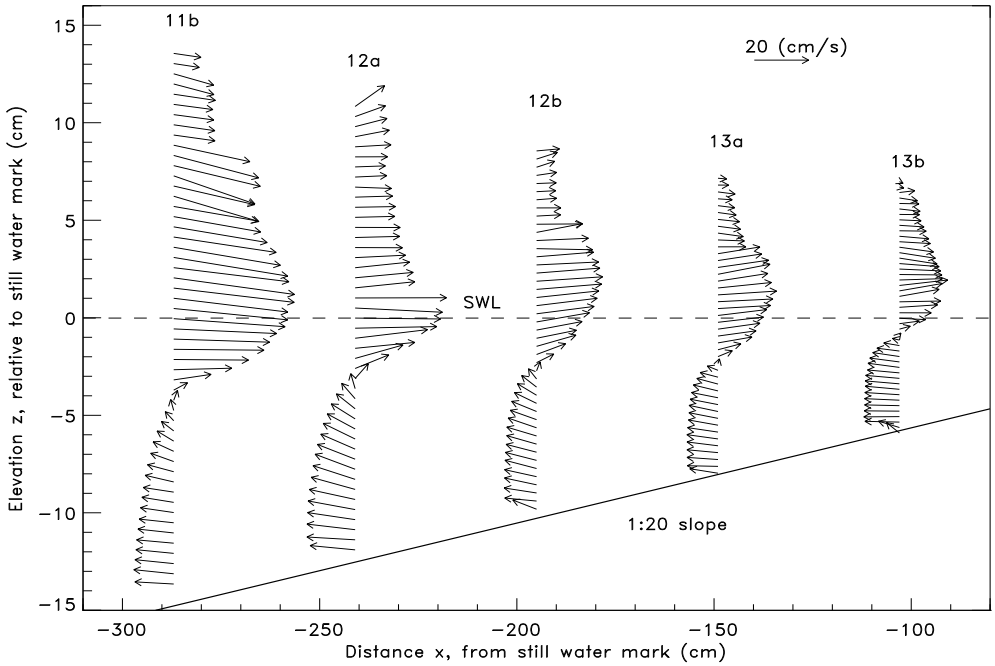

Figure 6.24: Stacks of the time-averaged velocity fields at the center of each of the five measurement stations along the flume. The SWL is at elevation $z = 0$ cm at all the stations.

Figure 6.24 shows in one plot, stacks of the time-averaged velocity fields measured at the center of each of the five stations which are about 0.50 m apart. Distances of each station center from the SWL mark are already given in Table 3.1. The position of the 1:20 flume bed as well as the SWL are shown in the figure. Elevations are measured relative to the SWL which is at $z = 0$ cm at all the stations. An arrow vector of magnitude 20 cm/s is shown in the upper right corner of the plot and velocity vectors at each station are plotted relative to this legend. There is a decrease in both the undertow and the forward flux or uprush towards the shore. Peak values of the uprush range from about 40 cm/s at station 11b which is in deepest water, to about 15 cm/s at station 13b which is closest to the shore. For the undertow, peak values range from about 20 cm/s in deeper water to 12 cm/s closest to the shore. Moving from deeper water towards the shore, it can be observed that the separation between the velocity vectors in the vertical direction gets narrower towards the shore. This is because towards the shore there is reduction in water depths, so the camera was placed closer to the flume wall for stations near the shore. This means the resolution used at the measurement stations gets larger and larger towards the shore. Calibration factors used at each measurement station, already given in Figure 4.1 confirm an increasing trend, implying increasing resolution towards the shore. Resolution of the measurements at 13b is about twice that used at 11b.

Relative density of the roller

The region of high horizontal velocity between the SWL and the crest corresponds to the wave roller, which is a body of fluid that rides on the front face of the wave. The relative density of the wave roller is

an important parameter in surf zone modeling. By integrating time-averaged horizontal velocity vectors shown in Figure 6.19, it is possible to determine the mass flux towards and away from the shore which can be used to estimate the relative density of the roller.

The flux of horizontal incoming mass across a unit area of a vertical plane is defined as :

$$M_x = \int_0^z \rho \overline{u(z)} dz \tag{6.2}$$

where ρ is the density of the fluid, and $\overline{u(z)}$ is the time-averaged velocity at some vertical position, z.

The density of the wave roller is given by,

$$\rho = \rho_r \rho_w \tag{6.3}$$

where ρ_w is the density of water and ρ_r is the relative density. Using subscripts U and L to refer to the upper and lower sections relative to some vertical position z', at which the horizontal velocity component changes sign, and assuming that the density is uniform through the crest, then,

$$M_U = \rho_r \rho_w \int_{z'}^{z} \overline{u(z)} dz \tag{6.4}$$

and

$$M_L = \rho_w \int_0^{z'} \overline{u(z)} dz \tag{6.5}$$

As shown in Figure 6.19, this position represented by z' is located close to the SWL at z = -3 cm. In the case where there are no sources or sinks of the water in the flume, the depth integrated mass flux towards the beach at any horizontal position equals mass flux away from the beach. Thus, the momentum in the positive flowing surface drift is roughly balanced by the lower return flow, so that the relative density of the wave roller is then given by :

$$\rho_r = \frac{\int_0^{z'} \overline{u(z)} \mathrm{d}z}{\int_{z'}^{z} \overline{u(z)} \mathrm{d}z} \tag{6.6}$$

The density of the flow in a location surrounded by foam should be lower than unity. The relative density for the roller obtained at our measurement station 12a is $\rho_{12a} = 0.44$. *Govender et al.* [62] estimated the relative density of the roller using the forward and reverse mass fluxes, and found the results to be in the range from 0.4 to 0.8 for a spilling breaker.

Figure 6.25 shows the estimated relative density of the water/air mixture as the wave propagates along the flume. This was obtained from the ratio of onshore and offshore velocity fluxes. Assuming conservation of mass across any vertical section, the depth integrated mass flux in the forward and reverse direction must be equal. The relative density is observed to increase from about 0.1 to about 0.6 towards the shore. The average relative density is around 0.4 and is consistent with results obtained by *Govender et al.* [79] and *Kimmoun & Branger* [43] who obtained a void fraction of approximately 0.6 for a spilling-plunging wave breaking on a plane beach slope. *Kimmoun & Branger* [43] also observed that the void fraction ranges

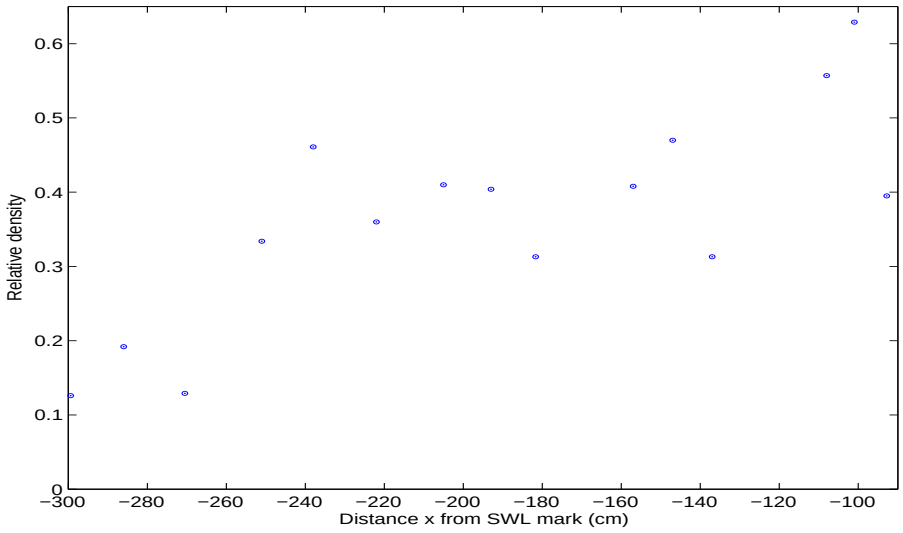

Figure 6.25: Variation of relative density of the roller along the flume.

between 0.2 and 0.3 near the shore. Similar results were obtained by *Cox & Shin* [56] who employed a conducting probe and also found the void fraction to vary between 0.2 - 0.3.

6.4 Convergence of turbulence statistics

It is often important to know how a random variable is distributed about the mean. Effects of sample size on the convergence of the mean are investigated by computing this quantity using various sample sizes and examining the manner in which they converge. It is important to use enough vectors to ensure statistically meaningful results (*Fairweather & Hargrave* [180]. Figure 6.26 shows the variation of instantaneous velocities and how they fluctuate around the phase ensemble average, for 100 sequences at one phase for a point near (a) trough and (b) crest. This was done to enable the selection of a clamp used for calculating turbulence intensity. A clamp of 75% above and below the average velocity was found appropriate. All instantaneous velocity values that lie outside the band were not used in calculating the turbulence intensities. As a result the number of valid instantaneous velocity vectors used in calculating turbulent intensity at any point can be less than the total number of samples, particularly near the free surface.

In the ensemble given above, the relative fluctuation level is 75%, so the fewest number of independent samples that must be acquired to measure the mean value to within 10 % can be estimated from the variability of the estimator, which depends inversely on the number of independent realizations, N, and linearly on the relative fluctuation level of the random variable itself, $\frac{\sigma_x}{\overline{x}}$ as :

$$\epsilon_{x_N} = \frac{1}{N}\left(\frac{\sigma_x}{\overline{x}}\right)^2 \tag{6.7}$$

where σ_x is the standard deviation of the random variable x. Substituting values and solving the above equation gives $N \geq 56$. Obviously if the relative fluctuation level is zero (either because the quantity being measured is constant or there are no measurement errors), then a single measurement will suffice.

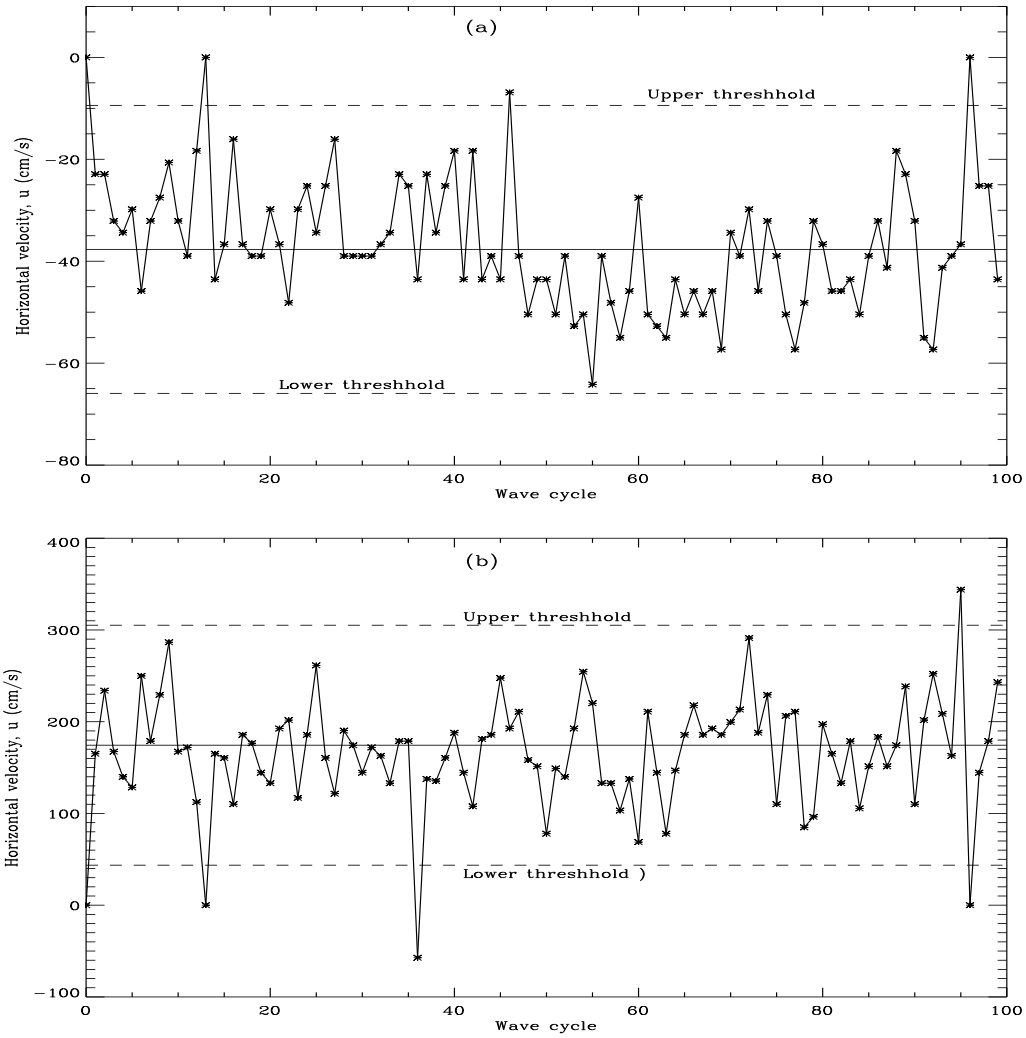

Figure 6.26: Instantaneous velocity fluctuations around the phase ensemble average, at elevations : (a) near the trough where the mean is -37.7 cm/s, and (b) near the crest where the measured mean is 174 cm/s. The dashed lines mark thresholds of 75 % above and below the mean values.

On the other hand, as soon as there is any fluctuation in the random variable x itself, the greater the fluctuation (relative to the mean of x, $\langle x \rangle = \overline{x}$), then the more independent samples it will take to achieve a specified accuracy. Higher order moments can take a long time to converge, and in some cases the experimenter just waits for the mean velocity($\langle u \rangle, \langle v \rangle$, and $\langle w \rangle$), and the root mean square velocity (u', v', and w') to converge. To test how many samples are needed to reach convergence, a point located in the crest region was selected and ensemble averaging was progressively done over samples ranging from 5 to 100. This was done to test the convergence status of relative errors of the ensemble-averaged quantities (*Huang et al.* [64]). In this section, the convergence of turbulent quantities of interest were examined. This was performed by calculating running averages of the turbulence statistics over the entire ensemble (*Misra et al.* [29]).

Figure 6.27 shows the extent to which the averages of 45 realizations converge to the true phase-ensemble average velocity components can be seen by comparing it with the averages taken over 100 repeats. Results show that few measurements (less than 30) are a poor indicator of the mean motion. Both phase-ensemble

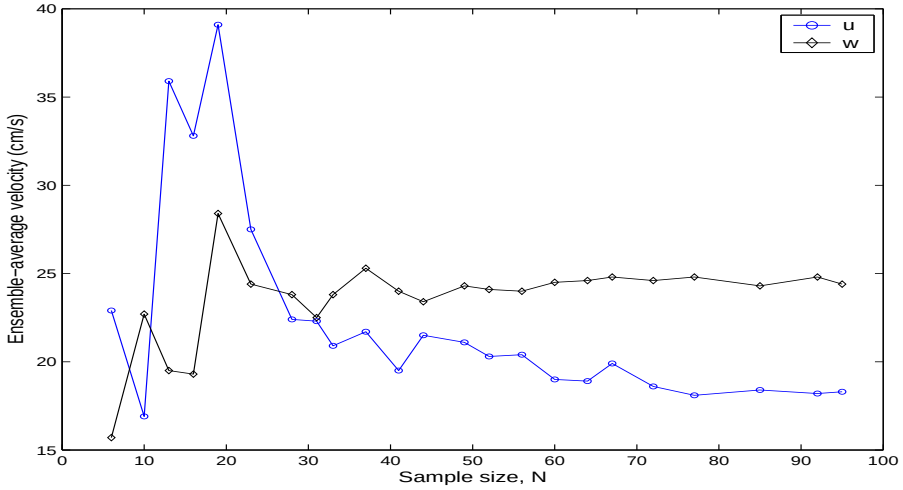

Figure 6.27: Convergence test of phase-ensemble averaged velocity (∘) - horizontal, $< u >$, ⋄ - vertical $< w >$ on sample size.

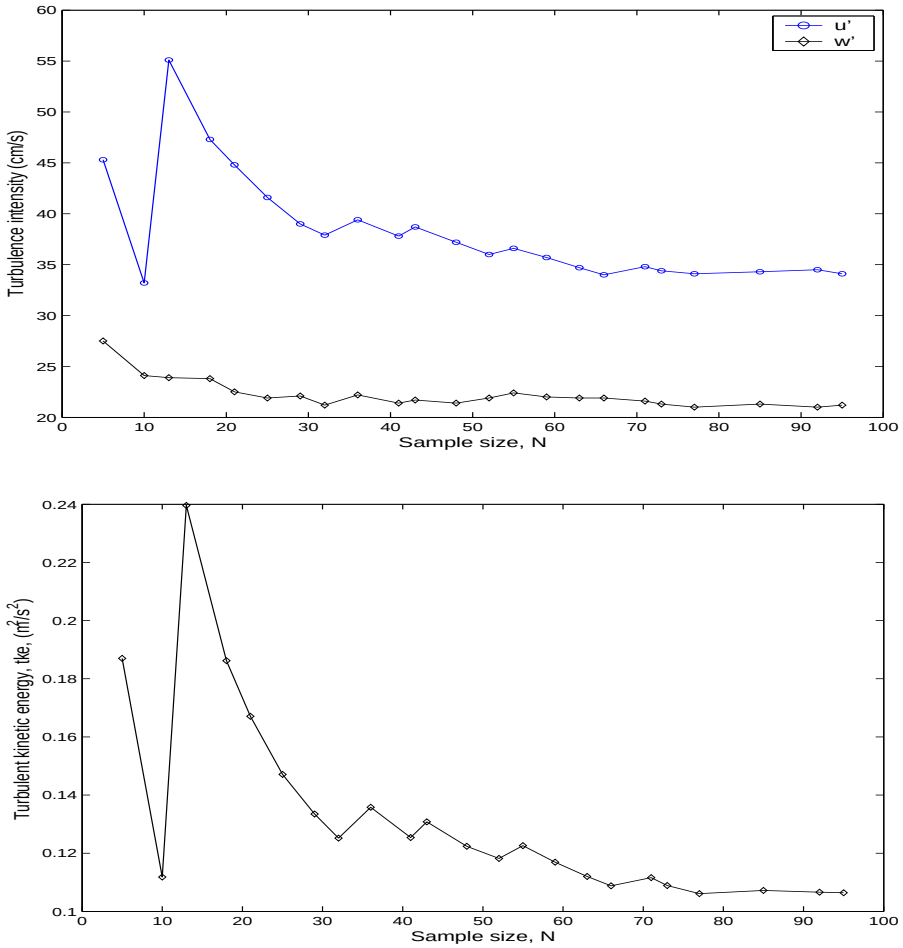

Figure 6.28: Convergence tests on turbulence statistics (a) $(-\circ-)$ - horizontal turbulence intensity, u', $-\diamond-$ - vertical turbulence intensity, w' (b) turbulent kinetic energy, k'.

average velocity components are observed to converge after about 45 samples. Averaging 45 or more samples does not significantly alter the result. Thus for this experiment convergence occurs after averaging 45 samples. The convergence rates for the turbulent statistics are shown in Figure 6.28. Figures 6.28 (a) shows convergence of turbulence statistics in the breaker region at x, z = (-240, -3) cm, showing $r.m.s$

horizontal turbulent velocity u' and $r.m.s$ vertical turbulent velocity w', while Figures 6.28(b) shows the convergence statistics of turbulent kinetic energy (k). Stable estimates of the turbulent quantities are also obtained near the end of the ensemble after about 40 realizations. The use of at least 70 samples in the ensemble averages is appropriate. *Ting & Kirby* [38] used 102 waves and checked the sensitivity of the ensemble averaged statistics on the number of waves used. They showed that ensemble averaged statistics for both average speed and turbulence intensities for both horizontal and vertical components were stable with relative deviation of less than ± 5% if the number of waves was greater than 40. *Shin & Cox* [67] observed that values of u' and w' converged when there were 40 or more observations at that phase.

6.5 Summary

Instantaneous fluid velocities were measured using digital correlation image velocimetry which provided synoptic view of flow measurements spanning the entire water column. Peak instantaneous velocities with an error estimate of ± 2.0 cm/s were observed near the front face of the crest with magnitudes which are about 2 times the wave phase velocity. The mean horizontal velocity component which is much greater than the vertical component, is positive (shore-ward) above the trough level and negative underneath. From the flume bed up to elevation z/h = -0.5, both horizontal and vertical mean velocities do not show a significant variation. Above this elevation, both horizontal and vertical velocity components, rise to peak values of 250 cm/s and 40 cm/s, respectively, as the crest comes into the camera field of view and decreases as flow progresses. Time averaging yielded estimates of the forward current in the upper water column, and the undertow below the trough level. The time-averaged horizontal velocity decreases almost linearly towards the shore while time-averaged vertical velocity is nearly uniform along the surf zone. Treatment of the mass fluxes gave roller density values ranging between 0.1 to 0.6.

Chapter 7: Turbulence results

" *Big whorls have little whorls, that feed on their velocity, and little whorls have lesser whorls, and so on to viscosity.*"

-Lewis F. Richardson [181]

7.1 Introduction

In order to gain insights into turbulence structures associated with breaking waves and how they evolve, it is important to compute higher order moments of the velocity flow fields. In this chapter results are presented of phase-ensemble averaged and time-averaged turbulence characteristics such as turbulence intensity and turbulent kinetic energy. colour contour plots of these turbulence parameters are presented to show their evolution and variation as flow progressed. In addition, profiles of these parameters with depth and phase are also presented. Time-averaged turbulent intensities and turbulent kinetic energy results obtained in the present study are normalized by Froude scaling and benchmarks and comparisons with previous similar measurements are reported.

7.2 Phase-ensemble averaged turbulence characteristics

Ensemble averages are performed on the instantaneous data measured at each phase. This section discusses results of phase-ensemble averaged turbulence statistics.

7.2.1 Turbulence intensity

The horizontal turbulence intensity, u', represents deviations of the measured instantaneous value, u_i, from the mean value $\langle u \rangle$, defined by the root-mean-square of velocity given by :

$$\sqrt{u'^2} = u'_{r.m.s} = \sqrt{\frac{1}{N}\sum_{i=0}^{N-1}(u_i - \langle u \rangle)^2} \tag{7.1}$$

A similar equation is used for the vertical turbulence intensity w'. In the remainder of the work reported here, the primed variables (u', w') will be used to represent the root-mean-square values of the horizontal and vertical turbulent fluctuations, respectively.

Figures 7.1 and 7.2 show contour plots of the spatial variation of the horizontal and vertical turbulence intensities, respectively, for the flow at station 12a. The colour code shows the magnitude and direction of the turbulence intensity component. The direction for the horizontal and vertical turbulence intensity components are the same as that defined previously for the mean horizontal and vertical velocity components. Each contour map shows the spatial distribution of the turbulent intensities at the different wave phases. These results show that turbulent intensities have peak values of 70 cm/s for the horizontal and 40 cm/s for the vertical. Both figures show that turbulence intensities which are initially present in almost the entire water column, gradually decrease with progress of the phase. A high horizontal turbulence intensity region appears between elevation z =- 5 cm and the free surface as observed at phases, 0.00, 0.05, 0.10 and 0.15 of Figure 7.1. These results are in agreement with results of *De Serio & Mossa* [68], who also observed that higher turbulence is localized near the surface rather than near the bottom. Consistent with results by *Liiv* [2], it is observed from the turbulence contours that as the wave propagates towards the shore in the surf zone, the horizontal and vertical turbulences generated near the surface due to breaking waves diffuse to the bottom of the bed where some of it is dissipated as heat by friction with the bed. Figure 7.2 shows that high vertical turbulence intensity is near the free surface and diffuses deeper into flow than the horizontal. The turbulence results obtained here are also consistent with the observation that high turbulent intensity occurs in the crest region as reported by previous researchers (e.g., *Govender et al.* [42]; *Kimmoun & Branger* [43]; *Huang et al.* [44]; *Huang et al.* [88]; *Okayasu et al.* [182]).

In order to compare the horizontal and vertical turbulence intensities of the flow, the variation of these components with depth are plotted on the same axis for each phase, as shown in Figure 7.3. During the early phases of the flow, vertical and horizontal turbulence intensities below elevation z = -5 cm are almost of the same order. From elevation z = -5 cm going towards the crest, horizontal turbulence intensity increases sharply to peak values of nearly 70 cm/s. The magnitude of the peak horizontal turbulence intensity decreases as the flow progress in phase. When the crest has passed the horizontal intensity reduces to about double the vertical as observed at phases 0.20 and 0.25. During the early phases, both horizontal and vertical turbulence intensities were found to rise linearly from the bed reaching about 20 cm/s near the elevation z/h = -0.5 cm. Thereafter it rises sharply to peak values of about 70 cm/s for the horizontal and about 40 cm/s for the vertical. Outside the aerated region, maximum horizontal turbulence intensity is of the order of 20 cm/s. *Chang & Liu* [41] obtained turbulence intensity of the order of 11 cm/s in the trough section for a wave height of 14.5 cm and deep water wavelength of 121 cm. These results are also in good agreement with results obtained by *Lennon & Hill* [120].

In order to show the phase evolution of turbulence intensities of the flow, separate plots of the variation of horizontal and vertical turbulence intensities with depth are presented for all six phases on the same axis as shown in Figure 7.4 and Figure 7.5, respectively. It is evident from the preceding figures that turbulence is generated near the free surface and gradually decays by diffusing to the flume bed as flow progresses. *Pedersen et al.* [183], pointed out that in breaking waves, most of the production of turbulence takes place near the surface and part of the turbulence spreads downward while it gradually dissipates into heat. These results are also in agreement with observations by *Ting & Kirby* [30], who showed

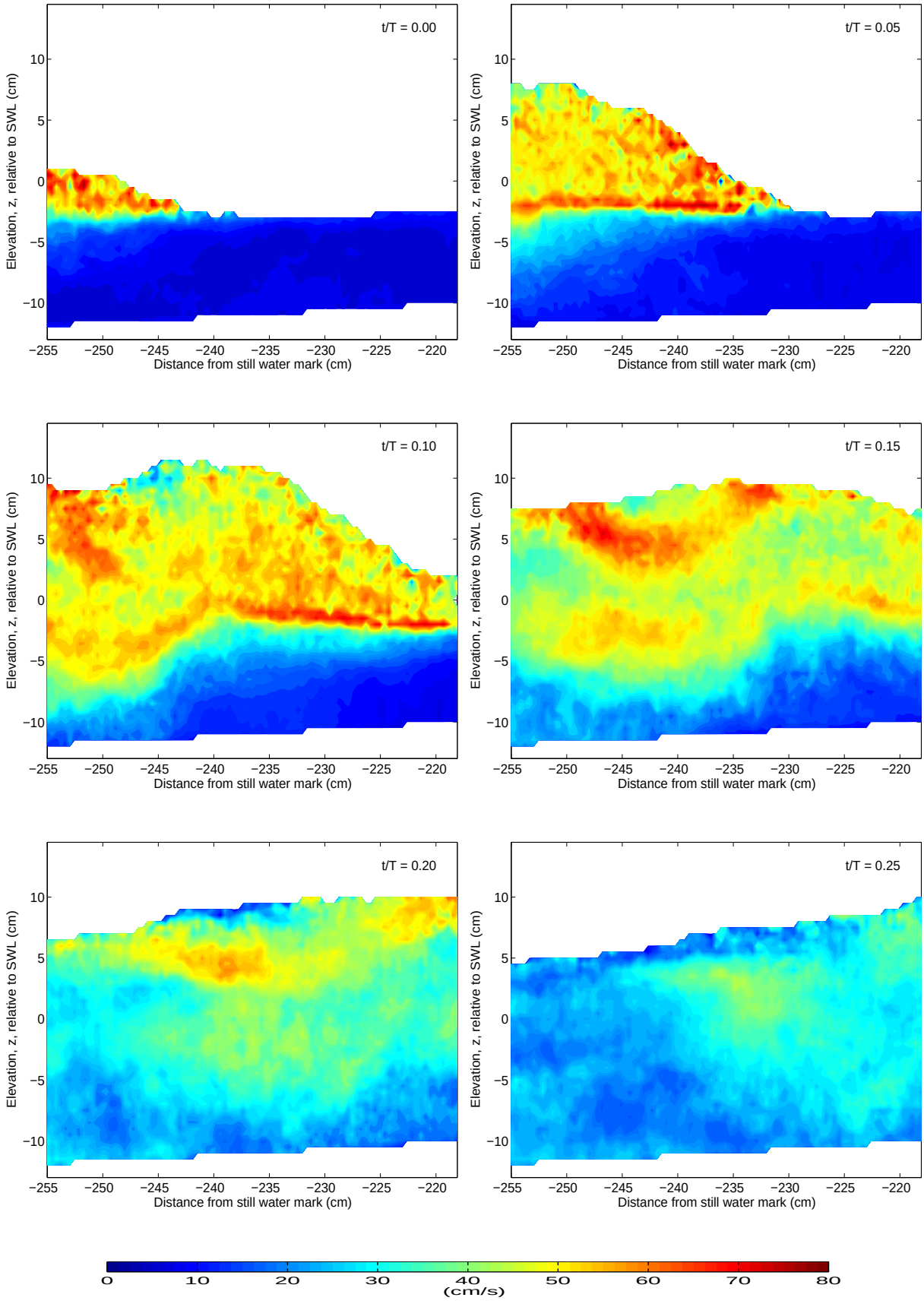

Figure 7.1: Contour plots showing the phase evolution of the horizontal turbulence intensity, u' for the six phases under consideration.

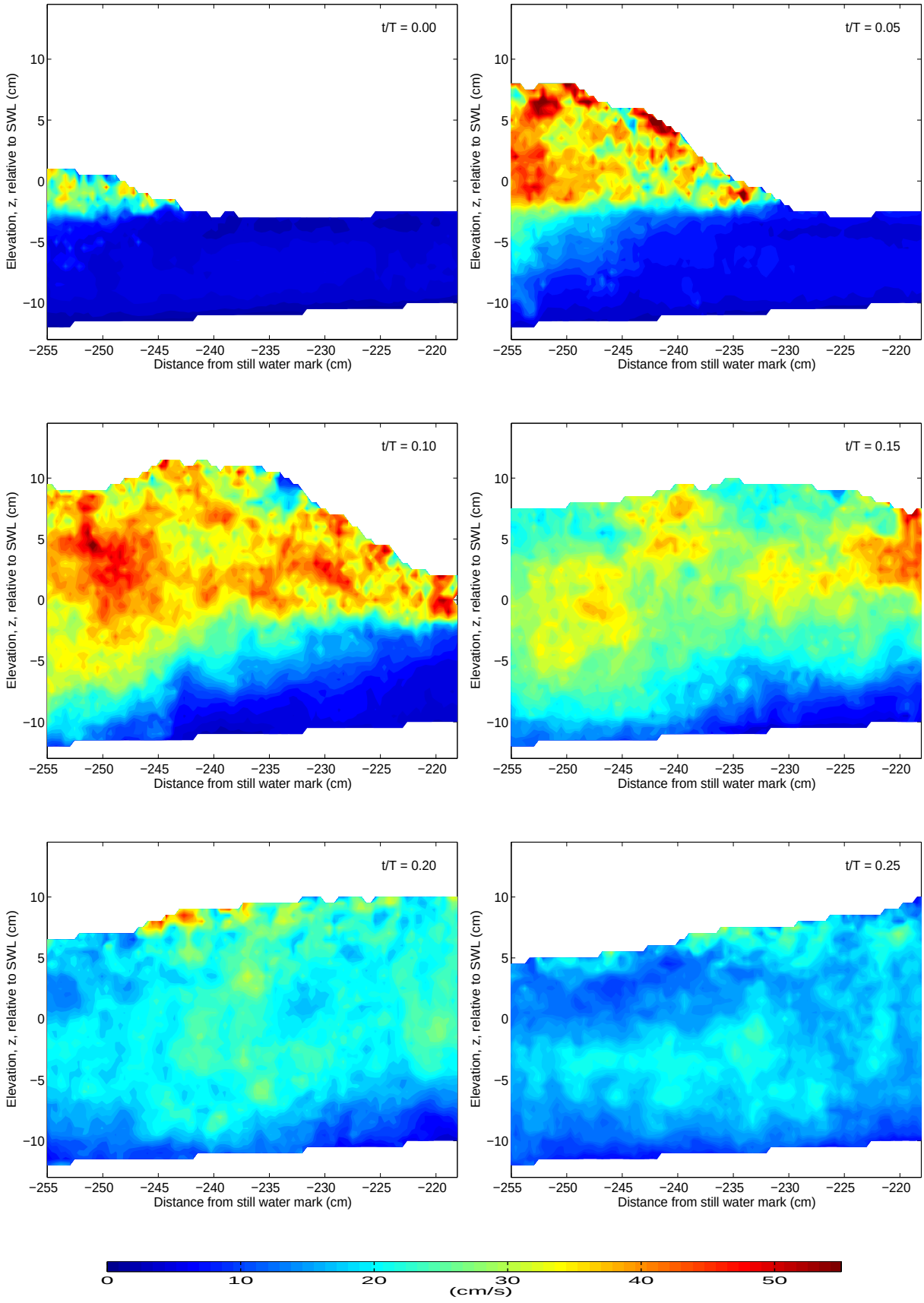

Figure 7.2: Contour plots showing the phase evolution of the vertical turbulence intensity, w' for the six phases under consideration.

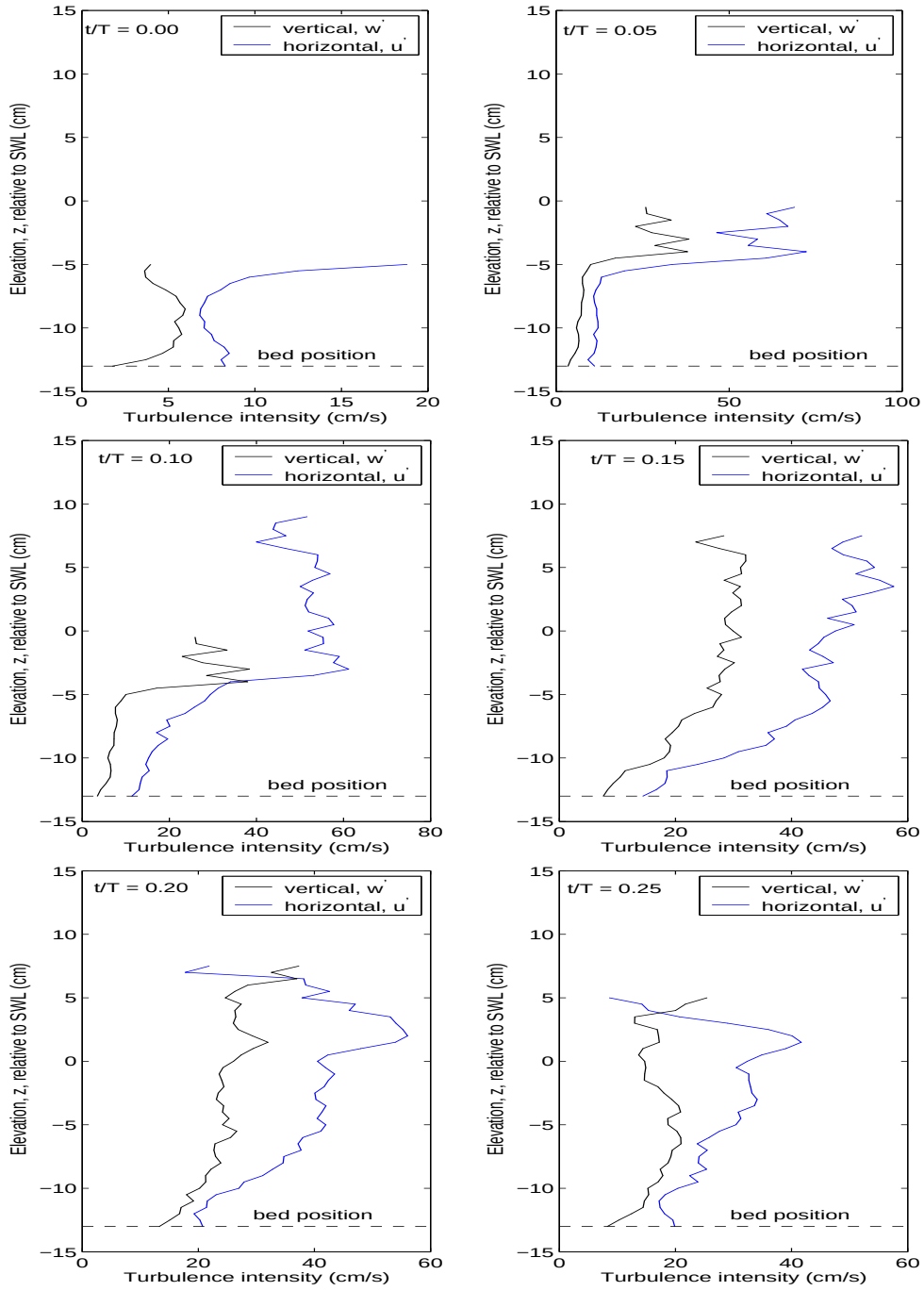

Figure 7.3: Profile of turbulence intensity as a function of depth measured at the center of the panel (at x= -238 cm) at each phase : horizontal component (u') - (black) and vertical component-(w')-(blue).

that turbulence intensity is higher under the wave front, showing a peak, and then decays rapidly after the wave crest passes. As previous researchers (e.g. *Longo et al.* [65]; *Peregrine* [184]; *Christensen et al.* [185]) noted, turbulence in the surf zone is primarily generated in the crest region of breaking waves and secondarily generated in the bottom layer.

Figures 7.6 and 7.7 show phase dependence of both horizontal and vertical turbulence intensity components near the trough level at three separate elevations from the flume bed. These results show that for the elevation in the trough, the variation of both horizontal and vertical turbulence components with phase is almost similar, with the horizontal being higher than the vertical at almost all phases. Both

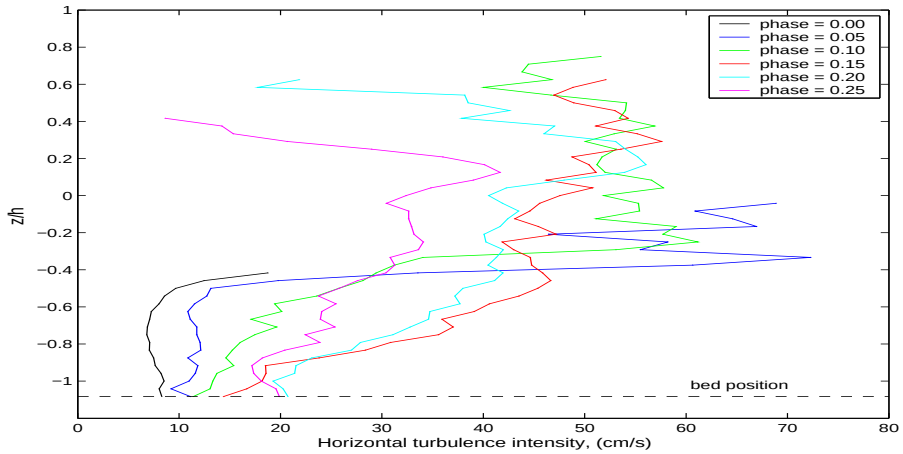

Figure 7.4: Evolution of the vertical profile of u' at x = -238 cm for the six phases as flow progresses.

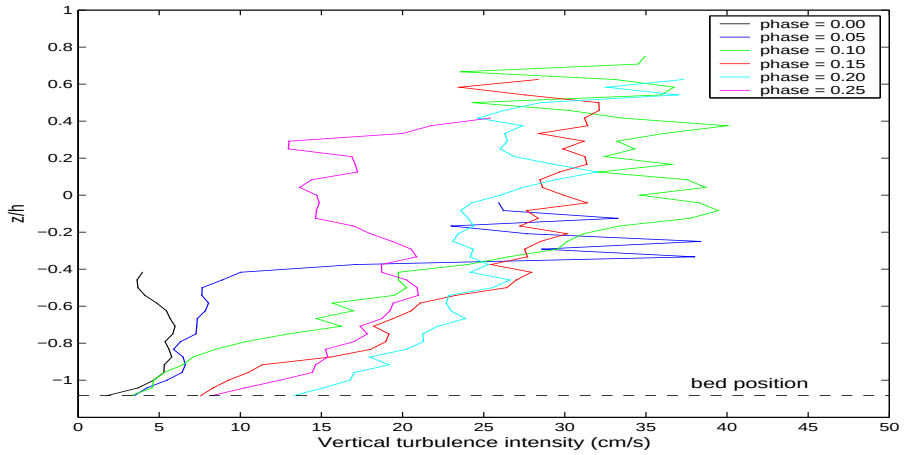

Figure 7.5: Evolution of the vertical profile of w' at x = -238 cm for the six phases as flow progresses.

turbulence components are observed to increase up to peak values at phase 0.15. After phase 0.20, there is a general decrease of both horizontal and vertical turbulence intensities at all elevations as flow progresses.

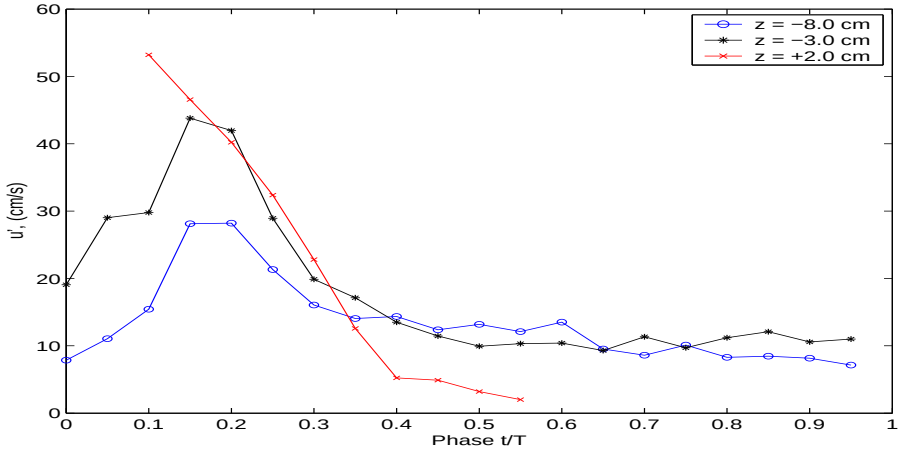

Figure 7.6: Phase variation of horizontal turbulence intensity, u' at different elevations from the flume bed : (blue) - near the bed, x = -8 cm ; (black)- between trough and crest, x = -3 cm, and (red)- near crest, x = +2 cm.

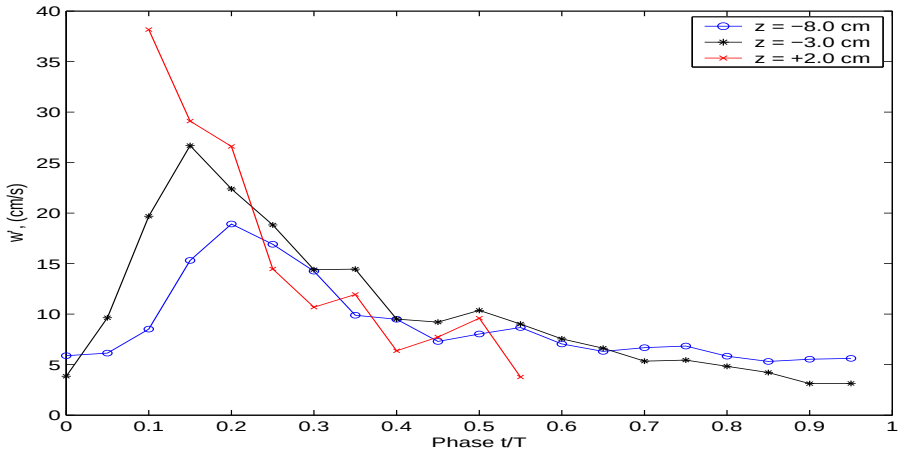

Figure 7.7: Phase variation of vertical turbulence intensity, w' at different elevations from the flume bed : (blue) - near the bed, x = -8 cm ; (black)- between trough and crest, x = -3cm, and (red)- near crest, x = +2 cm.

Figures 7.8 shows a comparison of the variation of turbulence intensity components with phase, for points at elevation z = -3 cm, for all the twenty phases. High horizontal and vertical turbulence intensities are observed during the early phases of the flow (t/T = 0.00 - 0.30). These are the phases of interest in this study. During the early phases of the flow, the horizontal component is higher than the vertical.

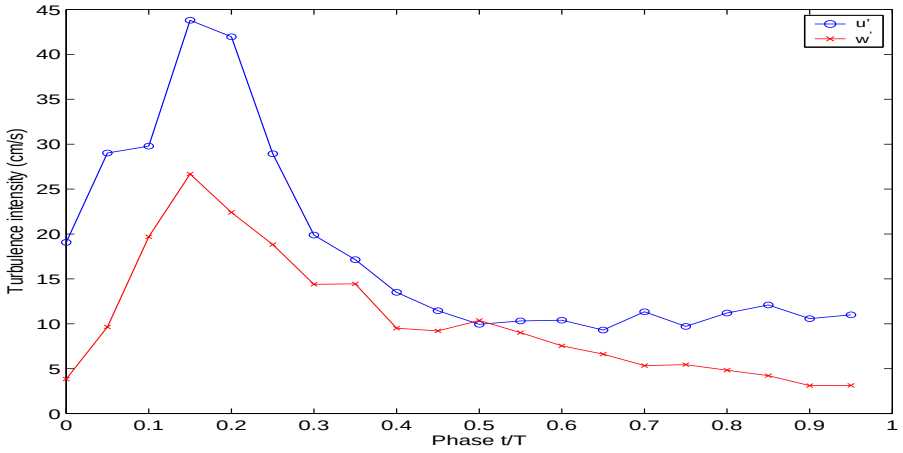

Figure 7.8: Phase variation of turbulence intensity components at elevation z = -3 cm.

Figure 7.9 shows the phase dependence of the ratio of the horizontal intensity to the vertical, $\frac{u'}{w'}$. Whilst there are some variations of this ratio with phase for elevations above z = -3 cm, there is an almost uniform variation of around 1.5 for all phases at elevation z = -8 cm. A much bigger variation in the ratio $\frac{u'}{w'}$ is largest at elevation z = -3.0 cm. Once again the missing data points at some phases imply that the wave profile for those phases was well below that point, so the turbulence intensity components do not exist.

In order to map the structure of turbulence in the plunging breaker, a simple index is considered which links the vertical and the horizontal turbulence components. Figure 7.10 shows the variation with depth of the ratio w'^2/u'^2 measured at x = -238 cm at each phase of the flow. In this plot, the elevation was limited to z/h = -0.2 cm (just below the SWL) so that comparisons could be made with the results of

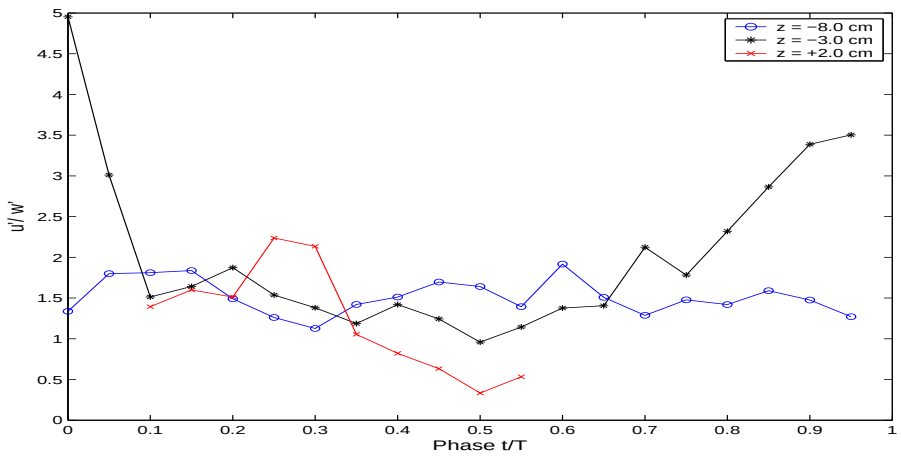

Figure 7.9: Phase dependence of the ratio of horizontal to vertical turbulence intensity components $\frac{u'}{w'}$, at points : (blue)- near the bed (x, z) = (-238, -8) cm ; (black)- between trough and crest (x, z) = (-238, -3) cm and (red)- near crest (x, z) = (-238, +2) cm.

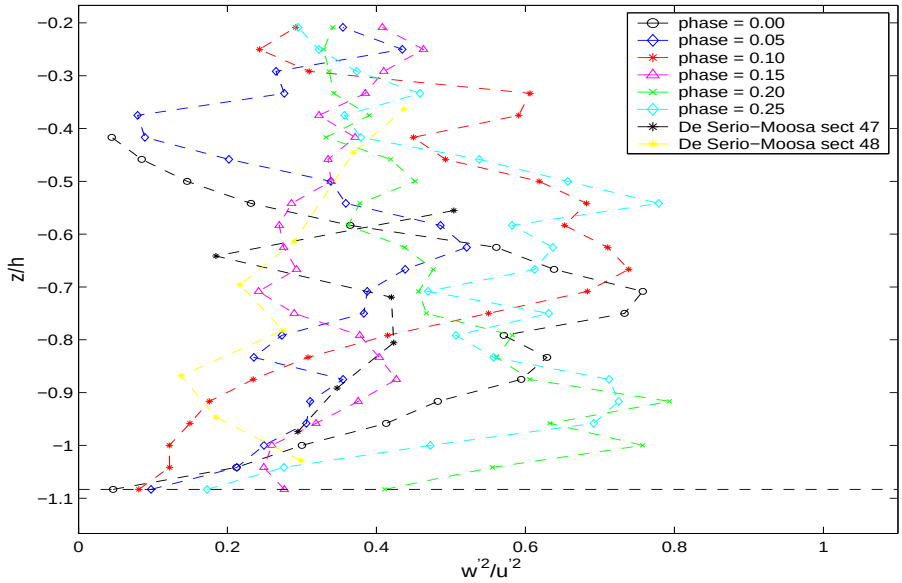

Figure 7.10: Variation with depth of the ratio of horizontal to vertical turbulence intensities, w'^2/u'^2 measured at x = -238 cm at each phase of the flow. Also included for comparisons are plunging wave results by *De Serio & Mossa* [68].

De Serio & Mossa [68]. Below the trough level, the ratio w'^2/u'^2 has peak values of up to 0.8 for phases most phases.The graph shows there is a reasonably good agreement between results from the represent experiment and those of *De Serio & Mossa* [68] for the elevations considered, particularly during the early phases of the flow.

7.2.2 Turbulent kinetic energy

A quantity that characterizes physical transfer of energy in the flume is the fluctuating or turbulent kinetic energy. Using velocity fluctuations extracted from the instantaneous velocity and the mean components, for both horizontal and vertical velocities, turbulent kinetic energy, k', per unit mass is estimated from

the fluctuations as :

$$k' = \frac{1}{2}\left(u'^2 + v'^2 + w'^2\right) \tag{7.2}$$

where u' ,v' and w' are the horizontal, (x), transverse, (y), and vertical, (z), turbulence intensity components in the indicated directions. In measurements such as the one presented here, where only two components u' and w' have been measured, and the transversal component v', missing, partial turbulent kinetic energy is given by :

$$k^* = \left(\frac{u'^2 + w'^2}{2}\right) \tag{7.3}$$

However, if the transversal component v' is missing, turbulent kinetic energy in the surf zone can be estimated as suggested by *Svendsen* [177]:

$$k' = \frac{4}{3}\left(\frac{u'^2 + w'^2}{2}\right) = 1.33\left(\frac{u'^2 + w'^2}{2}\right) \tag{7.4}$$

This means the transverse component is approximated (*Kimmoun* & *Branger* [43]) by :

$$v'^2 = \frac{1}{3}\left(u'^2 + w'^2\right) \tag{7.5}$$

A similar estimation was also used by *Ting* & *Kirby* [30], *Chang* & *Liu* [41], *Shin* & *Cox* [67], *Liiv* & *Lagemaa* [176], *Govender et al.* [78]. As stated by *Svendsen* [177], the value of 1.33 in Eqn. (7.4) is based on the assumption that breaking waves have turbulence characteristics similar to that of plane wakes, where $u'^2 : v'^2 : w'^2 = 0.43 : 0.26 : 0.3$, and hence $k'/k^* = 1.33$. The coefficient does not vary significantly for different turbulent flows, ranging from 1.33 for the plane wake to 1.36, 1.40, and 1.50 for the plane mixing layer, plane jet and homogeneous isotropic turbulence, respectively (*Chang* & *Liu* [41]).

Contour plots of turbulent kinetic energy for the six wave phases are shown in Figure 7.11. These results show that the region of highest kinetic energy levels is confined above elevations z = -5 cm as can be seen for phases 0.00, 0.05, 0.10 and 0.15 with peak values of up to 0.4 m^2/s^2 . This arises from the dominant contribution to k' coming from the horizontal turbulence intensity component. Peak values of k' observed are consistent with results using fiber optic LDV by *Shin* & *Cox* [67] for regular plunging breakers over a rough rigid bottom.

To get a picture of the evolution of the turbulent kinetic energy with depth as flow progresses, the variation with depth, of turbulent kinetic energy for the six phases are plotted on the same axis as shown in Figure 7.12. Results show that k' is concentrated in the wave crest with very negligible energy in the rest of the wave. High turbulent kinetic energy is confined above elevation z/h = -0.5 cm, and decreases with advance of the phase of the flow. After the passage of the crest, k' values gradually decrease with each phase. Turbulent kinetic energy below elevation z/h = -0.5 cm is observed to increase with phase. In agreement with the results of *Ting* & *Kirby* [30], it is observed that higher k' values lie on the front face of the wave, showing a peak that decays rapidly after the wave crest passes. A similar distribution of turbulent kinetic energy with depth was observed by *Yoon* & *Cox* [186]. *Misra et al.* [72] observed that

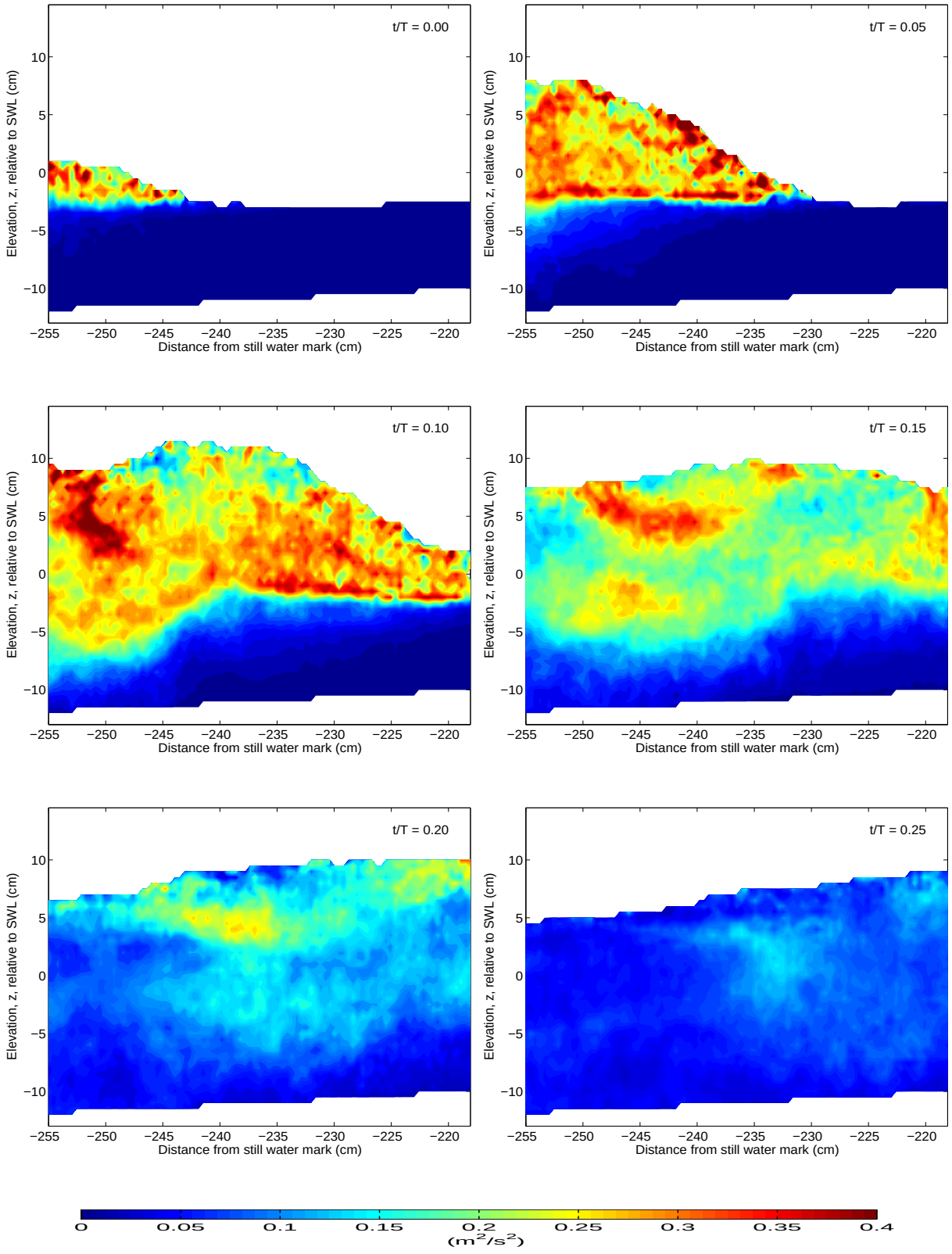

Figure 7.11: Contour plots showing the evolution of turbulent kinetic energy, k', for the six phases under consideration.

the distribution of both horizontal and vertical turbulence intensities are qualitatively very similar to the turbulent kinetic energy distribution and decay monotonically away from the mean surface. *Ting* [187] advocated the notion of k' in breaking waves being transported to the bottom by convection and turbulent

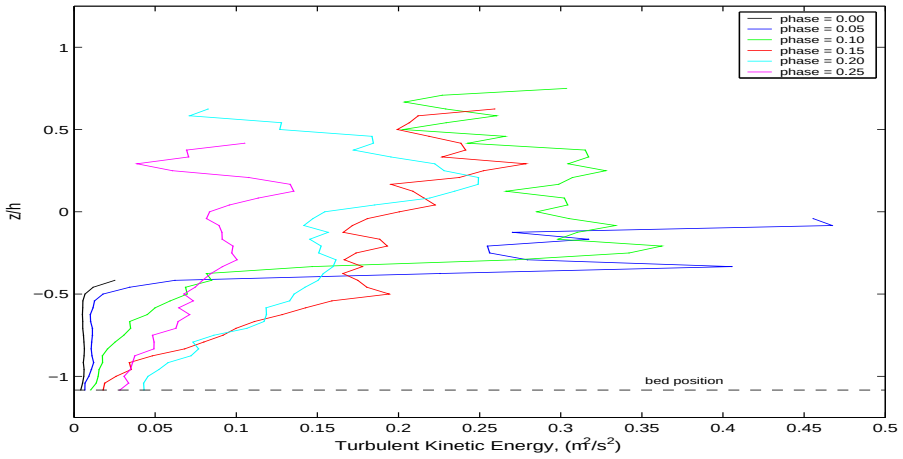

Figure 7.12: Evolution of the vertical profile of turbulent kinetic energy, k', as a function of depth, measured at x = -238 cm as flow progresses.

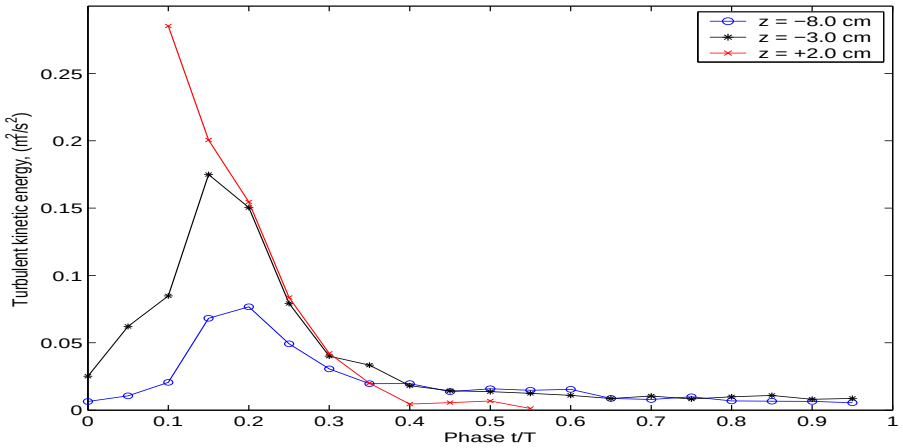

Figure 7.13: Phase variation of the turbulent kinetic energy at elevations z = -8 cm , -3 cm and + 2cm as flow progresses.

diffusion, and transported upwards by the undertow.

Figure 7.13 shows the phase variation of turbulent kinetic energy measured at different elevations for each of the twenty phases in the flow. During the early phases of the flow (0.00 - 0.30), turbulent kinetic energy is observed to increase with elevation from the flume bed. At all elevations presented in the figure, significant amounts of turbulent kinetic energy are observed at phases t/T = 0.05 - 0.30. Very little amounts of turbulent kinetic energy are observed to remain as flow progresses (phases t/T = 0.35 - 0.95). At later phases, 0.35 - 0.55, turbulent kinetic energy at elevation z = +2 cm is observed to be the least of the three. This suggests that turbulent kinetic energy in the flow, initially observed to be dominant near the free surface, diffuses to the flume bed when the crest has passed, and eventually gets dissipated.

7.3 Time-averaged characteristics

Averaging results of turbulence intensities and the turbulent kinetic energy over the 20 phases gives the time-averaged characteristics of the flow. While elevation is normalized by the local water depth, h = 0.12 cm, turbulence intensities are normalized by the wave phase velocity $c = \sqrt{(gh)} = 1.08$ cm/s, and kinetic energies by c^2. Available data in literature consider the flume bed to be at elevation $z/h = 0$, so throughout this section, the bed level is taken as at $z/h = 0$.

7.3.1 Time-averaged turbulence intensity

The variation with depth, of normalized time-averaged horizontal and vertical turbulence intensities, ($\overline{u'}/c$, and $\overline{w'}/c$) are presented in the same plot as shown in Figure 7.14. These were measured at x = -238 cm from the SWL mark. Both turbulence components are observed to increase rapidly from the bed and reaching their maximum values just around the still water level ($z/h = 1.0$) and decreases toward crest level. Peak values of normalized horizontal turbulence intensity of up to 0.2 are observed around $z/h = 1.0$, while for the vertical it is about 0.1 at this elevation. These peak values are observed around the shear boundary layer. This variation is consistent with laboratory observations using LDV by *Cox* & *Shin* [56].

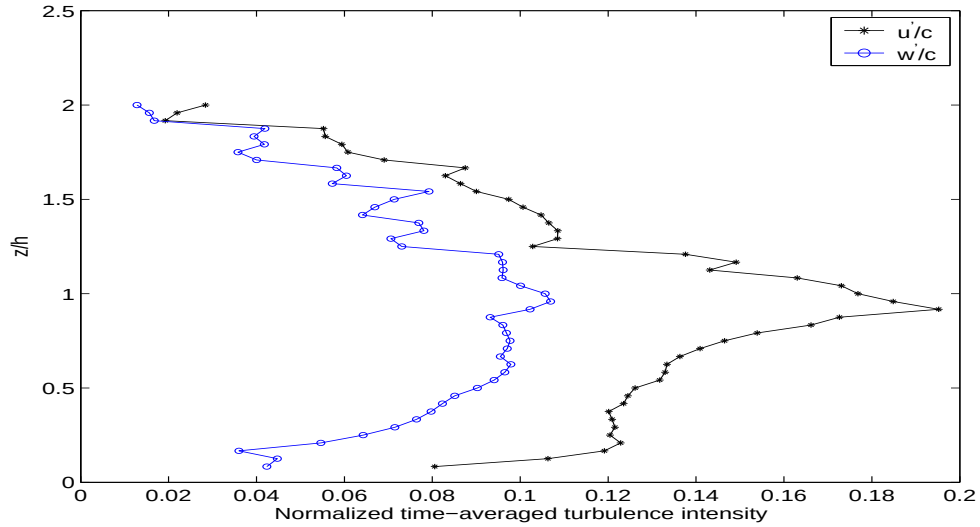

Figure 7.14: Profiles of normalized time-averaged horizontal (∗) and vertical (∘) turbulence intensities measured at x = -238 cm from the SWL mark on the beach at station 12 a. Note that $z/h = 0$ represents the bed level.

Figure 7.15 shows the variation with depth of the ratio of the time-averaged turbulence intensities, $\overline{u'}/\overline{w'}$. For elevations $0.50 < z/h < 2.0$, this ratio is observed to vary between 1.5 and 2.0 and increases to more than 3.5 near the bed and near the crest. Close to the bed, results for the ratio $\overline{u'}/\overline{w'}$ is high, which is expected because the bed constrains the vertical fluctuations (*Sou et al.* [75]). Using LDV techniques *Shin* & *Cox* [67] observed the time-averaged ratio $\overline{u'}/\overline{w'}$ for $z' > 1$ cm to range from 1.30 to 1.69.

Figures 7.16 and 7.17 show profiles of the variation of the normalized time-averaged horizontal and vertical

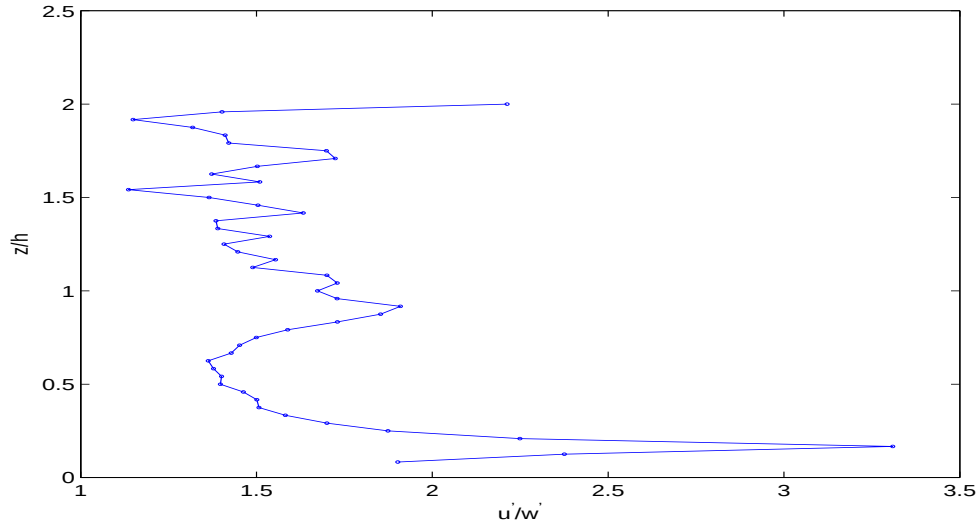

Figure 7.15: Ratio of time-averaged horizontal to vertical turbulence intensities, $\overline{u'}/\overline{w'}$, shown in Figure 7.14, measured at x=-238 cm from the SWL mark on the beach. $z/h = 0$ represents the bed level.

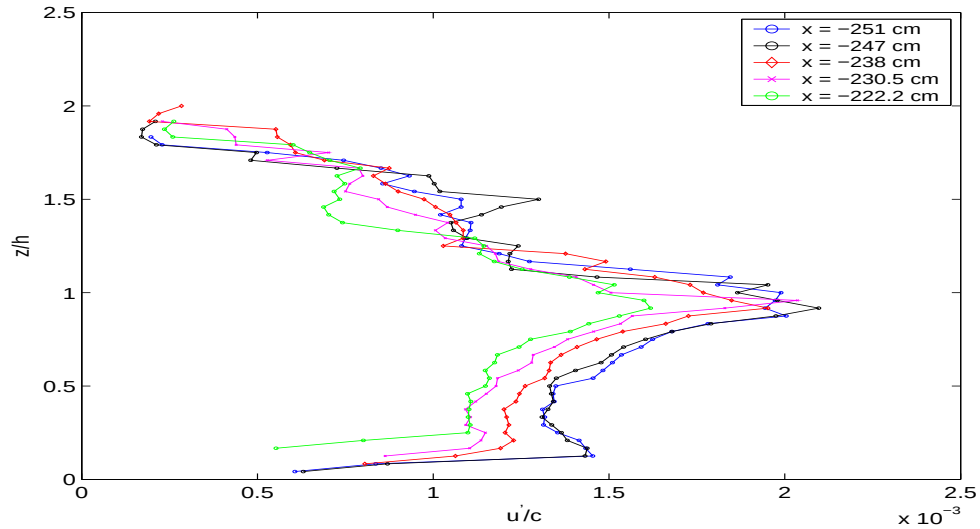

Figure 7.16: Profiles of normalized time-averaged horizontal turbulence intensity, $\overline{u'}/c$ as a function of depth measured at different x - positions within window 12a. $z/h = 0$ represents the bed level.

turbulence intensity components, respectively, as a function of depth for several positions at station 12a. Both horizontal and vertical normalized time-averaged turbulent intensities have peak values around the shear layer, and observed to decrease as flow progresses for elevations below $z/h = 1.0$.

Figures 7.18 and 7.19 show comparisons of the normalized time-averaged horizontal and vertical turbulence intensities, respectively, measured at the center of each of the 5 measurement stations. The plots of time-averaged intensities show that both the horizontal and vertical components increase from the bed upward, reaching maximum values near the approximate trough level and decreasing thereafter. As previously observed by *Svendsen* [177] and *Sakai et al.* [188], the turbulence levels shortly after breaking are generally lower than levels observed further shoreward.

Figures 7.20 and 7.21 show the horizontal variation of the time averaged horizontal and vertical turbulence intensities along the flume, respectively, measured at elevations z = -5 cm, 0 cm and + 5 cm. Horizontal

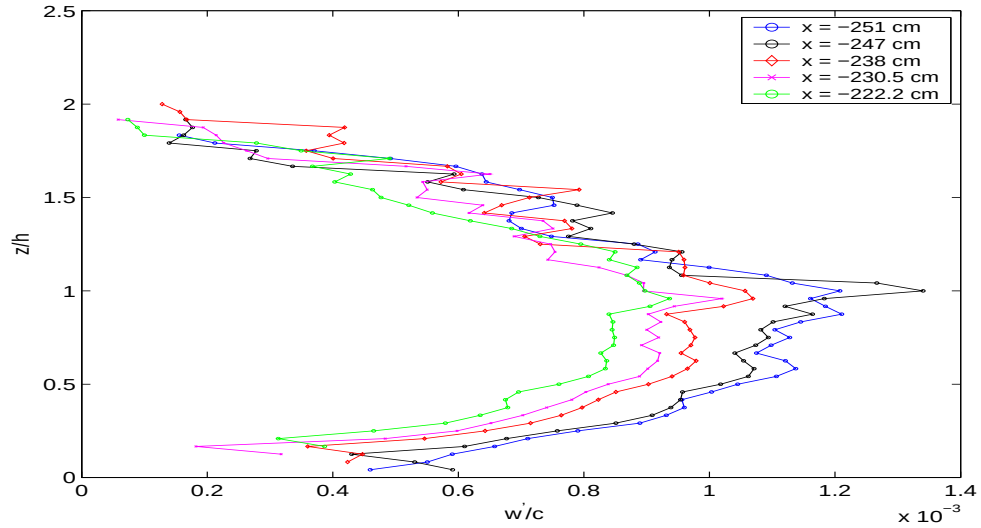

Figure 7.17: Profiles of normalized time-averaged vertical turbulence intensity, $\overline{w'}/c$ as a function depth, measured at different x - positions within window 12a. $z/h = 0$ represents the bed level.

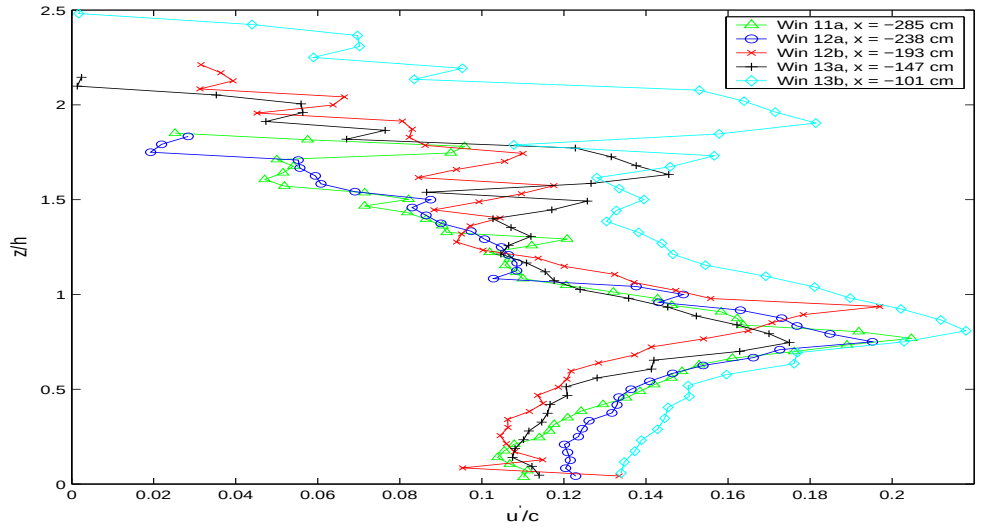

Figure 7.18: Comparison of profiles of normalized time-averaged horizontal turbulence intensity, $\overline{u'}/c$, as a function of depth, measured at five stations located at distances from the SWL mark shown in the legend.

turbulence intensity, u' is maximum at x = -240 cm, decreasing towards the SWL mark on the beach. Both figures show that much higher turbulences are observed elevation $z = 0$ cm for almost all flume positions, compared to the other elevations below and above the shear layer. Comparing turbulence intensities at the three elevations, Figure 7.21 shows that vertical turbulence is least near the crest, at elevation $z = +5$ cm. The vertical turbulence intensity along the flume shows an almost linear decrease from around 10.0 cm/s to about 6.0 cm/s.

7.3.2 Time average turbulent kinetic energy

Figure 7.22 shows the vertical profile of Froude-scaled time-averaged turbulent kinetic energy, $(\overline{k'}/c^2)^{1/2}$ measured at x = -238 cm from the SWL mark. It also shows the measurements of *Ting & Kirby* [38],

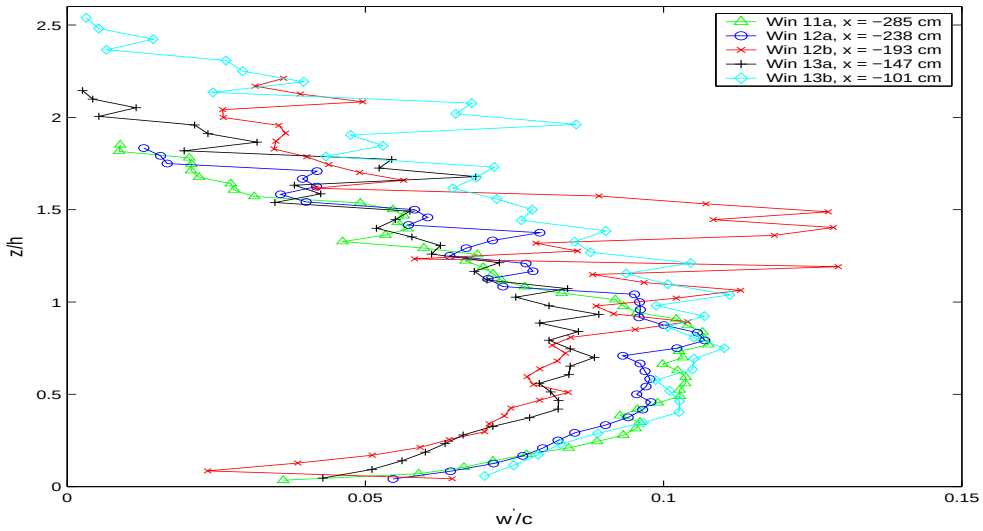

Figure 7.19: Comparison of profiles of normalized time-averaged vertical turbulence intensity, $\overline{w'}/c$, as a function of depth, measured at five stations whose locations from teh SWL mark are shown in the legend.

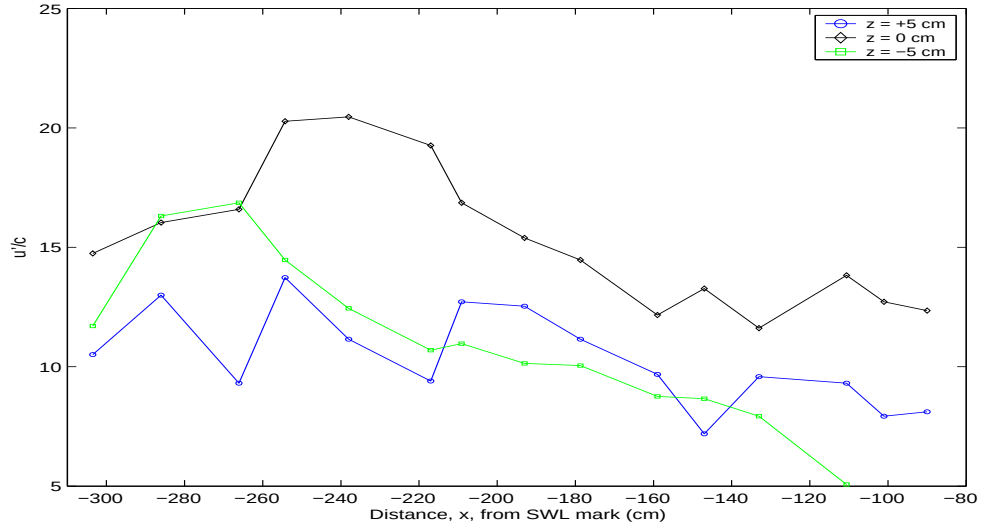

Figure 7.20: Variation of normalized time-averaged horizontal turbulence intensities $\overline{u'}/c$ along the flume at several elevations from the flume bed, relative to the SWL mark on the beach.

Govender et al. [42] and *Okayasu* [189] for comparison purposes. Above the trough level, $\overline{k'}$ increases rapidly, reaching maximum values near the mean water level before decreasing thereafter. Results from the present experiment are almost a factor of two higher and show that from the bed to about $z/h = 0.7$, values of $(\overline{k'}/c^2)^{1/2}$ increase rapidly reaching peak values peak values of 0.23 around elevation $z/h = 1.0$, before dropping to around 0.1 towards the crest. As pointed out by *Govender et al.* [78] this is further evidence that turbulence production occurs in the crest of the wave, where breaking is dominant.

To verify results of time-averaged turbulent kinetic energy presented in Figure 7.22 which were obtained using the phase-ensemble averaging method, a second method was used. This method eliminates errors if any that may be present due to either jitters in the wave maker or by the phase-ensemble averaging method. The method used is explained as follows : For each sequence in a particular phase, instantaneous values of u_i and w_i were averaged at each elevation resulting in a single column of velocities. New

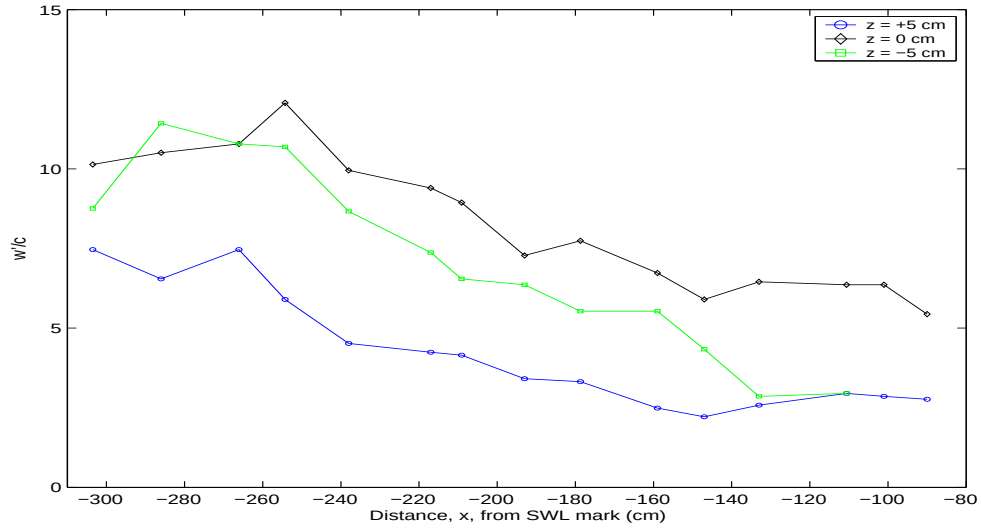

Figure 7.21: Variation of normalized time-averaged vertical turbulence intensities $\overline{w'}/c$ along the flume at several elevations from the flume bed, relative to the SWL mark on the beach.

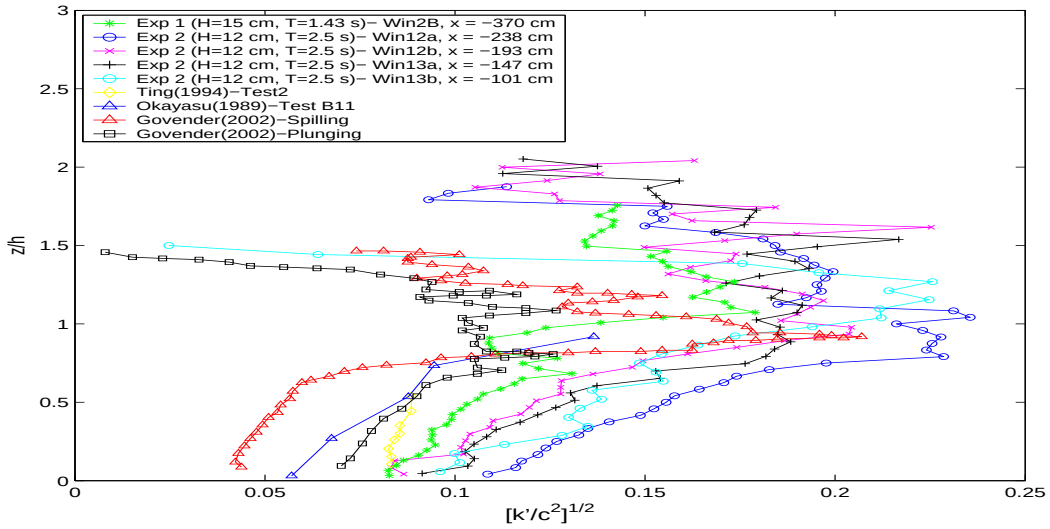

Figure 7.22: Profiles of Froude-scaled time-averaged turbulent kinetic energy, $(\overline{k'}/c^2)^{1/2}$, from different experiments, as a function of depth. x-values in the legend show the location of the measurement stations from the SWL mark. Included for comparisons are results by *Okayasu* [189], *Ting & Kirby* [38] and *Govender et al.* [42].

turbulence intensities u' and w' and the corresponding turbulent kinetic energy k' were then calculated for each sequence in the phase. The procedure was repeated for all the sequences in that phase from which average turbulent kinetic energy $\langle k' \rangle$ was obtained. This was done for all the phases resulting in 20 columns of $\langle k' \rangle$. These 20 columns were then averaged over the phases to get the new time-averaged turbulent kinetic energy, $\overline{k'}$. This was done for all the five stations. The variation with depth of the normalized time-averaged turbulent kinetic energy for the five stations is presented in Figure 7.23. These new results compare very well with the phase-ensemble averaged time-averaged turbulent kinetic energy obtained using the phase averaging method. The Froude-scaled time-averaged turbulent kinetic energy, $(\overline{k'}/c^2)^{1/2}$ was observed to increase almost linearly from the flume bed up to elevation $z/h = 1.2$, decreasing towards the crest. Figure 7.23 shows that $(\overline{k'}/c^2)^{1/2}$ also decreases towards the shore for elevations below $z/h = 1.2$.

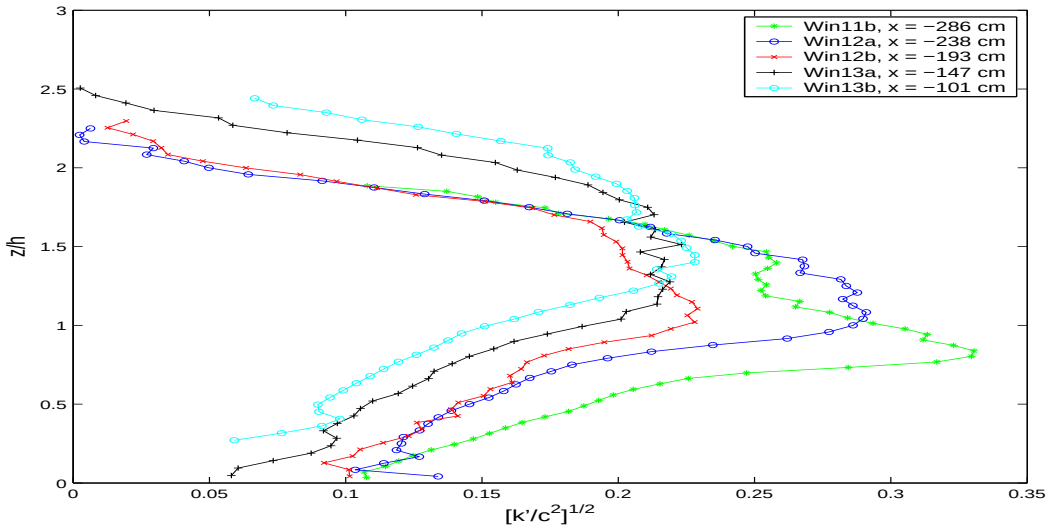

Figure 7.23: Profiles of Froude-scaled time-averaged turbulent kinetic energy, $(\overline{k'}/c^2)^{1/2}$, for the five measurement stations calculated using the 2^{nd} method.

In laboratory experiments involving waves breaking on sloping beaches, one of the fundamental tasks is to determine the characteristics of incident waves, because various experimental results are interpreted in terms of the incident wave parameters. Plunging results are few in literature so it is difficult to do a comprehensive comparison. However, Table 7.1 summarizes wave characteristics used in various experiments whose results are compared in Fig. 7.22. Comparison of our time-averaged turbulent kinetic energy with data that was available shows that results reported here are up to two times higher than the cited references (*Govender* [42], *Stive* [36], *Ting* & *Kirby* [38] and *Okayasu* [189]), especially in the trough section, below elevation $z/h = 0.7$. There are several possible explanations for the observed differences.

Table 7.1: Wave characteristics for experimental results compared in Figure 7.22.

	slope	T (s)	H_o (cm)	h/h_b	$x - x_b$ (cm)	H_b (cm)	h_o (m)	d (cm)	ξ	breaker type
Exp 1	1:20	1.43	16.2	0.711	100	19.5	0.48	15.0	0.28	spilling
Exp 2	1:20	2.5	12.0	0.558	162	21.5	0.62	12.0	0.36	plunging
T & K [38]	1:35	5.0	9.0	0.584	150	19.0	0.40	9.0	0.64	plunging
Govender [42]	1:20	2.5	11.0	0.764	101	16.1	0.77	11.9	0.18	plunging
Okayasu [189]	1:20	2.0	5.2	0.579	-	9.9	0.40	5.0	0.53	plunging

Previous measurements of the plunging breaker have been accomplished using point measuring techniques such as lase Doppler anemometry (LDA) (e.g *Stive* [36]). *Ting* & *Kirby* [38] and *Okayasu* [189] used fibre optic LDA. These LDA measurements have been restricted to positions below the wave trough level because of the sensitivity of these techniques to wave-related aeration. Laser techniques may not be accurate enough to do measurements especially in the plunging breaker where bubbles diffuse to the flume bed. This results in underestimation of turbulence. In their LDA experiments, *Ting* & *Kirby* [38][1] observed that signal dropout occurred when they measured above the wave trough and in the bubble

[1] In Table 7.1, T & K [38] refers to *Ting* & *Kirby* [38]

mass generated by wave breaking. These signal dropouts occurred when the tracker could not follow the velocity changes in the turbulent flow. They then observed that turbulence intensities were 5 % to 10 % higher if data obtained during signal dropout was used, and they interpretted these as invalid measurements. That means if their flow had bubbles in the trough, as the case in these experiments, they took that as an invalid measurement, leading to an underestimation of the turbulence. Measurement results by *Okayasu* [189] for the plunging breaker were only done up to an elevation $z/h = 0.8$, so the comparison is limited to below the wave trough level.

Experimental conditions by *Govender et al.* [42] are very similar to conditions of experiment 2 (Exp 2) reported here, and they also used DCIV techniques to study a plunging breaker. However, their results are also almost half compared to those from the present experiment. One reason could be that although the wave parameters used by *Govender et al.* [42] are similar to those used in these experiments, their wave height at the break point is only ∼17.0 cm compared to 21.5 cm in the present case. Thus the present case results in a more dynamic wave. Secondly, it has been observed that the instantaneous velocity fields by *Govender et al.* [42] for this plunging breaker, have many missing vectors up to 10 % in each instantaneous velocity vector field, even in the trough levels. This may have caused an underestimation of turbulence intensities and ultimately their time-averaged turbulent kinetic energy for the plunging case as shown in Figure 7.22. Thirdly, results from this study show intense vorticity (see Figure 6.4 in Chapter 6) which are observed to diffuse towards the bed for most of the phases. Intense vorticity is an indication that turbulence is high throughout the entire wave, leading to high values of $(\overline{k'}/c^2)^{1/2}$ observed in the trough section of the wave. The intense vorticity indicate high turbulence observed in this study and these eventually cause high k' values in the trough. As a result of some missing vectors, *Govender et al.* [42] may have missed valuable turbulence in this region, leading also to an underestimation of the turbulence in the breaker. Figure 7.24 shows a raw image and its instantaneous velocity vector field for a cycle at phase 0.20. The figure is intended to show high bubble concentrations in the trough section of the wave, supporting the idea of high turbulence though out the entire wave. High velocity vectors are observed throughout the entire wave. This therefore means there is high turbulence even in the trough section of the wave. Similar variations are also observed at other cycles of phase 0.20 and other phases. High time-averaged results obtained below the trough level are therefore consistent with these observations. If LDA and other optical methods are used in a flow such as the one used here, they may not be able to reveal this diffusion. The turbulence induced by breaking wave in crest region has been considered an important source to suspend and transport sediment by wave-induced currents if they penetrate downward as they do in Figure 7.24.

Kimmoun & *Branger* [43] observed maximum turbulent kinetic energies of $(\overline{k'}/c^2)^{1/2} \sim 0.4$ in the front part of the crest above the trough. In the present experiment, observed values below the crest go up to about 0.35 as shown in Figure 7.23. Around the trough level for this experiment, it was observed that this parameter has peak values of up to 0.2. *Ting* & *Kirby* [30] found a maximum value of 0.1 just below the trough, while *Kimmoun* & *Branger* [43] observed values up to 0.3 for the same region. Although the Froude-scaled turbulent kinetic energy results reported here are higher than some results in literature, they are consistent with other observed results.

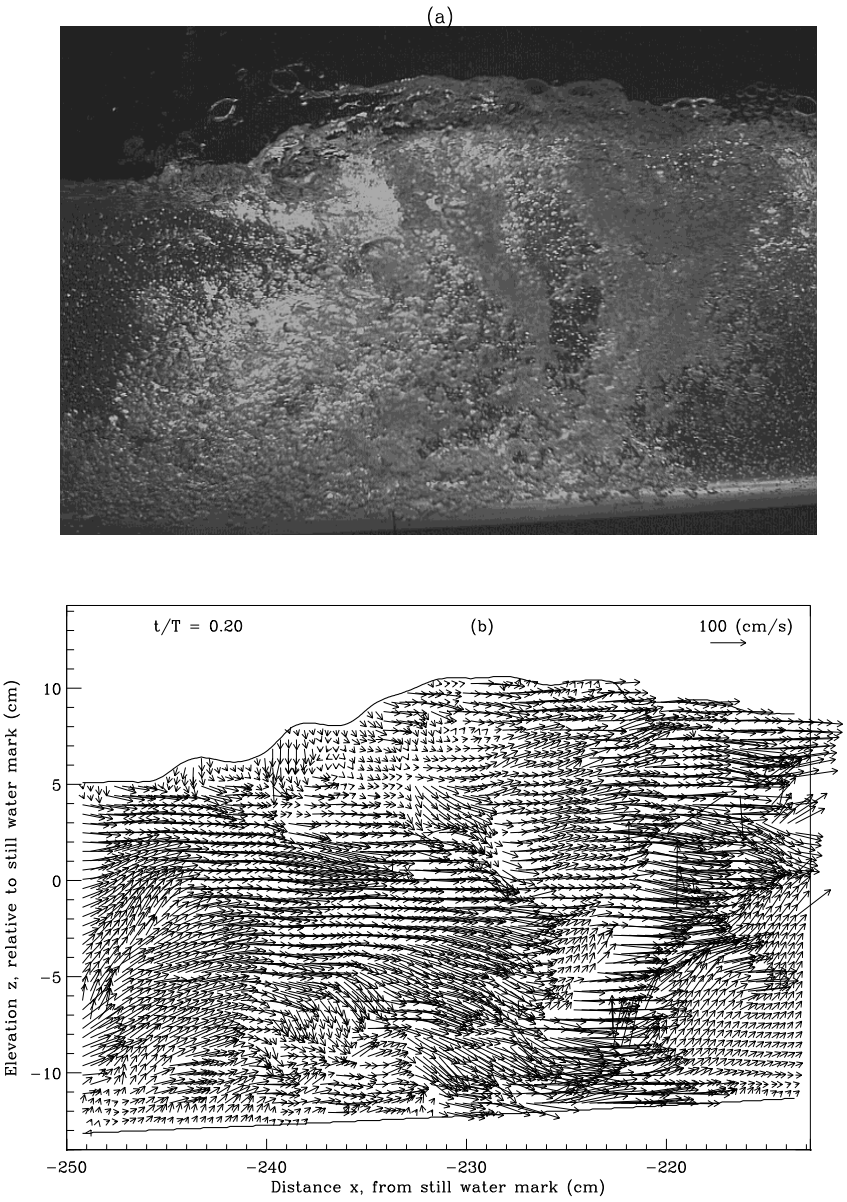

Figure 7.24: (a) Typical image at phase 0.20 and (b) corresponding velocity vector field. High turbulence is observed throughout the entire wave.

Figure 7.25 shows the variation of the Froude-scaled time-averaged turbulent kinetic energy $(\overline{k'}/c^2)^{1/2}$ at three different elevations of z = +5 cm, 0 cm and -5 cm, measured at different stations along the flume. Moving from the deep water towards the still water line mark on the beach, $(\overline{k'}/c^2)^{1/2}$ is highest at elevation $z = 0$ cm, reaching peak values of nearly 0.30 between -300 cm $\leq x \leq$ -220 cm from the SWL mark, dropping sharply to around 0.20 at x = -210 cm from the SWL. A general uniform decrease in the Froude-scaled time-averaged turbulent kinetic energy is observed from x = -210 cm towards the shore at all the three elevations considered.

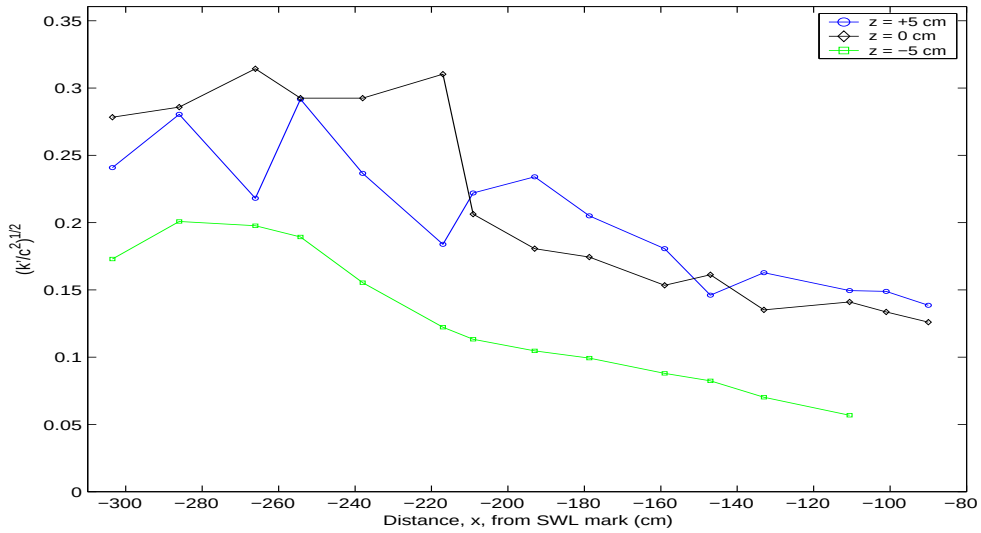

Figure 7.25: Variation of Froude-scaled time-averaged turbulent kinetic energy $(\overline{k'}/c^2)^{1/2}$ at different elevations along the flume.

7.4 Summary

Phase-ensemble-averaged and time-averaged statistics of turbulence intensity and kinetic energy, derived from the instantaneous vector fields have been presented. The spatial variation of turbulence intensity and turbulent kinetic energy for all phases appear to be almost constant below the SWL and increasing rapidly above the trough, reaching maximum values towards the crest. As expected, the turbulence intensity decays rapidly over depth, only to increase near the bottom due to the turbulence generated in the boundary layer. Horizontal turbulence intensity is about twice the vertical for elevations below $z/h = 1.0$. The horizontal and vertical root mean square turbulent velocities above $z/h = 1.0$ are of the same order as the mean velocities, with u' being slightly larger than w'. Peak turbulence intensities and turbulent kinetic energies were found to occur in the front part of the crest of the breaking waves, above elevation z = -5 cm. Quantitative figures of the spatial and temporal distribution of high concentrations of entrained air for plunging breakers indicate that higher concentrations are confined above the still water level. This is in agreement with results obtained by other earlier researchers. The distribution of $\overline{k'}$ is observed to have high values that are confined in upper region of the water column. The Froude-scaled time-averaged turbulent kinetic energy, $(\overline{k'}/c^2)^{1/2}$ was observed to increase almost linearly from the flume bed up to elevation $z/h = 1.0$, decreasing towards the crest. Below elevation $z/h = 1.0$, the time-averaged turbulent kinetic energy also decreases towards the shore. Froude-scaled time-averaged turbulent kinetic energy results obtained in this experiment are consistent with results obtained by *Ting & Kirby* [30] and *Kimmoun & Branger* [43]. However, these are almost a factor of 2 greater than other results reported in literature, even for almost similar experimental conditions. Several possible reasons have been suggested that may arise from an underestimation of the turbulence intensities leading to these observed differences in time-averaged turbulent kinetic energy. Normalized time-averaged turbulence components $\overline{u'}/c$ and $\overline{w'}/c$ and the Froude scaled time-averaged turbulent kinetic energy $(\overline{k'}/c^2)^{1/2}$ show nearly exponential decay towards the shore.

Chapter 8: Vorticity results

Fluid vorticity is a measure of the local spin or rotation of the fluid.

8.1 Introduction

Turbulence is a collection of weakly correlated vortical motions, which, despite their intermittent and chaotic distribution over a wide range of space and time scales, actually consist of local characteristic eddy patterns that persist as they move around under the influences of their own and other eddies' vorticity fields (*Hunt & Vassilicos* [190]). A turbulent flow, consists of high levels of fluctuating vorticity. At any instant, these eddies are present in the flow, ranging in size from the largest geometric scales of the flow down to small scales where molecular diffusion dominates. The eddies are continuously evolving in time, and the superposition of their induced motions leads to the fluctuating time records normally observed. The vorticity vector $\vec{\omega}$, plays an outstanding role in turbulence kinematics and dynamics of the flow (*Wang* [191]). By calculating the vorticity fields from the velocity field it is possible to follow the motion of coherent structures.

The key objective in this chapter is finding these strong vortical events in the turbulent flow. Vorticity analysis not only identifies vortex cores, but also any shearing motion present in the flow (*Adrian et al.* [192]). In order to describe the 2-D configuration of the large scale structure, instantaneous vorticity and vorticity of the mean flow were computed from the instantaneous velocity fields. Vortices or eddies are a characteristic features of turbulence and vorticity is an expression of the angular momentum of the fluid. Angular momentum being a conserved quantity, determines in large part how the fluid moves. Characteristics of the vorticity structures in the turbulent flow, and their evolution as phase progresses are presented. It should however be emphasized that most flows of practical interest are three-dimensional, and vorticity behaves very differently in three dimensions compared to two.

The underlying physical mechanism for this vorticity near the surface was explained by *Sou & Yeh* [12] as follows : The water on the front face must move faster than the propagation speed, hence the formation of a surface roller. On the other hand, the water behind the front face must move slower than the propagation speed, creating a divergence on the surface.

Vorticity is a measure of rotational spin in a fluid and is mathematically defined as the curl of the velocity

field (*Adrian et al.* [192]), given as :

$$\vec{\omega} = \nabla \times \vec{u} = \hat{x}\left[\frac{\partial w}{\partial y} - \frac{\partial v}{\partial z}\right] + \hat{y}\left[\frac{\partial u}{\partial z} - \frac{\partial w}{\partial x}\right] + \hat{z}\left[\frac{\partial v}{\partial x} - \frac{\partial u}{\partial y}\right] \tag{8.1}$$

where $\hat{x}$, $\hat{y}$ and $\hat{z}$ are the unit basis vectors for the three-dimensional Euclidean space R^3, and u, v and w are velocities in the x, y, and z directions, respectively.

8.2 Spatial distribution of vorticity

Vorticity has been described as the principal quantity that defines the flow structure (*Kim et al.* [193] and *Wu et al.* [194]). The velocity measurements obtained allowed the computation of instantaneous and mean flow vorticity components.

8.2.1 Instantaneous vorticity, ω_y

In-to-plane vorticity is easily derived from the measured velocity flow fields. Considering a two-dimensional fluid flow in the $x - z$ plane, whose velocity field is confined to a plane, the vorticity component, ω_y, which points in the orthogonal y-direction reduces to (*Sou & Yeh* [12] :

$$\omega_y = \frac{du_i}{dz} - \frac{dw_i}{dx} \tag{8.2}$$

where the index i denotes instantaneous velocities.

Instantaneous vorticity fields were computed from derivatives of the instantaneous horizontal, u_i, and vertical velocity, w_i components, using the central difference method (*Sou & Yeh* [12]; *Lee & Lee* [195]) as follows :

$$\omega_y = \frac{u_i(i, j+1) - u_i(i, j-1)}{2\Delta z} - \frac{w_i(i+1, j) - w_i(i-1, j)}{2\Delta x} \tag{8.3}$$

where Δx and Δz are the x and z-grid spacing, respectively and i and j are integers. Thus the instantaneous vorticity normal to the plane of the light sheet was obtained at each grid point by calculating the circulation. Figure 8.1 shows the grid points in a velocity mesh used for the calculation of vorticity at a particular point. The four yellow-shaded grid points were used to numerically estimate the vorticity at point (i, j). This vorticity was computed by the circulation around squares of 5.0 mm $\times$ 6.5 mm. To fully resolve the full turbulent vorticity field and reveal smallest scale structures of the flow may require a finer resolution.

Figure 8.2 shows the contour plots of instantaneous vorticity that reveals the evolution of the different vortex structures and vorticity fields. These plots were obtained from the instantaneous velocity fields presented in Figures 6.3 - 6.4 which are instantaneous velocity fields for those images shown in Figure 6.2.

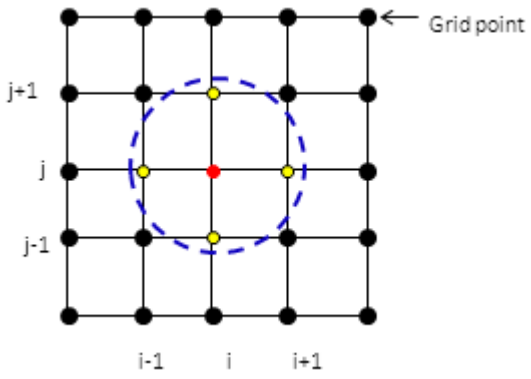

Figure 8.1: Velocity mesh grid used for the calculation of vorticity at point (i, j).

These six snapshots of vorticity field are here presented to best illustrate spatio-temporal evolution of near-surface eddies during the passage of the wave crest. The colour bar shows the magnitude and direction of the vorticity. Positive vorticity indicates motion in clockwise rotation and the direction is into the plane of the figure, while negative vorticity indicates anticlockwise rotation with direction out of the plane of the figure. Positive vorticity has been conveniently taken to point in the positive y direction. Red-filled contours indicate clockwise or positive vorticity whereas the blue-filled contours represent counterclockwise or negative vorticity.

The presence of high-frequency vorticity patches near the water surface, shows that wave breaking that occurs at the free surface is the major source of vorticity in the flow. It can be observed that the instantaneous vorticity distribution is extremely patchy, with isolated pockets of high and low vorticity. These patches begin to appear near the toe of the breaker as observed at phase 0.00. In between the patches and below the SWL are large expanses with nearly zero vorticity. Results also show the presence of pairs of counter-rotating fluid patches with peak vorticity of magnitude 150 s^{-1}. These patches have only been shown to exist, but it is not clear the mechanism by which they are set up. However these high vorticity eddies dissipate the remaining wave energy. It is the interactions between these adjacent counter-rotating eddies that produce a wake of complex vortex distribution behind the wave crest. These pairs have almost similar orientation in the flow. *Bakewell & Lumley* [196] and *Aubry et al.* [197] used the proper orthogonal decomposition in the near wall region and determined that a pair of counter-rotating streamwise vortices contain the largest amount of energy. *Ting* [198], [199] used PIV to study instantaneous turbulent velocity fields associated with a broken solitary wave on a plane slope and also observed that large eddies were composed of two counter-rotating vortices. Peak values of instantaneous vorticity are observed to decrease as flow progresses.

As the flow progresses, patches of intense vorticity are observed to be generated at the free surface and are observed to diffuse to the bottom of the flume reaching the bed after the crest has passed (phases 0.20 and 0.25). This may be an indication that large eddies in the flow become unstable and degenerate into moderate-scale structure of the main turbulent motion. Eddies with anticlockwise vorticity are observed to disappear as a result of mixing leaving the fluid volume mainly filled with clockwise vortex structures. According to *Longuet-Higgins* [200], vorticity is generated at the free surface with intensity proportional

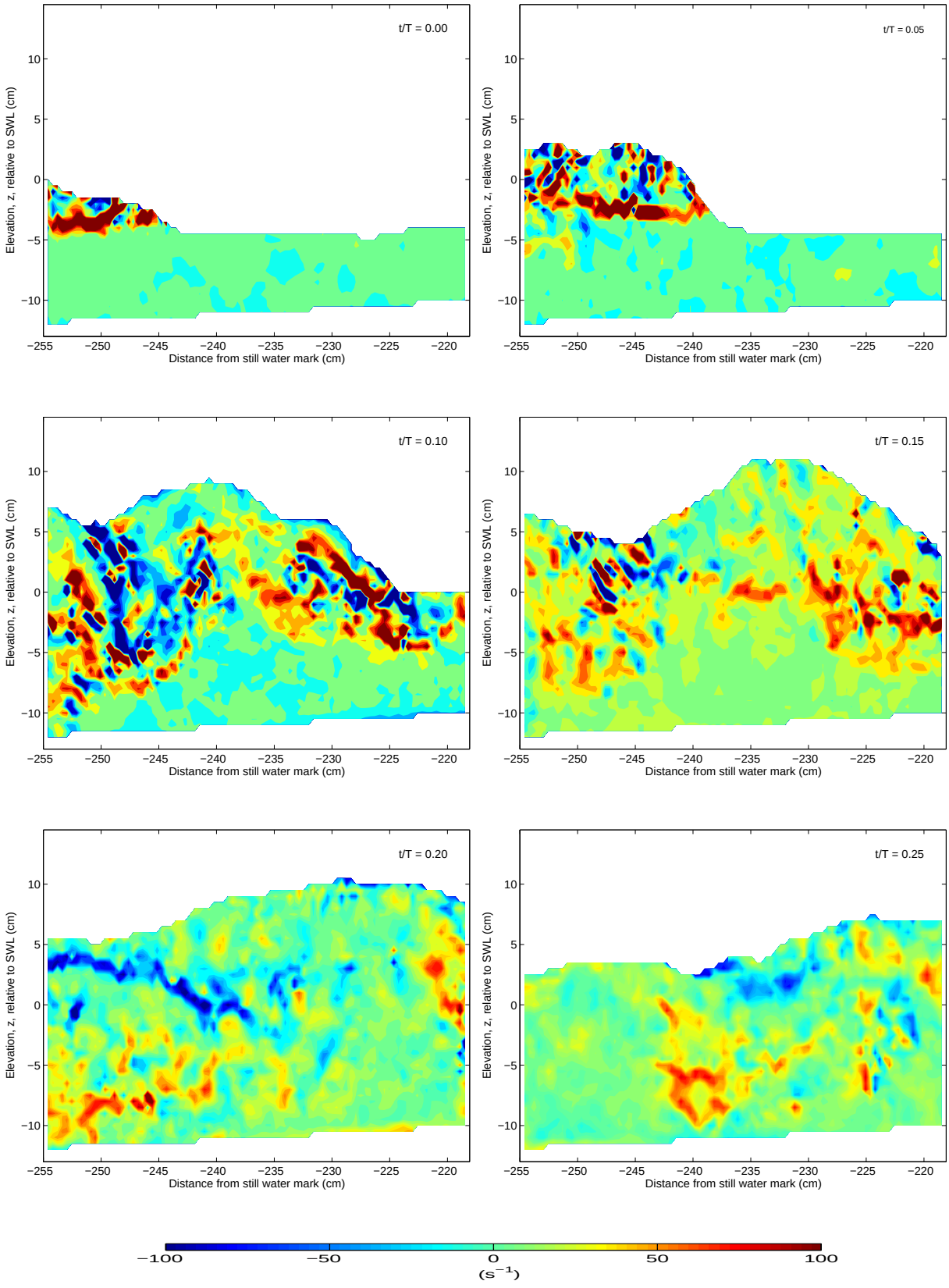

Figure 8.2: Typical contour plots showing the phase evolution of instantaneous vorticity, ω_y, for breaking wave images given in Figure 6.2.

to the tangential velocity and local curvature. Steepening of the wave naturally induces high curvature and consequently strong vorticity. The vortex structures deepen and diffuse towards the bottom as shown in phases 0.10 - 0.25. As pointed out by *Longo* [66] deepening is quite fast immediately after breaking and is slower at subsequent phases. *Nadaoka et al.* [201] observed that the large eddies are initially two-dimensional, but break down into three-dimensional eddies descending obliquely downward.

Saddle points near the crest are characterized by strips of strong obliquely descending positive and negative vorticity below them, which can be observed near the saddle points for $\frac{t}{T}$= 0.10 - 0.20. These eddies first observed at about x = -250 cm for phase 0.10 originate from the free surface and advect horizontally in the direction of wave propagation. They are an indication of strong mixing taking place there. It has been reported that two compact vortices of the same sign rotate around each other, while two vortices of opposite signs translate as a unit *Jimenez et al.* [202]. As flow progresses, these patches of counter-rotating vorticity interfere with each other by viscous vorticity cancellation leaving dominantly positive vorticity in the flow which diminish in magnitude with a relatively uniform distribution behind the crest. This cancellation is the key mechanism for the decay of two-dimensional vorticity distributions. While the energy moves to larger scales by amalgamation, the vortex debris being generated during shedding cancels with other structures of the opposite sign by viscous diffusion.

It is possible to make some rough estimate of the characteristics of the vortex structures in the flow, e.g. the vortex core radius, vortex length and velocity of the vortex between frames as the structures travel downstream in the flow. These strips are estimated to have length scales that stretch up to 12 cm and a typical mean vortex core radius of about 1 cm. In the contour plots a large clockwise vortex structure of magnitude about 60 s^{-1} is observed which is centered around (x, z) = (-250, -7) cm at phase 0.20, and is observed to develop into a vortex ring that has moved to position (x, z) = (-239, -7) cm in the plot of phase 0.25. Thus the vortex moves about 10 cm in 1.84 s so that roughly the vortex structures in the flow propagate at 6 cm/s. The wave speed is nearly twenty times the vortex speed, meaning that it would take the vortex twenty wave periods to move a wavelength. In agreement with observation by *Kimmoun & Branger* [43] the eddies associated with the flow under study are observed to be advected obliquely towards the bottom and moves slower than the wave crest. This type of plunging breaker generation produces a thin higher-velocity free-surface fluid layer that decelerates just prior to breaking, thus injecting a large amount of vorticity into the fluid bulk, entirely through a viscous process.

Figure 8.3 shows in one frame, the evolution of profiles of instantaneous vorticity with depth as flow evolves. From the flume bed up to the SWL, vorticity is about zero and increases to peak values of over 150 s^{-1} just above the SWL before dropping to negative vorticity values towards the top of the crest. In agreement with observations by *Misra et al.* [72], it is also observed that the variations of the instantaneous vorticity profiles with depth show well defined peaks, indicating coherent vortical motions in the shear layer.

Figure 8.4 shows instantaneous vorticity contours under the wave crests measured at five different cross-shore positions along the flume, corresponding to the five measurement stations. The position of the bed is different in each figure. While the size of counter-rotating vorticity patches decreases towards the shore,

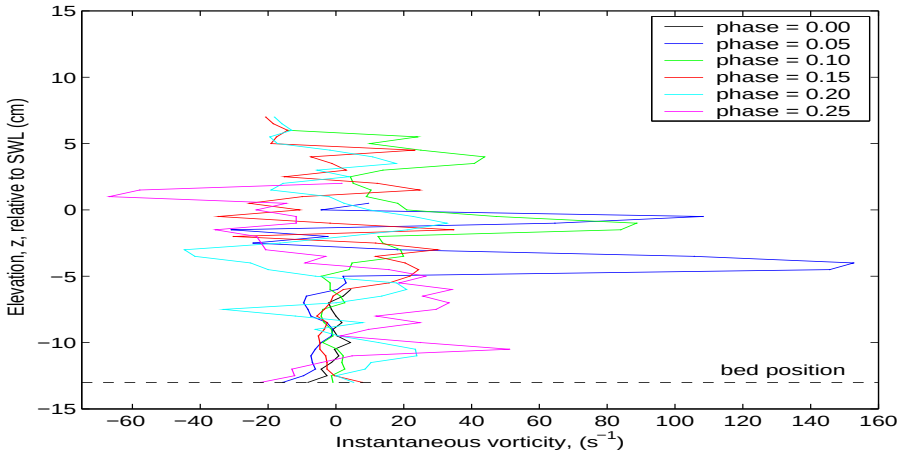

Figure 8.3: Profiles of instantaneous vorticity ω_y as a function of depth, measured at x = -238 cm as flow progresses.

the intensity is observed to increase. This may again be caused by increased resolution used towards the shore, which enables the identification of small but equally intense vorticity patches in the flow. Both negative and positive vorticity of magnitude up to 100 s^{-1} can be observed impinging the flume bed as flow progresses. Such high vorticity fluid elements are responsible for lifting sediments from the bed and transporting them. Statistics on the number of high vorticity patches impinging the bottom and their magnitudes can be determined and is vital information in sediment transport studies.

8.2.2 Mean flow vorticity

Vorticity of the mean flow is the transverse vorticity component calculated from the phase averaged velocity components $\langle u \rangle$ and $\langle w \rangle$, given by *Sou and Yeh* [12] as :

$$\langle \omega_y \rangle = \frac{d\langle u \rangle}{dz} - \frac{d\langle w \rangle}{dx} \tag{8.4}$$

This vorticity was estimated from the derivatives of the phase-ensemble averaged velocity components, using the central difference method that calculates circulation, as follows :

$$\langle \omega_y \rangle = \frac{\langle u(i,j+1) \rangle - \langle u(i,j-1) \rangle}{2\Delta z} - \frac{\langle w(i+1,j) \rangle - \langle w(i-1,j) \rangle}{2\Delta x} \tag{8.5}$$

Figure 8.5 shows contour plots of the variation of mean flow vorticity for the six phases of interest. The plots show that mean flow is characterized by a single, strong vortex located below the crest, at the shear boundary layer. By averaging over many images similar to that shown in Figure 8.2, the ensemble-averaged concentration field can be obtained, as shown in Figure 8.5. This distribution varies smoothly in space with moderate spatial concentration gradients, in contrast to the patchy instantaneous distribution. The mean flow vorticity is about a factor of 3 smaller than the instantaneous vorticity. During the early phases of the flow, there is a concentrated region $\sim$ 5 cm thick of positive vorticity in the breaker shear layer. This positive vorticity was due to the shear generated by the high-speed surface

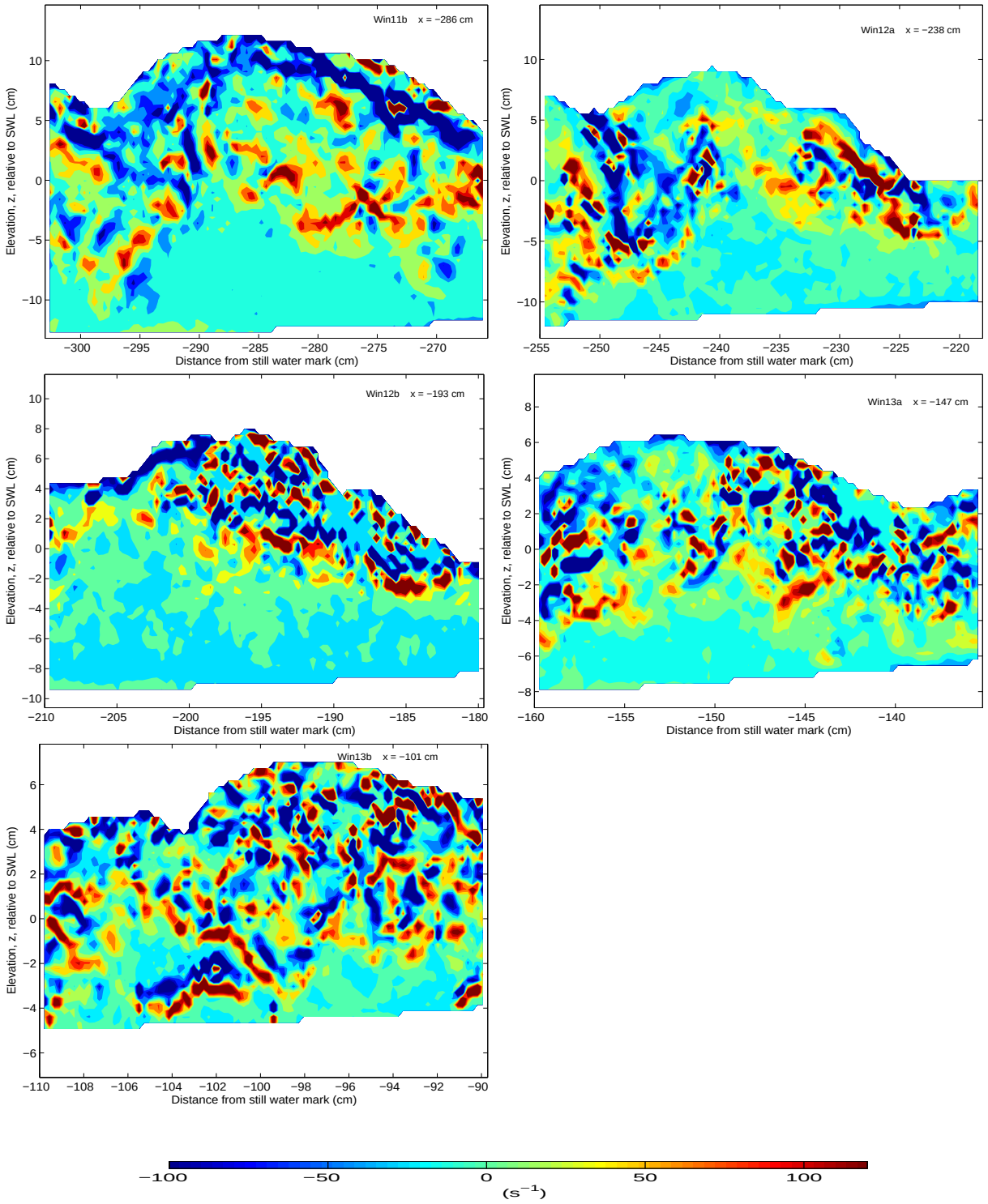

Figure 8.4: Contour plots of instantaneous vorticity, ω_y, under the wave crests, measured at the five stations.

layer overlaying a slower layer of fluid (*Misra et al.* [29]). The co-rotating instantaneous eddies observed earlier get coalesced to become a larger and stronger single vortex. The shear layer was earlier seen to arise from opposing flow of the fast moving mixture of crest water/bubbles and the slow moving water near the trough. The formation of the positive vortical layer represents shear resulting from the incoming uprush flow and receding downwash flow.

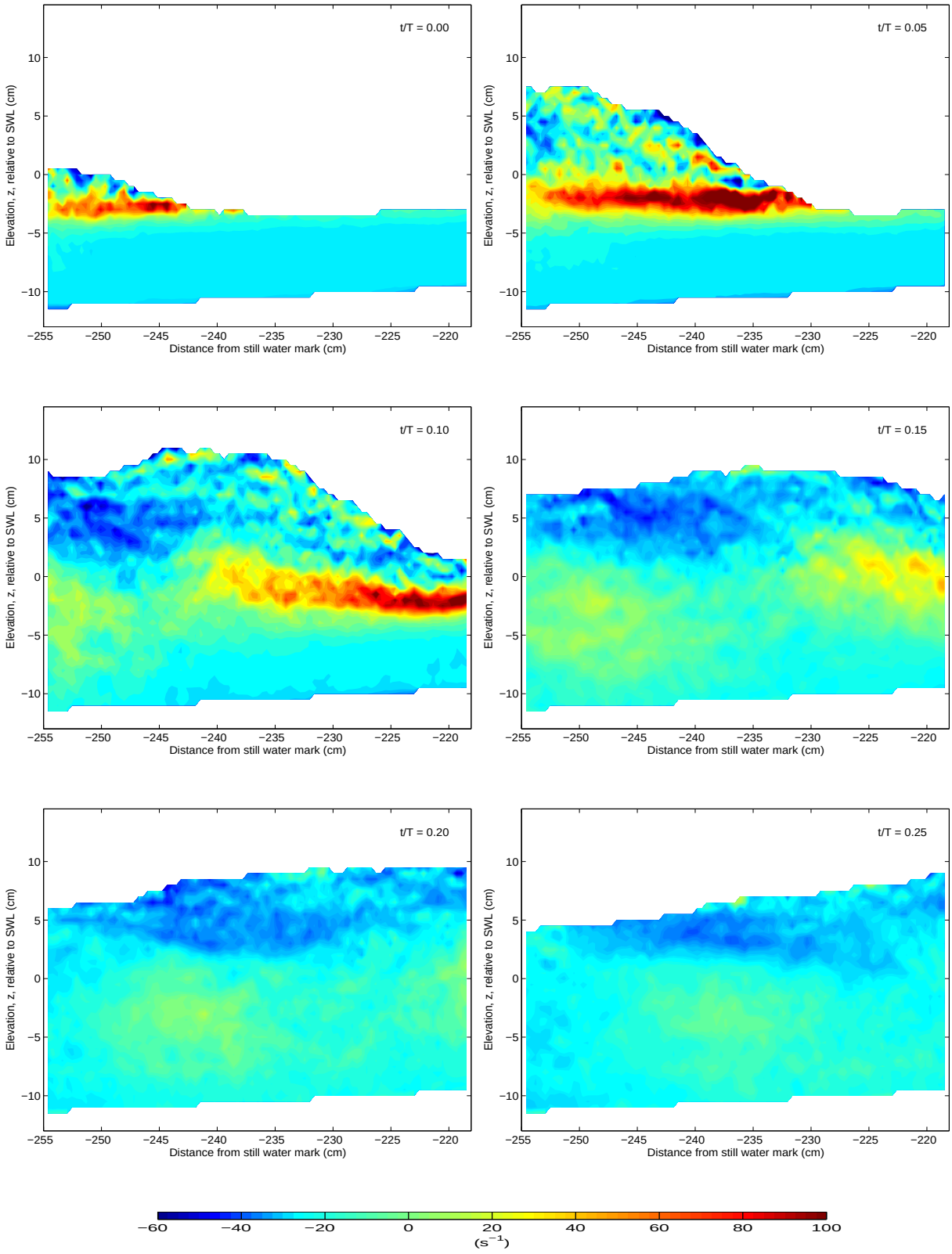

Figure 8.5: Contour plots showing the evolution of the vorticity of the mean flow.

Averaging the instantaneous data makes small scale eddies vanish so the contours of the mean flow vorticity, $\overline{\nabla \times \vec{u}}$, show the development of large scale structures within and around the shear layer, which develops and moves downstream. The fluid beneath the elevation of z= -5 cm is relatively vorticity-free

for the first two phases but for the last, it is observed that positive vorticity diffuses downwards towards the flume bed. As can be observed for phases 0.10 to 0.25, the fluid immediately behind the crest, at elevations centered around z = -5 cm, is characterized by negative vorticity that ride above positive vorticity. As pointed out by *Dabiri & Gharib* [203] the negative vorticity seen on the wave, below the surface, and above the positive shear layer above $z = 0$ cm, indicate the existence of a stagnation point at that location. In agreement with observations by *Sou & Yeh* [12] the maximum intensity of vorticity occurs around the shear layer and the intensity decreases in magnitude as flow progresses. It is also interesting to note that even though the flow between the shear layer and the free surface is turbulent, its vorticity field is quite weak with respect to the vorticity within the shear layer. This is consistent with observations by *Lin & Rockwell* [54]. Thus maximum positive vorticity will remain in the shear layer region between the upper, faster moving part of the breaking wave and the quiescent region below.

The contour plots also reveal the phenomenon of vorticity shedding at later phases of the flow in which the tail of the initially strong boundary layer vorticity breaks up or peels off, weakens and diffuses from the shear boundary layer, reaching the flume bed as phase progresses. This results in bleeding most of the vorticity from the neighbourhood of the initially stronger region (*Jimenez* [202]). The original layer breaks in this way into approximately circular cores. The strong negative vorticity patches near free surface directly above regions -255 cm$< x <$ -242 cm for phase 0.10, and -242 cm $< x <$ -232 cm for phase 0.15 may be responsible for the vortex shedding observed. The turbulent flow studied here is also in some sense a decaying flow since the mean flow vorticity and root-mean-square velocity decrease slowly with time or phase. The explanation for the observed decay is that at later phases, the effects of small-scale mixing due to the strong turbulence in the flow have greatly reduce the presence of patches of vorticity in the flow. It was shown by other researchers (e.g *Stanely* [204]), that while the large scales in the flow field adjust slowly to variations in the local mean velocity gradients, the small scales adjust rapidly. Intense vorticity structures are observed inside the shear layer region, which is the interface separating the turbulent and the irrotational flow regions. Near the trough level, there are occasional regions devoid of strong vorticity.

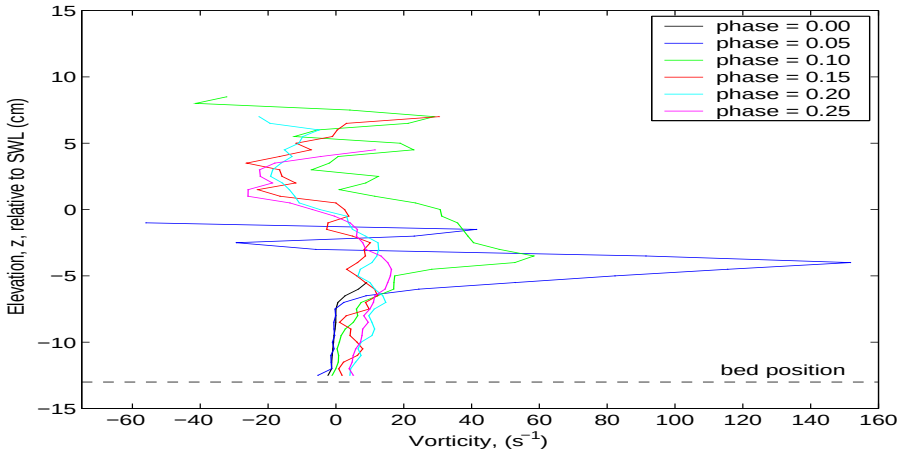

Figure 8.6: Profiles of the evolution of vorticity of the mean flow as a function of depth, measured at x=-238 cm as flow progresses.

Figure 8.6 shows the vertical variation of the evolution of mean flow vorticity in one frame, measured

at x= -238 cm, as phase progresses. From the flume bed up to an elevation of z = -5 cm, mean flow vorticity is about zero and increases sharply to peak values of about 150 s^{-1} just above this elevation, before oscillating between -20 s^{-1} and 20 s^{-1} towards the crest. Peak vorticity is observed near shear-layer as a result of the interaction between the downwash and uprush flows. The flow below the shear layer remain relatively irrotational for early phases of the flow. These results are also consistent with phase averaged vorticity results by *Sou & Yeh* [12] who observed that in the surf zone, the maximum intensity of vorticity occurs at the shear layer, with peak values of up to 200 s^{-1}. They also observed that an internal flow circulation is generated at the flow reversal phase as the flow near the bed responds to the gravitational force earlier than the flow in the upper water column, where the uprush momentum is sustained later in phase. Similar to results presented here, they also observed that in the surf zone, the maximum intensity of the phase averaged vorticity occurs at the shear boundary layer and the strength of vorticity in the water column decays as phase advances. *Melville et al.* [3] also observed that breaking generates at least one coherent vortex that slowly propagates downstream.

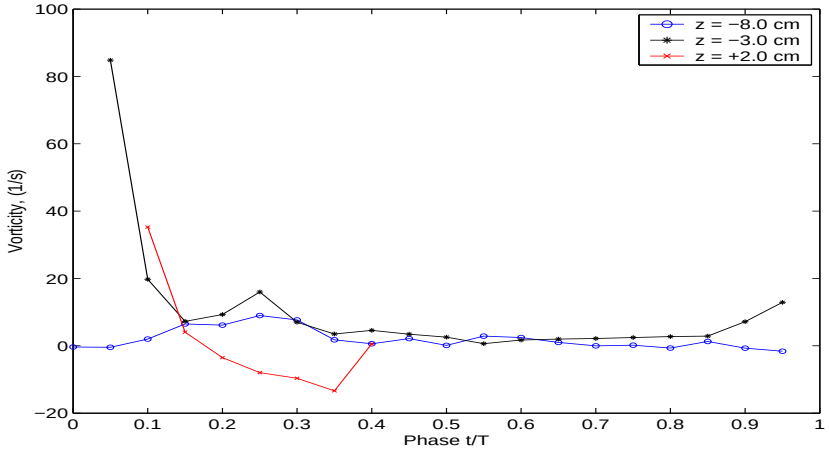

Figure 8.7: Phase variation of the mean flow vorticity, $\langle \omega_y \rangle$ measured at elevation x = -238 cm as flow progresses for three different elevations.

Figure 8.7 shows the profiles of mean flow vorticity as a function of depth measured at three different elevations, z = -8 cm, -3 cm and + 2 cm. For elevations close to the flume bed (z = -8 cm and -3 cm), most of the observed mean flow vorticity is positive for all phases. At elevation z = + 2 cm, mean flow vorticity is positive during the early phases of the flow and then becomes negative after phase t/T = 0.15. Again only a few phases have profiles that go up to z = +2 cm, which corresponds to 15 cm above the bed.

Figure 8.8 shows contour plots of the vorticity of the mean flow under the crests, measured at different cross-shore positions along the flume. The position of the SWL is at elevation z = 0 cm in all the plots. Vorticity intensity near the shear boundary layer decreases away from the break point towards the shore. As seen from the plots, this is a result of vorticity shedding as the flow approaches the shore.

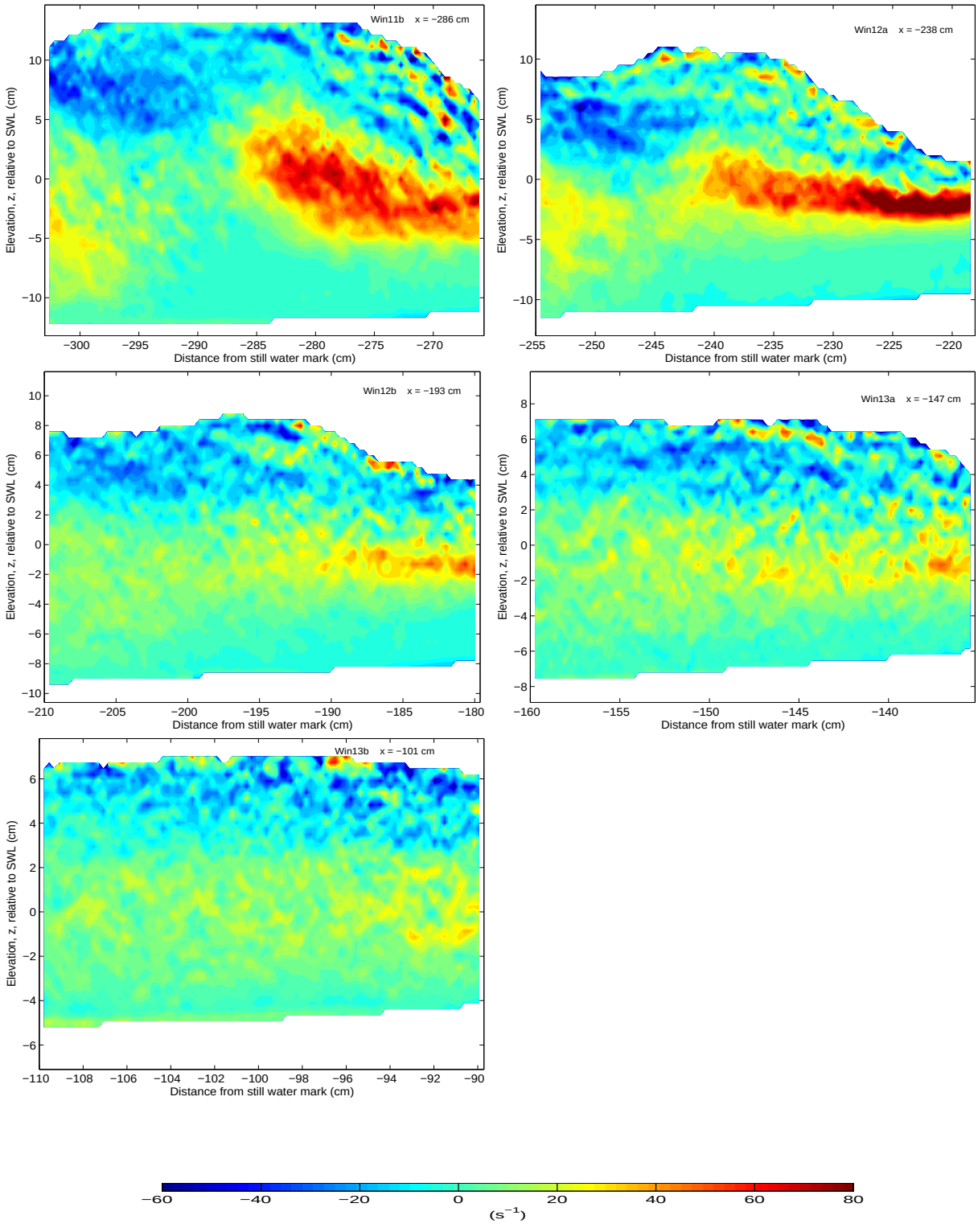

Figure 8.8: Contour plots of the vorticity of mean flow under the crests, measured at different cross-shore positions along the flume. The SWL is at elevation $z = 0$ cm in all the figures.

8.2.3 Summary

Results presented in this chapter include the analysis of instantaneous and the mean vorticity, aimed at determining their evolution and the roles they play as flow propagates. The present two-dimensional measurements yielded only a limited view of the vorticity dynamics, however, because the vorticity field

is dominated by three-dimensional structures. The vorticity fields, estimated using central difference method, revealed the circulation of the flow. Results have shown that the spatial distribution of instantaneous vorticity is extremely patchy near the crest, with isolated pockets of high positive and negative values that have steep gradients. The axis of each vortex is titled in the direction of wave propagation. In between the patches and below the SWL are large expanses with nearly zero vorticity. At the location where eddy interaction occurred, a zigzag pattern of the vorticity profile was observed due to the presence of counter-rotating vorticity around the region. As flow progresses, observed eddies slow-down and vanish slowly when they go deeper, dissipated by bottom friction and slowed down by mean return flow. Maximum intensity vorticity for the mean flow occurs near the shear layer, around $z/h \sim 0$, where the uprush opposes the undertow. At this point a large clockwise-rotating vorticity is formed underneath the wave crest. As the wave crest propagates along the flume, the width of the positive vorticity broadens as it sequentially interacts with downstream vorticity which are remnants of previous breaking waves. The principal feature of the phase-averaged vorticity is that a strong positive vortex appears in the flow near the shear boundary layer. This main vortex of the wave diffuses rapidly into the interior of the wave after breaking, as the eddies on the surface become more viscous. Advection and molecular diffusion play a part in stretching the vortex and redistributing the vorticity. Below the trough level, both instantaneous and mean flow vorticity are about two orders of magnitude smaller than the phase speed divided the local water depth, $\sqrt{(gh)}/h$. For the same region, *Chang* & *Liu* [41] and [69] found that the vorticity generated by wave breaking, was of the same order of magnitude as the phase speed divided the local water depth. Peak magnitudes of both instantaneous and mean flow vorticity generated by wave breaking, are one order of magnitude smaller than the phase speed divided by local depth, c/h.

Chapter 9: Wavelet analysis of the flow

"*The wavelet transform is a tool that cuts up data, functions or operators into different frequency components, and then studies each component with a resolution matched to its scale.*"

Ingrid Daubechies, Lucent, Princeton University

9.1 Introduction

Complex turbulent flow fields are described as the mixing of coherent vortical structures that are composed of different length scales of motion. In the study of turbulence, one commonly used technique for extraction and analysis of flow structures from instantaneous data, is the Fourier spectra which can exhibit a spectral density function distribution among various sizes of eddies (*Liu et al.* [205]). However, Fourier transforms can only provide spectrum information in the frequency domain, with the loss of the time domain information and which require the extra restriction on the stability of the flow. Therefore, as pointed out by *Liu et al.* [205], unconventional extraction and analysis techniques that involve continuous and discrete wavelet transforms for the PIV velocity fields are required to study the detailed local flow structures. The main advantage in using wavelets rather than the more classical Fourier decomposition, lies on the possibility of extracting localized properties such as local energy magnitudes by decomposing a given signal over basis functions. The present approach is based on this idea and is motivated by the successful results obtained by the application of wavelets to turbulent flow data by *Longo* [66].

One approach of finding strong events uses the wavelet decomposition technique (*Farge* [32]). This algorithm searches, at different scales, for similarities between the signal and a set of probing wavelet functions, which match the profile of a certain type of filamentary vortex. The wavelet analysis is a time-frequency analysis method, which plays an important role in processing non-stationary signals obtained by PIV to measure turbulent flow fields. Other applications of wavelet transforms for analyzing signals and turbulence can be found in *Farge* [32] and *Mallat* [91]. In the analysis, the signal is decomposed into different scales of frequencies (or wavenumber) using a continuous complex wavelet transform. The wavelets are generated based on a single basic wavelet, $\psi(x)$, called the *mother* wavelet, by scaling and translation. *Farge* [32] firstly introduced the wavelet analysis application to study turbulence.

Turbulent flows exhibit many different length and time scales. Hence, it is important to study energy transfer between the scales, in order to gain deeper insight into turbulence (*Joshi & Rempfer* [206]).

Wavelets offer potential for the analysis of the energy transfer in a turbulent flow. This is mainly due to their locality and scalability property. Locality here means that wavelets have compact support, which enables them to resolve local features in a flow. Wavelet representations thus have an ability to express and separate structures in a flow at different scales. *Farge et al.* [28] have performed substantial work in the field of coherent structure detection using orthonormal wavelets.

By decomposing the time series into time-frequency space, one is able to determine both the dominant modes of variability and how these modes vary in time. Application of wavelet analysis in flow structures, to detect, extract and analyze the characteristics of turbulence or eddy structures from our experimental data is presented. The main objective of this chapter is to use wavelets to decompose the velocity fluctuation signal and look at the percentage of signal energy in the various bands determined by the scales. This will enable the location of intervals where excess energy occurred in the breaker, in a certain frequency bands. In this application, the continuous wavelet transform (CWT) is employed to that effect. By analyzing the coefficients in a certain frequency band it is possible to locate the intervals where the energy was higher. A wavelet based algorithm developed by *Torrence & Compo* [82] was modified and employed to decompose the turbulence data into contributions at different frequencies and different locations from the still water line mark. The dominant frequencies and time period of the turbulent flow can be obtained from the temporal wavelet transform of the fluctuating velocity components. Furthermore, the energy contributions of structures at each scale were computed.

This chapter begins by exploring what is known about wavelet transforms and the characteristics of wavelet coefficients. The primary purpose of the discussion is to introduce notation and to provide a suitable background on the wavelet transform as a mathematical and microscopic tool for turbulent flow analysis. Reference to previous work on wavelets is made while the basic ingredients needed for the present analysis are given in sections below. The following description is limited to the needs of the present study, so readers are referred to other sources, such as *Farge* [32], *Torrence & Compo* [82], *Mallat* [91], *Muller & Vidakovic* [207] and *Labat et al.* [208], for a more thorough description of wavelet analysis capabilities. The main task of the present work, however, is to present and validate a technique for wavelet analysis of the fluctuating velocity vector fields. The wavelet based techniques that were applied to the turbulence flow are explained and the main results obtained are presented.

9.2 The standard Fourier Transform

The standard Fourier transform is defined using the continuous integration of the product of a function $f(t)$ by the trigonometric functions and it can be written as :

$$F(\omega) = \frac{1}{\sqrt{2\pi}} \int_{-\infty}^{\infty} f(t) e^{-i\omega t} dt \tag{9.1}$$

where $e^{-i\omega t}$ is the Fourier basis function with frequency, ω and time, t.

Fourier transform maps a function from time domain to frequency domain. Any function can be decomposed into a linear combination of Fourier vectors defined by their Fourier coefficients $F(\omega)$. However for

trigonometric functions it is characteristic to oscillate forever, so the information of $f(t)$ is completely delocalized among the spectral coefficients $F(\omega)$. Standard Fourier transform does not therefore provide any information of time-localization but it is an appropriate tool for frequency analysis and when studying harmonic or stationary signals or when there is no need for local information.

9.3 Windowed Fourier Transform

Often there are non-stationary or transitory characteristics, such as abrupt changes or beginnings and endings of events, in the signal. With the ordinary Fourier transform it is not possible to analyze when the singular event occurred, but using windowed Fourier transform some degree of time-localization can be achieved. The windowed Fourier transform is defined by :

$$F_w(\omega, t) = \int_{-\infty}^{\infty} f(t)g(t - t_o)e^{-i\omega t}dt \tag{9.2}$$

where $g(t - t_o)$ represents the window function.

The function$f(t)$ is multiplied by the window function $g(t-t_o)$ to cut off a well localized slice of f, like as shown in Figure 9.1. Though this method is a standard technique, it has its disadvantages. Namely the size of the time window, once chosen, cannot be changed during the analysis. This means that the window is same for all frequencies. If the window could be varied during the process, it would give a more flexible approach. For this need wavelets provide a good solution (*Jalali* [26]; *Farge* [32]; *Daubechies* [209]).

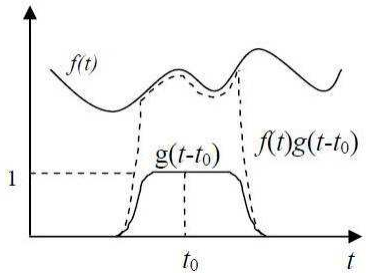

Figure 9.1: The windowed Fourier transform (*Daubechies* [209]).

9.4 Wavelet theory

A Wavelet Transform (WT) of a function is a decomposition of that function into a weighted sum of a particular family of functions generated from a mother wavelet and forming a basis for $\mathcal{L}^2(\mathbb{R})$. Wavelets are functions that satisfy certain mathematical demands in multiresolution analysis. In brief, a wavelet is an oscillation that decays quickly (*Sifuzzaman et al.* [210]. The name wavelet comes from the requirement that : (1) the average value of the function should be zero (2) the function has to be well localized (*Muller*

& *Vidakovic* [207]). A wavelet is a mathematical function used to divide a given function or continuous-time signal into different scale components. Usually one can assign a frequency range to each scale component. Each scale component can then be studied with a resolution that matches its scale.

The wavelets are scaled and translated copies (known as "daughter wavelets") of a finite-length or fast-decaying oscillating waveform (known as the "mother wavelet"). The fundamental idea behind wavelets is to analyze according to scale. Wavelet transform can be continuous or discrete. The CWT is performed in a smooth continuous fashion and represents the energy content of a signal that contains features on different scales at any instant in time (*Seena & Sung* [92]). As explained in *Farge* [32], for data analysis it is better to use a complex wavelet, since the modulus of the complex-valued wavelet coefficients gives the energy density, in a fashion similar to Fourier analysis.

It is important to notice the significant differences between Fourier analysis and wavelet analysis (*Strang* [211]). Fourier basis functions are localized in frequency but not in time. Small frequency changes in the Fourier domain will produce changes everywhere in the time domain. Wavelets are, however, local in both frequency (scale) and time. This localization is a major advantage of the WT. Another important feature is that a large class of functions can be represented by wavelets in a compact mode. For example, functions with discontinuities or with sharp transitions usually take substantially fewer wavelet basis functions than sine-cosine basis functions to obtain a comparable approximation. Furthermore, large data sets can be easily and quickly transformed by the WT. From the theoretical viewpoint, a brief discussion about the fundamentals of wavelet analysis is presented in *Torrence and Compo* [82].

The continuous wavelet transform (CWT) is simply the correlation of an input function $f(x) \in \mathcal{L}^2(\mathbb{R})$ with a family (in particular, an orthogonal family) of wavelet functions $\psi_{a,b}(x)$ (with $a, b \in \mathbb{R}$ and $a \neq 0$) generated by scaling (dilating or compressing) and shifting a single mother wavelet $\psi(x) \in \mathcal{L}^2(\mathbb{R})$, and is expressed mathematically (*Seena & Sung* [92]) as :

$$W_f(s,x) = \frac{1}{\sqrt{s}} \int_{-\infty}^{\infty} f(\tau)\psi^* \left(\frac{x-\tau}{s} \right) d\tau \tag{9.3}$$

where

$$\psi_{s,\tau}(x) = \frac{1}{\sqrt{s}} \psi \left(\frac{x-\tau}{s} \right) \tag{9.4}$$

represents a chosen wavelet family and s is the scale factor, τ is the translation factor, $\sqrt{s}$ is for energy normalization across the different scales, and * denotes the complex conjugate. The function $\psi(x)$ is the mother wavelet, which is dilated or contracted by s and translated by τ to generate a family of wavelets, $\psi_{s,\tau}$. Large values of the scaling parameter s mean large scale and they correspond to small frequency ranges, while small values of parameter s correspond to high frequencies and very fine scales. The variation of s has a dilatation effect (when $s > 1$) and a contraction effect (when $s < 1$) of the mother-wavelet function. By changing parameter τ, the wavelet function can be translated along the time axis : Each $\psi_{s,\tau}(t)$ is localized around $t = \tau$. Therefore, it is possible to analyze the long and short

period features of the signal or the low and high frequency aspects of the signal. As b varies, the function f is locally analyzed in the vicinities of this point.

The mother wavelet adopted in this analysis is the complex *Morlet* wavelet which has been found to be a common choice in fluid mechanics (*Farge* [32]). However it has been proven that the physical results obtained do not depend on the choice of the wavelet type (*Farge* [32] and *Camussi* & *Felice* [90]). The *Morlet* wavelet is a plane wave modulated by a Gaussian envelope defined as :

$$\psi(x) = \pi^{-\frac{1}{4}} e^{i\omega_o x} e^{-\frac{1}{2}x^2} \tag{9.5}$$

where the parameter ω_o is the wavenumber associated with the *Morlet* wavelet, roughly corresponding to the number of oscillations of the wavelet. The coefficient ω_o is usually taken equal to 6 in order to minimize errors related to the non-zero mean (*Torrence* & *Compo* [82]). The advantage of the Morlet wavelet over other candidates such as the Mexican hat wavelet resides in its good definition in the spectral space. For $\omega_o = 6$ (used here), the Morlet wavelet scale is almost identical to the corresponding Fourier period of the complex exponential, and the terms scale and period may conveniently be used synonymously (*Torrence* & *Compo* [82]; *Torrence* & *Webster* [212]). Figure 9.2 shows the real part of the complex *Morlet* wavelet adopted in the analysis reported here. Since this wavelet is a complex function it is possible to analyze the phase and the modulus of the decomposed signal (*Seena* & *Sung* [92]).

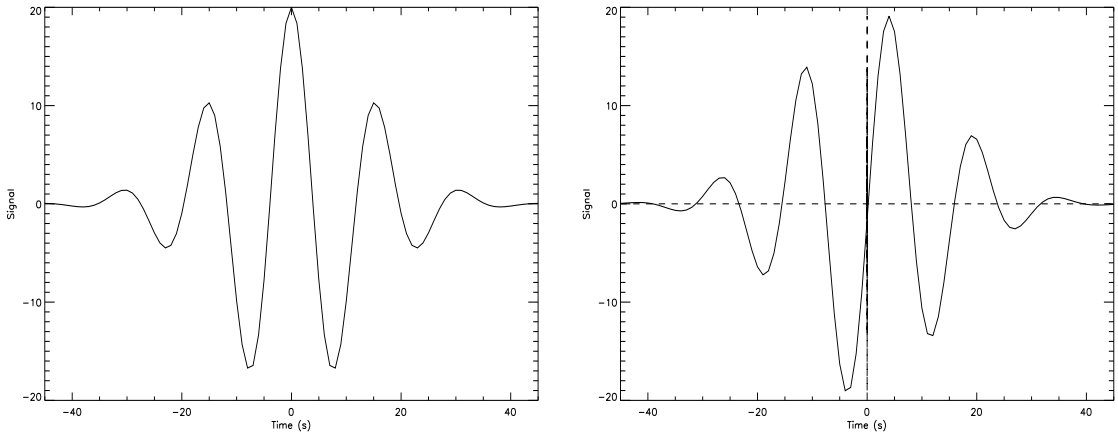

Figure 9.2: Complex *Morlet* mother-wavelet with $\omega_o = 6$, (a) real component (b) imaginary component

In practice, Eqn. (9.3) is implemented using digital techniques. The continuous wavelet transform W_n of a discrete sequence of observations x_n is defined as the correlation of x_n with a scaled and translated wavelet $\psi(\eta)$ that depends on a non-dimensional time parameter η,

$$W_n(s) = \frac{1}{\sqrt{s}} \sum_{n'=0}^{N-1} x'_n \psi^* \left(\frac{n' - n}{s} \right) \delta t \tag{9.6}$$

where n is the localized time index, s is the wavelet scale, δt is the sampling period, N is the number of points in the time series, and the asterik, * indicates the complex conjugate.

By varying the wavelet scale, s and translating along the localized time index, n, one can construct a picture showing both amplitude of any features versus the scale and how this amplitude varies in time. Such a transform is called the continuous wavelet transform, because the scale and localization parameters assume continuous values. By choosing N points, the correlation described by Eqn. (9.3) allows us to do all N convolutions simultaneously in Fourier space using discrete Fourier transform (DFT). The DFT of x_n is :

$$\hat{x}_k = \frac{1}{N}\sum_{n=0}^{N-1} x_n e^{-2\pi i k n/N} \tag{9.7}$$

where $k = 0 \cdots N-1$ is the frequency index. In the continuous limit, the Fourier transform of a function $\psi(t/s)$ is given by $\hat{\psi}(s\omega)$. By the correlation theorem, the wavelet transform is the *inverse* Fourier transform of the product :

$$W_n(s) = \sum_{k=0}^{N-1} \hat{x}_k \hat{\psi}^*(s\omega_k) e^{i\omega_k n \delta t} \tag{9.8}$$

To ensure that the wavelet transforms at each scale s are directly comparable to each other and to the transforms of other time series, the wavelet function at each scale is *normalized* to have unity energy as follows :

$$\hat{\psi}(s\omega_k) = \left(\frac{2\pi s}{\delta t}\right)^{\frac{1}{2}} \hat{\psi}_o(s\omega_k) \tag{9.9}$$

The result of these correlations are referred to as *wavelet coefficients*. When two signals are correlated with each other, a measure of similarity is obtained between them. Thus, when the WT is computed at a scale corresponding to the compressed wavelet, a measure of similarity between the signal and the high-frequency wavelet is obtained. Likewise, when the wavelet function is dilated, a measure of how similar the input signal is to the low-frequency wavelet is obtained. In other words, the WT can be interpreted as frequency decomposition with corresponding coefficients which provide information about the frequency contributions of the original signal, as well as their spatial position. This kind of analysis is also referred to as *multi-resolution analysis* (*Azimifar* [213]). As the wavelet function ψ is complex, the wavelet transform is also complex. The transform can then be divided into the real part $\Re[W_n(s)]$, and the imaginary part, $\Im[W_n(s)]$. The wavelet amplitude and wavelet energy are then calculated from the coefficients as :

$$W_A(s) = \Re[W_n(s)] \tag{9.10}$$

and

$$W_E(s) = (\Re[W_n(s)])^2 \tag{9.11}$$

respectively, while the wavelet phase is given by :

$$W_P(s) = tan^{-1}(\Im[W_n(s)]/\Re[W_n(s)]) \tag{9.12}$$

where $\Re$ and $\Im$ represent the *real* and *imaginary* parts of the wavelet coefficients.

The wavelet power spectrum is also complex and is defined as :

$$W_P(s) = |W_n(s)|^2 \tag{9.13}$$

The wavelet power spectrum is a convenient description of the fluctuation of the variance at different frequencies (*Torrence* & *Compo* [82] , *Ancti* & *Coulibaly* [214]). Further, when normalized by the variance σ^2, it gives a measure of the power relative to white noise, since the expectation value for a white-noise process is σ^2 at all n and s (*Anctil* & *Coulibaly* [214]).

The total energy in a signal is conserved under the wavelet transform, and the equivalent of *Parseval's theorem* for wavelet analysis is given by *Torrence* & *Compo* [82] as the variance of the signal, expressed as :

$$W_E = \sigma^2 = \frac{\delta j \delta t}{C_\delta N} \sum_{n=0}^{N-1} \sum_{j=0}^{J} \frac{|W_n(s_j)|^2}{s_j} \tag{9.14}$$

where C_δ is a scale independent constant, which for the Morlet wavelet is 0.776.

The scales are fractional powers of two given by :

$$s_j = s_o 2^{j\delta j}, \quad j = 0, 1, \cdots, J \tag{9.15}$$

and

$$J = \delta j^{-1} log_2(N\delta t / s_o) \tag{9.16}$$

where s_o is the smallest resolvable scale and J is the largest scale.

The distribution of energy in space at any prescribed scale can be obtained using Eqn. (9.14). The summation of energies at all spatial scales gives the total energy, E_T which can be expressed as :

$$E_T = E_{s_1} + E_{s_2} + E_{s_3} + \cdots \tag{9.17}$$

where $E_{s_1}, E_{s_2}, E_{s_3}, \cdots$ are energies at each scale, respectively. As mentioned previously and to recap, the Fourier Transform of a signal is a mapping from a function of time $x(t)$ to a function of frequency, $F(\omega)$. The function $F(\omega)$ gives information on the extent to which a signal component with frequency ω is present in the analyzed signal. It does not however indicate how that signal component evolves with time t. For that a transform is needed that returns a bivariate function of the form $F(t, \omega)$. Wavelet transform provides a time-frequency description of function f as did the windowed Fourier transform. A difference is in the shapes of the analyzing functions g and ψ. They are both shifted along the time axis but all the functions g have the same time-width while functions ψ have widths adapted to their frequency. At high frequencies $\psi_{s,\tau}$, are very narrow and at low frequencies they are much broader. This is why the wavelet transform gives a more flexible approach than windowed Fourier transform. With the

aid of a wavelet transform, it is possible to better zoom in on very short-lived high frequency phenomena, like transients in signals or singularities in functions. Wavelets are mathematical microscopes that are able to magnify a given part of a function with a certain factor represented by a value of scale parameter. This magnification is associated with the extraction of the information at a certain scale hidden in a local area of the analyzed function.

9.5 Verification of the wavelet algorithm

The application of the standard PIV measurement technique usually yields two dimensional maps associated with the turbulence parameters. In order for the 2-D fields to be studied, it is possible to extend Eqn. (9.3) to two dimensions in order for the 2-D turbulence data to be directly transformed. However, for the present purposes, only 1-D transforms are considered since in this way the energy in the signal can be retrieved. A similar analysis was reported by *Longo* [66], *Huang et al.* [88] and *Longo* [215]. It is most important to know how the available energy is distributed in the different wavelet scales. Firstly, results of the wavelet analysis of a test signal that comprises summing three sinusoids is presented. Thereafter, wavelet transform results for the fluctuating velocity shall follow. A wavelet analysis by *Torrence & Compo* [82] was adopted and modified for this analysis.

9.5.1 Wavelet scale versus period

To ascertain the significance of the wavelet transform used and demonstrate its capabilities, synthetic test signals comprising of various combinations of three sine waves with frequencies of 1 Hz, 5 Hz and 10 Hz were analyzed. The first synthetic signal that was analyzed had a mathematical representation :

$$\zeta(t) = 2.0\,[\sin(2\pi t) + \sin(2\pi 5t) + \sin(2\pi 10t)] \tag{9.18}$$

where all the three frequency components have amplitude of 2.0. This synthetic signal was used to establish the relationship between the scale s and the period T, and is shown in Figure 9.3(a).

This example demonstrates the kind of results which arise from a wavelet analysis and their interpretation. The spectrum of the test signal obtained from a Fourier analysis is shown in Figure 9.3(b) and confirms the presence of three frequency components (1 Hz, 5 Hz, 10 Hz) in the signal. Complex Morlet wavelet transform results on the test signal are shown in Figure 9.4, in which the colour-coded contours of the wavelet coefficients that form a wavelet map, are shown. The colour bars represent each wavelet spatial scale described in the legend with red colour denoting high wavelet amplitude or energy values while blue highlights low values. In this application, $N = 91$, $\delta t = 0.41$, $s_o = 2\delta t = 0.82$, $\delta j = 0.125$ and $J = 42$ giving a total of 43 scales ranging from 0.04 up to 10.4. A logarithmic scale, with smallest scales at the bottom, was chosen for the *scale* axis to prevent the smallest scale from vanishing completely (*Seena & Sung* [92]). Linear scaling for the contours suppresses coefficients of higher frequency components that

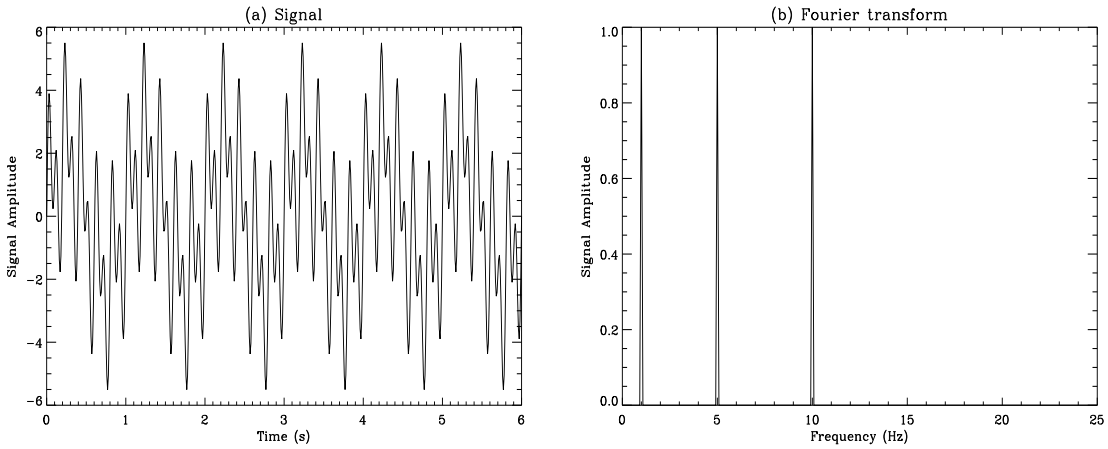

Figure 9.3: (a) Time domain plot of a synthetic test signal composed from summation of 1 Hz, 5 Hz, and 10 Hz frequency sinusoids. (b) Frequency domain plot (Fourier spectrum) of the test signal confirming the presence of three frequency components (1 Hz, 5 Hz, 10 Hz) in the signal.

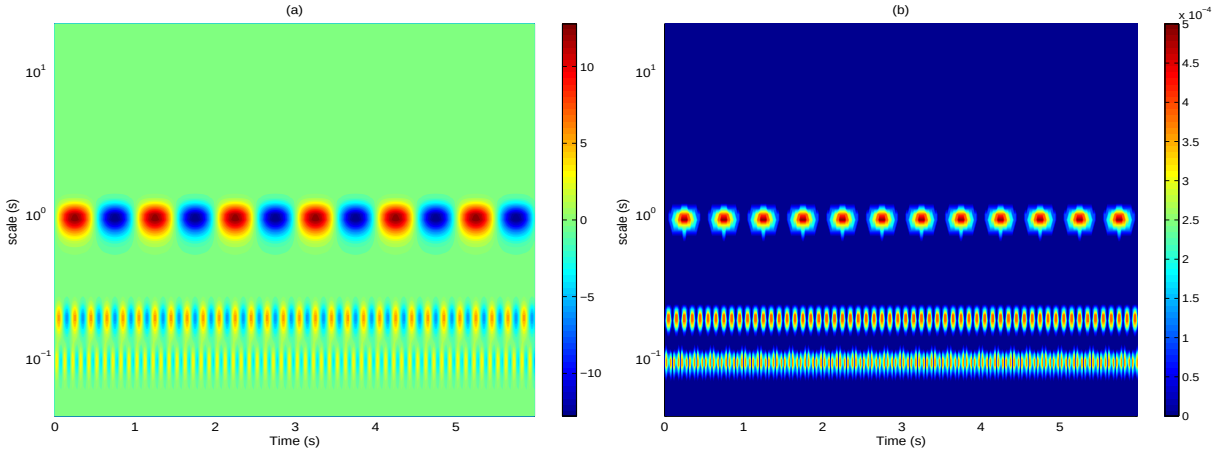

Figure 9.4: Plots of wavelet coefficients at different values of scale and time obtained from the Morlet wavelet transform showing : (a) amplitude, (b) wavelet energy spectrum of the test signal given in Figure 9.3(a).

possess lower energies. The maxima of the absolute values of $|W(s,a)|$ are concentrated in the periods of the three components. Moreover, they are distributed in time according to the periodicity of the resulting wave field (*Massel* [172]). Three dominant frequencies were detected using the wavelet scale s=1.0, 0.2 and 0.1. The repetition of features of colour-coded contours at s=1.0, 0.2 and 0.1 for all time shifts indicate the periodicity of the signal with a time period of 1.0, 0.2 and 0.1 s. Hence all three time periods 1.0, 0.2 and 0.1 are observed, which may have signified a one-to-one relationship between scale and period, written as :

$$s = \beta T \tag{9.19}$$

where β is a constant that depends on the analyzing wavelet. *Seena & Sung* [92] stated that for the complex Morlet wavelet, $\beta = 1$ while *Wang* [216] obtained the reciprocal relation between the temporal scaling factor and the equivalent Fourier frequency with constant $\beta = 0.97$. The energy spectrum results in Figure 9.4 (b) show that as expected, the same amount of energy is contained in the three wavelet scales.

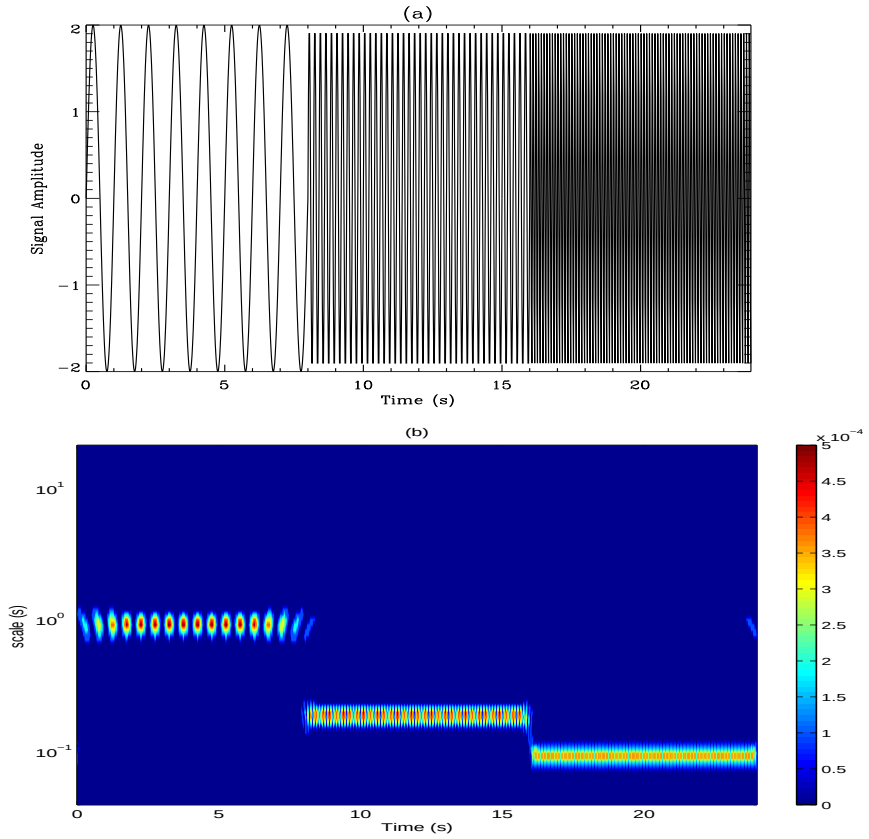

Figure 9.5: (a) Synthetic test signal composed of 1 Hz, 5 Hz, and 10 Hz frequency sinusoids with different starting times (b) corresponding wavelet energy spectrum of the test signal.

Figure 9.5 (a) shows another synthetic test signal consisting of three sinusoids of amplitudes 2.0 but with different starting times. The 1 Hz signal appears for times between 0 and 8 s, the 5 Hz for times between 8 and 16s, while the 10 Hz component appears between 16 and 24 s. Both frequency and the beginnings of the signal components are clearly visible in the wavelet energy spectrum results shown in Figure 9.5 (b). Results show that the three sinusoids occur at the same scales of 1.0, 0.2 and 0.1 (as before) but this time starting at different times. As expected, equal amounts of energy are contained at these three spatial scales. Unlike results for the previously given test signal, the energy for this particular test signal do not appear for all the time shifts. From these results it can be concluded that the wavelet spatial scale holds a one-to-one relationship with the period of the spatial synthetic structures presented here. Therefore the scales give information about the frequency. The finer the scale, the higher the frequency and vice-versa.

9.5.2 Energy contribution by the synthetic signal wavelet scales

The signal shown in Figure 9.6 (a) consisting of 1 Hz, 5 Hz and 10 Hz sinusoids were summed up and used to test the algorithm for examining the energy content in the various scales. The figure shows only up to a *time* of 6 s. The three frequency components of the signal have relative amplitudes of 1, 2 and 4 respectively. Figure 9.6(b) and (c) show results of the wavelet analysis of the synthetic signal showing the amplitude and energy spectrum. These three figures show presence of signals centered

around three main scales of 0.1, 0.2 and 1.0 which correspond to the periods of 10 Hz, 5 Hz and 1.0 Hz components, respectively. Most of the wave energy in the signal is confined around the smallest scale of 0.1 that correspond to the largest frequency of 10 Hz in the signal, since the component had the largest amplitude.

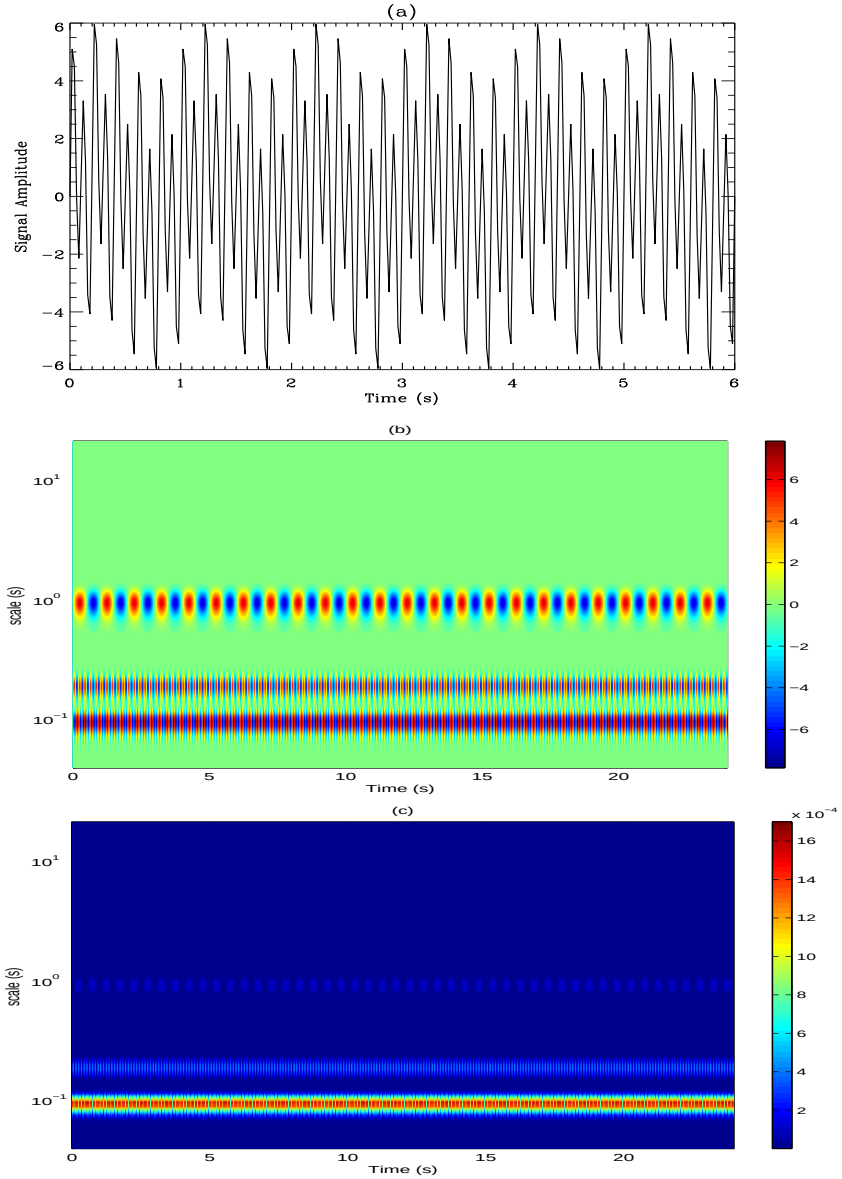

Figure 9.6: (a) Synthetic signal consisting of 1 Hz, 5 Hz and 10 Hz components, used for checking energy contribution at different scales, (b) amplitude of the signal, (c) wavelet energy spectrum of the signal.

In the wavelet analysis of the synthetic signal, once again a total of 43 wavelet scales were used and have values ranging between 0.04 - 10.4. It is important, therefore, to note that the wavelet results of Figure 9.6 do not show all the scales for this signal. As in *Longo* [215], the scales in the signal were subdivided into 3 bands, namely : 0.04 - 0.155, 0.170 - 0.60 and 0.65 - 10.4, which are here named *micro* scales, *mid* scales and *macro* scales respectively. The bands were intentionally set so that each frequency component in the test signal lies in at most one of the bands. The energies associated with the scales used here are labeled E_{micro}, E_{mid} and E_{macro}. The total amount of energy in each of the three spatial scale bands was obtained by summing up the energy for all scales in the band. Table 9.1 summarizes

the characteristics of the three components that make up the signal under study, and also presents the expected energy versus the wavelet energy for each of the three components. The energy obtained by wavelet analysis is very close to the expected, E_{rms}, but is a little less, because of the quantization errors involved in its calculation.

Table 9.1: Energy content of the signal shown in Figure 9.6(a).

	f (Hz)	scale band	A	E_{rms}	Wavelet energy, W_E	% of total energy
	10.0	micro	4.0	8.0	7.96	76.7
	5.0	mid	2.0	2.0	1.94	18.7
	1.0	macro	1.0	0.5	0.48	4.6
Total				10.5	10.38	100

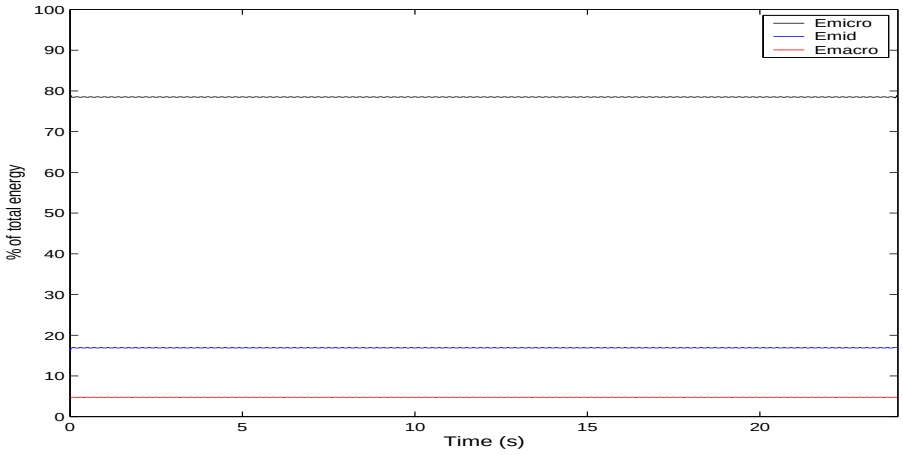

Figure 9.7: Variation of the energy contribution by different scale bands with time.

At each time, the energy available in each of the three scale bands was then normalized by the total available energy at that time, in order to get the percentage of the total energy existing at each scale. Figure 9.7 shows the percentage of the total energy contributed by each scale band at different times. As expected, the macro scales are observed to make the least base contribution of about 4.7 % to the total energy available at each time, for all the times. The mid scales contribute 17.3 %, while the micro scales contribute 78.0 %. These results are consistent with the percentage of the total energy given in the last column of Table 9.1.

Another signal shown in Figure 9.8 was also used to test the algorithm for examining the energy content in the various scales. All three components have an amplitude of 4.0. The 10 Hz signal is available for times between 2- 6 s, the 5 Hz between 10 -14 s and the 1 Hz between 18 - 22 s. For all other times the signal components are zero. The computed Morlet energy spectrum for this test signal is shown in Figure 9.9 and clearly shows the duration of each of the three components. As can be seen, energy in the signal is available in equal amounts only at wavelet scales 0.10, 0.20 and 1.0 which correspond to the periods of the three components. This confirms the ability of the wavelet algorithm employed here, to determine the energy contribution by the various scales to the total energy in the signal.

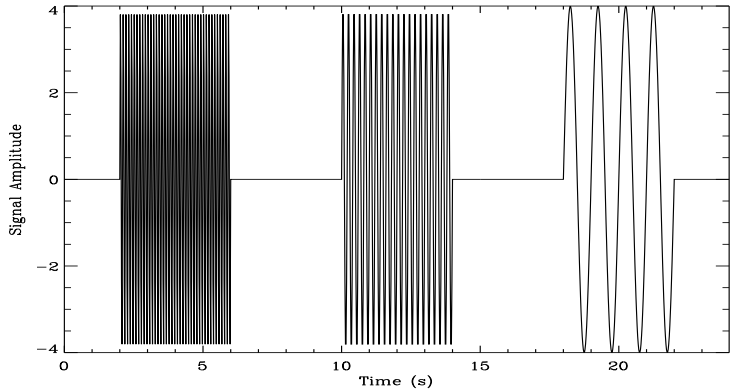

Figure 9.8: Synthetic signal consisting of 10 Hz, 5 Hz and 1 Hz sinusoids used for checking energy contribution at different scales.

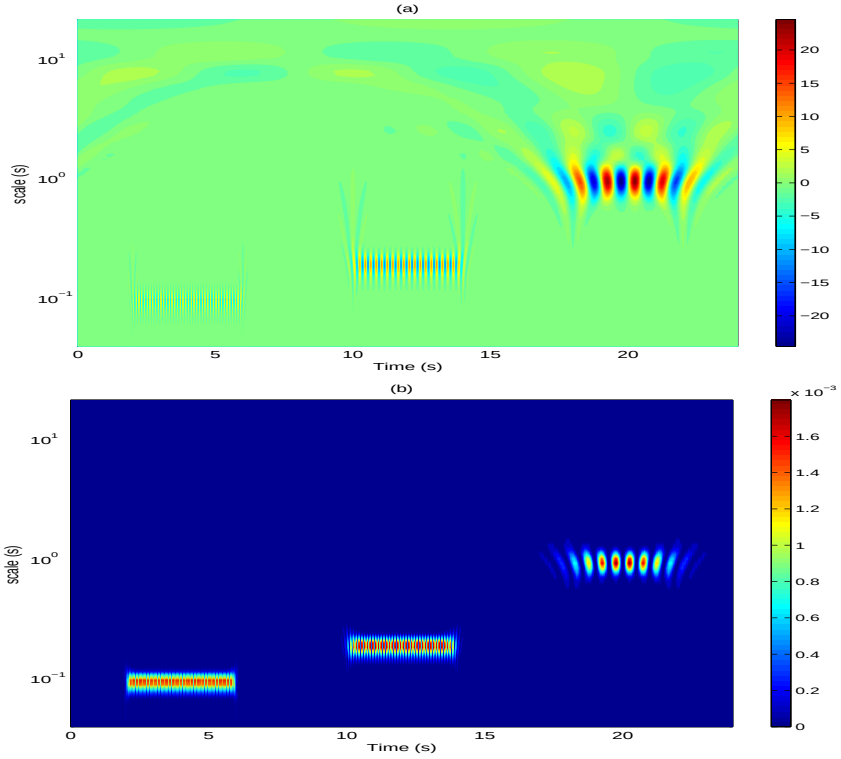

Figure 9.9: Wavelet analysis results of the test signal shown in Fig. 9.8 showing (a) amplitude and (b) energy spectrum.

9.6 Wavelet analysis of velocity fluctuations

Synthetic signals have been successfully used to calibrate the wavelet-based methodology from which a one-to-one relationship between the wavelet spatial scale, s, and the period, T, of the signal was obtained. The validity of the wavelet algorithm was checked and verified so the next task in this section is to apply wavelet transforms to our experimental data. The continuous wavelet transform was applied to horizontal and vertical velocity fluctuations, which have been defined by Eqn. (2.38) given in Chapter 3. The wavelet transform of the velocity components at any appropriate location may yield the dominant frequencies of its oscillation. The structures of the turbulent flow in terms of both spatial coordinates and scale are

studied on the basis of the wavelet coefficients.

9.6.1 Energy contribution by fluctuating velocity wavelet scales

The wavelet algorithm was then applied to velocity fluctuations to determine how much of the wave energy is contained in the spatial scale bands. The energy calculated from the wavelet coefficients shall herein be referred to as the wavelet energy. The wavelet transform coefficients provide information about both the amplitude and phase of the fluctuations at each time and frequency, and therefore, should be able to provide understanding of the evolving relationship between wave and turbulence characteristics. It important to recall that velocity vector fields were presented as a function of distance from the SWL mark. Therefore in the wavelet analysis of the velocity fluctuations, distance from the SWL mark will be used for the x-axis instead of time that was used for the synthetic signals.

Recall that each instantaneous velocity field consists of 91 samples horizontally and 56 samples vertically. Wavelet analysis was performed on each horizontal line of vectors in the instantaneous vector field. Adjacent velocity samples are spaced 8 pixels apart. Two samples of velocity fluctuations are spaced 8 pixels apart, which gives dx = 8 pixels/19.5 pix/cm = 0.41 cm. The total number of samples along each row is $N = 91$. A scale of dj=0.125 was used. Using Eqn. (9.16) gives $J = 44$, so that the total number of scales used in the wavelet analysis is 45. The scales range between 0.82 cm and 37.1 cm. As already stated the wavelet scales used (given by Eqn (9.15)) are fractional powers of 2 and as such are quantized. The scales were divided into scale bands, with 0.8 cm - 16.0 cm representing the micro scales, 16.0 cm - 27.0 cm the mid scales and 27.0 cm - 38.0 cm, the macro scales. This choice of scales used to define the energy bands is, however, arbitrary.

Figure 9.10 shows a flowchart that summarizes how the wavelet energy was obtained from the instantaneous velocity vector components. Wavelet analysis was performed for a given phase as follows : beginning with an instantaneous velocity vector field, the fluctuation was calculated by subtracting the phase-ensemble-average velocity of the phase in question. Each row of fluctuating velocities was then analyzed using wavelet, giving the wavelet coefficients from which the $r.m.s$ value is extracted using Eqn (9.14). This was repeated for other instantaneous vector fields for this phase and then an average $r.m.s$ value was computed. The $r.m.s$ value or energy were computed for each scale as mentioned previously and the average computed. The process was repeated for the other phases. Averaging the energies over all sequences in the phase gave the phase-ensemble averaged energy for each elevation. This was done for both horizontal and vertical fluctuating velocity components. Adding up the averaged energies at the same elevation for the two fluctuating velocity components gave the total phase averaged energy at that elevation. The total phase ensemble averaged energy calculated this way was compared with those calculated using statistical method as presented in chapter 7, at each elevation.

Figure 9.11 shows in column (a) instantaneous horizontal velocity fluctuations measured at elevation z = 0 cm for four phases, ($t/T = 0.05, 0.10, 0.15$ and 0.20) and in (b) the corresponding wavelet energy spectrum. The energy spectrum shows how much energy is available in the signal and at what scale and position. If there are no oscillations in the signal at a certain scale, and position, the corresponding wavelet

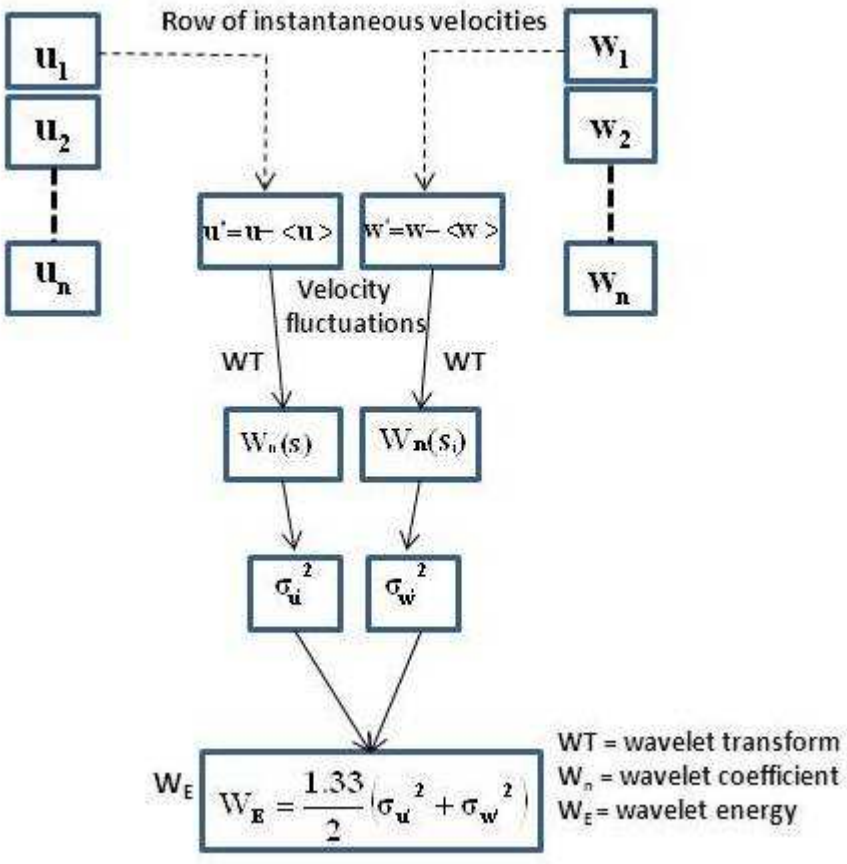

Figure 9.10: Schematic of flowchart showing how the wavelet energy, W_E, was derived from the instantaneous velocities.

coefficients are zero (*Farge* [32]) and therefore zero energy. As pointed out by *Seena* & *Sung* [92], the repetition of features at higher values of the wavelet spatial scale signifies the presence of large structures associated with low frequencies. The repetition of features at lower scales indicates the simultaneous shedding of additional small structures, validating the multi-scale characteristics of the turbulent flow. Figure 9.11(b) shows the energy spectrum with the log-scale y-axis. This approach does not spoil the spectral information but only allowed the amplification of higher frequency components, making them more pronounced in the wavelet spectrum. For phases 0.05 and 0.10, the horizontal velocity fluctuation signal is not observed over the entire field of view which ranges from -255 cm to -217 cm, due to that portion being above the wave profile. The energy spectrum for the signal at phase $t/T = 0.05$ shows that much of the energy in the signal is contained in scales less than 5 cm at distances centered around -250 cm. Figure 9.11(c) shows the horizontal velocity fluctuation signal for phase $t/T = 0.10$. The largest scale or period in this signal is about 5 cm, centered between -240 cm $\leq xle$ -235 cm. As expected, the energy spectrum for this signal shows most of the energy being confined in a wavelet scale of 5 cm, between -240 cm and -235 cm from the SWL mark.

Figure 9.12 shows the energy spectrum for phases $t/T = 0.05$ - 0.20 measured at other elevations z = -5 cm and -10 cm. Figure 9.13 shows the energy spectrum of horizontal velocity fluctuations at later phases of the flow measured at elevations z = 0 cm, -5 cm and -10 cm. Overall, during the early phases of the flow, in the vicinity of the crests, small scales contain most of the energy, and as flow progresses, flow

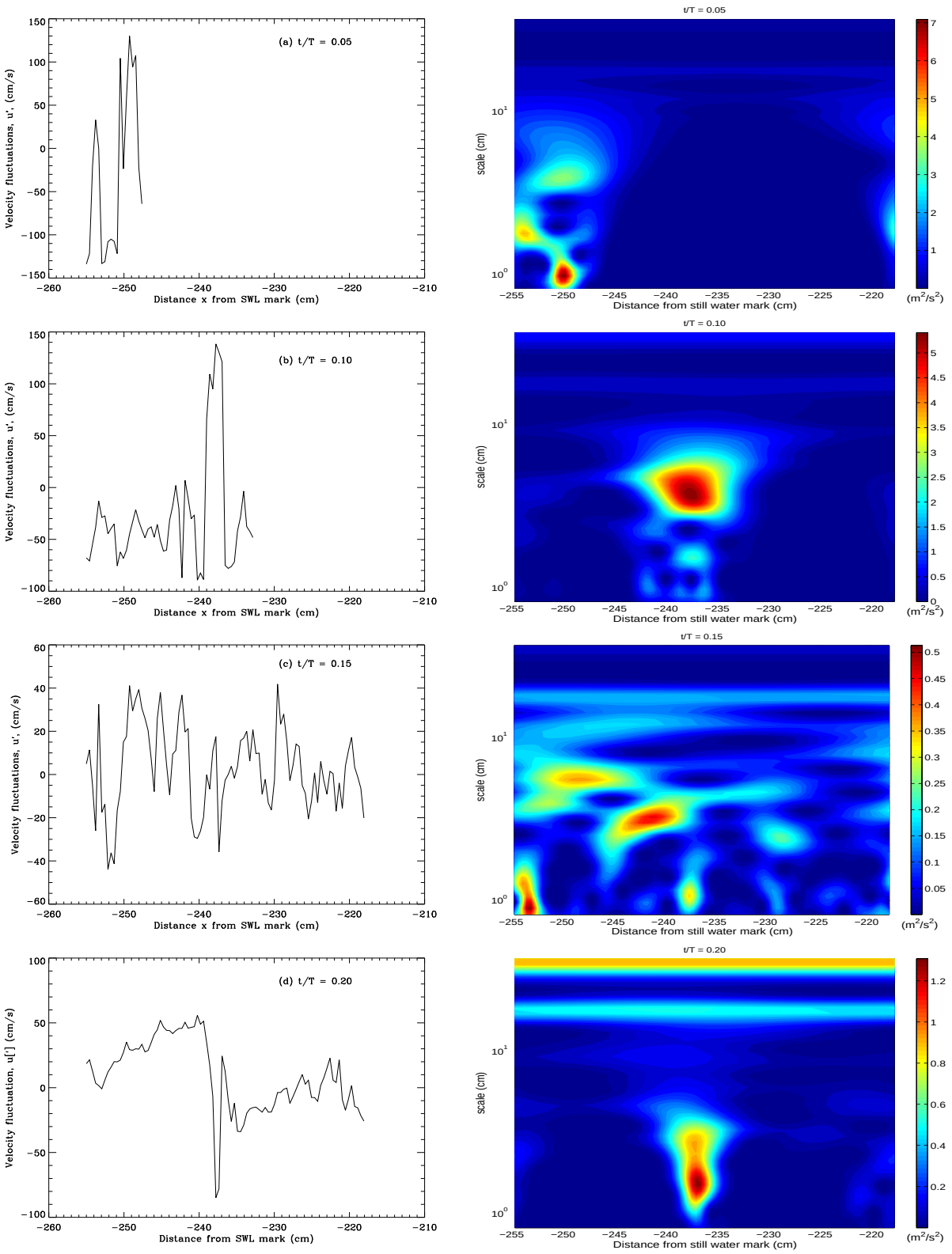

Figure 9.11: Results for station 12a showing, column (a) - horizontal velocity fluctuation signal at elevation $z = 0$ cm for four phases (b) corresponding energy spectrum. Note that the logarithmic scale was chosen for the *scale*-axis to prevent the smallest scales from vanishing completely.

becomes somewhat uniform and most of the energy is shifted to the larger scales.

Figure 9.14 (a) shows velocity fluctuation signals at elevation $z = 0$ cm measured at different cross-shore

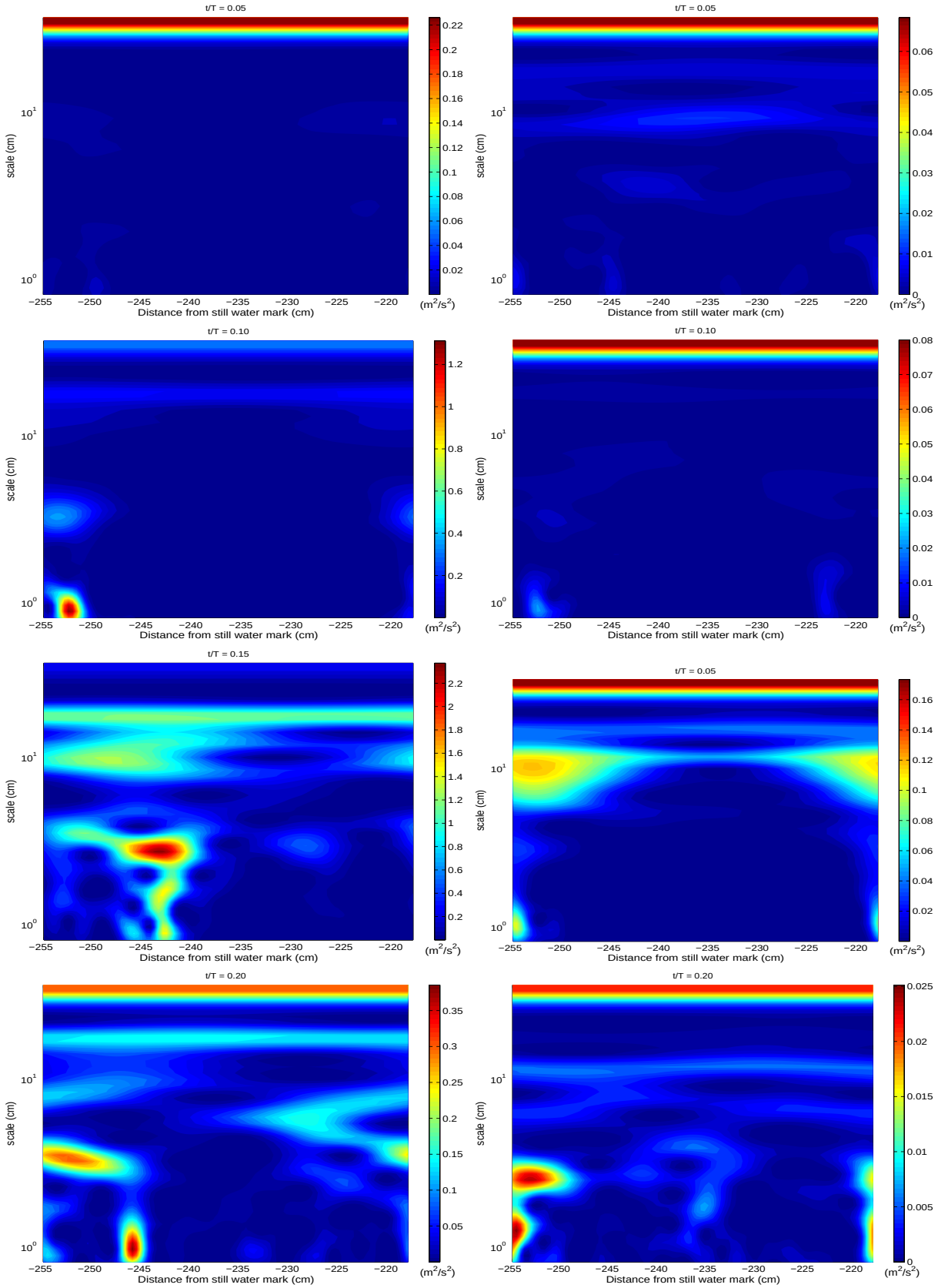

Figure 9.12: Energy spectra of horizontal velocity fluctuations measured at two other elevations : column (a) z = -5 cm and (b) z = -10 cm.

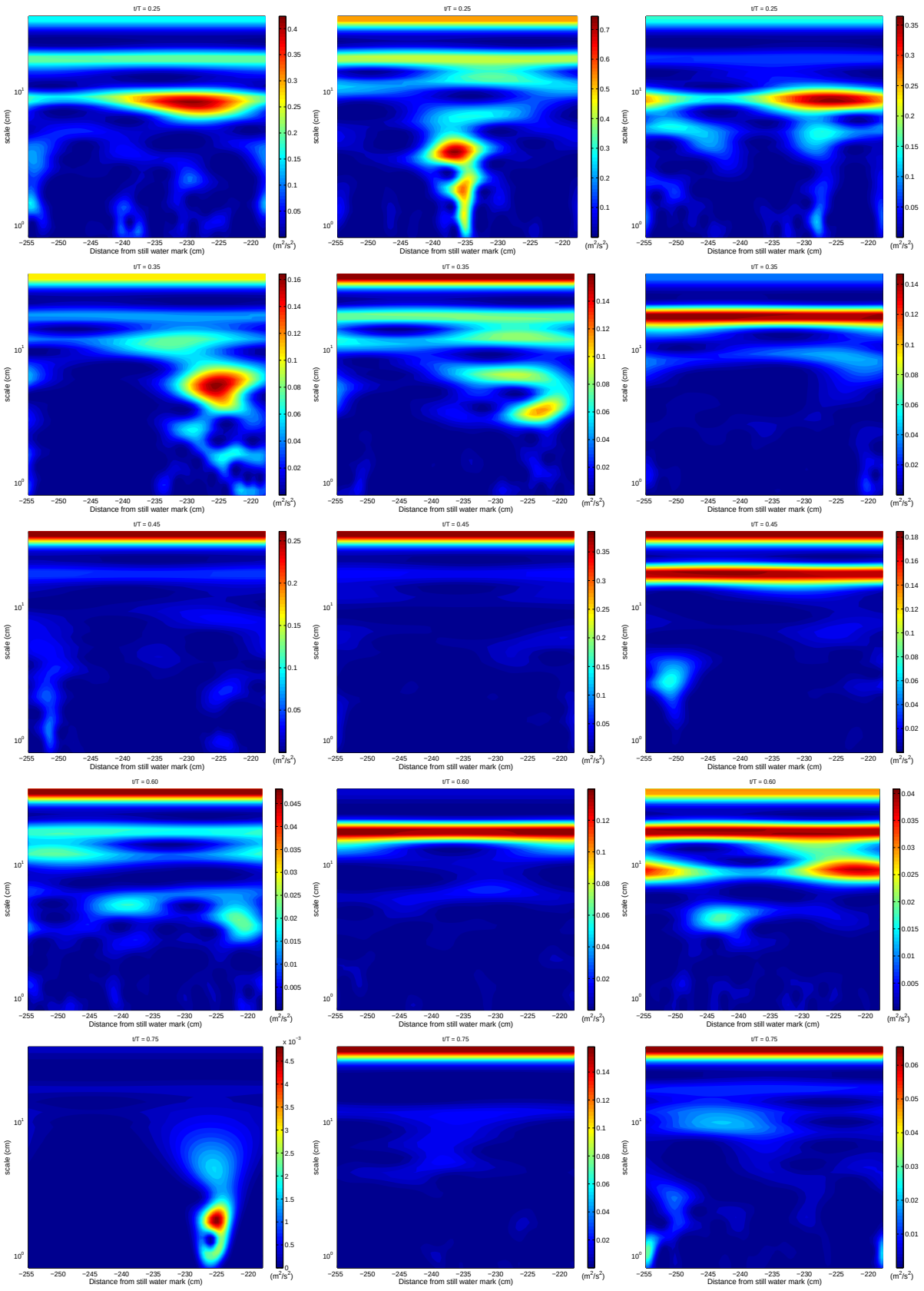

Figure 9.13: Energy spectrum of horizontal velocity fluctuations at later phases of the flow, measured at different elevations : column (a) z = 0 cm (b) z = -5 cm and (c) z = -10 cm.

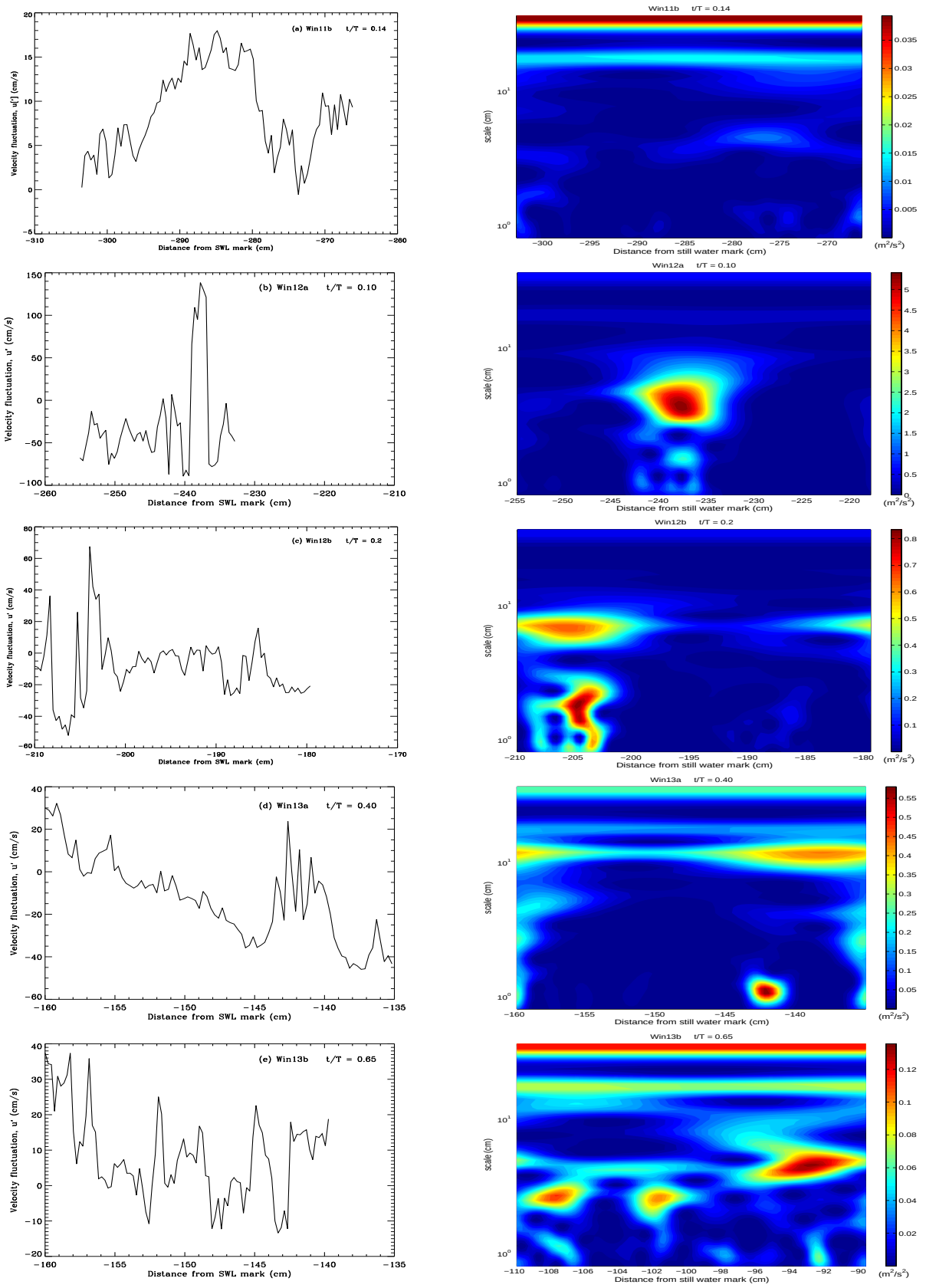

Figure 9.14: Column (a) Velocity fluctuation signals at elevation $z = 0$ cm measured at different cross-shore locations corresponding to the five measurement stations (b) corresponding energy spectrum.

locations corresponding to the five measurement stations, while Figure 9.14(b) shows the corresponding energy spectra. Just after breaking (win11b), most of the energy is confined in the large scales, moving to small scales as flow gets closer to the shore. Peak energies of up to 5 m^2s^{-2} are observed at station 12a, and decreases towards the shore.

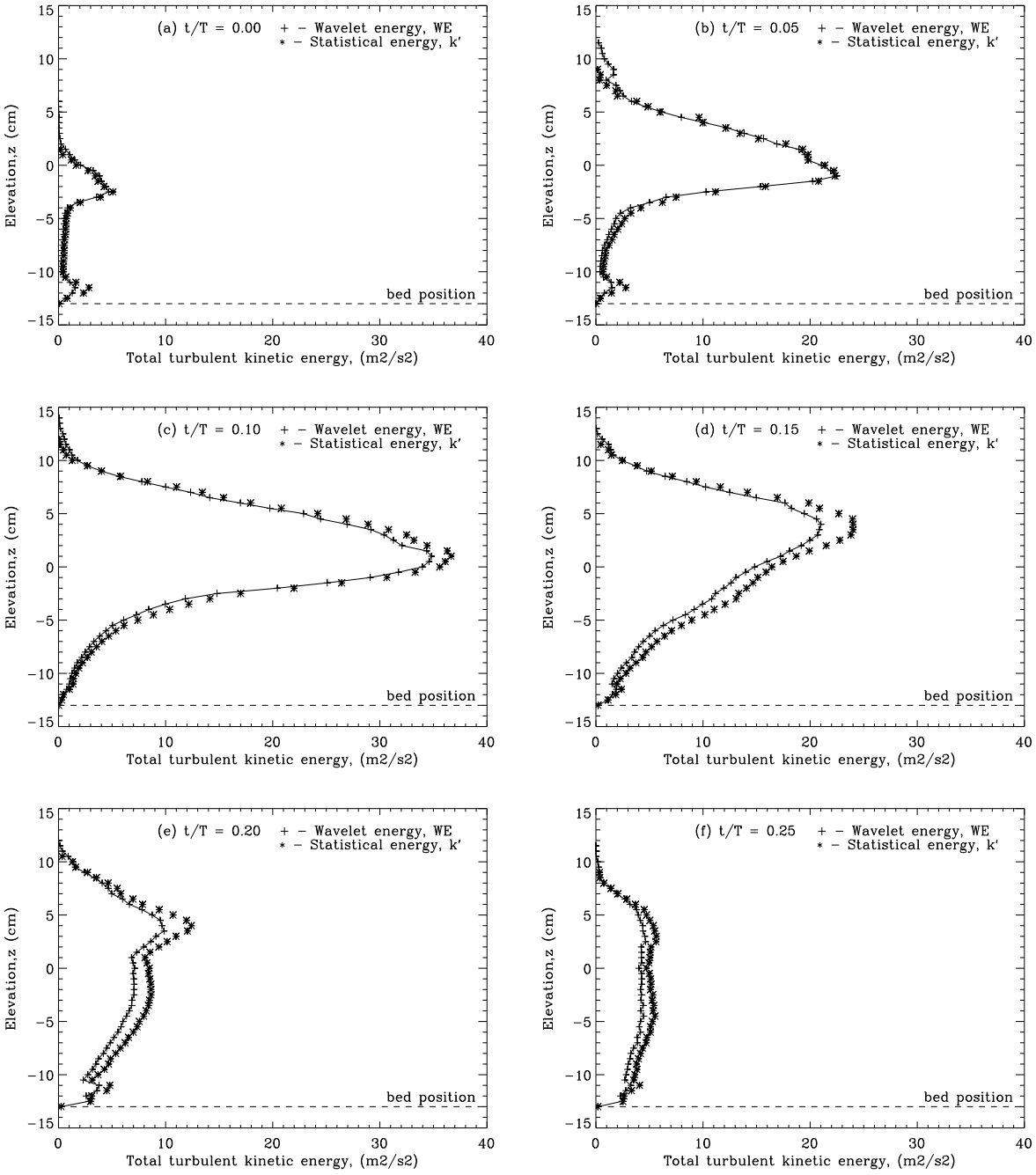

Figure 9.15: Comparison of the turbulent kinetic energy computed using wavelet coefficients, against turbulent kinetic energy, k', obtained using statistical approach, for the six phases at station 12a.

In order to authenticate wavelet results of turbulent kinetic energy, the statistical computation of the phase-ensemble -average turbulent kinetic energy, k', for each phase, presented in chapter 7, were summed up at each elevation and compared with the wavelet energy at the same elevation for station 12a. Figure 9.15 show plots that compare these two energies for the phases under consideration. There is good

agreement for all the phases. For those phases that include the crest, peak values of the total energy are observed around elevation $z = 0$ cm, which is near the shear layer region. The two approaches give total turbulent kinetic energy which is high for those phases corresponding to the wave crest. When the crest has passed, both turbulent kinetic energies are observed to decrease with increasing phase. Results for the rest of the trough phases show little variation as flow progresses.

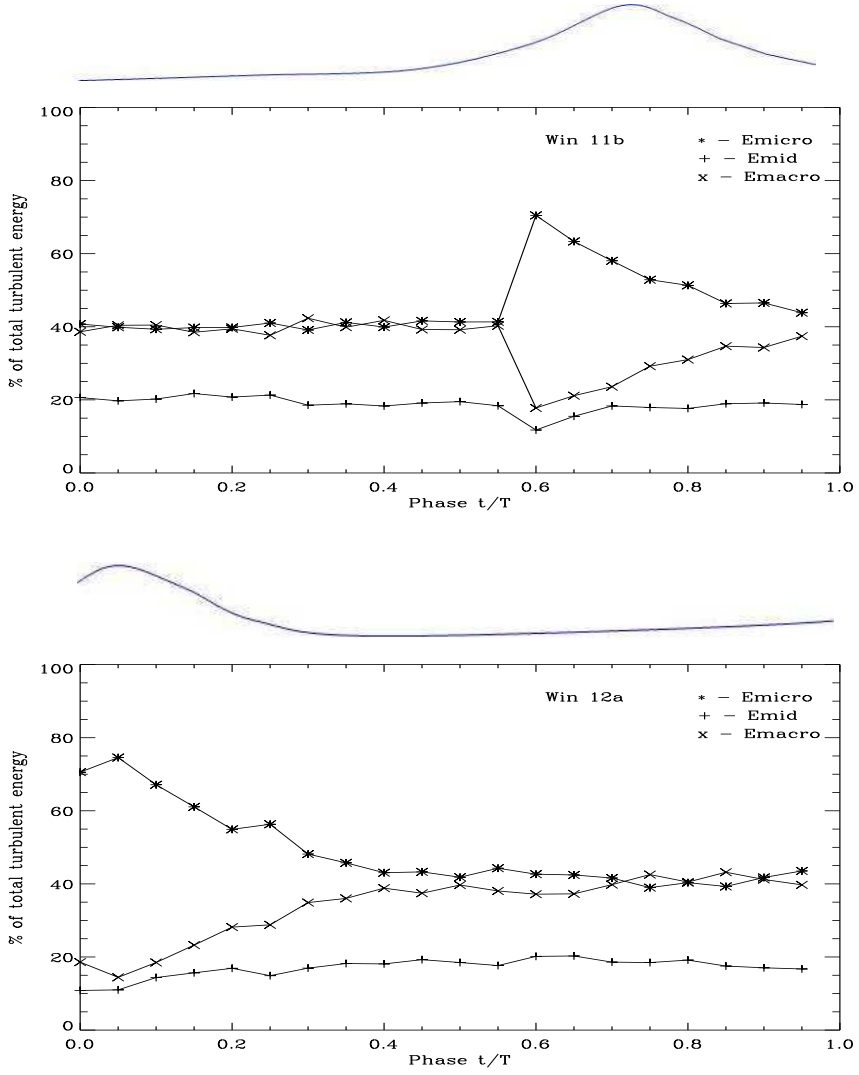

Figure 9.16: Phase variation of the energy contribution by scale bands to the total wave energy at stations 11b and 12a. The position of the crest in the cycle is shown by the wave profile provided at the top of each graph.

Figure 9.16 shows the phase variation of turbulent kinetic energy contained in the three scale bands for stations 11b and 12a, while Figure 9.17 shows the same information for stations 12b, 13a and 13b. *Longo* [215], observed that macro scale energies appear uniformly distributed at the different phases. Micro scales in this case contain more energy than in the *Longo* [215]. This may be because the scales which are used to define these energy bands are arbitrary. The micro scale band going up to 16 cm in this case, is wider than the 10 cm used by *Longo* [215]. The wavelength of the waves used is about 6.0 m, yet the camera could only view a section about 37.1 cm wide. This means the largest scales that could be measured was limited to 37.1 cm whereas *Longo* [215] could measure up to 4.0 m. The lack of well defined boundaries separating the scale bands makes direct comparisons difficult.

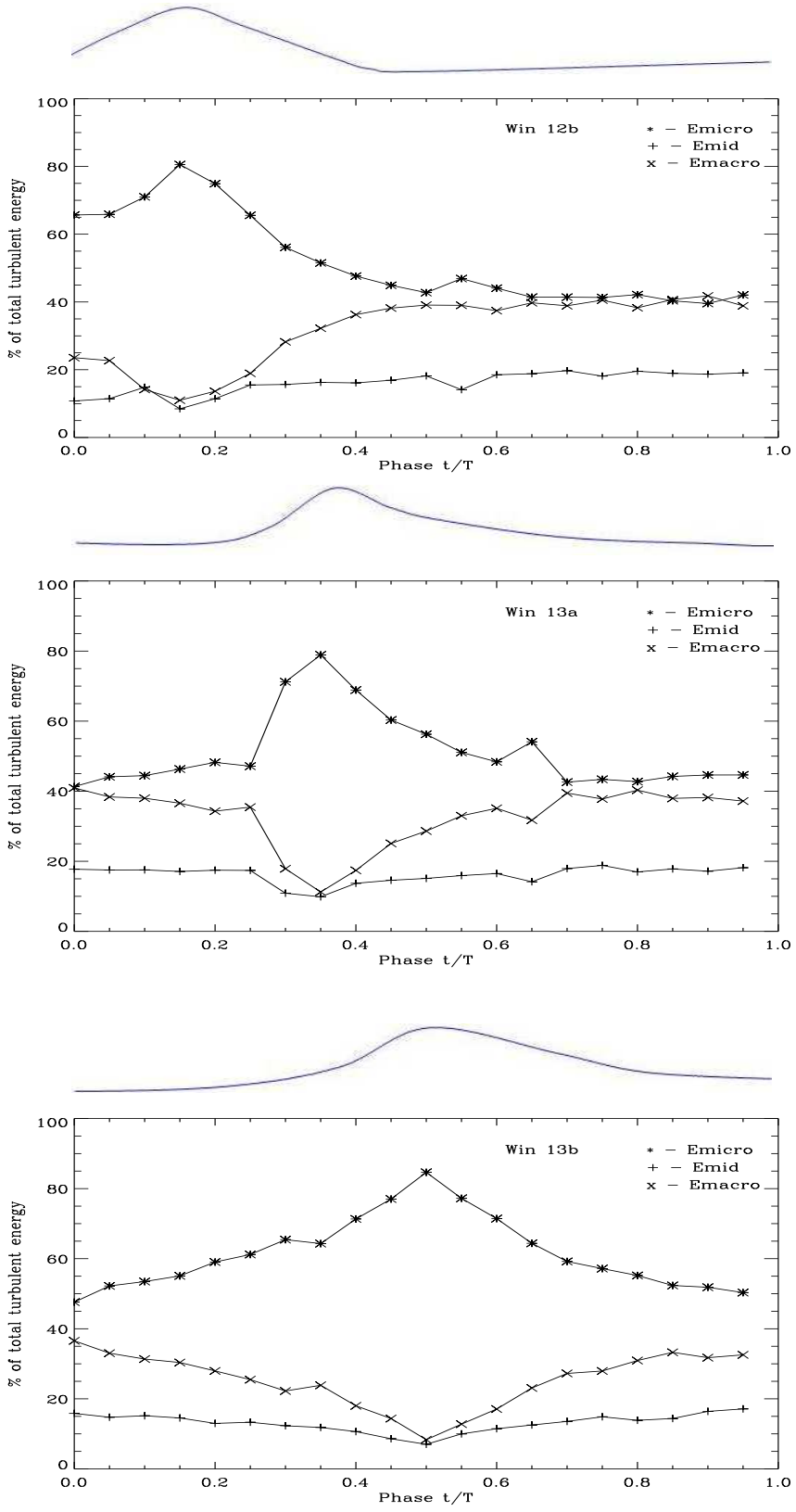

Figure 9.17: Phase variation of the energy contribution by scale bands to the total wave energy at stations 12b, 13a and 13b. The position of the crest in the cycle is shown by the wave profile provided at the top of each graph.

Results for all the stations show that mid scale energies are observed to uniformly contribute about 15 % of the total energy throughout the entire wave cycle. In addition, energy in the macro scales appear

almost uniformly at all phases that do not contain the crest, representing a base contribution of 40 % of the total energy. From the phase just before the crest appears, there is a sudden dip/decrease in the macro scale energies and a corresponding increase in the micro energies. This is an indication of transfer of energy from macro to micro scales due to breaking. As flow progresses from the early phases, macro scale energies are observed to gradually increase their contribution from about 20 % up to peak contributions of 40 %. The lost mid-scale energies is transferred to the micro scales which are observed to suddenly increase at the same phases reaching a maximum contribution of 80 % as observed at all the stations. As the crest passes, the micro energies decrease their contribution, from 80 % reaching and maintaining a 40 % contribution at later phases. After the crest has passed macro scales increase their energy while the micro scales decrease. The decrease in micro-scale energy observed at all stations is due to dissipation of these small scale energy while the increase for the macro scales signifies extraction of the energy from the wave. Micro scales are observed to contain most energy at all the 5 measurement stations and at all the elevations considered. Micro scale energies, which are dominant at the early phases, gradually decline. *Seena & Sung* [92] observed that micro-scale energies decrease, probably due to viscosity effects through which small scale features get dissipated as they convect downstream.

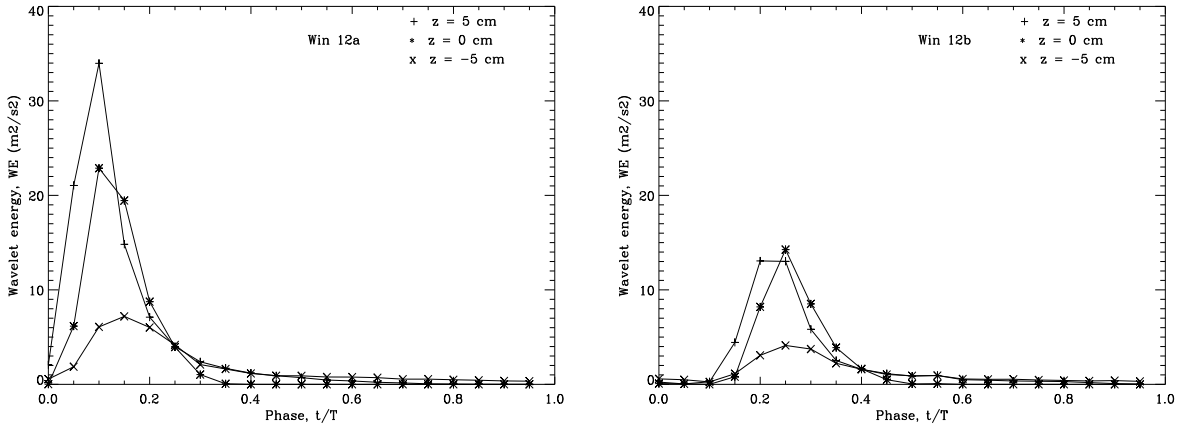

Figure 9.18: Phase variation of the total turbulent wavelet energy at different elevations for stations 12a and 12b.

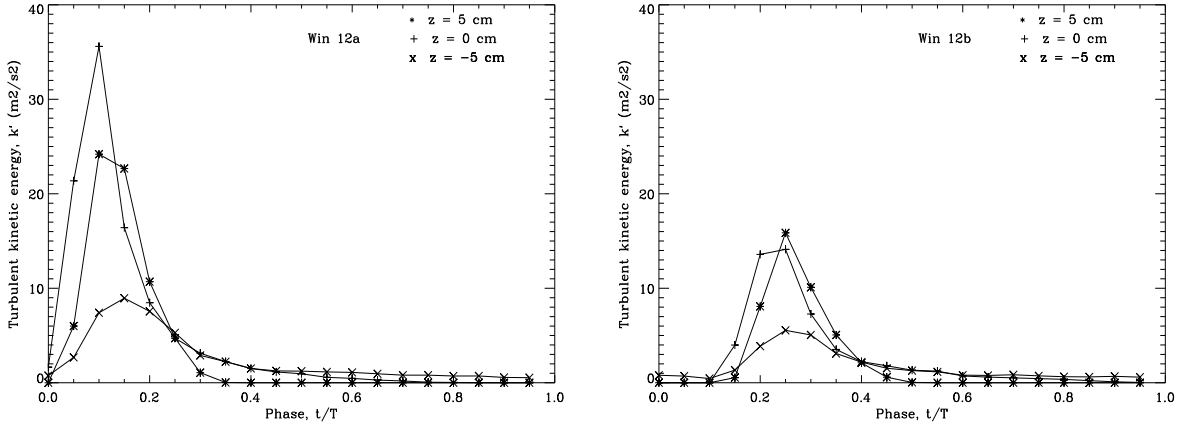

Figure 9.19: Phase variation of the total statistical turbulent kinetic energy, k', available at different elevations for station 12a and 12b.

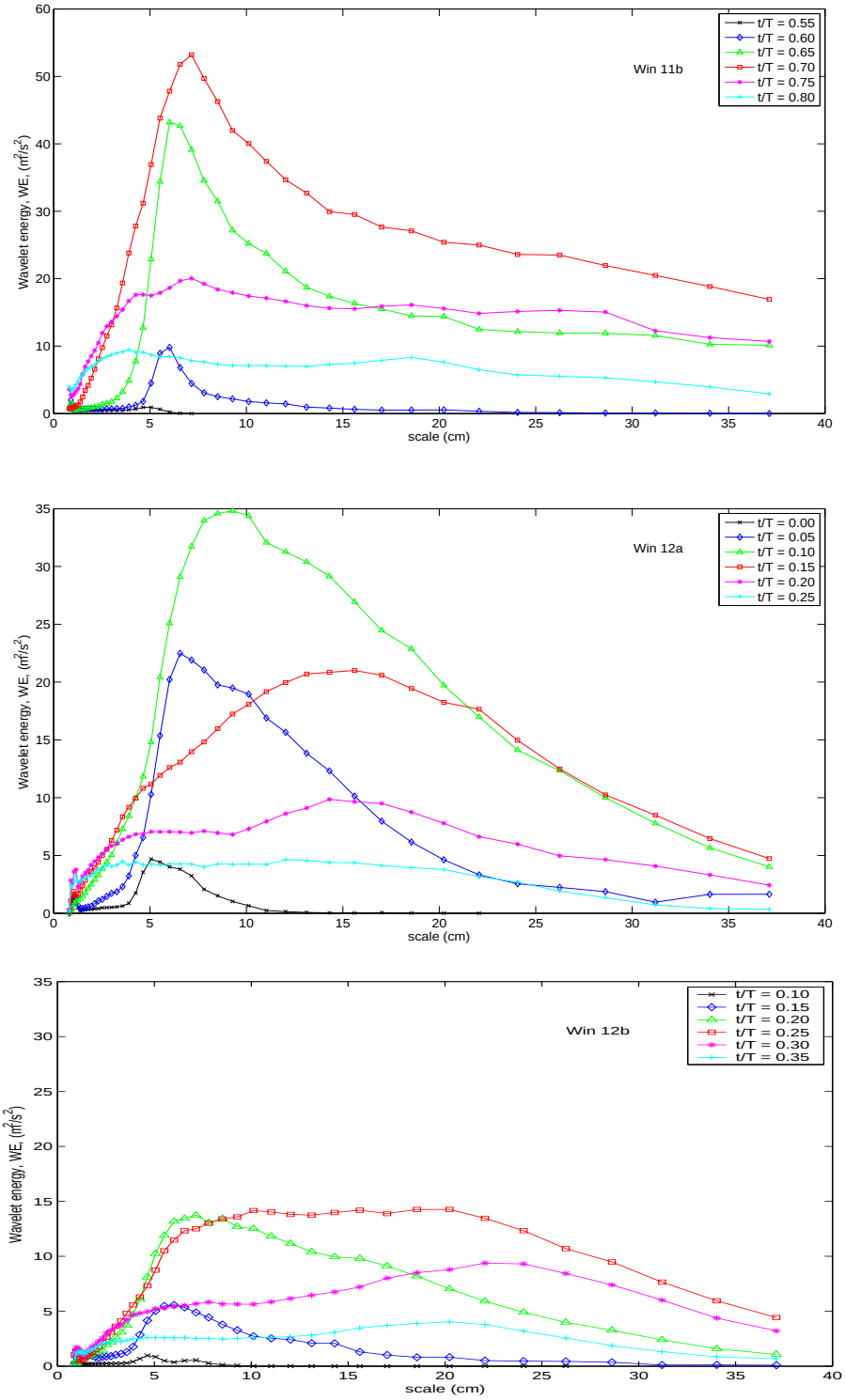

Figure 9.20: Variation of total wavelet energy with scales at different phases at stations 11b, 12a and 12b. Legends indicate the phases corresponding to regions in the vicinity of the crest.

Figures 9.18 shows the phase variation of total wavelet energy at different elevations $z = +5$ cm, 0 cm and -5 cm at stations 12a and 12b. These plots compare well with Figure 9.19 which shows the variation with phase of the total turbulent kinetic energy, k' available at the same elevations, calculated using the statistical approach. At all the three elevations, both wavelet and statistical kinetic energies are observed to be high for those phases that include the crest, and gradually decreases as flow progresses. Compared

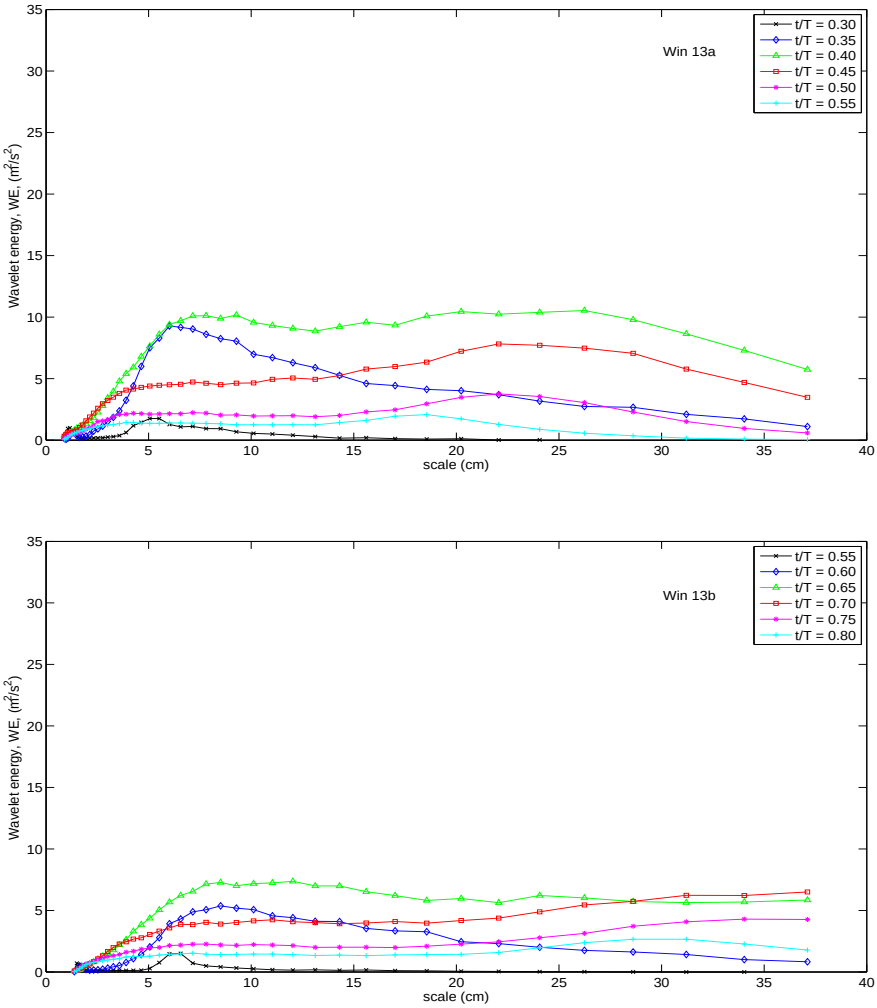

Figure 9.21: Variation of total wavelet energy with scales at different phases at stations 13a and 13b. The legends indicate the phases corresponding to regions in the vicinity of the crest.

to energies at other elevations, both wavelet and statistical energies are lowest at z = -5 cm for phases that include the wave crest.

Figure 9.20 shows the variation of total wavelet energy with scales for different phases as flow progresses, for stations 11b, 12a and 12b. Figure 9.21 shows wavelet energy at the other stations 13a and 13b. The total energy per each scale was obtained by summing the energy for a given scale over all the positions. The plots for stations 11b and 12, which are further away from the shore, show that the wavelet energy is skewed towards small scales. For stations 11b and 12a, it is observed that most of the energy is confined in the small scales, between 5 cm and 15 cm which correspond to the micro-scale band, for all the phases presented. Thus most of the energy is confined in the small scales and the available energy of the wave decreases towards the shore. On the contrary, for stations 13a and 13b, the plot of Figure 9.21 shows the available energy to be more or less uniformly distributed among the scales for all the phases presented. Results for all the stations tally with earlier observations noted in chapter 6 and 7 that showed the flow becoming almost homogeneous at later phases of the flow.

The available total wave energy was separated into three different energy bands at each elevation. Fig-

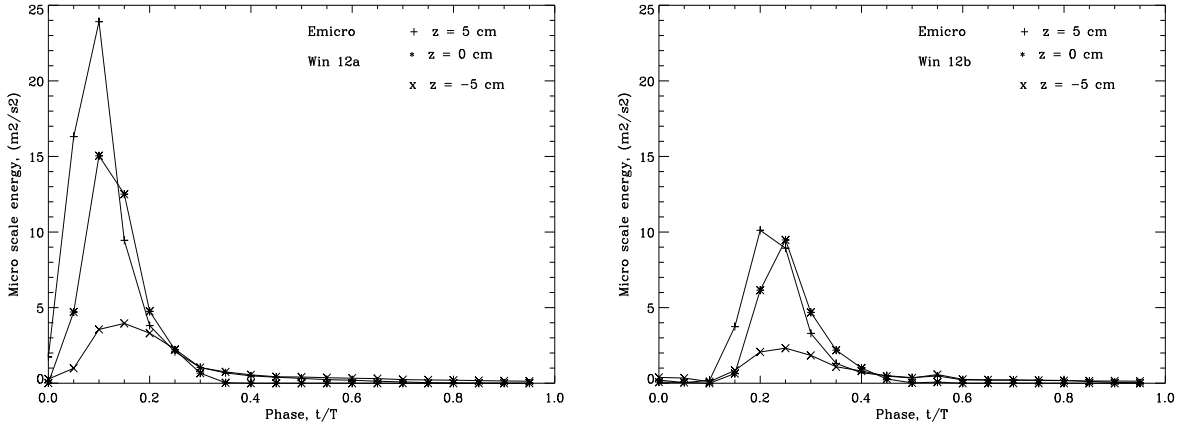

Figure 9.22: Phase variation of the micro-scales turbulent wavelet energy at different elevations for station 12a and 12b.

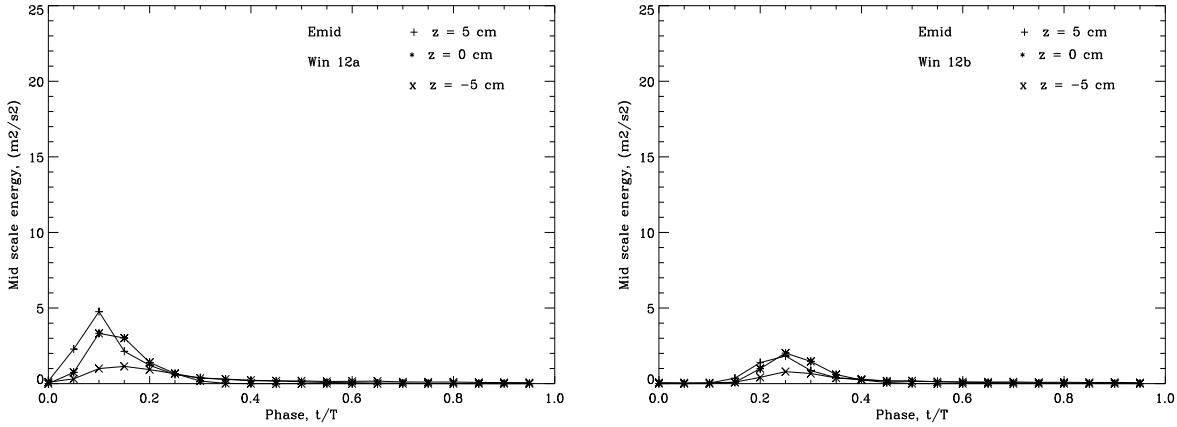

Figure 9.23: Phase variation of the mid-scales turbulent wavelet energy at different elevations for station 12a and 12b.

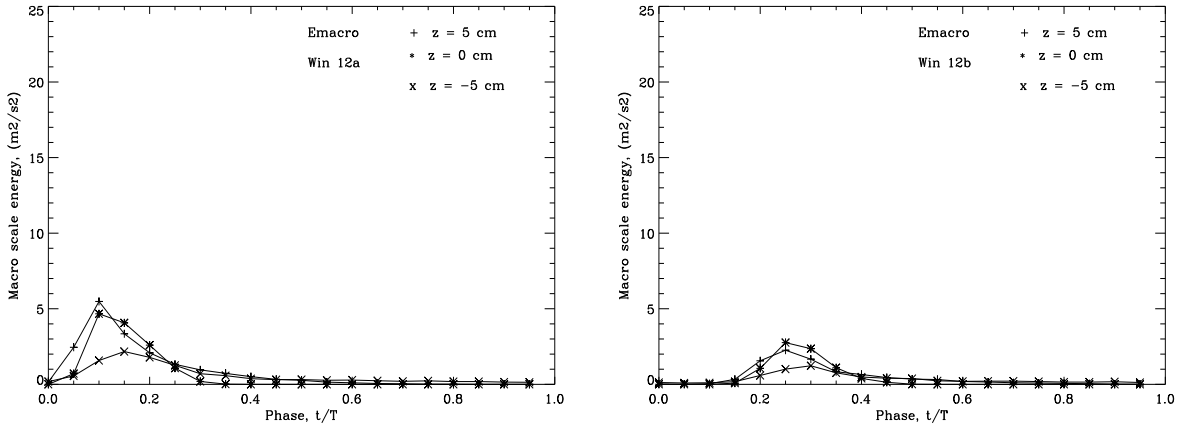

Figure 9.24: Phase variation of the macro-scales turbulent wavelet energy at different elevations for station 12a and 12b.

ures 9.22, 9.23 and 9.24 show the phase variation of the micro, mid and macro scale energies, respectively, with elevation at stations 12a and 12b. At both stations, the largest contribution comes from the micro scales, while the mid and macro scale energy contributions are almost the same at particular elevations

for both stations. For station 12a, the scale band energies are highest at all three elevations for phases 0.00 to 0.15 while for station 12b, highest scale band energies are observed at phases 0.10 to 0.25.

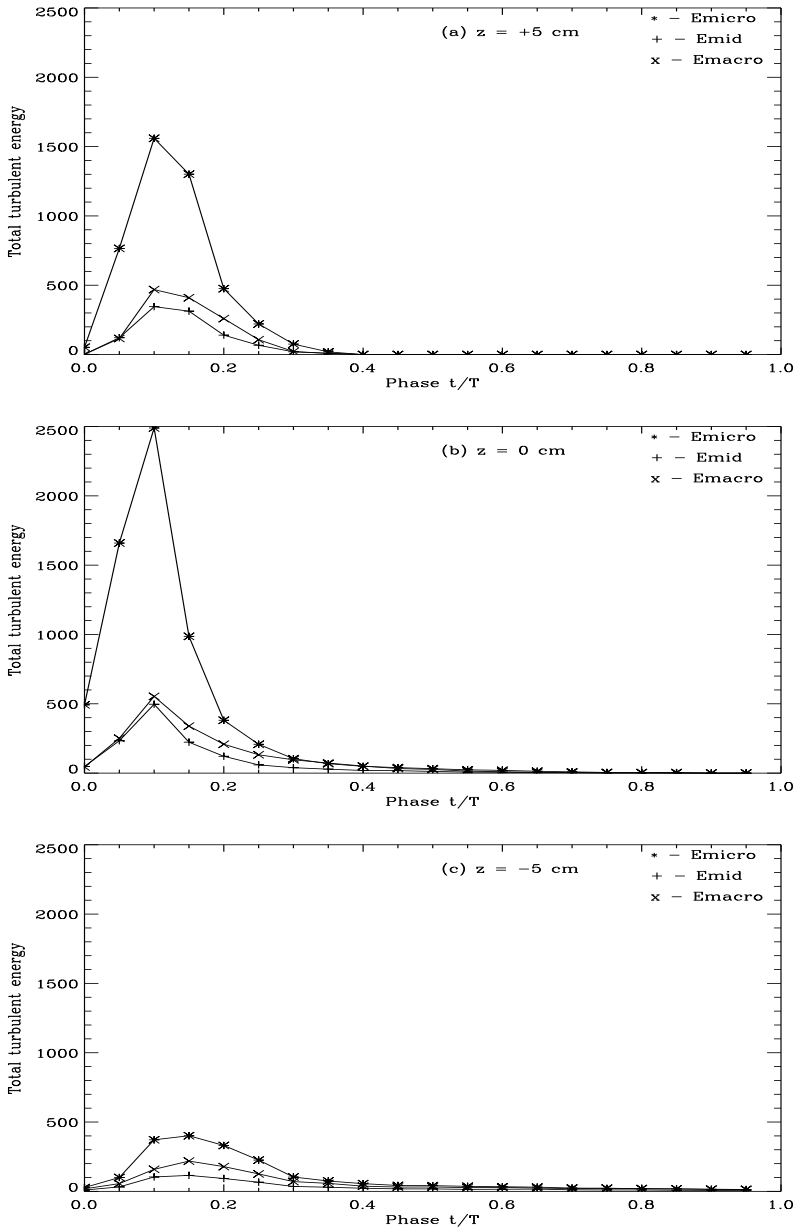

Figure 9.25: Phase variation of the average turbulent scale band energy at elevations z = +5 cm, 0 cm, and -5 cm for station Win 12a.

Figures 9.25 shows the phase variation of average turbulent kinetic energy measured at three different elevations at station 12a. The averages were computed at different elevations over several cycles for each phase. Appreciable energy is available only for the first few phases in the wave cycle. Results show that at all three elevations considered, the micro scale energies provide the highest contribution to the total energy, while the mid scales provide the least. Considering results from the three elevations, the micro energy is highest at elevation $z = 0$ cm and least below the SWL (z = -5 cm). There is very little change, if any, in the mid-scale and macro-scale energies at elevations $z = 0$ cm and $z = +5$ cm.

9.7 Summary

The continuous wavelet transform has been applied to analyze horizontal velocity fluctuations so that localized regions of energy concentration can be identified. The variation with depth of the total amount of turbulent kinetic energy obtained using wavelet analysis at each elevation was presented. The wavelet energy results show good agreement with the turbulent kinetic energy calculated using statistical approach, presented in chapter 7, for the entire wave including the aerated region above the troughs. The energy contribution at different scales and different phases of the wave cycle has been presented. Micro scales are observed to contain most energy at all the 5 measurement stations and at all the elevations considered. Mid scales contain about 15 % of the total energy, almost uniformly throughout the cycle. Energy analysis of velocity fluctuations reveal that at later phases, corresponding to the wave trough, most of the energy contribution comes from the macro scales while the energy content of the micro scales diminish as flow progresses. This is due to viscosity effects, where the smaller scale features are dissipated as they convect downstream (*Seena* & *Sung* [92]). During the early phases of the flow, which correspond to the approach of the crest, the micro scales contribute up to a maximum of 80 % of the energy. For the rest of the phases, the contribution drops to about half (40 %). During this time, much of the energy in the velocity fluctuations is confined in the small scales, gradually shifting to higher scales as flow progresses. It is observed that as flow progresses, there is strong exchange of energy between only the mid and the macro scales, with a negligible contribution from the micro scales. The normalized energy profiles revealed an accretion of energy in the mid scales for increasing wave phase. As was observed by *Seena* & *Sung* [92], maximum energy in the wave was observed near the shear boundary layer and almost centered around z = -5 cm or $h/h = 0.5$, in the transverse direction for most phases.

Chapter 10: Conclusions and recommendations

" *There will be a time when you believe everything is finished. That will be the beginning.*"

- Louis L'Amour

An experimental study was successfully undertaken to determine breaking wave transformation and turbulent flow hydrodynamics associated with a laboratory generated plunging breaker. Controlled laboratory experiments were conducted to determine the phase evolution of two-dimensional velocity flow fields. Spatio-temporal evolution characteristics of the flow structures generated by plunging wave breaking were investigated by performing the DCIV measurement of the flow fields. Images of the breaking wave were captured using a digital camera. Digital analysis that employed cross-correlation techniques was done to extract velocity flow fields from the images. Statistical and wavelet analysis were then performed on the velocity flow fields to understand how the turbulence evolves. Results of the evolution of turbulence structures such as turbulence intensity, turbulent kinetic energy and vorticity have been presented. The following sections summarize experimental results for water level and wave transformation measurements and velocity and turbulence flow field measurements. This chapter concludes by pointing out research directions for the future, which the experimental work and results reported in this dissertation could be further steered.

10.1 Water level measurements

Water level measurement results have been presented of the study that involved measuring, in the vicinity of the break point, external flow characteristics of a 0.4 Hz plunging breaker. This was done to get prior information about the breaking behaviour of the wave in terms of surface elevation, wave heights and wave phase velocities in the vicinity of the break point. Time series measurements of free surface elevation for monochromatic waves were made using capacitive wave gauges. Mean water levels, wave heights and phase velocities were determined from the water level time series. Results show that as the wave propagates from deep water towards shallow water, there is an increase in the wave height, reaching a maximum height at the break point, and then decreases sharply thereafter. The measured mean water levels were observed to vary from around -4 mm just before the break point to about 14 mm towards the shore. Wave heights at several positions along the flume were later estimated from the measured surface

elevations. The wave height rises from 12 cm near the wave generator to about 21.5 cm at the breakpoint before decreasing sharply to around 10 cm after breaking. This decrease in wave height after breaking is due to loss of energy through currents and turbulence. Local wave phase velocity for points 0.2 m apart was estimated using cross-correlation techniques and showed that linear shallow water approximation underestimates the phase speed. A comparison was made between the measured wave phase velocity, its linear shallow water and modified linear wave velocity approximation, at various points along the flume. In the vicinity of the break point, the measured phase velocity was observed to lie in the range $\sqrt{gh} < c < 1.3\sqrt{gh}$. It was observed in this study that the wave phase velocity does not depend on depth (linear theory), but increases just after the break point. This may be as a result of the energy released by the breaking process.

10.2 Velocity flow fields and turbulence measurements

A second set of experiments involved an experimental investigation of the spatial and temporal evolution of turbulence structures in the vicinity of the break point in regular breaking water waves. Measurements were made of horizontal and vertical velocities, including turbulent fluctuations, in a turbulent flow in both the aerated wave crest and the trough level. Fluid velocities were measured by tracking the motion of almost neutrally buoyant particles as well as bubble structures formed by breaking waves. Using a high-speed digital camera and digital correlation image velocimetry techniques, gray-scale image frames of the flow field were captured and analyzed to yield instantaneous velocity maps. The Reynolds decomposition technique was then applied to the measured instantaneous velocity fields to obtain the mean and turbulent components. Using decomposed instantaneous velocity fields, fundamental turbulence characteristics such as turbulence intensity, turbulent kinetic energy and vorticity were calculated to verify the contribution of the mean and turbulent components to the flow. Detailed measurements of the cross-shore and along shore profiles of the turbulence parameters have been presented.

The measurements showed that the horizontal component of the instantaneous and mean flow velocities were about 4 to 5 times the vertical component. Measurements of the forward and reverse mass fluxes indicate a relative fluid density in the crests of this plunging breaker to be in the range 0.3 to 0.4 at station 12a. Relative density measurements along the flume showed a general increase towards the shore. For a particular wave phase the spatial variation of the turbulence parameters increase rapidly above the trough, reaching maximum values just above the still water line and decreasing towards the crest. Quantitative figures of the spatial and temporal distribution of high concentrations of entrained air for plunging breakers indicate that higher concentrations are confined above the still water level. Peak turbulence parameters were observed near the front part of the wave crest with peak values of 0.11 and 0.06 for normalized horizontal and normalized vertical turbulence intensities, respectively. Time-averaged turbulent kinetic energy was observed to be twice that widely reported in literature, especially for the trough level. Reasons for the underestimation of this energy have been suggested. Peak turbulent kinetic energy values were of the order of 0.5 $m^2 s^{-2}$. It was observed that below elevation $z/h = 1.0$, the Froude-scaled time-averaged turbulent kinetic energy, $(\overline{k'}/gh)^{1/2}$ decreases towards the shore.

Normalized time-averaged turbulence components $\overline{u'}/c$ and $\overline{w'}/c$ and the Froude scaled time-averaged turbulent kinetic energy $(\overline{k'}/c^2)^{1/2}$ show nearly exponential decay towards the shore. The instantaneous vorticity fields were observed to be characterized by patches of pairs of counter-rotating eddies. These pairs are generated at the free surface and translated as single units in the direction of the flow. Peak magnitudes of both instantaneous and mean flow vorticity generated by wave breaking, are one order of magnitude greater than the phase speed divided by local depth, c/h.

Lastly, a 1-D continuous wavelet transform was applied to the velocity fluctuations data at each elevation. This wavelet-based algorithm was used to decompose turbulence energy into contributions at different scales/frequencies and different x-locations from the SWL mark. The energy in the signal was subdivided into micro, mid and macro scales and the contribution of each of these bands to the total energy, was determined. During the early phases of the flow, micro scales contribute 40 % of the total wave energy. Results from all five stations show that mid-scale energies were observed to uniformly contribute 15 % of the total energy throughout the entire wave cycle. Macro scales energy appear almost uniformly at all phases that do not contain the crest, representing a base contribution of 40 % of the total energy. As flow progresses from the early phases, macro scale energies are observed to gradually increase their contribution from about 20 % up to peak contributions of 40 %. The lost mid-scale energies is transferred to the micro scales which are observed to suddenly increase at the same phases reaching a maximum contribution of 80 % as observed at all the stations. As the crest passes, the micro energies decrease their contribution, from 80 % reaching and maintaining a 40 % contribution at later phases. The rest of the energy previously in the micro scales is transfered to the macro scales, leading to an increased contribution by macro-scales of about 40 % to the total energy for the remainder of the flow. Micro scale energies, which are dominant at the early phases, gradually decline, by giving away some energy to the macro scales. This is probably due to viscosity effects through which small scale features get dissipated as they convect downstream (*Seena & Sung* [92]). The variation of wavelet energy with scales measured at different stations has shown that most of the energy is confined in small scales and decrease towards the shore.

10.3 Research contributions

With the aim of developing a better understanding of the two-phase flow in laboratory breaking waves, detailed measurements have been made that provided insights into the breaking wave dynamics. The research project was successfully completed and the goals set have been met with specific research contributions listed below.

- First and foremost, little information is available in literature on the turbulence generated by plunging waves. The plunging wave used in this study is not easy to experiment with, because this wave is characterized by strong air entrainment which causes bubbly flows. If such a flow is imaged, the bubbles distort the optical rays between the image and acquisition planes. This usually results in blurred images of the illuminated seed particles which lead to poor image correlations and inaccurate flow velocity measurements. It is for this reason that most of the published work reported in literature are largely

for spilling breakers, or plunging breakers of very shallow depth (*Huang et al.* [115]; *Huang et al.* [44]). Unlike some previous researchers who were limited by their facilities and used only up to 5 cm of water in the flume (e.g *Huang et al.* [64]; *Sou et al.* [75]; *Cowen et al.* [60]), the flume used in this work was filled with water up to about 62 cm. This enabled the generation of big amplitude waves of about 12 cm. Many researchers have reported on laboratory observations of turbulence characteristics in the surf zone but have largely been restricted to below the trough level.(e.g. *Chang & Liu* [41]; *Shin & Cox* [67]; *Lennon & Hill* [120]). This contribution provides velocity measurements for the entire wave including the aerated region above the trough level.

- In this study ordinary white light and not lasers is employed to illuminate white polystyrene beads and bubble structures to obtain flow patterns. Laser light is coherent, so if used, scattering from bubbles and beads will cause speckle patterns making it difficult to do cross correlations that are necessary for obtaining particle displacements. Contrary to most measurement techniques reported in literature, internal flow structures of the surf zone were investigated by optically accessing the flow from vertically above the flow.

- In the wave transformation results, cross correlation techniques have been successfully employed to determine the phase difference between the reference wave near the generator and the wave at various points along the flume. The local wave velocity was then obtained by taking the phase difference between two points spaced 0.2 m apart. Measurements of the wave phase velocity are provided at various points along the flume. Results show that whilst the measured wave phase speed lies between the linear shallow water approximation and the non-linear, roller model concept values, the wave speed at the break point goes up to 38 % and 5 % times higher than the linear and non-linear values, respectively.

- Instantaneous velocity flow fields were successfully measured for several wave phases along the surf zone. These flow fields demonstrated that instantaneous velocity flow fields obtained reveal the structure formed by the whitecap in the images. These instantaneous velocities were further analyzed to yield turbulence intensities and turbulent kinetic energies whose peak values were found to occur in the crest of the breaking waves and were confined above the still water level. The extensive and highly resolved dynamic experimental database was obtained under plunging conditions in water depths of more than 20 cm.

- The spatial distribution of the velocity flow fields was presented for a plunging wave for different phases. Flow visualization was accomplished by using filled contour plots which showed the global flow structure of spatial and temporal evolution of the turbulence. In addition the vertical and cross shore profiles of the turbulence parameters are also presented, which reveal the phase evolution of turbulence structures in the flow. Quantitative figures of the spatial and temporal distribution of velocity flow fields and high concentrations of entrained air for plunging breakers indicate that higher concentrations are confined above the still water level. Profiles of the variation of mean and fluctuating turbulence parameters with depth are provided.

- One of the outstanding contributions from this work comes from time-averaged turbulent kinetic energy results. These were measured at several locations along the flume and show completely new

results. The energy is higher than what most previous researchers obtained, particularly in the trough part of the wave. Probable reasons for the differences include the fact that a more dynamic wave was used here in which turbulence was observed to be high throughout the entire wave. In addition laser techniques used by previous researchers may not be accurate enough to do measurements especially in the plunging breaker where bubbles diffuse to the flume bed. This may lead to an underestimation of turbulence.

- Other statistical quantities that were determined are the root-mean-square of the fluctuations of the horizontal and vertical velocities, turbulence intensity, turbulent kinetic energy and vorticity of the flow. In order to further understand the fluid dynamics in the breaker, vorticity components that include, instantaneous vorticity and vorticity of mean flow were presented. Instantaneous vorticity measurements revealed the existence of pairs of counter-rotating eddies near the free surface. These were observed to have the same orientation in the flow and propagated as units. As flow progresses, observed eddies slow-down and vanish slowly when they go deeper, dissipated by bottom friction and slowed down by mean return flow. The magnitudes of both instantaneous and mean flow vorticity generated by wave breaking, are one order of magnitude greater than the phase speed, c, divided by local depth, h.

- The complex Morlet wavelet was successfully employed to analyze velocity fluctuation data at each elevation, for all the cycles in each phase. This was done in order to determine the average amount of wave energy available. The wavelet energy results were compared against the statistically computed turbulent kinetic energy, and show very good agreement. Another significant contribution was the quantification of the contribution of different scales of the turbulent flow to the total energy. The variation of the wavelet energy as flow progressed is also presented, and so is the phase variation of the average wave energy at different elevations.

- Proper equipment and experimental procedures were employed to gather information relating to breaking waves. Then digital, statistical and wavelet analysis were successfully applied to study the spatial distribution and evolution of the generated turbulence. This dissertation has provided some new and interesting insights into the turbulent dynamics of plunging breakers through an experimental study which will lead to better understanding of the complicated phenomena in breaking waves. The research has generated an extensive and consistent data base of detailed flow field measurements of a plunging breaker. It is believed that the techniques developed and the procedures implemented for this study represent an efficient and effective means of investigating the phenomena of breaking waves. It is also believed that these results may provide a useful insight on the characteristics of turbulent flow which could be used for checking the validity of mathematical models normally developed for turbulence studies.

This DCIV technique was capable of capturing the fine spatial and temporal evolutions of the structure of the turbulent flow. The work presented here is just one step in attempting to understand the evolution of turbulence structures in breaking waves. As Louis L'Amour famously wrote, "*There will be a time when you believe everything is finished. That will be the beginning*". Further work is still required to fully understand turbulence dynamics.

10.4 Recommendations for future work

This research provided answers to key questions raised in section 1.6.1 of chapter 1, and perhaps raises new other questions. The author believes that the current state of knowledge about the turbulent flow under breaking waves is still nascent, and there are numerous other aspects beyond those few studied in this dissertation, which may need attention, both theoretically and experimentally. At this point a summary is made that outlines ideas for future research related to this work. Further work on this thesis could be extended in two ways, which could be divided into two broad areas, namely : (i) further data analysis and (ii) improvement of experimental techniques.

10.4.1 Further data analysis

The fundamental parameter that has been successfully measured is the velocity flow field. All turbulence parameters can be derived from this parameter. For the sake of brevity, this dissertation has only focused on a few turbulence parameters, such as turbulence intensity, mass flux, turbulent kinetic energy and vorticity. However, other parameters may be derived from the velocity data as when required. The most obvious extension to this study is further data analysis aimed at further extracting more useful information that could enhance our understanding of the phase evolution of turbulence in plunging waves. Further analysis of other specific turbulence parameters is suggested for a more full understanding of the processes dominating the breaking. There are several routes that can be taken to achieve this objective, namely:

- further analysis of the velocity flow fields to extract Reynolds stresses, turbulence production and dissipation rates, *Kolomogrov* length scales and mixing lengths, among others.

- coherent structures embedded in the flow field could be detected using the vorticity-based conditional sampling method which recognizes the coherent structures by applying a vorticity threshold and finding the points of higher vorticity than the threshold value. Statistics on the number of vortices impinging on the bottom and their magnitudes could also be done.

- it would also be interesting to extract and study more properties of the wave roller, such as, size, shape and density. Estimation of the void fraction can also be done and compared with existing data in literature. An accurate estimation of the bulk of the void fraction, bubble size, population distributions and bubble count rate in the surf zone are important for understanding the two-phase flow characteristics, solving engineering problems and elucidating environmental mechanisms of the coastal areas. Void fraction at each point of the domain may be estimated by means of light intensity image analysis and using light scattering theory with a *Lambert law* to relate void fraction with light intensity. A completely new experiment using a conductivity probe could be done.

- extraction of scale lengths associated with the turbulent flows. Once the small scale structures have been identified, it is necessary to assess their importance to the overall dynamics of the turbulence by

visualizing the motions they induce and the stresses they impose both on other small-scale eddies and on the large-scale field.

• chapter 9 discussed the fundamentals of the wavelet transforms of functions of one variable, i.e. the 1-D wavelet analysis. There are also wavelets in higher dimensions such as in 2-D. Further application of such wavelets to the 2-D vorticity field is suggested in order to extract turbulence scale lengths and coherent structures in the flow. A more robust quantification of the length scales can be obtained by an analysis of the coherent turbulent structures. Representing the wavelet domain correlation maps with a 2-D wavelet diagram is a useful tool which not only shows the exact patterns of wavelet statistics, without any guess or approximation, but also displays the significance of those correlations.

• some important questions about the origin, interaction and evolution of the structures are still to be answered, so results of the present research can be used to define suitable criteria for a variety of conditional techniques that can be used to address these issues.

• In most practical applications, the surface over which flow occurs is significantly rough. Further experimental and theoretical analyses are recommended to determine the significant effects created by surface roughness on skin friction and velocity distributions.

10.4.2 Improvements of experimental techniques

Another direction for future work involves further improvements of experimental techniques employed in this study. The weaknesses and limitations of some of the tools and techniques developed in the research study have indicated the following areas as recommendations for further work.

• Use of a camera with better resolution, such as 1200×1200 pixels - not only allows a larger area of the flume to be viewed, but will eliminate the procedure of doing DCIV in two parts. This way the flow field would be examined over a larger distance, also providing better resolution of the measurements.

• Sub-pixel interpolation process is very useful for the improvement of DCIV accuracy, and is especially effective for the case when the average displacement of the particles is small between two images. It is therefore recommended that efforts should be made to improve on subpixel interpolation which affects results especially for the trough part of the wave. In the trough part displacements at some stations further from the breakpoint, may be of nearly the same order of magnitude as DCIV accuracy. To this effect it is suggested that Gaussian interpolation should be employed and its results compared to FFT interpolation used in this work.

• As previously mentioned, there is some randomness in the position of the break point, resulting in smearing when phase ensemble average is performed. Other researchers (e.g., *Petti & Longo* [58]) suggested that if a well-identified trigger is available the variable interval time average, proposed by *Blackwelder & Kaplan* [217], can produce a more correct and unbiased result to reduce long wave components compared to other methods (e.g., phase-average, moving average)(*Huang et al.* [44]). Use of a such a variable trigger is proposed so as to get more accurate results.

- Improving on techniques to deal with the problem of bad or missing vectors in the velocity fields is also recommended.

- A high-resolution numerical model based on the Reynolds-averaged Navier-Stokes equations is suggested, which could be developed to evaluate the transient two-dimensional description of the flow field under plunging breakers, and results compared against the experimental data presented here.

Bibliography

[1] Dean, R. G., and Dalrymple, R. A., 1991 : *Water wave mechanics for engineers and scientists*, World Scientific Publishing Company, Teaneck, NJ.

[2] Liiv T. : Investigation of turbulence in a plunging breaking wave. *Proceedings of Estonian Acad. Sci. Eng.*, Volume 7, pp. 58-78, 2001.

[3] Melville W.K,, Veron F., and White C.J., 2002 : The velocity field under breaking waves : coherent structures and turbulence. *J. Fluid Mech.*, Volume 454, pp. 203-233.

[4] Puleo, J. A., Beach R. A., Holman R. A., and Allen J. S., 2000 : Swash zone sediment suspension and transport and the importance of bore-generated turbulence. *J. Geophys. Res.*, Volume 105, (C7), pp. 17021-17044.

[5] Komar, P.D., 1998 : *Beach Processes and Sedimentation*, Second Edition, Prentice-Hall, Inc.

[6] Longuet-Higgins, M.S., and Stewart R.W., 1962. Radiation stress and mass transport in gravity waves, with application to surfbeats. *Journal of Fluid Mechanics*, Volume 13, pp. 481-504.

[7] Huntley D.A., 1980 : Edge waves in a crescentic bar system. In S.B. McCain (Editor), *The Coastline of Canada, Geol. Surv. Canada*. 80-10, pp 111-121.

[8] Elfrink B., and Baldock B., 2002 : "Hydrodynamics and sediment transport in the swash zone: a review and perspectives. *Coastal Engineering*, Volume 45, pp.149-167

[9] Hsiao, S.C., Hsu, T.W., Lin, T.C., Chang, Y.H., 2008 : On the evolution and run-up of breaking solitary waves on a mild sloping beach. *Coastal Engineering* Volume 55, pp. 975-988.

[10] Grilli, S.T., Subramanya, R., Svendsen, I.A., Veeramony, J., 1994 : Shoaling of solitary waves on plane beaches. *Journal of Waterway, Port, Coastal, and Ocean Engineering* Volume 120, (6), p. 609-628.

[11] `http://en.wikipedia.org`

[12] Sou I.M., and Yeh H., 2011 : Laboratory study of the cross-shore flow structure in the surf and swash zones. *Journal of Geophysical Research*, Volume 116, C03002, doi : 10.1029/2010JC006700

[13] De Vries S., Hill D.F., De Schipper M. A., and Stive M. J. F., 2011 : Remote sensing of surf zone waves using stereo imaging. *Coastal Engineering*, Volume 58, pp. 239-250.

[14] Massel S. R., 1996 : On the largest wave height in water of constant depth. *Ocean Engineering*, Volume 23, No. 7, pp. 553-573.

[15] Raubenheimer B., Elgar S., and Guza R.T., 2004 : Observations of swash zone velocities : a note on friction coefficients. *Journal of Geophysical Research-Oceans*, pp. 109.

[16] Mory M., and Hamm L., 1997 : Wave height, setup and currents around a detached breakwater submitted to regular or random wave forcing. *Coastal Engineering*, Volume 31, Issues 1-4, pp. 77-96.

[17] Harris D. L., 1976 : Wind-generated waves for laboratory studies, *U.S. Army, CORPS OF ENGINEERS, Coastal Engineering Research Center*, Technical paper 76-12.

[18] Greben J. M., Gledhill I., Cooper A., and de Villiers R., 2010 : Characterization and properties of breakwater structures modelled by a Physics Engine. *Seventh South African Conference on Computational and Applied Mechanics*, (SACAM10), Pretoria.

[19] Baldock T. E., and Swan C., 1996 : Extreme waves in shallow and intermediate water depths. *Coastal Engineering*, Volume 27, Issues 1-2, pp. 21-46.

[20] Tsai C-P., Chen H.-B., Hwung H. H., and Huang M.-J., 2005 : Examination of empirical formulas for wave shoaling and breaking on steep slopes. *Ocean Engineering* Volume 32, pp. 469-483.

[21] `http://upload.wikimedia.org/wikipedia/commons/thumb/0/0a/Surfers_at_Mavericks.jpg/300px-Surfers_at_Mavericks.jpg`

[22] Geankoplis, C., J., 2003. *Transport Processes and Separation Process Principles*, Prentice Hall Professional Technical Reference. ISBN 0-13-101367-X.

[23] `http://en.wikipedia.org/wiki/Laminar_flow`

[24] `http://en.wikipedia.org/wiki/Talk:Turbulence`

[25] Kolmogorov, A. N., 1942 : Equations of turbulent motion of an incompressible fluid. *Izvestia Academy of Sciences*, USSR; Physics, Volume 6, No.s. 1 and 2, pp. 5658.

[26] Jalali P., 2004, *Wavelets analysis in turbulence*. MSc. Thesis, Lappeenranta University of Technology, Finland.

[27] White F., M., 1974 : Viscous fluid flow. Fourth Edition. Singapore. ISBN 0-07-069710-8. *The McGraw-Hill*, Inc. United States of America.

[28] Farge M., and Schneider K., 2001, *Coherent Vortex Simulations (CVS) A semi-deterministic turbulence model using wavelets*, Kluwer Acdemic Publishers, Netherlands.

[29] Misra S. K., Kirby J. T., and Brocchini M., 2005 : The turbulent dynamics of quasi-steady spilling breakers - theory and experiments. *Center for Applied Coastal Research*, Newark, Research Report No. CACR-05-08, Center for Applied Coastal Research.

[30] Ting, F.C. K. and Kirby, J. T., 1995 : Dynamics of surf-zone turbulence in a strong plunging breaker. *Coastal Engineering*, Volume 24, 177-204.

[31] Rapp R. J., and Melville W. K., 1990 : Laboratory measurements of deep-water breaking waves. *Philosophical Transactions of the Royal Society of London. Series A, Mathematical and Physical Sciences*, Volume 331, (1622), pp. 735-800.

[32] Farge M., 1992 : Wavelet transforms and their application to turbulence. *Annual Rev. Fluid Mech.*, Volume 24, pp. 395-457.

[33] White F., M., 1999, *Fluid Mechanics*, Fourth edition, The McGraw-Hill Book Co., Singapore

[34] Tennekes and Lumely, 1972 : A first course in turbulence. Cambridge MA. MIT.

[35] Ecke R., 2005 : The turbulence problem-an experimentalists perspective. *Los Alamos Science*, Number 29, 124-141.

[36] Stive, M.J.F., 1980 : Velocity and pressure field of spilling breakers. *Proceedings, 17th International Conference on Coastal Engineering*, ASCE, pp. 547-565.

[37] Nadaoka K., and Kondoh T., 1982 : Laboratory measurements of velocity field structure in the surf zone by LDV. *Coastal Engineering*, Volume 25, pp. 125-145.

[38] Ting, F.C. K. and Kirby, J. T. , 1994 : Observations of undertow and turbulence in a laboratory wave flume. *Coastal Engineering*, Volume 24, 51-80.

[39] Ting, F. C. K. and Kirby, J. T., 1996 : Dynamics of surf-zone turbulence in a spilling breaker. *Coastal Engineering Journal*, Volume 27, pp. 131-160.

[40] Cox, D.T., Kobayashi, N., and Okayasu, A., 1995 : Experimental and numerical modeling of surfzone hydrodynamics. *Technical Report CACR-95-07*, Center for Applied Coastal Research, University of Delaware, pp. 293.

[41] Chang K.A., and Liu P.L.F., 1999 : Experimental investigation of turbulence generated by breaking waves in water of intermediate depth. *Phys. Fluids*, Volume 11, pp. 3339-3400.

[42] Govender K., Mocke G., P., and Alport M., 2002 : Video-imaged surf zone wave and roller structures and flow fields. *Journal of Gephysical Research*, Volume 107 (C7), pp. 3072-3083, DOI : 10.1029/2000JC000755

[43] Kimmoun, O., and Branger, H., 2007 : A particle image velocimetry investigation on laboratory surf-zone breaking waves over a sloping beach. *Journal of Fluid Mechanics*, Volume 588, pp. 353-397.

[44] Huang Z.-C, Hsiao S.-C, Hwung H.-H and Chang K.-A., 2009 : Turbulence and energy dissipations of surf-zone spilling breakers. *Coastal Engineering*, Volume 56, pp. 733-746.

[45] Suhayda, J. N., and Pettigrew, N. R., 1977 : Observations of wave height and wave celerity in the surf zone. *Journal of Geophysical Research*, Volume 82, (9), pp. 1419-1424.

[46] Rattanapitikon, W. and Shibayama, T., 2000. Verification and modification of breaker height formulas. *Coastal Engineering*, Volume 42, (4), pp. 389-406.

[47] Stansel, P. and MacFarlane, C., 2002 : Experimental investigation of wave breaking criteria based on wave phase speeds. *Journal of Physical Oceanography*, Volume 32, pp. 1269-1283.

[48] Yoo, J.; Fritz, H. M.; Haas, K. A.; Work, P. A.; Barnes, C. F.; Cho, Y., 2008 : Observation of wave celerity evolution in the nearshore using digital video imagery. *American Geophysical Union*, Fall Meeting 2008, abstract *No.* OS13D-1224.

[49] Lippmann, T.C., and Holman R.A., 1991: Phase speed and angle of breaking waves measured with video techniques. *in Coastal Sediments, '91*, edited by N. Kraus, American Society of Civil engineers (ASCE)., New York, pp. 542-556.

[50] Tissier M., Bonneton P., Almar R., Castelle B., Bonneton N., and Nahon A., 2011 : Field measurements and non-linear prediction of wave celerity in the surf zone. *European Journal of Mechanics, B Fluids*, Volume 30, pp. 635-641.

[51] Holland T.K., 2001 : Application of the linear dispersion relation with respect to depth inversion and remotely sensed imagery. *IEEE Transactions on Geoscience and Remote Sensing*, Volume 39, (9), pp. 2060-2072.

[52] Yoo, J., Fritz, H.M., Hass, K. A., Work, P. A., and Barnes C. F., 2011, Depth inversion in the surf zone with inclusion of wave non-linearity using video-derived celerity. *Journal of Waterway, Port, Coastal and Ocean Engineering*, ASCE, Volume137, (2), pp. 95-106.

[53] Govender, K., Alport M.J., Mocke G., and Michallet H., 2002 : Video measurements of fluid velocities and water levels in breaking waves. *Physics*, Volume T97, pp. 152-159.

[54] Lin J.C. and Rockwell, D., 1994 : Instantaneous structure of a breaking wave. *Phys. Fluids*, Volume 6, pp. 2877-2879.

[55] Lin, J. C.and Rockwell, D., 1995 : Evolution of a quasi-steady breaking wave. *J. Fluid Mech.*, Volume 302, 29-44.

[56] Cox, D.T., and Shin, S. : Laboratory measurements of void fraction and turbulence in the bore region of surf zone waves. *Journal of Engineering Mechanics*, Volume 129, (10), pp. 1197-1205, 2003.

[57] Cox, D. T., and Anderson, S. L., 2001 : Statistics of intermittent surf zone turbulence and observations of large eddies using PIV. *Coastal Engineering*,Volume 43, (2), pp.121-131.

[58] Petti, M., and Longo, S., 2001 : Turbulence experiments in the swash zone. *Coastal Engineering*, Volume 43, (1), pp. 24.

[59] Archetti, R., Brocchini, M., 2002 : An integral swash zone model with friction : an experimental and numerical investigation. *Coastal Engineering*, Volume 44, (2), 89-110.

[60] Cowen E.A, Sou I.M, . Liu, P. L.-F and Raubenheimer B, 2003 : Particle image velocimetry measurements within a laboratory-generated swash zone. *Journal of Engineering Mechanics*, Volume 129, (10), pp. 1119-1129.

[61] Jansen, P. C. M., 1986 : Laboratory observations of the kinematics in the aerated region of breaking waves. *Coastal Eng.*, Volume 9, pp. 463-477.

[62] Govender K., Michallet H., Alport M.J., Pillay U., Mocke G.P., and Mory M., 2009 : Video DCIV measurements of mass and momentum fluxes and kinetic energies in laboratory waves breaking over a bar. *Coastal Engineering*, Volume 56, pp. 879-885.

[63] Ryu, Y., Chang, K.-A. and Lim, H.-J., 2005 : Use of bubble image velocimetry for measurement of plunging wave impinging on structure and associated greenwater. *Measurement Science and Technology*, Volume 16, pp. 1945-1953.

[64] Huang Z.-C., Hsiao S.C., and Hwung H.-H., 2009 : Observation of coherent turbulent structure under breaking wave. *International Journal of Offshore and Polar Engineering*, Volume 19, (1), pp. 15-22. ISSN 1053-5381

[65] Longo S., Petti M., and Losada I., J., 2002 : Turbulence in the swash and surf zones : A review. *Coastal Engineering*, Volume 45, 129-147.

[66] Longo S., 2008 : Vorticity and intermittency within the pre-breaking region of spilling breakers. *Coast. Eng.*, Volume 56, (3) , pp. 285-296. doi:10.1016/j.coastaleng

[67] Shin S., and Cox D., 2006 : Laboratory observations of inner surf and swash-zone hydrodynamics on a steep slope. *Continental Shelf Research*, Volume 26, pp. 561-573.

[68] De Serio F., and Mossa W., 2006 : Experimental study on the hydrodynamics of regular breaking waves. *Coastal Engineering*, Volume 53, pp. 99-113.

[69] Chang K.-A., and Liu P. L.F., 1998 : Velocity, acceleration and vorticity under a breaking wave. *Phys. Fluids*, Volume 10, pp. 327-329. DOI:10.1063/1.869544.

[70] Hoque A., and Akoi S., 2005 : Distributions of void fraction under breaking waves in the surf zone. *Ocean Engineering*, Volume 32, pp. 1829-1840.

[71] Stansby, P.K., Feng, T., 2005 : Kinematics and depth-integrated terms in surf zone waves from laboratory measurement. *Journal of Fluid Mechanics*, Volume 529, pp. 279310.

[72] Misra, S. K., Kirby, J. T., Brocchini, M., Veron, F., Thomas, M. and Kambhamettu, C., 2008 : The mean and turbulent flow structure of a weak hydraulic jump. *Physics of Fluids*, Volume 20, (3), pp. 035106-21.

[73] Govender K, Mocke G. P. and Alport M. J., 2004 : Dissipation of isotropic turbulence and length-scale measurements through the wave roller in laboratory spilling waves. *Journal of Geophysical Research*, Volume 109, C08018, doi : 10.1029/2003JC002233.

[74] Roussinova V., Shinneeb A.M., Balachandar R. : Investigation of fluid structures in a smooth open-channel flow using proper orthogonal decomposition. *Journal of Hydraulic Engineering*, Volume 136, (3) , 143-154, 2010.

[75] Sou I.M, Cowen E.A., and Liu P.L.F., 2010 : Evolution of the turbulence structure in the surf and swash zones. *Journal of Fluid Mechanics*, Volume 644, pp. 193-216. doi:10.1017/S0022112009992321

[76] Cowen E.A., and Monismith S.G., 1997 : A hybrid digital particle tracking velocimetry technique *Experiments in Fluids*, Volume 22, pp. 199-211.

[77] Ting F. C.K., and Nelson J.R., 2011 : Laboratory measurements of large-scale near-bed turbulent flow structures under spilling regular waves. *Coastal Engineering*, Volume 58, pp.151-172.

[78] Govender K., Michallet H, and Alport M.J., 2011 : DCIV measurements of flow fields and turbulence in waves breaking over a bar. *European Journal of Mechanics - B/Fluids*, Volume 30, pp. 616-623. doi : 10.1016/j.euromechflu.2011.09.001

[79] Govender K., Michallet H., Alport M.J., Pillay U., Mocke G.P., and Mory M., 2009 : Video DCIV measurements of mass and momentum fluxes and kinetic energies in laboratory waves breaking over a bar. *Coastal Engineering*, Volume 56, pp. 876-885.

[80] Collineau S., and Brunet Y., 1993 : Detection of turbulent motion in a forest canopy. Part 1 : Wavelet analysis. *Boundary-Layer Meteorology*, Volume (65), pp. 357-379.

[81] Kumar, P., Foufoula-Georgiou, E., 1997 : Wavelet analysis for geophysical applications. *Rev. Geophys.*, Volume 35, 4, pp. 385-412.

[82] Torrence, C., Compo, G.P., 1998 : A practical guide to wavelet analysis. *Bulletin of the American Meteorological Society*, Volume 79, pp. 61-78.

[83] Camussi, R., Guj, G., 1997 : Orthonormal wavelet decomposition of turbulence flows : intermittency and coherent structures. *Journal of Fluid Mechanics*, Volume 346, pp. 177-199.

[84] Bienkiewicz, B., Ham, H. J., 1997 : Wavelet study of approach-wind velocity and building pressure. *J. Wind Eng. Ind. Aerodyn.*, 69-71, pp. 671-683.

[85] Jordan, D.A., Hajj, M. R., Tieleman H. W., 1997 : Wavelet analysis of the relation between atmospheric wind and pressure fluctuations on a low-rise building. *J. Wind Eng. Ind. Aerodyn.*, 69-71, pp. 647-655.

[86] Geurts, C. P. W., Hajj, M. R., Tieleman, H. W., 1998 : Continuous wavelet transform of wind and wind-induced pressures on a building in suburban terrain. *J. Wind Eng. Ind. Aerodyn.*, 74-76, pp. 609-617.

[87] Kareem, A., Kijewski, T., 2002 : Time-frequency analysis of wind effects on structures. *J. Wind Eng. Ind. Aerodyn.*, 90, pp.1435-1452.

[88] Huang, Z.-C., Hwung, H.-H. and Chang, K.-A., 2010 : Wavelet-based vortical structure detection and length scale estimate for laboratory spilling waves. *Coastal Engineering*,Volume 57, pp. 795-811.

[89] Schram C., Rambaud P., and Riethmuller M., L., 2002 : Wavelet based eddy structure eduction from a backward facing step flow investigated using particle image velocimetry. *Exp. Fluids*, Volume 36, pp. 233-245.

[90] Camussi R., and Felice F., D., 2006 : Statistical properties of vortical structures with spanwise vorticity in zero pressure gradient turbulent boundary layers. *Phys. Fluids*, Volume 18, pp. 035108.

[91] Mallat S., 1989 : A theory of multiresouluion signal decomposition : the wavelet representation. *IEEE Trans. Pattern and Anal. Machine Intell.*, Volume 11, pp. 674-693.

[92] Seena A., and Sung H.J., 2011 : Wavelet spatial scaling for educing dynamic structures in turbulent open cavity flows. *Journal of Fluids and Structures*, Volume 27, pp. 962-975.

[93] Schneider, K., and Vasilyev, O., 2010 : Wavelet methods in computational fluid dynamics. *Annu. Rev. Fluid Mech.*, Volume 42, pp. 473-503.

[94] Govender K., 1999 : *Velocity, vorticity and turbulence measurements in the suf zone*, PhD Thesis, University of KwaZulu-Natal, Durban.

[95] Fredsoe, J., Deigaard, R., 1992 : Mechanics of coastal sediment transport. *World Scientific Advanced Series on Ocean Eng.*, Volume 3.

[96] Mei, C. C., 1991 : *The Applied Dynamics of Ocean Surface Waves*, World Scientific Pub. Co., Teaneck, NJ.

[97] Catalan P.,A., and Haller M.C., 2008 : Remote sensing of breaking wave phase speeds with application to non-linear depth inversions. *Coastal Engineering*, Volume 55, pp. 93-111.

[98] Le Mehaute B., 1976 : *An introduction to hydrodynamics and water waves*, Springer-Verlag, New York.

[99] Nelson R., 1997 : Height limits in top down and bottom up wave environments. *Coastal Engineering*, Volume 32, Issues 2-3, pp. 247-254.

[100] Miche R., 1944 : Mouvements ondulatoires des mers en profondeur constante ou decroissante. *Annales des Ponts et Chaussees*, pp. 25-78, 131-164, 270-292, 369-406.

[101] Stockdon H. F., and Holman R. A., 2000 : Estimation of wave phase speed and nearshore bathymetry from video imagery. *Journal of Geophysical Research*, Volume 105, (C9), pp.22015-22033.

[102] Stive M. J. F., 1984 : Energy dissipation in waves breaking on a gentle slope. *Coastal Engineering*, Volume 8, pp. 99-127.

[103] Dean R.G, and Darlymple R. A, 2000 : *Water Wave Mechanics for Engineers and Scientists- Advanced Series on Ocean Engineering*-Volume 2, World Scientific Publishing Co.

[104] Svendsen, I.A., Madsen, P.A., Buhr Hansen, J., 1978 : Wave characteristics in the surf zone. *Proceedings, 16th International Conference on Coastal Engineering*, ASCE, pp. 520539.

[105] Schaffer H., Madsen P., Deigaard R., 1998 : A Boussinesq model for wave breaking in shallow water. *Coastal Engineering*, Volume 20, (3-4), pp. 185-202.

[106] Madsen, P. A., Sorensen O.R, and Schaffer H.A., 1997 : Surf zone dynamics simulated by a Boussinesq type model. Part I. Model description and cross-shore motion of regular waves. *Coastal Engineering*, Volume 32, pp. 255-287.

[107] Thornton, E.B., and Guza R.T., 1982 : Energy saturation and phase speeds measured on a natural beach. *Journal of Geophysical Research*, Volume 87, (C12), pp. 9499-9508.

[108] Puleo, J. A., G. Farquharson, S. J. Frasier, and Holland K. T., 2003 : Comparison of optical and radar measurements of surf and swash zone velocity fields. *Journal of Geophysical Research*, Volume 108, (C3), pp. 3100.

[109] Longuet-Higgins M. S and Stewart R.W., 1964 : Radiation stress in water waves - a physical discussion with applications. *Deep Sea Res.*, Volume 11, pp. 529-562, 1964.

[110] Longuet-Higgins, M. S., and Stewart R. W., 1962 : Radiation stress and mass transport in gravity waves, with application to 'surf beats,' *Journal of Fluid Mechanics*, Volume 13, pp. 481-504.

[111] Stive M.,J.,F., and Wind H.G., 1982 : A study of radiation stress and setup in the nearshore region. *Coastal Engineering*, Volume 6, pp. 1-25.

[112] Mathieu, J., and Scott, J., 2000 : *An Introduction to Turbulent Flow*. Cambridge University Press, Cambridge, United Kingdom.

[113] Stull, R. B., 1988 : *An introduction to boundary layer meteorology*, Vancouver, Canada : Kluwer Academic Publishers.

[114] Pope S.B., 2000 : *Turbulent Flows*, Cambridge University Press.

[115] Huang Z. C., Hsiao S. C, Hwung H. H., and Chang K.A., 2009 : Turbulence and energy dissipations of surf-zone spilling breakers. *Coast. Eng.*, Volume 56, pp. 733-746.

[116] `http://www.hrwallingford.co.uk`
e-mail : info@hrwallingford.com

[117] Lara J.,L., Losada I.J., and Liu P.L.-U., 2006 : Breaking waves over a mild gravel slope : Experimental and numerical analysis. *Journal of Geophysical Research*, Volume 111, C11019, doi:10.1029/2005JC003374.

[118] Sakai, T., Sandanbata, I., and Uchida, M., 1984 : Reynolds stress in the surf zone. *In Proc. 20th Coastal Engineering Conference*, 4253.

[119] Melville, W. K., 1996 : The role of surface wave breaking in air-sea interaction. *Annu. Rev. Fluid Mech.*, Volume 28, pp. 279-321, doi:10.1146/annurev.fl.28.010196.001431.

[120] Lennon J.M., and Hill D.F., 2006 : Particle image velocity measurements of undular and hydraulic jumps. *Journal of Hydraulic Engineering*, Volume 132, (12) ,December 1.

[121] She K., Greated C.A and Easson W. J., 1997 : Experimental study of three dimensional breaking wave kinematics. *Applied Ocean Research*, Volume 19, pp. 329-343.

[122] Raffel M., Willert C.E and Kompenhans J., 1998 : Particle imagevelocimetry, A practical guide. *Springer*, Berlin.

[123] Skyner, D. J. and Easson, W. J., 1998 : Wave kinematics and surface parameters of steep waves traveling on sheared currents. *J. Waterw., Port, Coastal Ocean Eng.*, Volume 124, (1), pp. 1-6.

[124] Jensen, A., Sveen, J. K., Grue, J., Richon, J.- B. and Gray, C., 2001 : Accelerations in water waves by extended particle image velocimetry. *Exp. Fluids*, Volume 30, pp. 500-510.

[125] Buick, J. M., Martin, A. J., Cosgrove, J. A., Greated C. A. and Easson, W. J., 2003 : Comparison of a lattice Boltzmann simulation of steep internal waves and laboratory measurements using particle image velocimetry. *European J. Mech. B/Fluids*, Volume 22, pp. 27-38.

[126] Fritz, H. M., Hager, W. H. and Minor, H.-E., 2003 : Landslide generated impulse waves. Part 1. instantaneous flow fields. *Exp. Fluids*, Volume 35, pp. 505-519.

[127] Chang, K.-A., Hsu, T.-J. and Liu, P. L.-F., 2001 : Vortex generation and evolution in water waves propagating over a submerged rectangular obstacle. Part I. Solitary waves. *Coastal Engineering.*, Volume 44, pp. 13-36.

[128] Jo., C. H., Lee, S. B., Shin Y. S., Hong, S. G. and Min, K. H., 2002 : Numerical and experimental study of offshore pipeline stability in trench. *J. Waterw., Port Coastal Ocean Eng.*, Volume 128, (6), pp. 258-270.

[129] Grue J., Clamond D., Huseby, M.,and Jensen, A., 2003 : Kinematics of extreme waves in deep water. *Applied Ocean Research*, Volume 25, 355-366.

[130] Westerweel, J., 1997 : Fundamentals of digital particle image velocimetry. *Measurement Science and Technology*, Volume 8, pp. 1379-1392.

[131] Abolhassani M.D., Norouzy A., Takavar A,. and Ghanaati H., 2007 : Noninvasive temperature estimation using sonographic digital images. *J., Ultrasound Med.*, Volume 26, pp. 215-222.

[132] Huang H., Dabiri D. and Gharib M., 1997 : On errors of digital particle image velocimetry. *Measurement Science and Technology.*, Volume 8, pp. 1427-1440.

[133] Willert C.E, Gharib M., 1991 : Digital particle image velocimetry. *Exp. Fluids*, Volume 10, pp. 181-193.

[134] Billy F, David L, Pineau G., 2004 : Single pixel resolution correlation applied to unsteady flow measurements. *Measurement Science and Technology*, Volume 15, 1039-1045.

[135] Brigham, E.O., 1974 : *The Fast Fourier Transform*. Englewood Cliffs, NJ: Prentice-Hall, Chapter 13.

[136] Bendat, J. S. and Piersol, A. G., 2010 : *Random Data, analysis and measurement procedures*, 4^{th} Edition, John Wiley and Sons.

[137] Prieto C.A., 2007 : Velocities from cross-correlation : A guide to self-improvement. *The Astronomical Journal*, Volume 134, pp. 1843-1848.

[138] Weng W.G, Fan W.C., Liao G.X, and Qin J., 2001 : Wavelet-based image denoising in (digital) particle image velocimetry. *Signal Processing*, Volume 81, pp. 1503-1512.

[139] Ruan Xiaodong, Weng Feng and Yamamoto Fujio, 2003 : Precision of direct measurement of vorticity from digital particle images. *Meas. Sci. Technol.*, Volume 14, 1314.

[140] Hyun B.S, Balachandar, R., Yu K. and Patel V.C., 2003 : Assessment of PIV to measure mean velocity and turbulence in open-channel flow. *Experiments in Fluids*, Volume 35, 262267. DOI 10.1007/s00348-003-0652-7.

[141] Zeilstra C., Collignon J.G., M.A. van der Hoef , Deen N.G., Kuipers J.A.M., 2008 : Experimental and numerical study of wall-induced granular convection. *Powder Technology*, Volume 184, pp. 166-176.

[142] Hu H, Saga T, Kobayashi T, Okamoto K, and Taniguchi N., 1998 : Evaluation of cross-correlation method by using PIV standard images. *Journal of Visualization*, Volume 1, (1), pp. 87-94.

[143] Adrian, R.J., 1991 : Particle imaging techniques for experimental fluid mechanics. *Annual Rev. Fluid Mechanics*, Volume 23, pp. 261-305.

[144] Silva, G., 2006 : *Experimental Characterization of a Microfluidic Flow*, Graduation Thesis, Mechanical Engineering Department, Instituto Superior Tcnico, Technical University of Lisbon.

[145] Devasenathipathy S.; Santiago J. G.; Wereley S. T.; Meinhart C. D.; Takehara K., 2003 : Particle imaging techniques for microfabricated fluidic systems. *Exp. Fluids*, Volume 34, pp. 504-514.

[146] Prasad A. K, Adrian R. J., Landreth C. C. and Offutt E.W., 1992 : Effect of resolution on speed and accuracy of particle image velocimetry interrogation. *Exp. Fluids*, Volume 13, pp. 105-116.

[147] Silva G., Leal N., and Semio V., 2008 ; Effect of wall roughness on fluid flow inside a microchannel. *14th Int Symp on Applications of Laser Techniques to Fluid Mechanics*, Lisbon, Portugal.

[148] Jones J.D.C. (ed.), 1997. Particle image velocimetry. *Meas. Sci. Technol.*, Volume 8, (12), pp. 1379-1583.

[149] Scarano F., Riethmuller M.L., 1999 : Iterative multigrid approach in PIV image processing with discrete window offset. *Experiments in Fluids*, Volume 26, (6), pp. 513-523.

[150] Hyun BS, Balachandar R, Yu K, Patel V.C., 2003 : PIV/LDV measurements of mean velocity and turbulence in a complex open-channel flow. *IIHR report* no. 424, The University of Iowa.

[151] Santiago J.G, Wereley S.T, Meinhart C. D., Beebe D. J., and Adrian R. J., 1998 : A particle image velocimetry system for microfluidics. *Experiments in Fluids*, Volume 25, pp. 316-319.

[152] Fairweather M., and Hargrave G.K. 2002 : Experimental investigation of an axisymmetric, impinging turbulent jet. 1. Velocity field. *Experiments in Fluids*, Volume 33, pp. 464-471. DOI 10.1007/s00348-002-0479-7

[153] Keane, R. D., and Adrian R. J., 1990 : Optimization of particle image velocimeters. Part I : double pulsed systems. *Meas. Sci. Technol.*, Volume 1 (1), pp. 1202-1215.

[154] Stansell P., and MacFarlane C., 2002 : Experimental investigation of wave breaking criteria based on wave phase speeds. *Journal of Physical Oceanography*, Volume 22, pp. 1269-1283.

[155] Mukaro R., Govender K., Gledhill I., and Kokwe N. L., 2010 : Velocity flow field and water level measurements in shoaling and breaking water waves. *Proceedings of the Seventh South African Conference on Computational and Applied Mechanics*, (SACAM10), Pretoria.

[156] Mukaro R., and Govender K., 2012 : Experimental study of turbulence and water levels in shoaling and breaking water waves using digital image processing techniques. *Journal of South African Institute of Civil Engineers*, (SAICE). Volume 55 (2), pp. 55-74.

[157] Mukaro R., Govender K., and McCreadie H., 2013 : Wave height and wave velocity measurements in the vicinity of the break point in laboratory plunging waves. *Journal of Fluids Engineering*, ASME, Volume 35 (6), pp. 061303-1 - 061303-13.

[158] Lakehal D., and Liovic P., 2011 : Turbulence structure and interaction with steep breaking waves. *J. Fluid Mech.*, Volume 674, pp. 522577. Cambridge University Press. doi:10.1017/jfm.2011.3

[159] Battjes, J., 1975 : *Modelling of turbulence in the surf zone*. In : Symposium on Modeling Techniques, ASCE, pp. 10501061.

[160] Rivillas-Ospina G., Pedrozo-Acuna A., Rodolfo Silva R., Alec Torres-Freyermuth A. and Gutierrez C., 2012 : Estimation of the velocity field induced by plunging breakers in the surf and swash zones. *Experiments in Fluids*, Volume 52, pp. 53-68. DOI 10.1007/s00348-011-1208-x

[161] Camenen B. and Larson M., 2007, Predictive formulas for breaker depth index and breaker type. *Journal of Coastal Research* Volume 23, (4), pp. 1028-1041.

[162] Shore Protection Manual, 1984 : U.S. Army Engr. Waterways Experiment Station, *Coastal Engineering Research Center*, U.S. Government Printing Office, Washington, D.C.

[163] Lesnik J. R., 1977, Wave Setup on a sloping beach, *Coastal Engineering Technical Aid*, Number 77-5, U.S Army, Corps of Engineers, Coastal Engineering Research Center.

[164] Sakai S., and Kobayashi N., 1990 : Breaking conditions of shoaling waves on opposing current. *Journal of Waterway, Port, Coastal, and Ocean Engineering*, Volume 116, (2), pp. 302-306.

[165] Miche, M., 1951 : Le Pouvoir Reflechissant des Ouvrages Maritimes Exposes a l Action de la Houle, *Annals des Ponts et Chaussess*, 121e Annee, pp. 285-319 (translated by Lincoln and Chevron, University of California, Berkeley, Wave Research Laboratory, Series 3, Issue 363, June 1954).

[166] McKee Smith J., 1999 : Wave breaking on an opposing current. *Coastal Engineering*- Technical Note IV-17, US Army Corps of Engineers.

[167] Le Blond P.H., and Mysak L.A., 1978 : *Waves in the Ocean*, Elsevier - Oceanography Series.

[168] Battjes, J. A., 1988 : Surf zone dynamics, *Annual Review of Fluid Mechanics*, Volume 20, (1), pp. 257-291.

[169] Mocke, G., 2001 : Structure and modeling of surf zone turbulence due to wave breaking. *Journal of Geophysical Research*, Volume 106 (C8), pp. 17039-17057.

[170] Oppenheim A. V., and Schafer R. W., 1975, *Digital Signal Processing*, Prentice-Hall, MIT. ISBN 0-13-214635-5.

[171] Okamoto T., Fortes C. J., and Basco D. R., 2010 : Bore propagation speed at the termination of wave breaking. *Proceedings of 32nd International Conference on Coastal Engineering*, China, pp. 2-14.

[172] Massel S. R., 2007 : *Ocean waves breaking and marine aerosol fluxes*, Springer

[173] Ruessink B.G., 2010 : Observations of turbulence within a natural surf zone. *Journal of Physical Oceanography*, Volume 40, pp. 2696-2712. DOI : 10.1175/2010JPO4466.1

[174] Ubaldi M., Zunino P., 2000 : An experimental study of the unsteady characteristics of the turbulent near wake of a turbine blade. *Experimental Thermal and Fluid Science*, Volume 23, Issues 1-2, pp. 2333.

[175] Sakakiyama T., and Liu, P.L.-F., 2001 : Laboratory experiments for wave motions and turbulence flows in front of a breakwater. *Coastal Engineering*, Colume 44, 117-139.

[176] Liiv T. and Lagemaa P., 2008 : The variation of the velocity and turbulent kinetic energy field in the wave in the vicinity of the break point. *Estonian Journal of Engineering*, Volume 14 (1), pp. 42-64.

[177] Svendsen I.A., 1987 : Analysis of surf zone turbulence. *Journal of Geophysical Research- Oceans*, Volume 92, (5), pp. 5115-5124.

[178] Pedrozo-Acuna A., Alegra-Arzaburu A. R., Torres-Freyermuth A., Mendoza E, and Silva R., 2011 : Laboratory investigation of pressure gradients induced by plunging breakers. *Coastal Engineering*, Volume 58, pp. 722-738.

[179] Coakley and J.Duncan J., 1997 : The flow field in steady breaking waves. *Twenty-First Symposium on Naval Hydrodynamics*, Commission on Physical Sciences, Mathematics, and Applications (CPSMA), pp. 534-549.

[180] Fairweather M., Hargrave G.K., 2001 : DPIV measurements in axisymmetric, impinging turbulent jets, Paper 1031 (CD-ROM). In : Kompenhans J (ed) *Proc. 4th Int. Symposium on Particle Image Velocimetry*, DLR, Gottingen, Germany.

[181] Richardson, L.F, 1922 : *Weather prediction by numerical process*, Cambridge University Press.

[182] Okayasu A., Shibayama T., and Mimura M., 1986 : Velocity field under plunging waves. *Coastal Engineering Proceedings*, Number 20.

[183] Pedersen C, Deigaard R, and Sutherland J., 1998 : Measurements of the vertical correlation in turbulence under broken waves. *Coastal Engineering*, Volume 35 , pp. 231-249.

[184] Peregrine D. H., 1983 : Breaking waves on beaches. *Annu. Rev. Fluid Mech.*, Volume 15, pp. 149-178.

[185] Christensen, E.D., Walstra, D.J., Emerat, N., 2002 : Vertical variation of the flow across the surf zone. *Coastal Engineering*, Volume 45, (1), 165-198.

[186] Yoon H.-D., and Cox D. T., 2010 : Large-scale laboratory observations of wave breaking turbulence over an evolving beach. *Journal of Geophysical Research* Volume 115, C10007, pp. 1-16. doi:10.1029/2009JC005748

[187] Ting, F. C. K., 2001 : Laboratory study of wave turbulence velocities in a broad-banded wave surf zone. *Coastal Engineering.*, Volume 43, pp. 183-208.

[188] Saka T., Inada Y., and Sandanbata I., 1982, Turbulence generated by breaking on a beach, paper presented at the *18th International Conference on Coastal Engineering*, Society of Civil Engineering, Cape, Town, South Africa.

[189] Okayasu A., 1989 : Characteristics of turbulence structure and undertow in the surf zone. *Ph.D. thesis*, Yokohama Natl. Univ., Japan.

[190] Hunt J. C. R. and Vassilicos J. C., (Editors), 2000 : *Turbulence Structure and Vortex Dynamics*, Cambridge University Press.

[191] Wang L., 2012 : Structures of the vorticity tube segment in turbulence. *Physics of Fluids*, Volume 24, 045101.

[192] Adrian R.J., Christensen K.T., and Liu Z.-C., 2000 : Analysis and interpretation of turbulent velocity fields. *Experiments in Fluids*, Volume 29, pp. 275-290.

[193] Kim W.Y., Walker P.G., Pedersen E.M., et al., 1995 : Left ventricular blood flow patterns in normal subjects: a quantitative analysis by three-dimensional magnetic resonance velocity mapping. *J. Am. Coll. Cardiol.*, Volume 26, 224-238.

[194] Wu J.Z., Ma H.Y., and Zhou M.D., 2006 : Vorticity and vortex dynamics. *Berlin-Heidelberg*, Germany: Springer-Verlag.

[195] Lee S.-J., and Lee S.-H, 2001 : Flow field analysis of a turbulent boundary layer over a riblet surface. *Experiments in Fluids*, Volume 30, pp.153-160.

[196] Bakewell, P., and Lumley, J.L., 1967 : Viscous sublayer and adjacent wall region in turbulent pipe flow. *Physics of Fluids* Volume 10, pp.1880.

[197] Aubry, N., Holmes, P., Lumley, J.L., and Stone, E., 1988 : The dynamics of coherent structures in the wall region of a turbulent boundary layer. *Journal of Fluid Mechanics.*, Volume 192,pp. 115.

[198] Ting, F. C. K., 2006 : Large-scale turbulence under a solitary wave. *Coastal Engineering*, Volume 53, pp. 441-462.

[199] Ting, F. C. K., 2008 : Large-scale turbulence under a solitary wave: Part 2 Forms and evolution of coherent structures *Coastal Engineering*, Volume 55, pp. 522-536.

[200] Longuet-Higgins, M.S., 1992 : Capillary rollers and bores. *Journal of Fluid Mechanics*, Volume 240, pp. 659 679.

[201] Nadaoka K. S, Hino M.,, and Koyano Y., 1989 : Structure of the turbulent flow field under breaking waves in the surf zone. *J. Fluid Mech.*,Volume 204, 359-387.

[202] Jimenez J.T., 2004 : Turbulence and vortex dynamics. `http://www.scribd.com/doc/80320496/8/Vorticity-in-two-dimensions`

[203] Dabiri D., and Gharib M., 1997 : Experimental investigation of the vorticity generation within a spilling water wave. *J. Fluid Mech.*, Volume 330, pp. 113-139.

[204] Stanely A. S., Sarkar S., and Mellado J. P., 2002 : A study of the flow-field evolution and mixing in a planar turbulent jet using direct numerical simulation. *Journal of Fluid Mechanics*,Volume 450, pp. 377-407. DOI: 10.1017/S0022112001006644

[205] Liu Z., H., Zeng Q.,Q., Zhou X.,X., Wei Z.,N., Rui X.,S., Chang Y. T., 2011 : Research progress of wavelet analysis in flow structure characterization. *Advanced Materials Research*, Volumes (291-294), pp. 2787-2793.

[206] Joshi V., J., and Rempfer D., 2007 : Energy analysis of turbulent channel flow using biorthogonal wavelets. *Phys. Fluids*, Volume 19 (085106), pp.1-12 ; doi: 10.1063/1.2760277

[207] Muller P., and Vidakovic B., 1999 : *An introduction to wavelets. Bayesian inference in Wavelet based Models*, Springer, New York, pp 118.

[208] Labat D., Ababou R., Mangin A.,: Rainfallrunoff relations for karstic springs. Part II: continuous wavelet and discrete orthogonal multiresolution analyses. *Journal of Hydrology*, Volume 238, (3-4), pp. 149-178, 2000.

[209] Daubechies I., 1992 : *Ten Lectures on Wavelets*, PA: SIAM, Philadelphia, [3, 4, 25,26, 28].

[210] Sifuzzaman M., Islam M. R., and Ali M.Z., 2009 : Application of wavelet transform and its advantages compared to Fourier Transform. *Journal of Physical Sciences*, Volume 13, pp. 121-134, ISSN: 0972-8791 : www.vidyasagar.ac.in/journal

[211] Strang H., 1993 : Wavelet transforms versus Fourier transforms. *Bull. Amer. Math. Soc.* (N.S.), Volume 28, pp. 288-305.

[212] Torrence C., and Webster, P., 1999 : Interdecadal changes in the ENSO monsoon system. *Journal of Climatology*, Volume 12, pp. 2679-2690.

[213] Azimifar Z., 2005 : *Image models for wavelet domain statistics*, PhD Thesis, University of Waterloo, Ontario, Canada.

[214] Anctil F., and Coulibaly P., : Wavelet analysis of the interannual variability in Southern Quebec streamflow. *Journal of Climate*, Volume 17, pp. 163-173, 2004.

[215] Longo S., 2003 : Turbulence under spilling breakers using discrete wavelets. *Experiments in Fluids*, Volume 34, pp. 181-191.

[216] Wang, Z.Q., So,R.M.C., and Xie,W.C., 2007 : Features of flow-induced forces deduced from wavelet analysis. *Journal of Fluids and Structures*, Volume 23, pp. 249-268.

[217] Blackwelder, R.F., Kaplan, R.E., 1976 : On the wall structure of the turbulent boundary layer. *Journal of Fluid Mechanics*, Volume 76 (1), pp. 89112.

APPENDICES

Appendix A : Typical three point calibration details for three wave gage probes used for water level measurements

Calibration of PCI6031E Channel 1 12:31 01 February 2011

Calibrated by: Raphael Mukaro — Calibration Status: NORMAL
Project: DCIV Water level measurements — Facility: CSIR
Sensor: WP1 — Model: WG50 — Serial No. N/A
Programmable Gain: 1 — Plug−In Gain: 1 — Filter Frequency: 1000.0 Hz

Data Point No.	Input Signal (volts)	Physical Value (m)	Fitted Curve (m)	Error (m)
1	−4.860	−0.050000	−0.049718	0.00028225
2	−3.302	0.000000	−0.000555	−0.00055527
3	−1.692	0.050000	0.050273	0.00027300
Maximum Error = −0.555% of Calibration Range				

$$Y = C_0 + C_1 V$$

where $Y(t)$ = Wave Elevation (m)
$V(t)$ = input signal at A/D converter (volts)
C_0 = 0.103663 m
C_1 = 0.0315604 m/volt

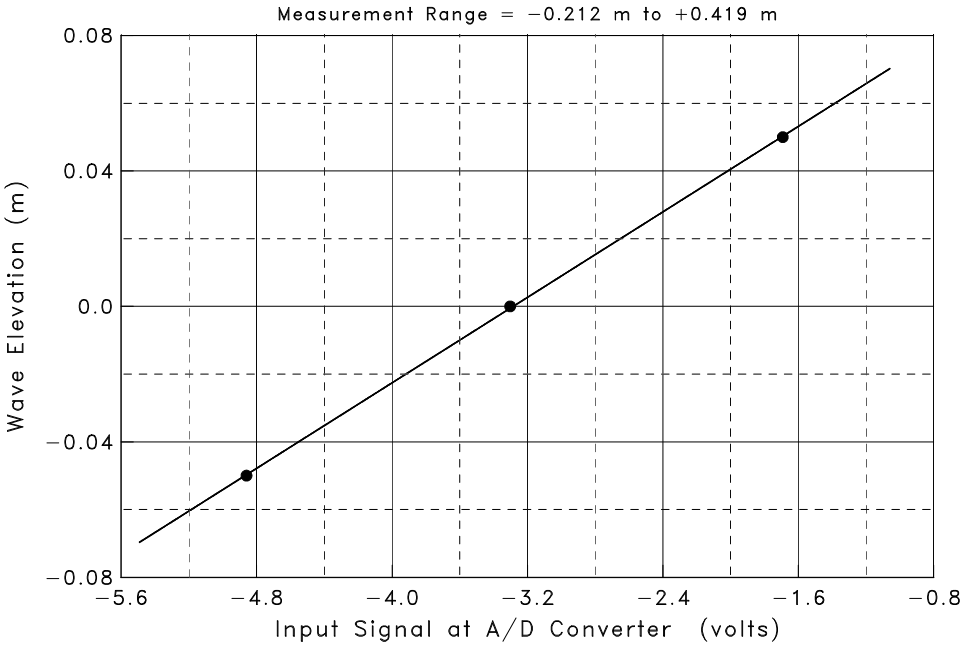

Calibration of PCI6031E Channel 2 12:31 01 February 2011

Calibrated by: Raphael Mukaro — Calibration Status: NORMAL
Project: DCIV Water level measurements — Facility: CSIR
Sensor: WP2 — Model: WG50 — Serial No. N/A
Programmable Gain: 1 — Plug-In Gain: 1 — Filter Frequency: 1000.0 Hz

Data Point No.	Input Signal (volts)	Physical Value (m)	Fitted Curve (m)	Error (m)
1	−5.529	−0.050000	−0.049943	0.00005723
2	−3.781	0.000000	−0.000114	−0.00011408
3	−2.021	0.050000	0.050057	0.00005684
Maximum Error = −0.114% of Calibration Range				

$$Y = C_0 + C_1 V$$

where $Y(t)$ = Wave Elevation (m)
$V(t)$ = input signal at A/D converter (volts)
C_0 = 0.107666 m
C_1 = 0.0285064 m/volt

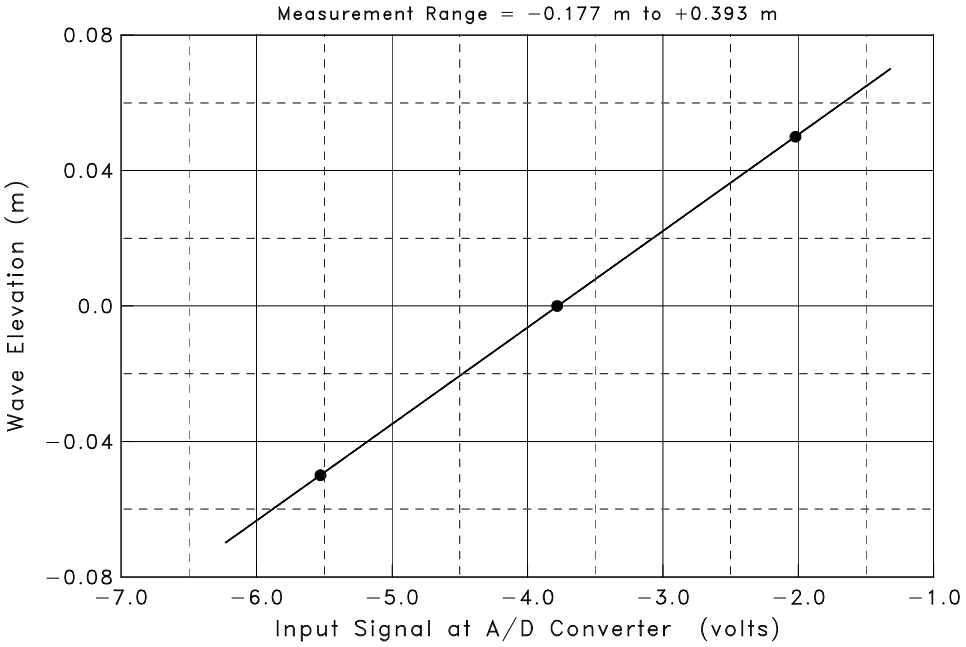

Calibration of PCI6031E Channel 3 12:31 01 February 2011

Calibrated by: Raphael Mukaro — Calibration Status: NORMAL
Project: DCIV Water level measurements — Facility: CSIR
Sensor: WP3 — Model: WG50 — Serial No. N/A
Programmable Gain: 1 — Plug-In Gain: 1 — Filter Frequency: 1000.0 Hz

Data Point No.	Input Signal (volts)	Physical Value (m)	Fitted Curve (m)	Error (m)
1	−5.532	−0.050000	−0.049946	0.00005414
2	−3.756	0.000000	−0.000108	−0.00010792
3	−1.968	0.050000	0.050054	0.00005379
Maximum Error = −0.108% of Calibration Range				

$$Y = C_0 + C_1 V$$

where $Y(t)$ = Wave Elevation (m)
$V(t)$ = input signal at A/D converter (volts)
C_0 = 0.105280 m
C_1 = 0.0280603 m/volt

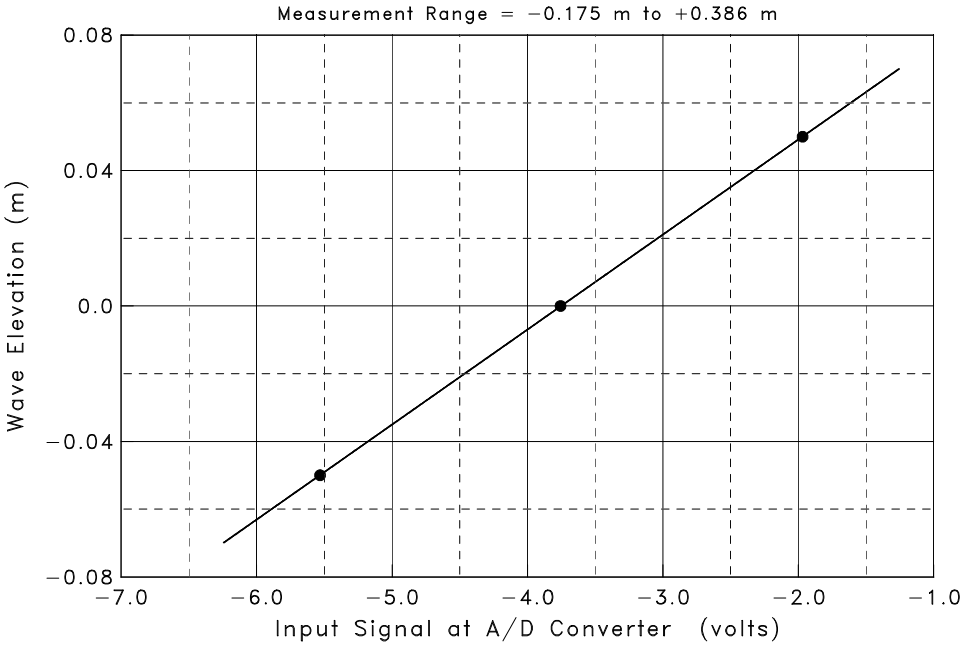

Appendix B : Typical wave images captured at each of the 20 phases in a full wave cycle.

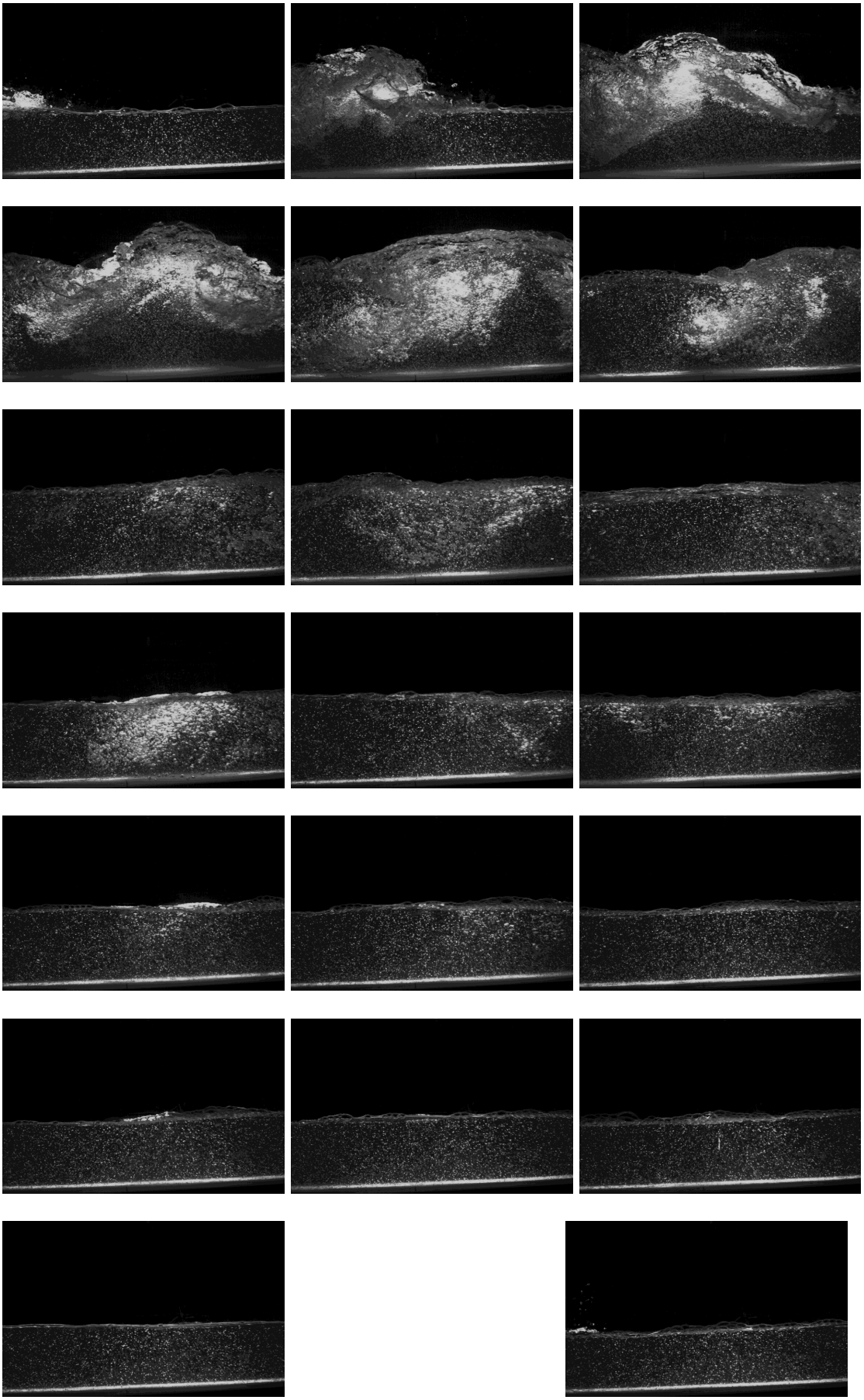

"Never measure the height of a mountain until you have reached the top. Then you will see how low it was."
- Dag Hammarskjold - Swedish Statesman and United Nations official, 1905-1961.

The beautiful Stellenbosch mountain is near CSIR Coastal and Hydraulics Engineering laboratory where experiments reported here were carried out. This spectacle inspired and kept me going when things got tough. Picture courtesy of *9th International Workshop on Adaptive Optics for Industry and Medicine (AOIM)*, Stellenbosch, South Africa, 2013.